Republic of Iraq
Ministry of Higher Education and Scientific Research
University of Babylon
College of Engineering
Civil Engineering Department

Structure Behavior of Hybrid Reinforced Concrete Corner Beam-Column Joints Under Effect of Monotonic and Cyclic Loading

A Thesis
Submitted to the College of Engineering at the University of Babylon in Partial Fulfillment of the Requirements for the Degree of Doctor of Philosophy in Engineering / Civil Engineering /Structures.

By

Wissam Nadir Najim Abdullah

Supervised By

Prof. Dr. Ammar Yaser Ali

2023 A.D. 1444 H.D.

بِسْمِ اللَّهِ الرَّحْمَنِ الرَّحِيمِ

فَأَمَّا الزَّبَدُ فَيَذْهَبُ جُفَاءً وَأَمَّا مَا يَنفَعُ النَّاسَ فَيَمْكُثُ فِي الْأَرْضِ

صَدَقَ اللَّهُ العلي العَظِيمُ

سورة الرعد (اية 17)

Acknowledgments

Praise be Allah, the most Gracious, most Merciful, Who gave me the ability and desire to complete this study.

I would like to express my deepest gratitude to my supervisor **Dr. Ammar Yaser Ali** for his exceptional guidance, and mentorship throughout my doctoral studies. His knowledge, and expertise were instrumental in helping me navigate the complexities of the research process. I am grateful for his encouragement, and constructive feedback, which helped me refine my ideas and strengthen my arguments.

I would like to acknowledge the Civil Engineering Department at the University of Babylon members, staff, and colleagues who have contributed to my academic journey.

Also, I would like to express my deepest appreciation to the staff of civil engineering at the University of Kerbala especially **Dr. Bahaa Hussain** and **Dr. Alaa Shaban** for their critical role in helping me achieve my experimental program.

I would like to express my heartfelt gratitude to my wife for her support, and understanding throughout my journey towards obtaining my PhD.

I would also like to thank my parents and siblings for their support, and encouragement throughout my life. I hope to make them proud with my achievements.

To my friends, **Dhafer Mardan, Mustafa Kareem, and Mustafa Salah** who have played a part in my PhD journey, I am deeply grateful. Their support and encouragement have been instrumental in my success, and I could not have done it without them.

Last but not least, I would like to acknowledge **Dr. Majid Mohammed Ali** and **Dr. Mohammed Kareem, Mohammed Al Ammar** who have contributed to my academic journey. I am grateful for the knowledge and skills I have acquired from them.

Wissam Nadir

Abstract

The beam-column joints play an important role in maintaining the integrity of reinforced concrete (RC) structures, especially during earthquake. These joints cause significant damage and even lead to building collapse if not adequately designed. In recent years, various advancements have been made to improve the seismic performance of building components, including beam-column joints. However, despite these improvements, external beam-column joints, particularly corner joints, are still susceptible to severe damage during earthquakes.

To address this issue, an experimental study was conducted to enhance the performance of corner beam-column joints utilizing ultra-high performance concrete (UHPC) instead of normal strength concrete (NSC) in the joint region. Twenty-two scaled RC corner beam-column joints were constructed and tested under cyclic and monotonic load. The key variables were the presence of transverse reinforcement in the joint core or not, joint material, the configuration of UHPC in the joint region, spacing of transverse reinforcement in adjoining members, anchorage length passing through the joint core, and loading protocol.

The results of the study showed that using UHPC in the joint region can lead to a shift the failure mechanism from joint shear failure (brittle) to flexural failure (ductile), which is caused by the generation of a plastic hinge out of the joint core. Moreover, the use of UHPC enhances the joint shear capacity by approximately 27% to 54%, increases energy absorption by up to 163%, and improves damage tolerance, all while completely eliminating transverse reinforcement in the joint core. Furthermore, the use of UHPC in the joint region allows for the reduction of transverse reinforcement in beams and columns, which eliminates the congestion of steel reinforcement in the joint region. In addition, replacing the NSC in the joint area with UHPC reduces

the anchorage length of the longitudinal bar in the beam required to pass through the joint core from 25 diameter of beam bar which is recommended by most national codes to 15 diameter of beam bar owing to the superior bond strength of UHPC.

On the other hand, utilizing GFRP bars as a Near Surface Mounted (NSM) reinforcement shows superior performance compared to the use of internally reinforced GFRP bars.

In theory study, most national codes tend to overestimate the shear strength of beam-column joints and may not be suitable for use in design. This can lead to inadequate joints and compromise the overall structural integrity of reinforced concrete buildings during earthquakes or other events. Based on the analytical study, a modified code provision was proposed that offers a more accurate calculation of the shear strength for exterior beam-column joints.

List of content

Subject	Page
Acknowledgment	I
Abstract	II
List of Contents	IV
List of Tables	VII
List of Figures	VIII
Notation	XIII
Abbreviation	XIV
Chapter One: Introduction	01
1.1 Introduction	01
1.2 Beam-column joint classification	06
1.3 The challenges in the application of modern building code requirements	07
1.4 Ultra high-performance concrete (UHPC)	09
1.4.1 Application of UHPC	12
1.5 Problem statement	16
1.6 Research objectives	16
1.7 Thesis Layout	18
Chapter Two: Literature Review	19
2.1 Introduction	19
2.2 Shear strength mechanism of beam-column joints	19
2.3 The failure mode of beam-column joint	21
2.4 Experimental database	21
2.5 Factors affecting the response of RC beam-column joints	22
2.5.1 Effect of concrete compressive strength	23
2.5.2 Effect of eccentric connection	24
2.5.3 Effect of joint aspect ratio	25
2.5.4 Effect of column axial load	27
2.5.5 Effect of end anchorage of beam longitudinal bars in joint region	30
2.5.6 Effect of development length of flexural bars in beam passing/terminated in the joint core	32
2.5.7 Effect of the transverse reinforcement in the joint core	33
2.5.8 Effect of beam longitudinal reinforcement ratio	35
2.6 Structural Behavior of Hybrid RC Beam-Column Joints under Cyclic Load	36
2.6.1SFRC/NSC hybrid beam-column joints	37
2.6.2 Utilize hybrid fibers in SFRC/NSC beam-column joints	46
2.6.3 HPFRCC/NSC hybrid beam-column joints	48
2.7 Summary and Concluding remarks	58
Chapter Three: Experimental Program	62
3.1 Introduction	62
3.2 Test Matrix	63
3.3 Specimens details	65
3.3.1 Details of group I	67
3.3.2 Details of group II	70
3.3.3 Details of group III	71
3.3.4 Details of group IV	73
3.3.5 Details of group V	77
3.4 Material properties	77
3.4.1 Ultra-high performance concrete (UHPC)	77

Subject	Page
3.4.2 UHPC constituents material	81
3.4.2.1 Cement	81
3.4.2.2 Fine sand	81
3.4.2.3 Silica fume (SF)	81
3.4.2.4 Superplasticizer (SP)	81
3.4.2.5 Steel fiber	82
3.4.3 Normal strength concrete (NSC)	83
3.5 Mechanical properties and testing method for concrete	83
3.5.1 Mechanical properties of UHPC	83
3.5.1.1 Compressive strength	83
3.5.1.2 Splitting tensile strength	85
3.5.1.3 Flexural strength (Modulus of rupture)	86
3.5.1.4 Direct tensile strength	87
3.5.2 Mechanical properties of NSC	92
3.5.2.1 Compressive strength	92
3.5.2.2 Splitting tensile strength	93
3.5.2.3 Flexural strength (modulus of rupture)	94
3.5.3 Mechanical properties of reinforcing bars	95
3.6 Construction method	96
3.7 Test setup	107
3.8 Loading protocol	111
Chapter Four: Experimental Results and Discussions	114
4.1 Introduction	114
4.2 Specimens Tested under Cyclic Load	115
4.2.1 Cracks pattern and failure mode of the tested specimens under cyclic load	115
4.2.1.1 Cracks pattern and failure mode of group I tested under cyclic load	116
4.2.1.1 Cracks pattern and failure mode of group II tested under cyclic load	126
4.2.1.1 Cracks pattern and failure mode of group III tested under cyclic load	132
4.2.1.1 Cracks pattern and failure mode of group IV tested under cyclic load	136
4.2.1.1 Cracks pattern and failure mode of group V tested under cyclic load	144
4.2.2 Load-drift response	147
4.2.2.1 Load-drift response of group I tested under cyclic load	148
4.2.2.2 Load-drift response of group II tested under cyclic load	152
4.2.2.3 Load-drift response of group III tested under cyclic load	155
4.2.2.4 Load-drift response of group IV tested under cyclic load	157
4.2.2.5 Load-drift response of group V tested under cyclic load	160
4.2.3 Ductility of the tested specimens under cyclic	162
4.2.3.1 Energy dissipation capacity of group I tested under cyclic load	163
4.2.3.2 Energy dissipation capacity of group II tested under cyclic load	165
4.2.3.3 Energy dissipation capacity of group III tested under cyclic load	166
4.2.3.4 Energy dissipation capacity of group IV tested under cyclic load	167
4.2.3.5 Energy dissipation capacity of group V tested under cyclic load	168
4.2.4 Stiffness	170
4.2.4.1 The stiffness of group I tested under cyclic load	171
4.2.4.2 The stiffness of group II tested under cyclic load	172
4.2.4.3 The stiffness of group III tested under cyclic load	173
4.2.4.4 The stiffness of group IV tested under cyclic load	173
4.2.4.5 The stiffness of group V tested under cyclic load	174

Subject	Page
4.2.5 Joint principle stresses for the specimens that tested under cyclic load	175
4.2.6 Joint shear strength of tested specimens under cyclic load	179
4.3 Specimens Tested under Monotonic Load	180
4.3.1 Cracking pattern and failure mode for specimens tested under monotonic load	181
4.3.1.1 Cracks pattern and failure mode of group I tested under monotonic load	182
4.3.1.2 Cracks pattern and failure mode of group II tested under monotonic load	184
4.3.1.3 Cracks pattern and failure mode of group III tested under monotonic load	186
4.3.2 load-drift response of tested specimens under monotonic load	190
4.3.3 Ductility of tested specimens under monotonic load	191
4.3.4 Stiffness of tested specimens under monotonic load	192
4.3.5 Joint principle stresses	193
Chapter Five: Assessment of codes provision for predicting joint shear strength	**196**
5.1 Introduction	196
5.2 Code provisions for predicting joint shear strength	196
5.2.1 ACI-ASCE committee 352	197
5.2.2 ACI 318-19	198
5.2.3 IS 13920:2019	198
5.2.4 National Standard of Canada CSA A23.3:19	199
5.2.5 Architectural Institute of Japan AIJ:2010 Standard	199
5.2.6 NZS 3101-1	200
5.2.7 BS EN 1998-1:2004	201
5.3 Analysis of code provisions via experimental result	201
5.4 Application of ACI 318 code on the experimental results of the present study.	214
Chapter Six: Conclusions and Recommendations	220
6.1 Introduction	220
6.2 Experimental conclusions	221
6.3 Theoretical conclusions	224
6.4 Recommendations	235
References	**226**
Appendix A	**A-1**
Appendix B	**B-1**
Appendix C	**C-1**

List of Tables

No.	Title of Tables	Page
3.1	Specification of the tested specimens	65
3.2	Moderate code provision for calculating the development length passing through the joint core	74
3.3	Mix proportions of UHPC	79
3.4	Physical properties of micro steel fiber	82
3.5	Conversion factor to determine the UHPC cylinder compressive strength	84
3.6	Test results of UHPC compressive strength	85
3.7	Test results of UHPC splitting tensile strength	86
3.8	Test results of UHPC flexural strength	87
3.9	Test result of UHPC direct tensile strength	91
3.10	Test result of NSC compressive strength	93
3.11	Test result of splitting tensile strength of NSC	93
3.12	Test results of modulus of rupture test for NSC	95
3.13	Mechanical properties of steel and GFRP bars used in the present study	96
4.1	Cracking load, ultimate load, and failure mode of the tested specimens	115
4.2	Cracking load, ultimate load, and failure mode of the tested specimens under monotonic load	181
5.1	Confinement factor (λ) for different cases in ACI-ASCE	197
5.2	Confinement factor (λ) for different cases in ACI 318-19	198
5.3	Confinement factor (φ) for different cases in CSA A23.3:19	199
5.4	Confinement factor (λ) for different cases in AIJ:2010	200
5.5	Statistical analysis of predicted joint shear strength to experimental shear strength	203
5.6	Experimental results of the tested specimens	216

List of Figures

No.	Title of Figures	Page
1.1	Shear force and bending moment diagram for beam-column join during the earthquake	02
1.2	Collapsed or partially collapsed buildings due to failure of beam-column joints	03
1.3	Buildings collapse due to failure of beam-column joints, Izmit, Turkey, Earthquake in 1999	03
1.4	Collapse of the reinforced concrete building	04
1.5	Damage to partial damage of reinforced concrete building due to beam-column failure in Chi-Chi, Taiwan, earthquake, 1999	04
1.6	Damage of corner beam-column joint due to earthquake	05
1.7	Geometrical classification of RC beam-column joints	07
1.8	Typical tensile strain behavior in tension for concrete	11
1.9	Rehabilitation of Chillon Viaducts along Lake Geneva	13
1.10	Strengthening of CN rail bridge	14
1.11	Rehabilitation process of Canada's Mission Bridge	14
1.12	The world's first UHPC bridges	15
2.1	Forces transmitted to the joint core	20
2.2	Effect of concrete compressive strength on the joint shear strength	24
2.3	Forces acting on the eccentric beam-column connection	24
2.4	Effect of joint aspect ratio on unreinforced exterior joints shear strength	26
2.5	Effect of joint aspect ratio on the reinforced exterior and interior joints shear strength	27
2.6	Details of diagonal strut through the joint core	29
2.7	Effect of axial load on unconfined exterior joint shear strength	29
2.8	Effect of axial load on the confined exterior and interior joint shear strength	30
2.9	Failure mode of common end anchorage of beam longitudinal bars in joint core	31
2.10	Effect of beam longitudinal reinforcement ratio on the joint shear strength	35
2.11	Details of the tested specimens, Ref. 26	38
2.12	Details of the tested specimens, Ref. 141	39
2.13	Details of the tested specimens, Ref. 144	41
2.14	Details of the tested specimens, Ref. 120	43
2.15	Rigid-framed railway bridges	44
2.16	Damage at the column external face of exterior joints specimens	45
2.17	Failure modes of the tested specimens, Ref. 160	47
2.18	Specimens details, Ref. 163	50
2.19	Details of the tested specimens, Ref. 151	51
2.20	Pull out of beam longitudinal bar, Ref. 151	51
2.21	Cracks patterns at the end of the test, Ref. 171	52
2.22	Details of the examined specimens, Ref. 172	53
2.23	Crack patterns at the end of test, Ref. 173	54
2.24	Failure mode of the tested specimens, Ref. 175	55
2.25	Different patterns to use ECC in beam-column joint	56
2.26	Failure mechanism of tested beam-column joint, Ref 179	58
3.1	Detail of the designation of tested specimens	63

No.	Title of Figures	Page
3.2	Configuration of UHPC in the joint region of the tested specimens	67
3.3	Specimens details of group I	69
3.4	Specimens details of group II	71
3.5	Specimens details of group III	72
3.6	Specimens details of group IV	76
3.7	Specimens details of group V	77
3.8	The UHPC constituent material and its percentage by total mix weight	79
3.9	UHPC mixing procedure	80
3.10	Flow test procedure for UHPC	80
3.11	Photo of copper-coated micro steel fiber	82
3.12	Compressive strength test and failure mode of tested specimen	84
3.13	UHPC splitting tensile strength test and failure mode of tested specimen	85
3.14	Flexural strength test under one point load, and failure mode of tested specimen	87
3.15	Direct tensile strength specimen	89
3.16	Setup and preparation for direct tensile strength test of UHPC	89
3.17	Failure mode of UHPC dog-bone specimens under direct tension	90
3.18	Tensile stress-strain curve for UHPC used in the present study	91
3.19	Compressive strength test of NSC	92
3.20	NSC splitting tensile strength test and failure mode of tested specimen	94
3.21	Modulus of rupture test and failure mode for NSC	95
3.22	Steel bar test and failure mode	96
3.23	Casting specimens process	98
3.24	Preparing for construction of the cold joint	102
3.25	Rehabilitation of specimens processing (cold joint)	103
3.26	Process of bonging NSM steel bars	104
3.27	Reinforcement detail of specimen $CJ_2NT_3S_{50}C$	105
3.28	Flexural strengthening of specimen $CJ_2NT_4S_{50}C$ using NSM-GFRP bars	106
3.29	Test setup and instrumentation	108
3.30	Loading condition	109
3.31	Installation the vertical LVDTs	110
3.32	The side of the specimen monitored by DIC	110
3.33	Ends restrained condition	111
3.34	Cyclic load protocols examined by Takemura and Kawashima	112
3.35	Comparison of load-drift response under six different loading protocols	112
3.36	Cyclic load protocol history	113
4.1	Damage process and crack pattern of specimen $CJ_1NT_1S_{50}C$ monitored by DIC	117
4.2	Failure mechanism and crack propagate at the end of test specimen $CJ_1NT_1S_{50}C$	118
4.3	Damage process and crack pattern of specimen $CJ_2NT_1S_{50}C$ monitored by DIC.	119
4.4	Failure mode and crack pattern at the end of the test specimen $CJ_2NT_1S_{50}C$	119
4.5	Failure mechanism and crack pattern at the end of the test specimen $CJ_2U_{1h}T_1S_{50}C$	123

No.	Title of Figures	Page
4.6	Failure mode and crack pattern at the end of the test specimen $CJ_2U_{2h}T_1S_{50}C$	124
4.7	Failure mode and crack pattern at the end of the test specimen $CJ_1U_{1h}T_1S_{50}C$	124
4.8	Damage process and crack pattern of UHPC specimen monitored by DIC	125
4.9	Failure mode and crack pattern at the end of the test specimen $CJ_2NT_1S_{100}C$	128
4.10	Failure mode and crack pattern at the end of the test specimen $CJ_2U_{1h}T_1S_{100}C$	129
4.11	Failure mode and crack pattern at the end of the test specimen $CJ_2U_{2h}T_1S_{100}C$	130
4.12	Damage process and crack pattern of tested specimen in group II monitored by DIC	131
4.13	Failure mode and crack pattern at the end of the test specimen $CJ_2U_{1c}T_1S_{50}C$	134
4.14	Failure mode and crack pattern at the end of the test specimen $CJ_2U_{1c}T_1S_{100}C$	135
4.15	Damage process and crack pattern of tested specimen in group III monitored by DIC	136
4.16	Failure mode and crack pattern at the end of the test specimen $CJ_2NT_2S_{50}C$	138
4.17	Failure mode and crack pattern at the end of the test specimen $CJ_2NT_2S_{100}C$	139
4.18	Failure mode and crack pattern at the end of the test specimen $CJ_2U_{1h}T_2S_{50}C$	141
4.19	Failure mode and crack pattern at the end of the test specimen $CJ_2U_{1h}T_2S_{100}C$	142
4.20	Damage process and crack pattern of tested specimen in group IV monitored by DIC	143
4.21	Failure mode and crack pattern at the end of the test specimen $CJ_2NT_3S_{50}C$	145
4.22	Failure mode and crack pattern at the end of the test specimen $CJ_2NT_4S_{50}C$.	146
4.23	Damage process and crack pattern of tested specimen in group V which was monitored by DIC	147
4.24	Drift response measurement	148
4.25	Load-drift response of the tested specimens in group I	150
4.26	Load-drift envelopes curves for specimens tested under compression cyclic load in group I	152
4.27	Load-drift response of the tested specimens in group II	154
4.28	Load-drift envelopes curves for specimens tested under compression cyclic load in group II	155
4.29	Load-drift response for cold joint specimens	156
4.30	Compares the load-drift envelopes of cold joint and hot joint specimens	157
4.31	Load-drift response of the tested joints in IV group	158
4.32	4.32 compares the load-drift envelopes of the tested specimens in group IV	160
4.33	Load-drift response of the tested specimens in group V	161

No.	Title of Figures	Page
4.34	The envelope curves for the tested specimens in the V group compared to the control specimen	162
4.35	Cumulative dissipated energy with respect to drift ratio for the tested specimens in group I	164
4.36	Cumulative energy of the tested specimens in group I at the ultimate load	164
4.37	Cumulative dissipated with respect to drift ratio for the tested specimens in group II	165
4.38	Cumulative energy of the tested specimens in group II at the ultimate load	166
4.39	Cumulative dissipated with respect to drift ratio for the tested specimens in group III	166
4.40	Cumulative energy of the tested specimens in group III at the ultimate load	167
4.41	Cumulative dissipated with respect to drift ratio for the tested specimens in group IV	168
4.42	Cumulative energy of the tested specimens in group IV at the ultimate load	168
4.43	Cumulative dissipated with respect to drift ratio for the tested specimens in group V compared with that reinforced by steel bar	169
4.44	Cumulative energy of the tested specimens in group V at the ultimate load	169
4.45	The energy absorbed by the tested specimens under cyclic load	170
4.46	Determination of the initial stiffness	171
4.47	The initial stiffness of the tested specimens in group I	172
4.48	The stiffness of the tested specimens in group II	172
4.49	The initial stiffness of the tested specimens in group III	173
4.50	The initial stiffness of the tested specimens in group IV	174
4.51	The stiffness of the tested specimens in group V	174
4.52	The initial stiffness evaluated from the tested specimens under cyclic load	175
4.53	Free body diagram of the joint region	176
4.54	Principle stresses at mid-hight of the joint	178
4.55	Comparison of maximum principal tensile stress induced in joint with the tensile strength of concrete	178
4.56	Comparison the joint shear strength for both types of concrete	180
4.57	Failure mode and crack pattern at the end of the test specimen $CJ_2NT_1S_{50}M$	183
4.58	Failure mode and crack pattern at the end of the test specimen $CJ_2U_{1h}T_1S_{50}M$	183
4.59	Failure mode and crack pattern at the end of the test specimen $CJ_2NT_1S_{100}M$	185
4.60	Failure mode and crack pattern at the end of the test specimen $CJ_2U_{1h}T_1S_{100}M$	185
4.61	Failure process of tested specimens in groups I and II that were monitored by DIC	186
4.62	Failure mode and crack pattern at the end of the test of the specimens in group III	188
4.63	Failure process of tested specimens in group III that mentored by DIC	189

No.	Title of Figures	Page
4.64	Load-drift response of the tested specimens in groups I,II, and III which tested under monotonic load	191
4.65	The Energy absorption for tested specimens under monotonic load	192
4.66	The initial stiffness of the tested specimens under monotonic load	193
4.67	Comparison of maximum principle tensile strength of materials with the direct tensile strength of concrete	194
4.68	Comparison between the joint shear strength of conventional NSC specimens and that of UHPC specimens	195
5.1	Confinement condition of beam-column joint by transverse beams	197
5.2	Predicted joint shear strength based on ACI-ASCE 354R vs experimental joint shear strength	204
5.3	Predicted joint shear strength based on ACI 318-19 vs experimental joint shear strength	205
5.4	Predicted joint shear strength based on IS 13920 vs experimental joint shear strength	206
5.5	Predicted joint shear strength based on CSA A23.3:19 vs experimental joint shear strength	207
5.6	Predicted joint shear strength based on AIJ vs experimental joint shear strength	208
5.7	Predicted joint shear strength based on NZS 3101-1 vs experimental joint shear strength	209
5.8	Predicted joint shear strength based on BS EN 1998-1 vs experimental joint shear strength	210
5.9	The percentage of exterior joints that shows overestimated joint shear strength based on different codes	212
5.10	The percentage of interior joints that shows overestimated joint shear strength based on different codes	212
5.11	The percentage of joints confined by all four sides that shows overestimated joint shear strength based on different codes	213
5.12	Relationship between the predicted and experimental joint shear strength	216
5.13	Relationship between the predicted and experimental joint shear strength factor	217
5.14	Predicted joint shear strength based on modified ACI 318 vs. experimental joint shear strength for exterior beam-column joints	219
5.15	Relationship between the predicted joint shear strength based on modified ACI 318 and experimental result of the present study	219

Notations	
A_{str}	Cross-sectional area of the concrete strut
A_g	Cross-sectional area of column
a_s	Depth of concrete strut
b_c	Total width of the column
b_s	Width of concrete strut
b_j	Joint width
β_c	Angle of strut inclination
D_c	Maximum force generated by concrete struts
d_b	Bar diameter
d_f	Fiber diameter
f_t	Diagonal tension stresses in the joint core
f_c	Diagonal compression stresses in the joint core
$f_c^{`}$	Cylinder concrete compressive strength
f_{ctm}	Average concrete tensile strength
f_y	Yield strength of steel bar
f_{yd}	Design steel yield strength
h_b	Total beam depth
h_c	Total column depth
jd	lever arm between the tensile force and centroid of compression force
K_i	Initial stiffness
l_c	Total length of the column
l_f	Fiber length
l_{dh}	Minimum development length
M_b	Bending moment developed at joint-beam interface
N	Axial load supported by column
T	Tensile forces developed by longitudinal reinforcements of beams
V_{jh}	Horizontal joint shear force
$V_{col.}$	The column shear force
γ_j	Joint shear strength coefficient
ρ_b	Longitudinal reinforcement ratio in beam
$\propto_b$	Parameters used in determining development lengths for straight reinforcing bars
$\propto_1, \propto_2$	Parameters used in determining development lengths for standard hooks
v_d	Normalised design axial force in the column
γ_{Rd}	The model uncertainty factor on the design value of resistances, taken as being equal to 1,2 or 1,0 respectively for DCH or DCM
ϕ	Diameter of the reinforcement bar
σ_s	Permissible stress in the reinforcement bar
τ_{bd}	Bond stress between reinforcement and concrete
μ	Ductility index
Δ_u	Displacement at peak load
Δ_y	Displacement at yield of steel reinforcement
Δ_i	Displacement corresponding to 0.75 of ultimate load
σ_1	Principle tensile stress (f_t)
σ_2	Principle compressive stress (f_c)
σ_N	Normal axial compressive stresses on the column
τ_{xy}, τ_{jh}	Horizontal joint shear stress

Abbreviations

3D	Three Dimension
ACI	American Concrete Institute
ACI-ASCE	Joint of American Concrete Institute with American Society of Civil Engineers
ASTM	American Society for Testing and Materials
BS EN	British Standard
COV	Coefficient of Variation
CSA	Canadian Standard Code
DIC	Digital Image Correlation
ECC	Engineering Cementitious Composite
FRC	Fiber-Reinforced Concrete
GFRP	Glass Fiber Reinforced Polymer
HPFRCC	High-Performance Fiber Reinforced Cementitious Composite
HSC	High-Strength Concrete
IQS	Iraqi Specifications
IS	Indian Standard
LVDT	Linear Variable Differential Transducer
MAE	Mean Absolute Errors
NSC	Normal Strength Concrete
NSM	Near-surface mounted
NZS	Standards of New Zealand
RC	Reinforced concrete
SD	Standard Deviation
SEAOC	Structural Engineers Association of California
SF	Silica Fume
SFRC	Steel Fiber Reinforced Concrete
SP	Superplasticizer
UHPC	Ultra-High Performance Concrete

Chapter One

Introduction

1.1 Introduction

Reinforced concrete (RC) structures consist of various structural elements that work together to provide stability and support. Among these elements, beam-column joints are of particular significance as they play a critical role in transferring the forces between the beams, columns, and stories. During an earthquake, beam-column joints are exposed to higher levels of shear forces than the surrounding beam and column members. This makes the design and construction of beam-column joints a crucial consideration in ensuring the structural safety and performance of RC buildings. Figure 1.1 illustrates the shear forces acting on a beam-column joint during an earthquake, highlighting the significance of this element in RC structures. Post-earthquake analyses have indicated that the beam-column joints of many existing RC structures contributed to their partial or complete collapse. This was attributed to severe damage sustained by the joints, which resulted in a loss of axial load continuity to the lower level [1]–[3]. Several structural deficiencies have been identified as the reason behind the severe damage sustained by the beam-column joints in many RC structures. These deficiencies include inadequate transverse reinforcement in the joint region,

insufficient anchorage of longitudinal bars in the beam, a strong beam-weak column design, and the use of inferior quality materials. As a result of these deficiencies, the beam-column joints were unable to withstand inelastic deformation generated during an earthquake, ultimately leading to their failure and the partial or complete collapse of the RC structures [4]–[6].

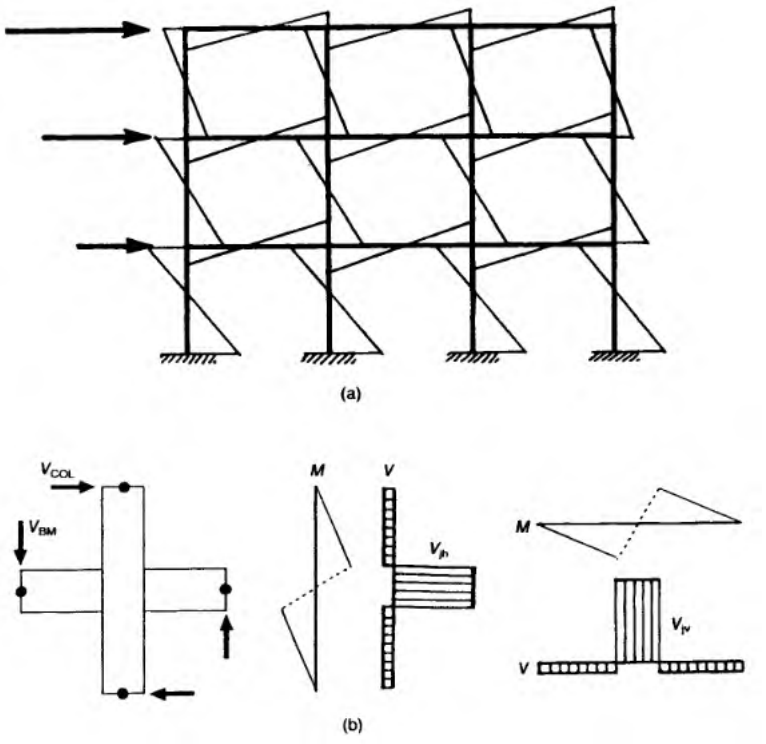

Figure 1.1 Shear force and bending moment diagram for beam-column joins during the earthquake [7].

Figures 1.2 through Figure 1.6, visually demonstrate the severe consequences that can result from the failure of beam-column joints in RC buildings. The examples depicted in the figures showcase the devastating effects of structural deficiencies in beam-column joints, such as inadequate transverse reinforcement, insufficient anchorage of longitudinal bars, strong beam-weak column design, and the use of substandard materials. By studying the visual examples provided, engineers can better understand the significance of beam-column joints in ensuring the safety and stability of RC structures during seismic events.

(a) (b) (c)

Figure 1.2 Collapsed or partially collapsed buildings due to failure of beam-column joints,(a)beam-column joint failures due to insufficient transverse reinforcement at the joint [2],(b) Strong beam-weak column and failure of beam-column joints [1], and (c) collapsed building due to poor details of joint [3]

Figure 1.3 Buildings collapse due to failure of beam-column joints, Izmit, Turkey, Earthquake in 1999 [8], [9].

(a) (b)

Figure 1.4 Collapse of the reinforced concrete building; a) Turky, Duzce earthquake,1999; b) Sarpole-Zahab earthquake, Iran 2017 [10][11].

Figure 1.5 Damage to partial damage of reinforced concrete building due to beam-column failure in Chi-Chi, Taiwan, earthquake, 1999 [12].

Figure 1.6 Damage of corner beam-column joint due to earthquake [8], [13]–[15].

1.2 Beam-column joint classification

The beam-column joints are classified based on their loading conditions and deformation capacity. ACI-ASCE [16] classified the joints into two types: Type-1 is constructed for strength alone, without considering the ductility necessary to withstand inelastic deformation. These joints can be designed using ACI 318 [17], except for chapter 18 (earthquake-resistant structures). Type-2 connections, on the other hand, are designed to endure seismic loads or blast impacts and must dissipate energy through reversal deformations in the inelastic region. These joints must meet the requirements outlined in chapter 18 of ACI 318 [17].

However, The beam-column joint can also be classified based on the confinement by transverse beams and columns to: the knee joint, exterior joint, interior joint and corner joint, as illustrated in Figure 1.7.

The findings of previous earthquake reports indicate that the external beam-column joints exhibit a greater susceptibility to damage in comparison to the internal beam-column joint. This increased vulnerability can be attributed to several factors, including the low level of confinement provided by transverse beams and the presence of high unbalanced moments resulting from the discontinuity of the beam and slab in the external joint. Additionally, the bond condition of the beam bar is less robust, which contributes to the increased vulnerability of the external beam-column joint [18][19]. Corner joints are considered to be the most vulnerable among all exterior joints. This is because they experience the lowest level of confinement and are subjected to biaxial shear demands [20]. Furthermore, due to their location at the edges of the building, they are the farthest away from the center of rigidity of the structure. As a result, they are more prone to the torsional behavior of the entire building, which can further exacerbate the vulnerability of the joint [18].

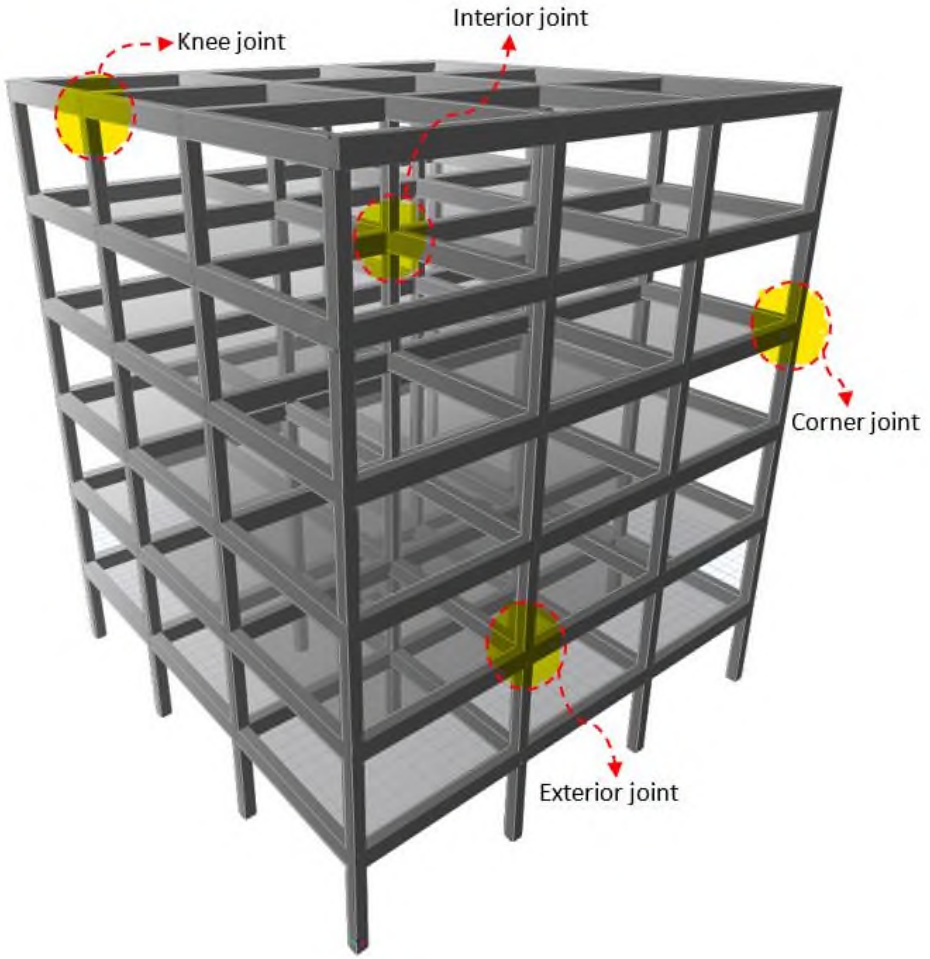

Figure 1.7 Classification of RC beam-column joints based on confinement condition

1.3 The challenges in the application of modern building code requirements

The Structural Engineers Association of California (SEAOC) suggested the first ductile joint details in 1963 and 1965, which included a method for determining the necessary transverse reinforcement in the joint core and the shear strength of beam-column joints [21]. On the other hand, the first building code, ACI 318-71 [22], proposed the use of transverse reinforcement in the joint core of the beam-column joint in high seismic areas. In 1973, Park and Paulay expressed that the transverse reinforcement specified by ACI 318-71 was insufficient [23].

In 1976, the ACI-ASCE committee developed guidelines for beam-column joint design, following extensive research on the topic. These guidelines focused on several key factors, including moment strength ratio, shear strength, transverse reinforcement that confined the joint core, and development length of the longitudinal bar in the beam that should pass/terminate through the joint core. The purpose of these guidelines was to ensure that structures in high seismic areas would have the required strength and ductility to withstand inelastic deformation caused by earthquakes [24][25].

All building codes advise using a significant amount of transverse reinforcement in the joint area, which has made it difficult to construct, pour, and vibrate the concrete in that location. This has resulted in the formation of weak joints that are unable to withstand inelastic deformations [26]–[28]. Moreover, meeting the minimum required anchoring length of the steel beam bar passing/terminating through the joint core required larger cross-sections for both the column and beam. Alternatively, multiple smaller-diameter steel bars can be used, which could lead to additional difficulties during casting and construction [29].

Tsonos [30][31] examined the performance of exterior RC beam-column joint designed based on different modern codes. The specimens were; A1 was designed according to ACI 318 [32] and ACI-ASCE [33], E1 and E2 were designed according to Eurocode 2 and Eurocode 8 [34][35]. In contrast, G1 was designed based on Greek Earthquake-Resistant Code [36]. According to the results, the failure mode of specimens A1 and E2 was due to the creation of a plastic hinge in the beam near the column face. Although both specimens had this failure mode, E2 had additional cracks in the joint area and partial loss of concrete cover on the back face of the joint.

Conversely, specimens E1 and G1 had joint shear failure in the early stages of loading despite having seismic details, which is not what was expected.

It is worth noting that compliance with code requirements did not prevent the occurrence of wide diagonal cracks in joint core during high seismic loads. The provisions are primarily intended to prevent loss of life and complete collapse of structures and to reduce the cost of post-earthquake rehabilitation [37].

Numerous studies have been conducted in the last four decades using different methods to enhance the functionality of beam-column joints and decrease the steel reinforcement congestion in this zone. One of the most frequently utilized approaches was the utilization of a more ductile and robust type of concrete in the joint area to withstand high shear stress, while normal strength concrete (NSC) was used in the remainder of the sample. This technique is known as a **reinforced hybrid concrete beam-column joint**.

1.4 Ultra high-performance concrete (UHPC)

During the 1970s and 1980s, there were significant advancements in concrete technology which led to the development of new and improved cementitious composite materials. These advancements included the use of high-strength steel micro-fibers, superplasticizers, gradation optimization, and supplemental cementitious materials. These materials were combined together to create a new generation of cementitious composites that offered greater strength, durability, and ductility than traditional concrete [38]–[40].

In the 1990s, this new class of materials was brought to the market under the name ultra-high performance concrete (UHPC). UHPC is characterized by its extremely high strength, durability, and resistance to cracking and deformation under high loads. It is made by combining a carefully selected

mix of materials, including cement, silica fume, quartz flour, and high-strength steel fibers with a low water-cement ratio. This results in a very dense and tightly packed microstructure that can withstand high compressive and tensile stresses [40][41]. In addition to the use of carefully selected materials and a low water-cement ratio, UHPC is also reinforced with high volumes of high-strength steel microfiber reinforcement. Typically, the volume of fibers used in UHPC is equal to 2 percent by volume. This high volume of steel fibers helps to reinforce the matrix and provides post-cracking tensile ductility [40].

Over the last forty years, there have been numerous attempts to improve the seismic performance of concrete by incorporating steel fiber reinforcement. However, research has shown that insufficient steel fiber content can result in only negligible improvements in tensile strength and limited property enhancements after cracking [42]. Despite improvements in tensile strength, ductility, and energy absorption, Steel Fiber Reinforced Concrete (SFRC) exhibits tensile strain softening and crack localization immediately following first cracking, as depicted in Figure 1.8(a). On the other hand, UHPC displays tensile strain hardening accompanied by multiple micro-cracks after the formation of the first crack, as illustrated in Figure 1.8 (b) [43][44].

The behavior of UHPC under direct tension is demonstrated in Figure 1.8, which can be divided into three stages: OA, AB, and beyond B. The initial stage (OA) represents the elastic response common in all FRC materials before the first crack formation. The second stage (AB) is exclusive to UHPC and characterized by multiple cracking and strain hardening. The third stage is beyond post-cracking strength (B) and represents the pullout of fibers following crack localization. When comparing UHPC's tensile response to

conventional SFRC, it's apparent that UHPC results in lower crack widths and spacing [45].

Although there is no widely accepted definition for UHPC, it is generally agreed that UHPC should possess the following characteristics:

1. Compression strength that is greater than 120 MPa as indicated by several references [46]–[49].
2. Exhibits strain-hardening behavior when subjected to uniaxial tension [50].
3. Adequate fiber reinforcement allows for sustained post-cracking tensile resistance that is equal to or greater than 5 MPa [51].
4. The maximum aggregate size is less than 5 mm, and the flow measured by the modified flow table ranges between 200-250 mm [47].

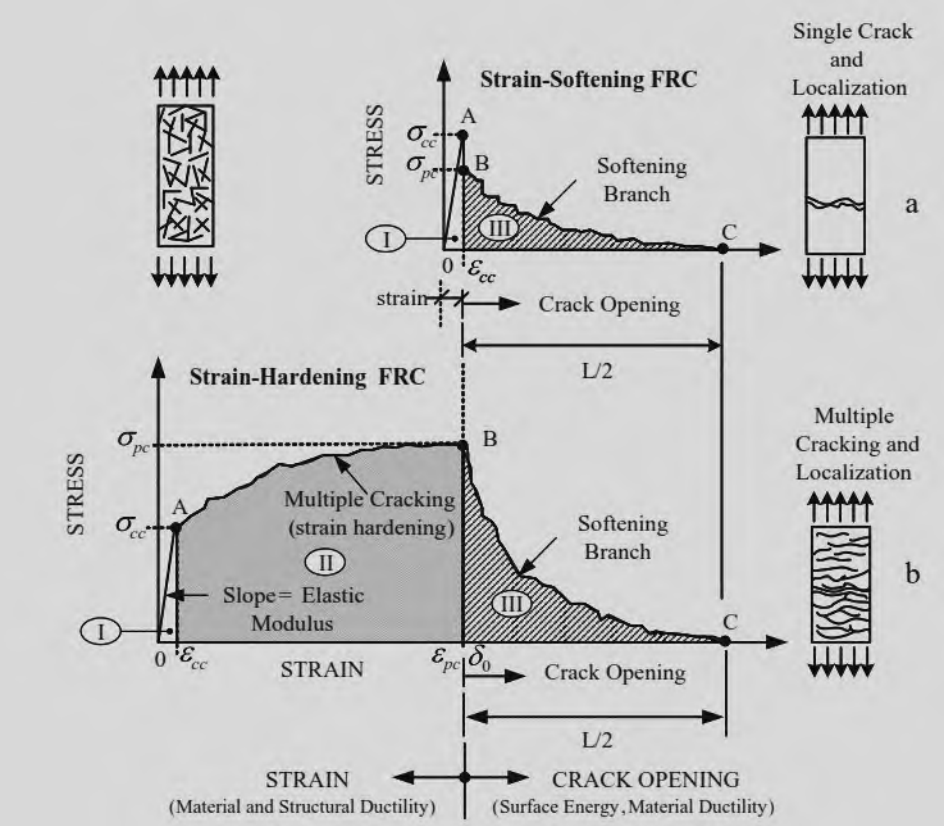

Figure 1.8 Typical tensile strain behavior in tension for concrete, a) strain-softening FRC composite, b) strain-hardening UHPC [43]

1.4.1 Application of UHPC

UHPC has become an increasingly popular material in construction projects worldwide. Its applications can be broadly categorized into two categories: first, as a rehabilitation or strengthening solution for existing structures, and second, as a material for building new structures, often involving precast elements. In both cases, UHPC offers advantages over traditional materials, such as improved durability, enhanced mechanical properties, and the ability to reduce the size of structural members while maintaining or even increasing their load-carrying capacity. Additionally, UHPC's unique properties, such as its strain-hardening behavior and sustained post-cracking tensile resistance, make it an attractive material for seismic retrofitting of existing structures [52].

UHPC is mostly used in bridge components, such as rehabilitating decks and piers, connecting precast RC elements, and repairing bridge structures[46], [53]–[55], which become popular in Asia due to the high demand for infrastructure and durability issues [41][56].

Between 1997 and 1998, the steel beams of the cooling towers in Cattenom and Civaux power plants were substituted with UHPC beams. The reason for this replacement was the harsh environment of the cooling towers that led to extensive corrosion of the steel structures. UHPC was chosen due to its exceptional durability, allowing the replacement of steel beams with lightweight elements that could have an extended lifespan without the need for maintenance or repair [57].

Switzerland has been using UHPC overlay as a technique for strengthening existing structures since 2004. The first project involved strengthening and widening the short-span bridge over the river la Morge in Chateauneuf in 2004. The cost of using UHPC for this project was comparable to traditional solutions [58]. In 2015, the Chillon Viaduct near Montreux, Switzerland,

was rehabilitated using a UHPC overlay due to the deterioration from alkali aggregate reactivity, high traffic volumes, and excessive truck weights. The UHPC was chosen for its superior durability, waterproofing, and its ability to increase capacity through a thin UHPC deck that was an integral part of the box girders. The overall cost of using UHPC for the project was less than the estimated cost of conventional strengthening methods. Figure 1.9a shows the Chillon Viaduct before rehabilitation, while Figure 1.9b shows it after the UHPC overlay was installed [52][59].

The Canadian National Railway Bridge in Quebec had its pier wall strengthened using UHPC in 2014. The existing core and reinforcing were enclosed by pouring UHPC into the formwork. This process helped to restore the pier to a condition comparable to when it was new. Figure 1.10 illustrates this process [59].

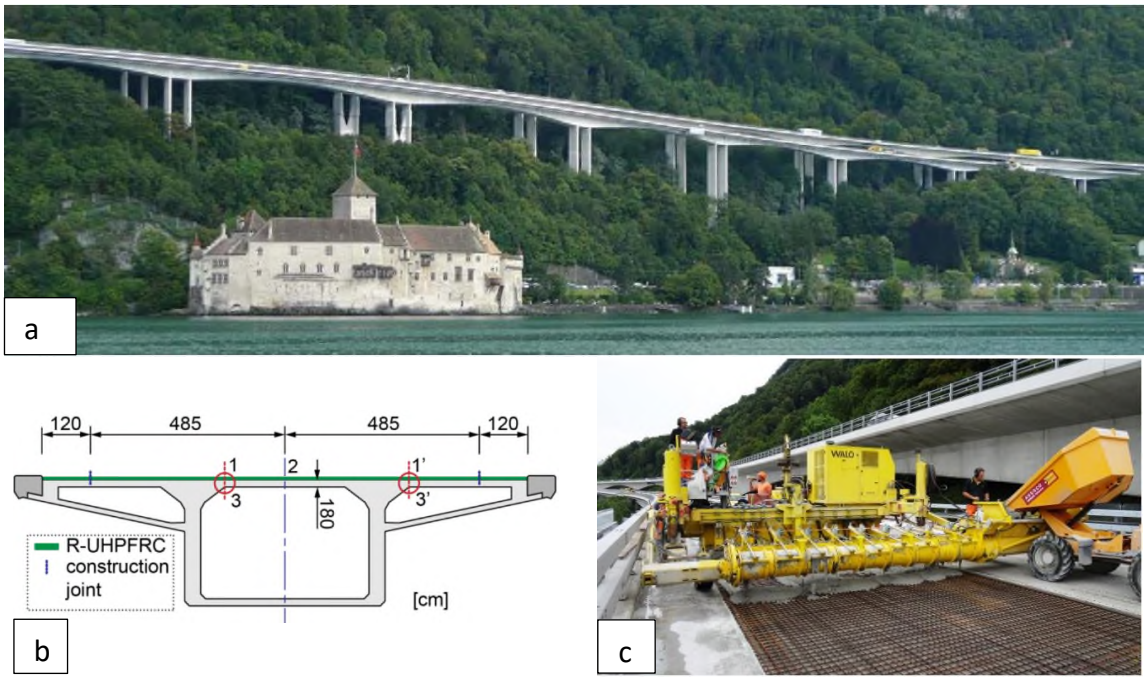

Figure 1.9 Rehabilitation of Chillon Viaducts along Lake Geneva a) Chillon Viaducts along Lake Geneva, b) Geometry of the box girders cross-section and c) UHPC casting machine [52].

Figure 1.10 Strengthening of CN rail bridge, a) CN rail bridge with concrete cover removed from the pier, b) Completed UHPC pier repair [59].

Another example of using UHPC for rehabilitation is the retrofitting of the V-shaped concrete piers of Canada's Mission Bridge, which is illustrated in Figure 1.11. The piers were encased in 3.15-meter-high UHPC jackets, making this the first application of UHPC as a seismic retrofit solution for large rectangular concrete columns. The UHPC jackets remain in excellent condition, as confirmed by a post-installation inspection conducted one year after installation. In 2015, the project received an "ACI Excellence in Concrete Award" in the Repair & Restoration category [54] [60].

Figure 1.11 Rehabilitation process of Canada's Mission Bridge [60].

UHPC has also been employed in the construction of modern structures. The first-ever engineering structure to utilize UHPC material was a prestressed pedestrian bridge in Sherbrooke, Canada, completed in 1997 [57]. In 2001,

the Bourg-lès-Valence bridges in France became the world's first UHPC road [52]. More recently, South Korea built the world's first UHPC cable-stayed road bridge in 2017 [46]. Figure 1.12 show the world's first UHPC bridges.

Figure 1.12 The world's first UHPC bridges a) Sherbrooke pedestrian bridge, completed in 1997 [57], b) Bourg-lès-Valence bridges in France, completed in 2001 [52], c) UHPC cable-stayed bridge in South Korea completed in 2017 [46]

The previous discussions suggest that UHPC could be an effective solution for enhancing the behavior of beam-column joints and eliminating the requirement for closely spaced transverse reinforcement in this area. This is due to the outstanding performance of UHPC regarding compressive, tensile, and bond strength, as well as shear resistance.

1.5 Problem statement

Many studies have looked into ways to improve the behavior of RC joints using SFRC/high-performance fiber cementitious composite (HPFCC), but they have not been able to completely eliminate the need for transverse reinforcement and prevent diagonal cracks in the joint core of exterior connections. However, there have been limited experimental investigations on corner beam-column joints under biaxial monotonic or cyclic loadings due to the complexity of the test setup. Based on the author's knowledge, no experimental studies have been conducted to improve the performance of corner beam-column joints under biaxial monotonic or cyclic loadings using UHPC material in the joint region .

1.6 Research objectives

The aim of this study is to investigate the potential of using UHPC in the joint region of reinforced concrete corner beam-column joints to improve their performance. The study will have the following objectives:

1. Conduct an extensive literature review on the hybrid behavior of beam-column joints under cyclic loads.
2. Investigate the key factors that affect the behavior of beam-column joints.
3. Experimentally explore the effect of using UHPC material in the joint region to achieve the following:
   a) Attempt to change the mode of failure from brittle to ductile failure due to the superior performance of UHPC.

b) Try to completely eliminate the need for closely transverse reinforcement in the joint core.
c) Eliminate the need for close stirrups and ties in the plastic hinge region of adjoining members.
d) Enhance damage tolerance.
e) Reduce the development length of longitudinal bars in beams that pass or terminated through the joint core.

4. Experimentally investigate the effect of UHPC configuration on the behavior of corner beam-column joints.
5. Compare the two methods of casting UHPC material in the joint region, i.e., monolithically (hot joint) or cold joint.
6. Explore the performance of the joint when utilizing hybrid tension reinforcement (GFRP bars+steel bars) in beams.
7. Strengthening the beams through near-surface mounted technique using GFRP bars.
8. Evaluate the code provisions used to calculate the shear strength of beam-column joints based on an extensive experimental database.

Furthermore, a comparison between the loading protocol (monotonic/cyclic) subjected to the corner beam-column joint in both cases.

1.7 Thesis Layout

This thesis is organized into six chapters, the following is a brief overview of each chapter.

Chapter Two is concerned with identifying and developing an understanding of the effect of key factors influencing the seismic behavior of reinforced and unreinforced beam-column joints. In addition**,** this chapter makes a deep review on the structural behavior of hybrid beam-column joints.

Chapter Three presents a comprehensive description of the experimental program and methodology employed in the current research. The chapter provides a detailed overview of the test specimens, outlining the parameters investigated, construction methods, material properties, instrumentation utilized, and the experimental setup.

In **Chapter Four,** the results and discussions of the current experimental investigation are presented in this chapter. The crack pattern and failure mode of each tested specimen are explained. Moreover, the behavior of tested specimens is presented in terms of load-drift response, stiffness, ductility, energy absorption, and joint shear strength.

In **Chapter Five**, numerous national code provisions used to estimate joint shear strength are assessed using data from an extensive and costly experimental database.

Finally, the concluding remarks of the current research, based on the findings of each part of the work, are presented in **Chapter Six**. Furthermore, recommendations for future research are also included.

Chapter Two
Literature Review

2.1 Introduction

The behavior of the RC beam-column joint is a subject of ongoing interest in structural engineering due to its complex nature, which is influenced by a diverse set of factors. The objective of this chapter is to outline the primary variables that impact the performance of beam-column joints under cyclic loads. Additionally, it aims to provide an in-depth review of the materials commonly employed in the hybrid concrete technique, which is aimed at enhancing the behavior of beam-column joints.

2.2 Shear strength mechanism of beam-column joints

During an earthquake, beam-column joints sustain shear forces greater than those generated in adjacent framing beams and columns [61]. If the joint is not appropriately designed, collapse or partial collapse might occur due to the shear failure of the beam-column joints.

In 1978, Paulay et al. [62] suggested two mechanisms governing joint shear strength: a diagonal compressive strut and a truss mechanism. Figure 2.1 (a) illustrates that internal forces transferred from adjoining framing members to the joint core, causing diagonal tension (f_t) and compression (f_c) stresses.

As a result, the joint is subjected to shear, compressive, tensile, and sometimes torsion forces.

The truss mechanism is mainly composed of the combined effect of beam and column forces transmitted by bond stresses through longitudinal bars to the joint core. Consequently, tensile resisting forces develop within the joint transverse reinforcement, as illustrated in Figure 2.1(b) [63][64]. However, the joint truss mechanism can't be developed without joint transverse reinforcement owing to the limited contribution of the force transmitted by bond stresses along the longitudinal bar of the beam and column. Furthermore, this small contribution of the longitudinal bar rapidly diminishes once bond deterioration initiates within the core [64].

Based on previous research studies, the diagonal concrete compression strut plays an important role in resisting horizontal and vertical shear forces. The diagonal concrete strut transmits a compression force at an angle (β_c), as shown in Figure 2.1 (c). The concrete strut mechanism is capable of transmitting a significant amount of both horizontal and vertical shear forces across the joint core [62].

The strut is anchored in a node formed inside of the standard hook of the beam longitudinal reinforcement, which establishes the requirement that hook should be bent into the joint core, as indicated in Figure 2.1 (d).

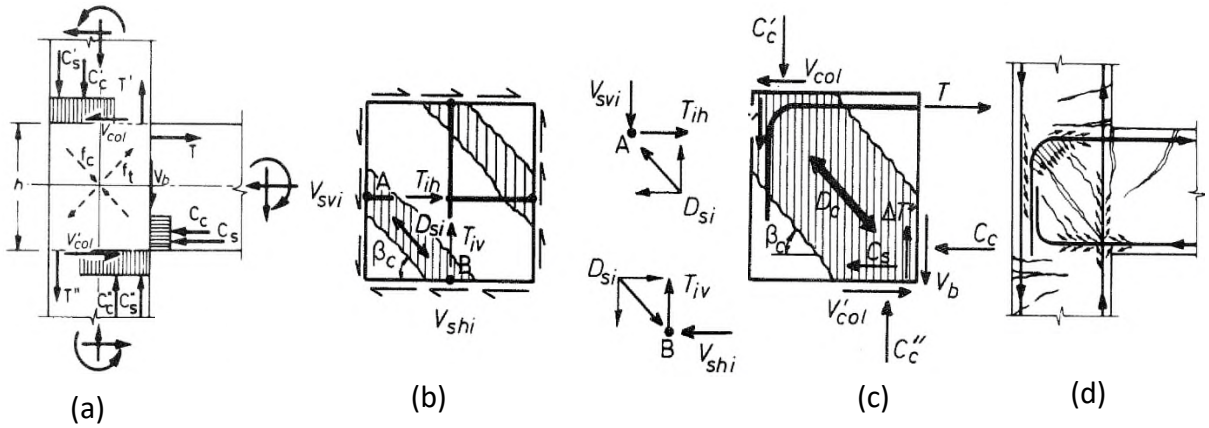

Figure 2.1 Forces transmitted to the joint core (a) forces acting on the joint core, (b), (c) strut mechanism, and (d) truss mechanism [63].

2.3 The failure mode of beam-column joint

The beam-column joint is generated from the intersection of the beam and column. As a result, each component (beam, column, and joint) may fail in various ways, including beam flexural/shear failure, column flexural/shear failure, joint shear failure, and so on. It is well known that shear and anchorage failure mechanisms should be avoided if the beam-column joint undergoes large plastic deformations. Due to the limited deformation capacity of such failure mechanisms, they may result in the collapse of the entire frame [65].

Joint shear failure (J-failure) occurs when the maximum shear capacity of the joint is reached without yielding beam and column (i.e. pure shear failure). This indicates that the structure will collapse before the beam and column have reached their maximum flexural capacity [66]. The second type of failure mechanism is called (BJ-failure). In this type of failure, the top or bottom reinforcement of the beam yields at the face of the column shortly before the joint shear failure occurs. This type of failure is considered more ductile than pure joint shear failure [12]. The failure also may occur due to the pullout of beam reinforcement bar from the joint core (P-failure) before reaching its joint shear capacity. This is due to the poor anchorage condition of the longitudinal beam bar.

If the joint shear capacity remains greater than the demand to the end. In that case, the maximum strength may be controlled by the beam flexure capacity (B-failure) or column flexural capacity (C-Failure) [67].

2.4 Experimental database

An extensive experimental database covering a wide range of design parameters was developed to study the key factors affecting the joint shear capacity of reinforced beam-column joints. As shown in Appendix-A, the experimental database consists of 254 beam-column joints; 129 were

exterior joints collected from Ehsani and Wight [68]; Kaku and Asakusa [69]; Fujii and Morita [70]; Ehsani and Alameddine [71]; Scott [72]; Chen and Chen [73]; Hamil [74]; Hegger et al. [75]; Hwang et al. [76]; Wong [77]; Hwang et al. [78]; Lee and Ko [79]; Chalioris et al. [80]; Li and Kulkarni [81]; Kaung and Wong [82]; Chun and Shin [83].

Similarly, 115 interior joints were collected from Durrani and Wight [84]; Fujii and Morita [85]; Kitayama et al. [86]; Oka and Shiohara [87]; Gentry and Wight [88]; Raffaelle and Wight [89]; LaFave and Wight [90]; Hegger et al. [75]; Kusuhara et al. [91]; Goto and Joh [92]; Teraoka and Hayashi [93]; Teng and Zhou [94]; Li and Leong [95]; Yang et al. [96]; Shiohara and Kusuhara [97]; Alaee and Li [98]; Burak and Wight [99].

In addition, 10 specimens confined by all four sides were collected from Kitayama et al. [86]; Oka and Shiohara [87]; Guimaraes et al. [100] and Quintero and Wight [101].

Experimental horizontal joint shear force was normalized as $\gamma_j = V_{jh}/b_j h_c \sqrt{f_c^`}$, named joint shear strength coefficient. Noting that, V_{jh} is the maximum horizontal joint shear force, the effective joint width b_j is calculated based on ACI-ASCE [33] and h_c is the total depth of column in the loading direction.

It is worth mentioning that all the collected data were for traditional joints, reinforced by transverse reinforcement in the joint core without spatial kind of concrete or special reinforcement detail.

2.5 The key factors affecting the behavior of RC beam-column joints

The key factors affecting the response of beam-column joints are presented and discussed in the following sections.

2.5.1 Effect of concrete compressive strength

The compressive strength of concrete significantly affects the behavior of beam-column joints. The 2019 CSA Standard A23.3.19 [102] restricts the application of the design equations to concrete compressive strengths of up to 80 MPa ($\sqrt{f_c`}$ not exceed 8 MPa) for ductile structures. While New Zealand Standard [103] limits the compressive strength to 70 MPa. This cautious limit was selected because of concerns regarding the brittleness of high-strength concrete (HSC) under compression. Ehsani and Alameddine [71] found that using high compressive strength concrete improves joint shear strength but shows low ductility. Furthermore, the bond strength of the HSC specimen was higher than the corresponding to NSC specimen under cyclic load [95]. Despite the fact that HSC improves the ultimate shear capacity of the joint, once failure occurs, the high strength specimens lose their strength more rapidly than their corresponding NSC specimens [74]. Sarsam and Al-Azzawi [104] reported that using HSC in exterior joints without fibers exhibited sudden failure, even with transverse reinforcement in the joint region. Many codes and proposals models assumed that the joint shear strength is a proportion of the square root of concrete compressive strength ($\sqrt{f_c`}$) [17], [33], [105], [106]. The same assumption is also adopted in the current study. Figure 2.2 shows the relation between the square root of concrete compressive strength and joint shear strength coefficient for the reinforced joints. The results were agreed well with the previous assumption that the joint shear strength is significantly affected by the concrete compressive strength of joint, but this was only for the interior joints. However, the assumption was not true for the exterior joints. The general trend of results showed that the shear strength of exterior joints was not affected by the concrete compressive strength. This could be attributed to the confinement provided by the transverse beam in the interior joints.

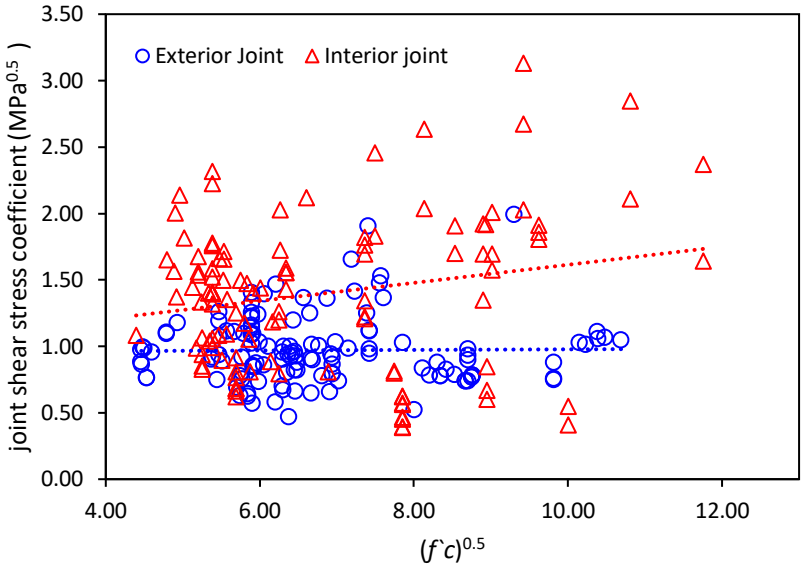

Figure 2.2 Effect of concrete compressive strength on the joint shear strength

2.5.2 Effect of eccentric connection

An eccentric connection occurs when the beam centerline is offset from the column centerline. This is often utilized for architectural consideration within an external frame of a reinforced concrete building. As illustrated in Figure 2.3, tension and compression forces are transferred from the spandrel beam to the joint with an eccentricity that may cause torsion in the joint region. This torsion will generate extra shear stresses, which may affect the joint's inelastic performance.

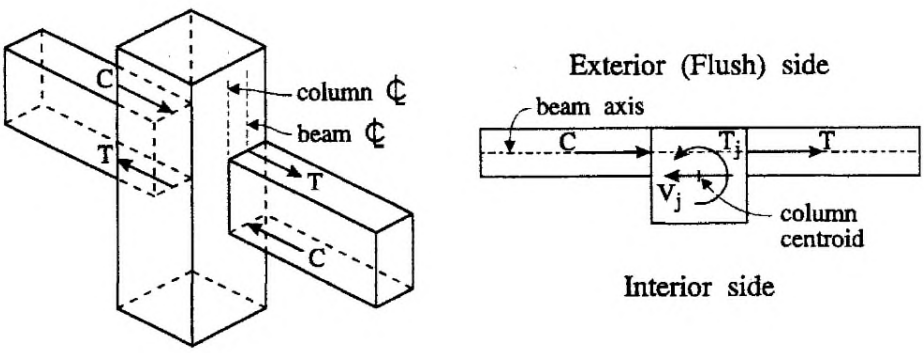

Figure 2.3 Forces acting on the eccentric beam-column connection [89].

In 1973, Ohno and Shibama [107] investigated the reason of the collapse of just one school building at Hakodate College in Japan, which had been severely damaged by the 1968 Tokachiokrk earthquake. However, little or no damage was observed in the other reinforced concrete constructions in the same area. It was found that the structure suffered damage due to a large eccentricity between the columns and spandrel beam.

The eccentric connection resulted in more severe crack damage on the flush side of the joint than interior side, significant bond degradation for the main reinforcement of beams, and a reduction in the joint's shear strength[2][3][89]. Raffaelle and Wight [89] reported that joint shear strength calculated based on ACI-ASCE Committee 352 [109] does not adequately account for the torsion in eccentric connections. However, It was concluded that floor slabs diminished the effect of eccentricity. Moreover, the differences between the seismic performance of these eccentric connections and current ACI building code provision [17] for estimating nominal joint shear strength were quite conservative for the case of the tested eccentric beam-column connections with floor slabs [110][111]. Other than that, ACI code needs much more investigation about this topic since its predictions in many cases were unsafe.

2.5.3 Effect of joint aspect ratio

The joint aspect ratio is defined as a beam depth (h_b) to the column depth (h_c). As stated previously, the strut is the primary mechanism that contributes to the shear strength of the beam-column joints. The angle of strut inclination (β_c) shown in Figure 2.1 (c), has a significant influence on the efficacy of the strut in resisting shear force. It is reasonable that maximum strut shear capacity developed when the (β_c) is equal to 45^o (i.e. h_b=h_c). When the joint aspect ratio increases, the strut gets steeper, and the horizontal component of the strut is unable to equilibrate the horizontal joint shear stress, resulting in

decreased shear strength. This is true for unreinforced beam-column joints [77]. Based on the analysis of a database for unreinforced beam-column joints, Hassan [12] concluded that joint shear strength is inversely proportional to the joint aspect ratio, as shown in Figure 2.4.

Figure 2.5 shows the relationship between joint aspect ratio and joint shear strength coefficient based on the database used in the current investigation. Here, the results are divided into two trends: (1) for the exterior joints, the shear strength was unaffected by the aspect ratio and (2) for the interior joints, the trend seems opposite to that of unreinforced joints when the shear strength of joints was increased with the greater aspect ratios. This is thought to be caused by the contribution of confinement which is higher for the greater aspect ratios.

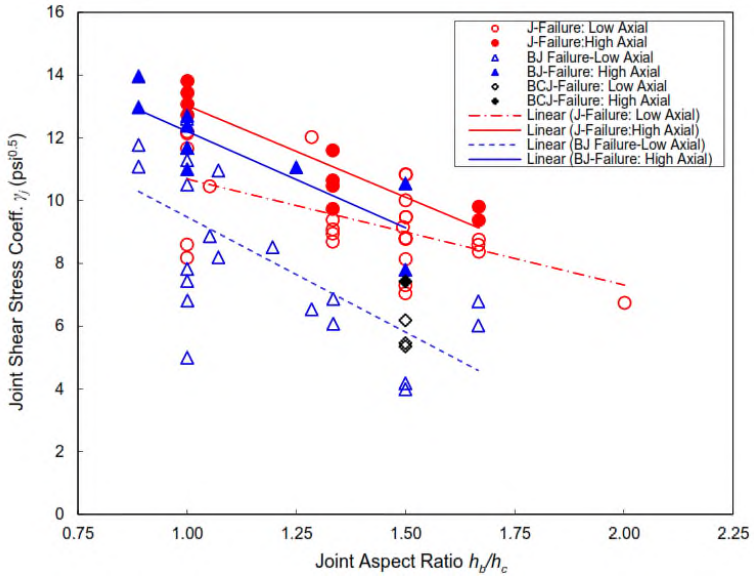

Figure 2.4 Effect of joint aspect ratio on unreinforced exterior joints shear strength [12].

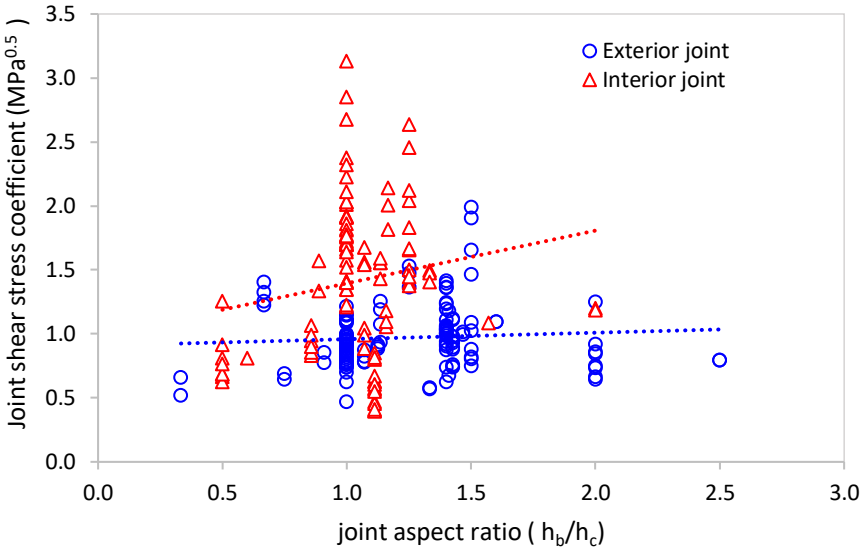

Figure 2.5 Effect of joint aspect ratio on the reinforced exterior and interior joints shear strength.

2.5.4 Effect of column axial load

The axial load has a complicated effect on the behavior of beam-column joints. The effect of axial load level on the shear strength of beam-column joints has been studied by many researchers. According to some of these studies, the axial load level on the column has little effect on the shear strength of the unreinforced beam-column joints [112][113]. On the other hand, other researchers found that the shear strength of the beam-column joints increased as the axial load increased [114][115].

In general, axial loads affect the behavior of beam-column joints in both positive and negative ways.

As discussed previously, the joint shear strength of unreinforced beam-column joints mainly depends on diagonal struts. The maximum force generated by concrete struts (D_c), as shown in Figure 2.6, can be computed as per Eq. (2.1):

$$D_c = f_c \times A_{str} \quad \ldots\ldots\ldots\ldots\ldots\ldots\ldots\ldots\ldots\ldots\ldots\ldots\ldots\ldots\ldots\ldots\ldots\ldots\ldots\ldots\ldots\ldots \quad 2.1$$

where, f_c is the compressive strength of concrete, A_{str} is the cross-sectional area of the concrete strut, which can be determined as ($A_{str} = a_s b_s$), a_s and b_s are the depth and width of concrete struts, respectively [116].

Zhang and Jirsa [114] reported that the depth of concrete struts (a_s) depends on the depths of compression zones in columns and beams. The depth of compression zones in a column is considered proportional to the column axial load [64][98]. Under the same concrete strength, higher compression zones develop in the column by increasing the column axial load, resulting in a larger compressive force in the struts. As a result, it is anticipated that column axial load would increase joint shear strength, which positively impacts axial load.

On the other hand, the principal tensile strain in a direction perpendicular to the diagonal concrete strut increases when the axial compression load increases, owing to Poisson's effect. Therefore, it is expected to decrease the shear strength of the beam-column joint [116].

Based on analysis of the extensive data on the unreinforced external joint, it was found that axial loads (N) between (0) and $\left(0.2 f_c' A_g\right)$ have a little effect on joint shear strength compared to that beyond this level ($N > 0.2 f_c' A_g$), as shown in Figure 2.7 [106][12]. The relation between joint shear strength coefficient and axial load ratio ($N/f_c` A_g$) for the reinforced beam-column joints was examined on the basis of the database used in this study. As demonstrated in Figure 2.8, the shear strength capacity of the exterior beam-column joints is somewhat enhanced by the column axial load. In comparison, the shear strength of the interior joints shows much enhanced than exterior joints. This is due to the confinement provided by joint reinforcement which reduces the impact of lateral strain resulting from Poisson's effect. Since the confinement level provided by interior joints is

higher than that of exterior ones, the higher axial load level provided much more shear strength in interior beam-column joints.

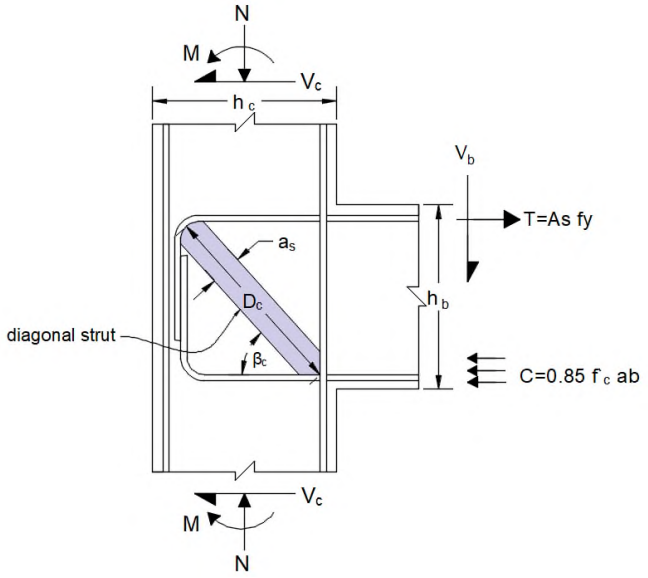

Figure 2.6 Details of diagonal strut through the joint core

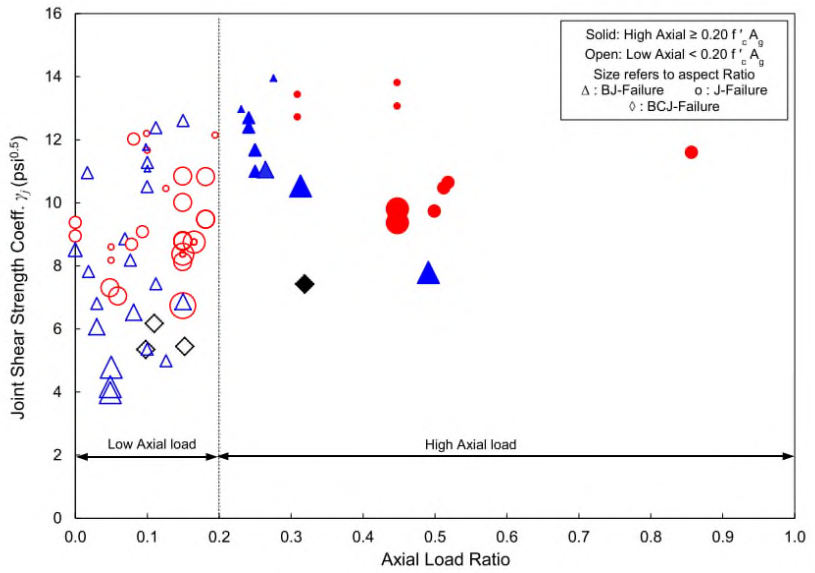

Figure 2.7 Effect of axial load on unconfined exterior joint shear strength[12]

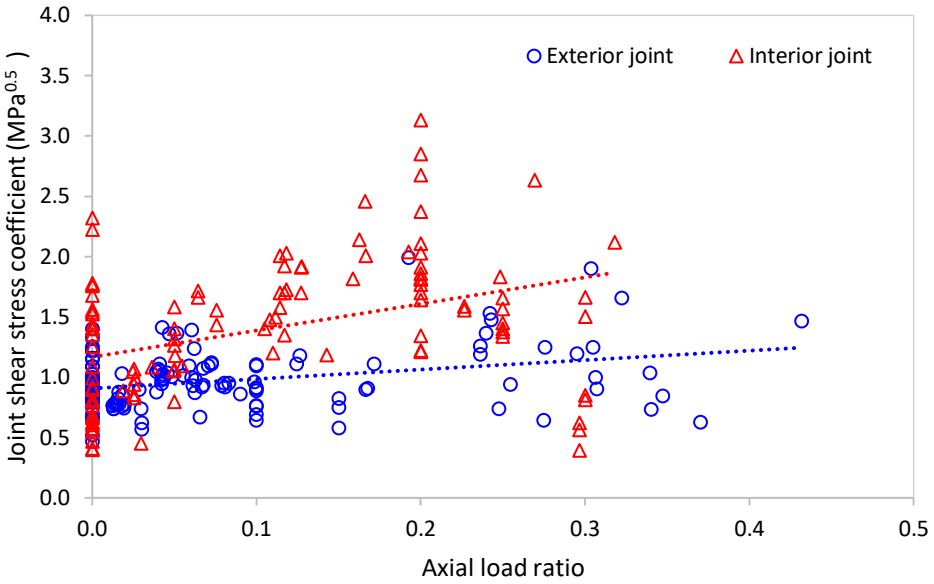

Figure 2.8 Effect of axial load on the confined exterior and interior joint shear strength.

2.5.5 Effect of anchorage detail of longitudinal bars in beam that terminated in the joint core.

The forces in beam and column are transmitted across the joint core primarily through a diagonal compression strut. As shown in Figure 2.9 (a), bending the hooks at the ends of the longitudinal beam reinforcement into the joint core, as recommended by all practice codes, allows the diagonal compression strut to transfer bearing stresses effectively with the hooks bending into the joint core, because the bearing stresses at the bend in the bar act in the direction of the strut.

Before the 1970s, it was common to anchor the longitudinal beam bars at exterior joints by bending the hooks out of the joint core or in the form of hook bend in 180° to avoid congestion of steel reinforcement in this region. Pampanin et al. [5] investigated the behavior of external beam-column joints reinforced with a plain bar bent in 180° at the end. The experimental results revealed a localized concentrated force generated at the compression bar edge after the joint diagonal crack coupled with an ineffective strut mechanism. It results in concrete expulsion in the form of a wedge, as shown in Figure 2.9 (b). Similarly, when the hook bends away from the joint core,

the diagonal compression strut does not effectively engage the beam hook. But, rather pushed against the longitudinal column reinforcing bars, resulting in a wide splitting crack along column reinforcement which can then cause a joint failure at early stage, as illustrated in Figure 2.9 (c) [117][118]. This old detail does not provide an effective node point at the top of the diagonal compression strut to equilibrate the horizontal component force of the compression strut[12][118][5]. When the beam longitudinal bars end in the joint region with a short length, as illustrated in Figure 2.9 (d), the bond mechanism becomes the key factor. The crack begins near the end of the short bar. And thus, it may cause the bond to breakdown before the diagonal compressive strut mechanism was completely developed [119].

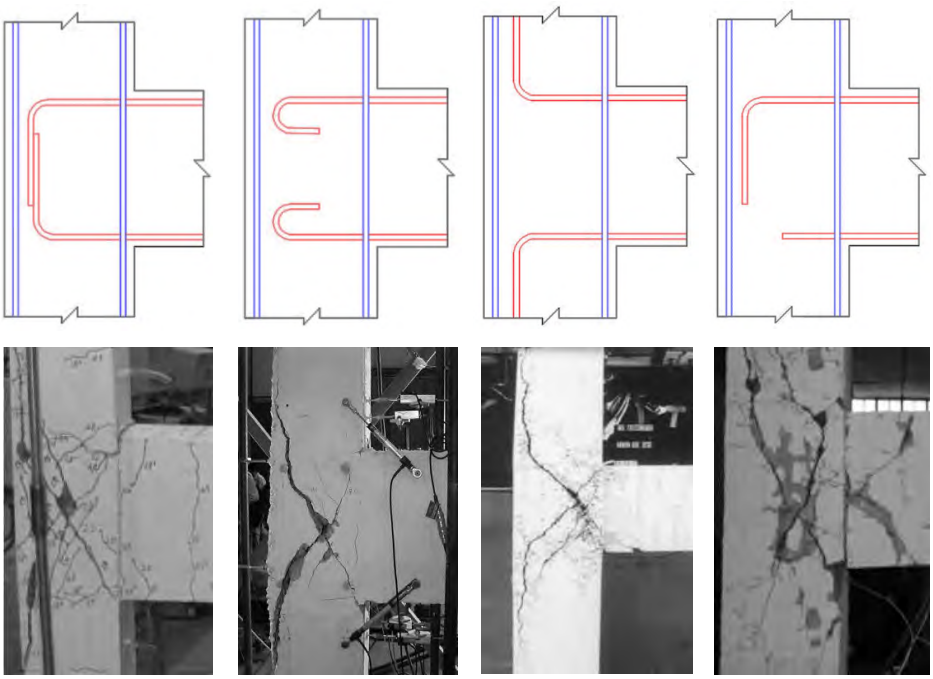

Figure 2.9 Failure mode of common end anchorage of beam longitudinal bars in joint core (a) beam bar bend in the joint core [120],(b) end-hook bend by 180^{o} [5],(c) beam bar bend away from joint core [118] and, (d)short bar terminated in the joint core [119].

2.5.6 Effect of development length of flexural bars in beam passing/terminated in the joint core

One of the controversial concerns in the design of beam-column joints is the anchorage length of flexural reinforcement passing or terminating in the joint core. According to the findings from the experimental test conducted by Leon [121] on interior beam-column joints, it was recommended to have a development length of 28 times the diameter of the reinforcing bar in order to ensure a weak beam-strong column principle. In 1980, the New Zealand code recommended that the column depth to bar diameter (h_c/d_b) be equal to 35 [121]. However, Hakuto et al. [122] later found that the column depth designed based on NZS 3101:1995 [123] should be between 25 to 55 times the diameter of the flexural beam bar in order to ensure an effective bond with the beam bars. This requirement is crucial to ensure that the reinforcing bars can adequately bond with the concrete and avoid any potential bond failure, which could compromise the integrity and safety of the structure.

Mag et al. [124] found the limit of h_c/d_b in ACI 318-19 [17] was too small to ensure bar bond performance of reinforced geopolymer concrete, even with this type of concrete shows a bond strength of 10% than normal strength concrete. Megget et al. [125] conducted experiments on four beam-column joints, using flexural reinforcing bars of yield strength of 588 MPa. The specimens were designed based on a h_c/d_bratio of 32.5, following the previous design provisions NZS 3101:1995 [123]. The test results revealed a significant bond-slip behavior in the beam-column joint, despite the relatively larger h_c/d_b ratio. The minimum joint depth requirement of 20 d_b, as stated in ACI 318, was determined based on test data involving Grade 420 reinforcement may not be adequate for bars with (*fy*) exceeding 420 MPa. ACI-ASCE Committee 352 suggests a simple multiplier of *fy*/420 for the $20d_b$ criterion without considering the varying concrete strengths. This

approach is conservative for high-strength concrete and may not be conservative enough for low-strength concrete, as indicated by the findings of study done by Lee et al. [126]. Hwang et al. [127] conducted experiments to assess the seismic performance of beam-column joints using Grade 600 *MPa* bars for beam flexural reinforcement. Seven beam-column joints, four interiors, and three exteriors were tested under lateral cyclic loading in accordance with the special seismic provisions in ACI 318-11[128]. The h_c/d_b ranged from 20.5 to 25.0. For interior joints, the load-carrying capacity and maximum deformation of the specimens with 600 *MPa* bars were similar to those with 400 *MPa* bars. However, the energy dissipation capacity of the specimens with 600 *MPa* bars decreased by up to 25% due to increased bond-slip at the joints. For exterior joints, significant bond slip occurred at the bottom bars of the beam due to insufficient development length, resulting in decreased deformation and energy dissipation capacities of the specimens.

2.5.7 Effect of the transverse reinforcement in the joint core

The joint transverse reinforcement can directly contribute to the overall joint behavior. There are two viewpoints on the function of transverse reinforcement.

- First, it can provide shear forces resistance with an upper limit equal to the area of the transverse reinforcement times its yield stress (tie action), which is adopted by the New Zealand building code [129].
- Second, the transverse reinforcement can provide confinement to the joint, which is proportional to the number of transverse reinforcement placed in the joint. This is adopted by ACI-ASCE, and most building codes [68].

Many studies have shown that diagonal compression struts withstand shear forces in the joint core. In contrast, joint transverse reinforcement confined

the joint concrete core, thereby enhancing joint diagonal compressive strength, thus, transverse reinforcement contributes indirectly to the shear resistance of the joint [130][131]. The ACI 318 [17] and ACI-ASCE 352 [132][16] assumed that joint transverse reinforcement provides confinement for the joint core and can not withstand shear force due to severe bond deterioration and the shear forces are resisted by diagonal compression strut only.

On the contrary, the New Zealand standard code [129] assumes that the bond of reinforcement bars in the joint core is sufficient to resist shear forces in transverse reinforcement, and therefore, the internal shear force is resisted by diagonal compression strut and joint transverse reinforcement [133].

Hwang et al. [78] investigated the role of joint transverse reinforcement of external beam-column joints under reversed cyclic load through an experimental program consisted of nine specimens. The results indicated that the joint transverse reinforcement plays no role in confining the concrete core. This is because the confinement role by transverse reinforcement can be achieved for the structural elements controlled by Bernoulli's compatibility. Whereas the beam-column joint element is subjected to high shear, thus the joint deformation is governed by Mohr's compatibility. Therefore, joint transverse reinforcement are added to retard the strength deterioration of concrete and not to enhance the strength of concrete.

Ehsani and Wight [68] experimentally investigated the effect of transverse reinforcement in the joints core of beam-column joints. The results indicated that specimens with lower flexural strength ratios (the sum of the flexural capacities of the columns to that of the beam) can only slightly improve the shear strength of joints when additional transverse reinforcement. Furthermore, providing a larger number of transverse reinforcement with a lower yield stress is more advantageous than providing fewer transverse

reinforcement with a greater yield stress, even though the maximum potential shear capacity for both cases may be the same.

2.5.8 Effect of beam longitudinal reinforcement ratio

The beam reinforcement ratio (ρ_b) plays an important role in controlling the ductility of the beam-column joints. The experimental results conducted on the exterior and interior unconfined beam-column joints indicated the dependency of joint shear strength on the amount of beam reinforcement [66][134]. Based on the database adopted in this study, as the longitudinal reinforcement ratio (ρ_b) increases, the joint shear strength also increases, as illustrated in Figure 2.10. This is because the increasing of the beam longitudinal reinforcement ratio leads to an increase in the horizontal joint shear force without yielding of the beam longitudinal bars and with less deterioration of bond resistance around the bars in the joint region. Consequently, a wider diagonal strut was produced which can carry greater horizontal joint shear forces [135]. However, Dabiri et al. demonstrated that increasing the longitudinal reinforcement ratio of a beam reduces both displacement and curvature ductility. As a result, in a structure with a high need of ductility, the computed reinforcement of beams and columns should be adjusted for the necessary ductility [136].

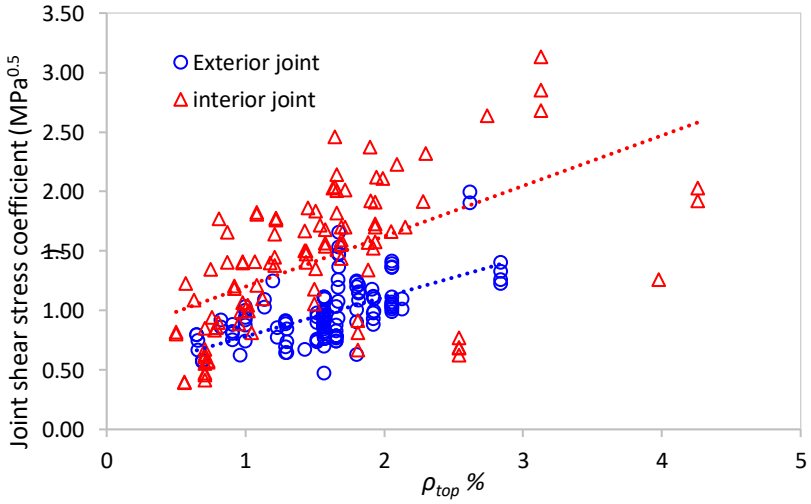

Figure 2.10 Effect of beam longitudinal reinforcement ratio on the joint shear strength.

2.6 Structural behavior of hybrid RC beam-column joints under cyclic load

As previously stated in chapter one, RC beam-column joints are prone to substantial damage during earthquakes, leading to the collapse or partial collapse of the structure.

Many studies have been performed during the last four decades utilizing various techniques to improve the seismic behavior of beam-column joints and reduce the congestion of steel reinforcement in this region. One of the most commonly used techniques was the hybrid joint in which a special kind of concrete is cast in the joint region to withstand the high shear stress, and NSC was used in the rest of the specimen; this is called a **hybrid RC beam-column joint**.

Fiber-reinforced concrete (FRC) was one of the choices used in the joint region due to its superior mechanical properties. Among these properties is the higher ductility compared to NSC, which is caused by the ability of fibers to arrest crack formation and propagation in concrete. Steel fiber reinforced concrete (SFRC) was utilized in the joint region to improve seismic performance and minimize transverse reinforcement. In the same context, high-performance fibers reinforced cementitious composites (HPFRCC) which exhibit strain-hardening characteristics accompanied by multiple microcracks under tension stresses [45][137]. These characteristics make HPFRCC efficient material utilized in the beam-column region to resist large inelastic deformation.

The following sub-sections reviews the literature for most materials used to improve the behavior of beam-column joints through the hybrid concrete technique. To the best authors' knowledge, there is no available work trying to provide such kind of review. Since the emphasis of this review is on the hybrid joints, each kind of hybrid joints is reviewed with focus on its

response and relative advantages and disadvantages. Based on that, two kinds of hybrid joints are discussed in this review. The first was a hybrid joint that utilized steel fiber reinforced concrete in the joint region, while the rest of the specimen were cast with NSC (SFRC/NSC). The second kind of joint was hybrid joints, which employed high-performance fibre reinforced cementitious composite in the joint area and NSC in the other portions of the beam-column joint (HPFRCC/NSC).

2.6.1 SFRC/NSC hybrid beam-column joints

Adding fibers to concrete is the conventional technique for improving its mechanical performance since concrete is a quasi-brittle material with a limited strain capacity, especially when subjected to tensile stress. The steel fiber may be attributed primarily to their localized reinforcing ability. Their presence in the mortar matrix surrounding coarse aggregates prevents the opening, widening, and later extension of microcracks already present in the concrete [138]. In addition, steel fibers can also serve as bridging mechanisms during cracking and have an ability to change the brittle failure of concrete to more ductile failure [139]. The following section provides an overview of most studies using steel fibers to enhance the behavior of beam-column joints with/without reducing transverse reinforcement.

One of the first attempts to use steel fibers reinforced concrete in joints was by **Henager in 1977** [26], who examined the use of steel fibers in beam-column joints region instead of transverse reinforcement to reduce steel congestion in this region. Two full-scale exterior beam-column joints were tested under cyclic load. The first one was ductile specimen designed based on the seismic requirement of ACI 318 [22], while the second specimen was constructed using steel fibers reinforced concrete (SFRC) in the joint zone (modified joint) without the use of transverse reinforcement, as shown in Figure 2.11. The result indicated that both specimens were very effective in

the confinement of the joint zone. Furthermore, no cracks were observed in the SFRC/NSC hybrid beam-column joint, while some hairline cracks and one major crack appeared in the intersection of the beam and column of the conventional specimen. Finally, the SFRC/NSC hybrid joint showed better performance in terms of damage tolerance, ductility, and shear capacity than the conventional specimen.

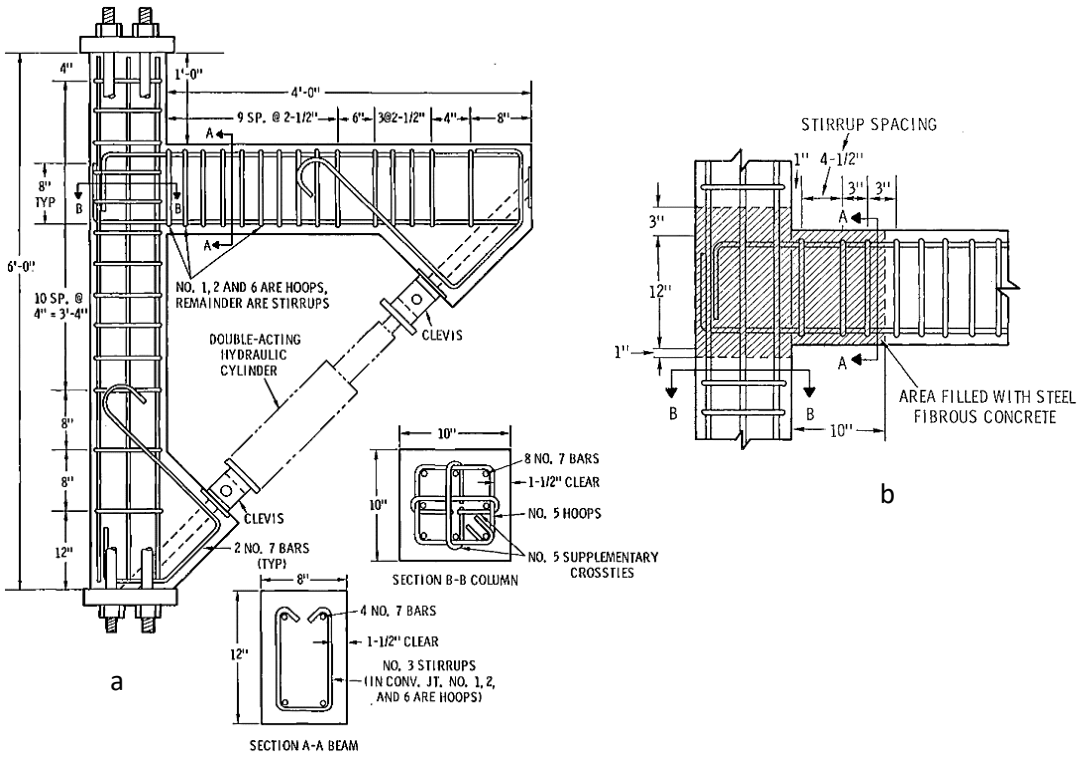

Figure 2.11 Details of the tested specimens, a) ductile specimen, b) modified specimen [26]

Jindal and Hassan [140] also investigated the use of SFRC to reduce reinforcement congestion. Three groups were used in the experiment, including A, B, and C. Group A represents a conventional specimen, whereas in group B and group C, SFRC was used through the specimen length and in the joint region only, respectively. In comparison to the conventional specimen, the result indicated that utilizing SFRC instead of shear reinforcement increased shear capacity by 29% and 19% for groups B and C, respectively. Despite specimens with SFRC (group B and C) failed with

shear cracks, more ductile response was observed compared to conventional specimens (group A).

John Craig et al. [141] studied the performance of SFRC to improve the seismic behavior of beam-column joints and reduce steel congestion in joints zone. Two specimens were examined; the first one was constructed with reducing transverse reinforcement in the joint region and used SFRC instead of conventional concrete, while in the other one was NSC joint, as shown in Figure 2.12. The results showed that the inclusion of SFRC in the joint region is significantly increased the shear and moment capacities of the joint. Furthermore, SFRC specimens exhibited better concrete confinement, maintained greater structural integrity, and showed less structural damage than the NSC joint. Even though the presence of SFRC in the joint region improved the seismic performance of the beam-column joint, the mechanism of failure was almost identical to that of the conventional specimens.

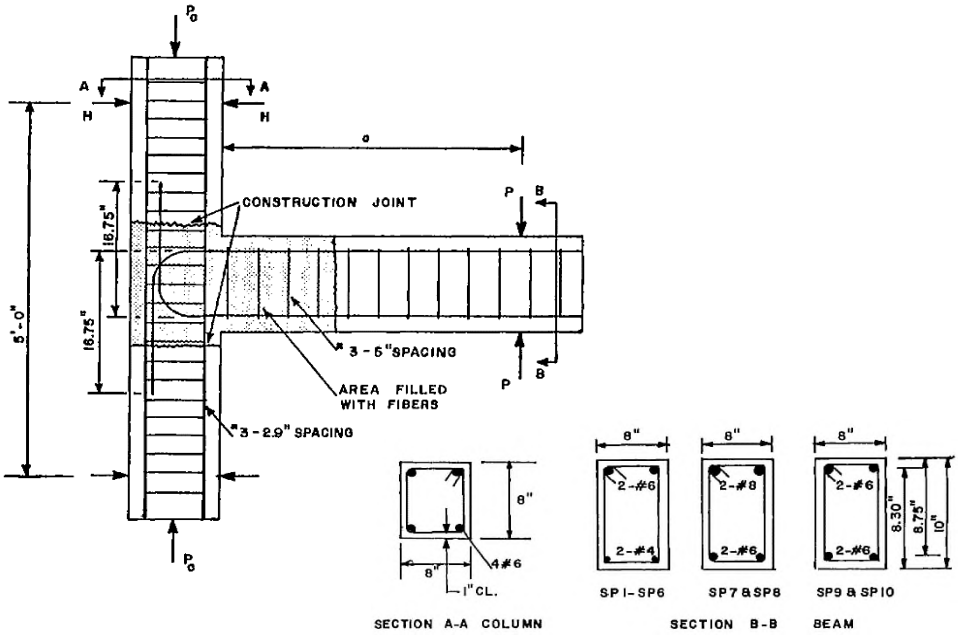

Figure 2.12 Details of the tested specimens [141]

The experimental program performed by **Gefken and Ramey** [117] included testing of a series of Type-2 exterior beam-column joints comprising of two control specimens (made from NSC only) and eight

hybrid specimens. the variable was the spacing of transverse reinforcement. It was found that when SFRC was used in the joint region, the spacing of transverse reinforcement in the joint can be increased to 1.7 times the recommended value in ACI-ASCE 352 [109]. The authors recommended using Type-1 beam-column joints with SFRC in the joint region rather than Type-2 beam-column joints. Bond failure caused by the longitudinal bar of the cantilever beam were the most apparent mechanism of concrete failure in all specimens. This may be due to bending the hook of the longitudinal beam bar away from the joint core. Even though specimens with SFRC exhibited little or no spalling compared with the NSC specimen, using of SFRC did not change the failure mode compared to NSC specimen.

SFRC was also used by **Filiatrault et al.** [142] to eliminate transverse reinforcement in the joint region. Four full-scale exterior beam-column joints were examined under reversed cyclic load. Two types of SFRC were used to enhance the non-seismic specimens and compare the result with the full seismic detailed specimens constructed based on the National Building Code of Canada [143]. The experimental results demonstrated that specimen with steel fiber of 1.6% and fiber aspect ratio (l_f/d_f) equal to 100, had greater shear strength allowing to develop a plastic hinge in the beam rather than joints. Furthermore, these specimens have a higher level of energy dissipation, with around 95% of the total energy dissipated in the complete seismic detailed specimen. Finally, the results showed that the efficiency of SFRC/NSC hybrid joints was influenced by the volume fraction and aspect ratio of the steel fiber. Despite the use of SFRC in the joint region, shear cracks in the joint region cannot be avoided.

Filiatrault et al. [144] studied the use of SFRC to improve the seismic performance of internal beam-column joints and reduce transverse reinforcement. Three full-scale specimens were examined, including a

specimen without seismic details, one meeting seismic requirements, and one without seismic details but with SFRC in the joint region (hybrid joint), as illustrated in Figure 2.13a. The SFRC/NSC hybrid specimen, according to the results, represented a transition between the first and second specimens. Finally, the hybrid specimen was able to dissipate about 85% of the energy dissipated via the full seismic detailed specimen. Again, the diagonal shear crack at the joint cannot be prevented even with using SFRC in the joints region, as shown in Figure 2.13b. Similarly, **Mustafa and Ilhan** in 2002 [145] investigated the response of SFRC/NSC joints but for exterior joints only by testing four full-scale specimens. The variables were the spacing between transverse reinforcement in the joints region and the material used in the joints zone. The result reported that SFRC could not avoid the development of a shear crack in the joint zone. It is worth noting that using a single transverse reinforcement in addition to SFRC in the joint region was insufficient to avoid shear cracking.

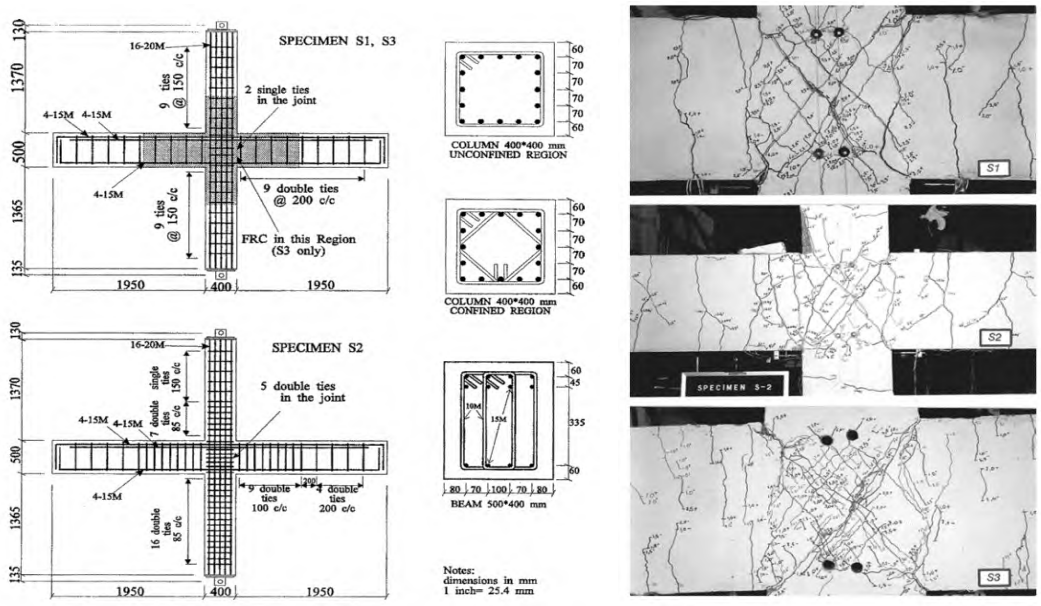

Figure 2.13 a) Details of the tested specimens, b) crack pattern of examined specimens [144].

In tests conducted by **Liu** [120] on three groups of exterior beam-column joints under lateral cyclic load in order to determine the contribution of SFRC on the shear capacity of joints. The first group represents the specimens designed without seismic detail similar to joints prior the 1970s but by replacing the conventional concrete by SFRC in the joint region. The second group was designed according to NZS 3101 [103] and minimized shear reinforcement in the joint and the plastic hinge region, then the conventional concrete was replaced by SFRC in these regions. Simultaneously, the third group was constructed as a reference specimen according to NZS 3101 (full seismic details), as shown in Figure 2.14. This study revealed that the use of SFRC in beam-column joints can improve shear resistance, ductility, energy absorption, and confining stress. Additionally, the necessity for closely spaced joint transverse reinforcement was reduced. It was also observed that using SFRC in joints region has the ability to change the failure mode from the joint shear failure to beam or column flexural failure. Finally, the presence of SFRC in the joint region alone could not prevent the longitudinal bars in columns from buckling. As a result, a minimum amount of transverse reinforcement should be placed in joints to provide sufficient confinement which can prevent the longitudinal bars in columns from buckling.

Using of high-strength concrete (HSC) in exterior beam-column joints was found to be causing a sudden failure [146]**.** However, adding steel fibers to HSC in the joints region can only help maintain better specimens' integrity at failure.

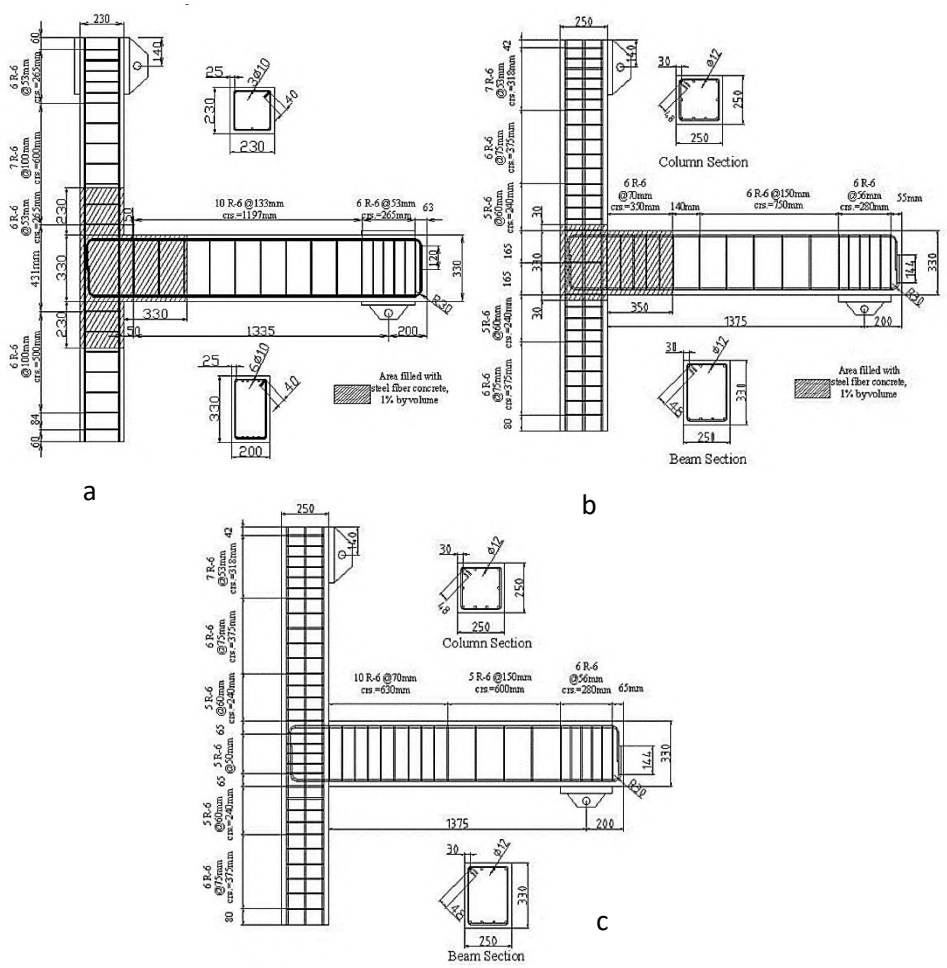

Figure 2.14 Details of the tested specimens, a) first group, b) second group and c) tired group [120].

As shown in Figure 2.15a, the piers of railway bridges are braced by intermediate beams to provide a rigid frame. This will produce a large number of joints. In 1995, the Hyogo-ken Nambu earthquake occurred near the city of Kobe, Japan, railway structures suffered severe damage (Figure 2.15b) [147]–[149]. According to the new railway design standards (Design standards for railway structures and commentary,2004) [133], huge steel reinforcement with special seismic details was mandatory in rigid-framed railways. Practically, closely spaced joint transverse reinforcement and large number of rebars often make it impossible to install beam longitudinal rebars at the beam-column joints. **Niwa et al. in 2012** [150] tested eight one-sixth

scale specimens, four of which were external joints, and the others were knee joints. The reference specimens were designed based on Japan's rigid-framed railway bridge [133]. The transverse reinforcement in the T-joints and Knee-joints were reduced by roughly 29.2 % in the other specimens. Steel fibers (0, 1%, and 1.5 %) were utilized to compensate the loss of strength due to the reduction in the steel reinforcement. The results indicated that adding steel fiber by 1.5% of volume improved the specimens' performance in terms of load capacity, ductility, stiffness, and energy dissipated compared to the reference specimens.

The test also revealed that, except the reference T-joint, all others showed longitudinal rebar debonding and anchoring failure in varying degrees depending on the volume fraction of fiber, as shown in Figure 2.16. As a result, even with the above-mentioned enhancement, 1.5 % steel fiber was insufficient to prevent anchoring failure.

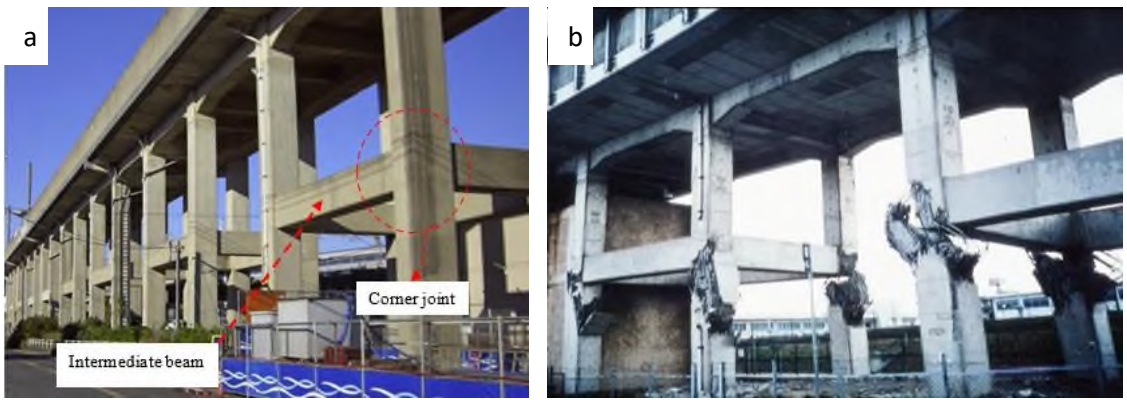

Figure 2.15 a) Rigid-framed railway bridges [151],b) collapse the railway bridge due to the Kobe earthquake/Japan.

Figure 2.16 Damage at the column external face of exterior joints specimens, a) reference specimen, b) modified specimen 0% steel fibers, C) modified specimen 1% steel fibers and d) modified specimen 1.5 % steel fibers [152].

Six exterior beam-column specimens were tested under reversed cyclic load by **Röhm et al.** [153]. The investigated parameters were the longitudinal reinforcement ratio, number of transverse reinforcement in the joint region, length of the SFRC portion, and steel fibers volume fraction. It was found that, as compared to the reference specimen, the damage in the joint zone was not severe. It has been demonstrated that the steel bar was yielding in the joint region, meaning that the addition of steel fibers did not enhance the large bar diameter anchorage state.

A numerical study conducted by **Abbas** [154] assesses the effect of introducing steel fibers into the concrete mix to compensate for a reduced amount of transverse steel reinforcement in the joint core for both interior joint and exterior joint. It was found that the spacing of transverse reinforcement in the joint core can be duplicated, compared to those having full seismic detail by adding 1% and 1.5% steel fiber for interior and exterior joints, respectively. Nevertheless, the transverse reinforcement in the joint core can’t be omitted even with 2.5% steel fiber.

Shi et al. [29] in 2021 used high-strength steel fiber reinforced concrete in the joint area to improve the performance of interior beam-column joints. This study considers the effect of concrete strength, stirrups ratio in the joint core, the volume ratio of steel fiber, and column axial load were considered

in this study. Seven ½ scale interior RC beam-column joints were tested under cyclic load. It was found that utilizing high-strength concrete with 1% steel fiber improves the ductility and energy consumption by 45.2% and 120%, respectively, compared with the control specimen. Moreover, the failure mode was changed to a plastic hinge at the face of the column rather than joint shear failure in control specimens. On the other hand, it was found that specimens with smaller stirrup ratios or volume ratios of steel fiber in the joint core were subjected to joint shear failure. As mentioned previously, steel fibre reinforced concrete alone without transverse reinforcement in the joint core can't prevent joint shear failure. Furthermore, a small amount of steel fiber shows no significant enhancement in the behavior of tested specimens with respect to NSC specimens.

2.6.2 Utilize hybrid fibers in SFRC/NSC beam-column joints

It is well-known that the presence of fibers in concrete can improve the resistance of concrete to develop cracks, and when the cracks exist in concrete, even before loading in the form of microcracks. Then these microcracks develop and connect to produce macrocracks when the concrete member is subjected to load. These kinds of cracks (macrocracks) can propagate further to cause fractures and since the fibers can only offer reinforcement for one level of cracking (micro or macro-cracks) with a limited field of strains. Therefore, a hybrid form of several kinds of fibers can be provided a better performance[155]–[158]. One form of fiber is stronger, resulting in sufficient initial crack strength and ultimate strength, while another type of fiber is more flexible, resulting in greater post-crack toughness. Another combination uses a smaller fibre to restrict microcracks growth and a larger fiber to stop macrocracks propagation and hence improves the ductility of concrete [159].

Based on that, **Kheni et al.** [160] investigated the use of hybrid fibers RC (HyFRC) to enhance the ductility of beam-column joints rather than seek increases in strength. Four 2/3 scale exterior beam-column joints were designed based on IS 13920 [161] to satisfy ductile performance. The first specimen was used as a reference specimen, whereas the second and third specimens utilized HyFRC in the joint region containing (1% steel fiber+0.15% polypropylene) and (1% steel fiber+0.15% polyester), respectively. The last specimen utilized 1% steel fiber only in the joint region. The test demonstrated the superior performance of HyFRC joints compared to the SFRC specimen. The ductility for the second and third specimen increased by about 140 % and 90%, respectively, compared to the reference specimen, whereas the ductility of SFRC specimen increased by only 44%. The degree of damage in all the HyFRC specimens was significantly less than in the reference specimen, as shown in Figure 3.8. Furthermore, maximum ductility and dissipated energy was observed for the joint with a combination of 1% steel fibers plus 0.15% polypropylene fibers. However, despite the presence of HyFRC in the joint region improved the ductility and dissipated energy, the mode of failure was still joint shear failure, as shown in Figure 2.17.

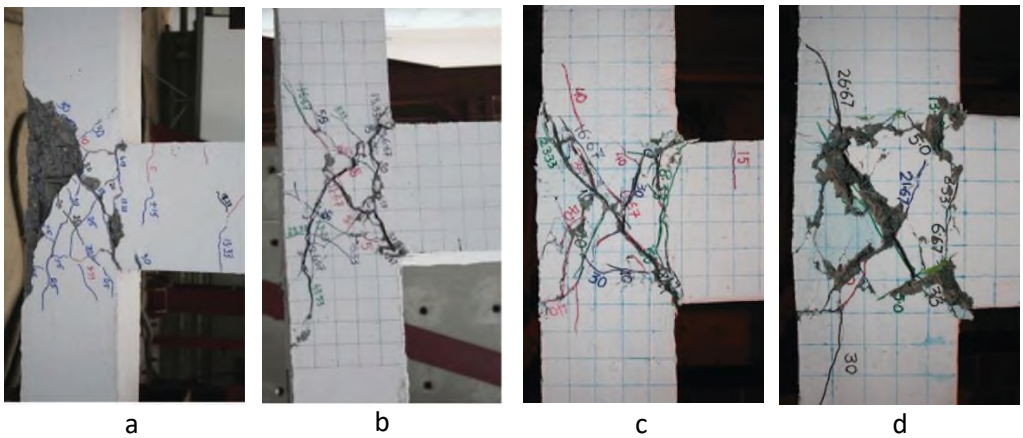

Figure 2.17 Failure modes of the tested specimens a) no fibers, b) 1% steel fibers +0.15% polypropylene fibers, c) steel fibers + polyester and d) steel fibers only [160].

Annadurai and **Ravichandran** [153] also investigated the employment of HyFRC in the exterior joints. Fourteen specimens were examined under forward cyclic load, one of which was constructed using seismic code IS 13920 [161] and the other specimens were designed without seismic details following ACI 318 [32] and replacing the NSC in the joints region by HyFRC. The results showed that high-strength concrete containing 80 % steel and 20% polyolefin has increased ductility, energy absorption, and overall strength for all volume fractions. However, as compared to the seismic detail specimen, the hybrid fibers specimen of volume fraction 2% (80% steel+20% polyolefin) exceeded the seismic details specimen in terms of energy absorption capacity and ductility.

2.6.3 HPFRCC/NSC hybrid beam-column joints

HPFRCC has made significant progress in recent years due to several technical developments in producing material and a better understanding of the basic mechanisms that control their behavior [162]. This section highlights the majority of research that used HPFRCC to improve beam-column joint performance.

The first attempt to use HPFRCC as complete replacement for transverse reinforcement in the joint region was by **Montesinos et al.** [37] in 2005. Two full-scale HPFRCC interior beam-column joints were tested under reversed cyclic load. HPFRCC was utilized instead of NSC for a length equal to twice the beam depth adjacent to the column face. The beam transverse reinforcement for the plastic hinge and out plastic hinge regions was designed using ACI 318, chapter 11 [132]. No transverse reinforcement were placed in the joint region. The peak joint shear stress in the first specimen was designed according to the ACI maximum allowable limit, whereas the joint shear stress demand in the second specimen was designed to exceed the ACI joint stress limit. Based on the test results, it was concluded that the

current joint shear stress limitations stated in the ACI and ACI-ASCE 352 may be safely applied to HPFRCC beam-column connections without transverse reinforcement. Furthermore, HPFRCC materials in beam plastic hinge region have increased the transverse reinforcement spacing to half the effective beam depth rather than one-fourth of the effective depth recommended in ACI 318, chapter 21.

Similar to the previous study, **Shannag et al.** [163], tested six specimens of 1/3 scale designed to support gravity load based on the recommendations of ACI 318 [164]. The details of reinforcement represented the case of old Jordanian buildings, as illustrated in Figure 2.18a. The HPFRCC with 2% or 4% of brass coated steel fibers or hooked steel fibers was utilized instead of NSC in the joints region, as shown in Figure 2.18b. HPFRCC specimens with hooked steel fibers had performance significantly better than those with brass-coated fibers. HPFRCC specimens provided load capacity equal to three times the maximum load capacity of the reference specimen and ductility of two times the corresponding value of the reference one.

Another form of HPFRCC was used in exterior joints [165] called Engineering Cementitious Composite (ECC). Six beam-column joints were tested under cyclic load. The key factors were; joint material (NSC/ECC), the confinement reinforcement ratio in the joint core, and the column axial load level. The test results showed that using ECC in the joint zone instead of NSC improved the load capacity, ductility, and energy dissipation of the beam-column joint specimens. However, even the joints having ECC provided excellent ductility, shear failure mode was not avoidable without transverse reinforcement in the joint region. Using a ratio of 0.69% as a transverse reinforcement in combined with ECC in the joint region can change the failure mode from brittle shear failure in the joint zone to flexural failure owing to the development of a plastic hinge at the base of the beam.

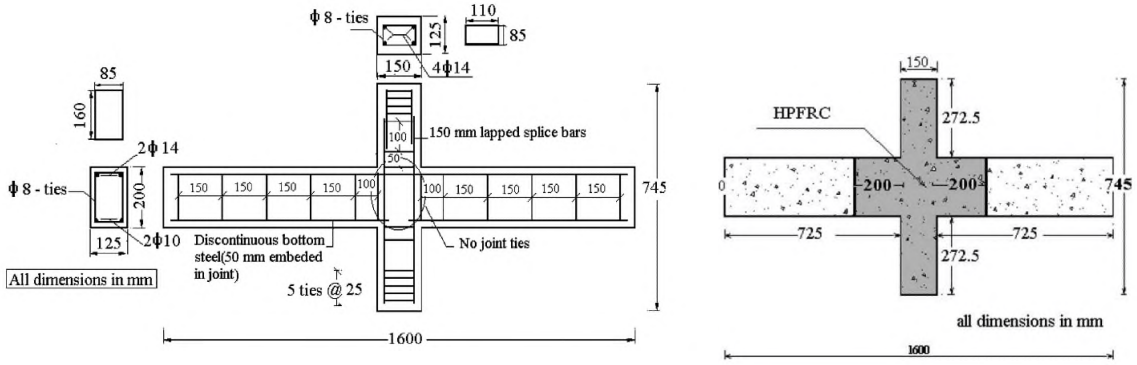

Figure 2.18 a) Specimens details, b) hybrid concrete specimen [163].

A hybrid form of fibers which consisted of crimped steel fibers and micro polypropylene fibers was used to produce HPFRCC [166]. A series of hybrid external beam-column joints were tested under reversed cyclic loading. The results indicated that hybrid fibers incorporating 1% steel fibers and 0.15 % polypropylene fibers considerably enhanced the performance of the beam-column joint in terms of the first crack, load-carrying capacity, energy absorption capacity, and displacement ductility factor. Steel congestion in beam-column joints may be reduced as a result of the improvements provided by HPFRCC.

Nine interior beam-column joints designed in accordance to the ACI 352R and ACI 318, chapter 21 [16][167] were tested under reversed cyclic loading [168]. Compared to the code requirement, the joint was modified using ECC instead of NSC and reduced the transverse reinforcement in the joints by (50%, 25%, and 0%). The results indicated that all ECC specimens exhibit superior seismic performance than reference specimens. The results also demonstrated that the transverse reinforcement in the joint could be omitted using ECC material in the joint and plastic region.

Another form of HPFRCC was used by **Zhang et al.** [151], so-called Polypropylene Fibre-reinforced Engineered Cementitious Composite (PP-ECC). Three specimens of $1/6$ scale exterior beam-column joint prepared based on existing railway bridges in Japan [169] were tested under laterally

reversed cyclic load. The main variables were the amount of transverse reinforcement in the beam and column also the concrete type, as shown in Figure 2.19. It was found that, even after removing the transverse reinforcements from the column, beam, and joint, the failure mechanism of the PP-ECC specimens was still flexural failure. Despite the superior structural performance of the PP-ECC specimens, bond degradation was observed in all specimens having PP-ECC owing to slippage between the longitudinal reinforcement of the beam and the PP-ECC material at the joints, as shown in Figure 2.20.

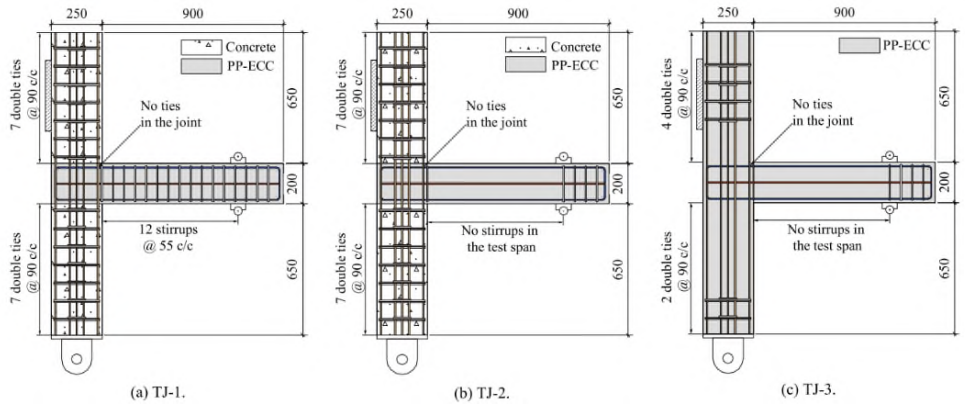

Figure 2.19 Details of the tested specimens [151].

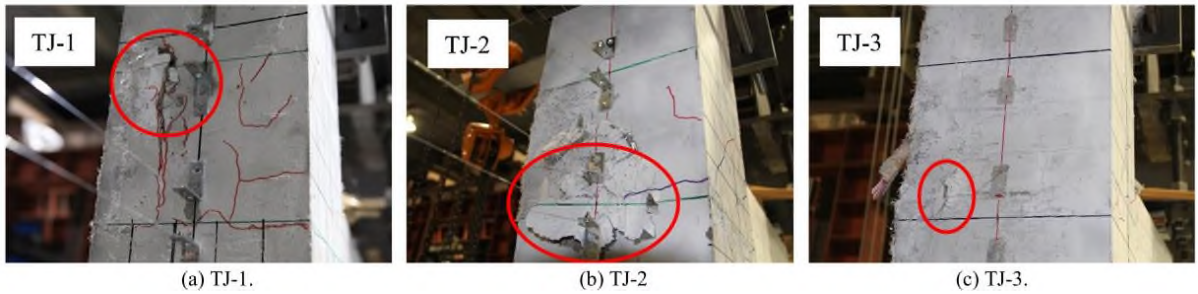

Figure 2.20 Pull out of beam longitudinal bar [151].

HPFRCC produced by hybrid fibers or by polypropylene fibers were used in joints region examined by **Chidambaram and Agarwal** [170]. It was found that HPFRCC specimens with hybrid fiber (1.5% polypropylene + 2% hooked end steel fibers) were extremely impressive in terms of strength, ductility and post-yield deformation capacity. Moreover, at the same ductility level, the damage index of HPFRCC joint specimens is much lower than the reference specimens.

Two full-scale exterior beam-column joint specimens, including one entirely made from NSC and the second one had ECC in the joint region [171]. Both specimens were cast without transverse reinforcement in the joint region. The test results indicated that replacing NSC with ECC in the joint region can improve load and shear capacities, less damage tolerance, better ductility, and energy absorption capacity. Despite the superior improvement achieved by utilizing ECC material, the failure mechanism was the same as in the reference specimen, which was the shear failure at the joint with a greater ductility and shear strength. This demonstrated that transverse reinforcement in joints could not be totally removed in the external beam-column joints even when ECC is used in the joints region. Figure 2.21 illustrates the cracks pattern of the tested specimens.

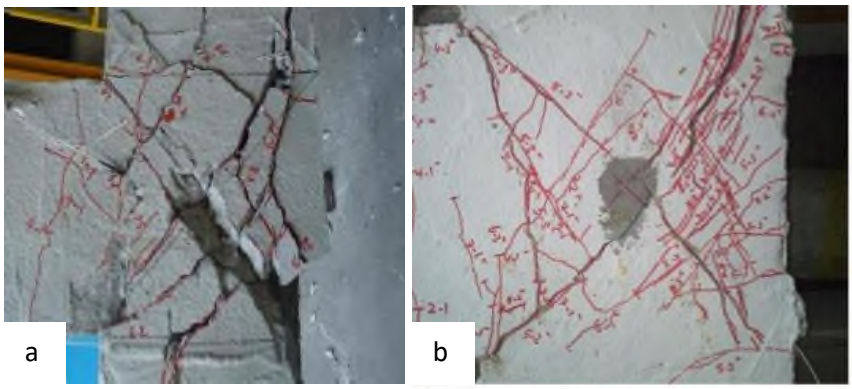

Figure 2.21 Cracks patterns at the end of the test, a) reference specimen, b) ECC specimen [171].

Two groups of specimens were examined under cyclic load by **Shariatmadar and Saghafi** [172]. Both groups were designed based on the seismic requirements mentioned in ACI 318 [128], apart of transverse reinforcements at the joint core were ignored in the second group. Each group was modified by using HPFRCC in the joint region in two forms, as shown in Figure 2.22. The results demonstrated that all HPFRCC specimens failed by forming a plastic hinge near the column face, despite removing the transverse reinforcement in joints. However, HPFRCC specimens exhibited

a significant improvement in load carrying capacity and enhance the seismic performance for both groups. The second pattern of HPFRCC shown in Figure 2.22c, showed better performance than the first pattern, especially for specimens with full seismic details. Finally, in the non-seismic specimens, the inclusion of HPFRCC in the joint region did not prevent the development of a diagonal crack in the joint region.

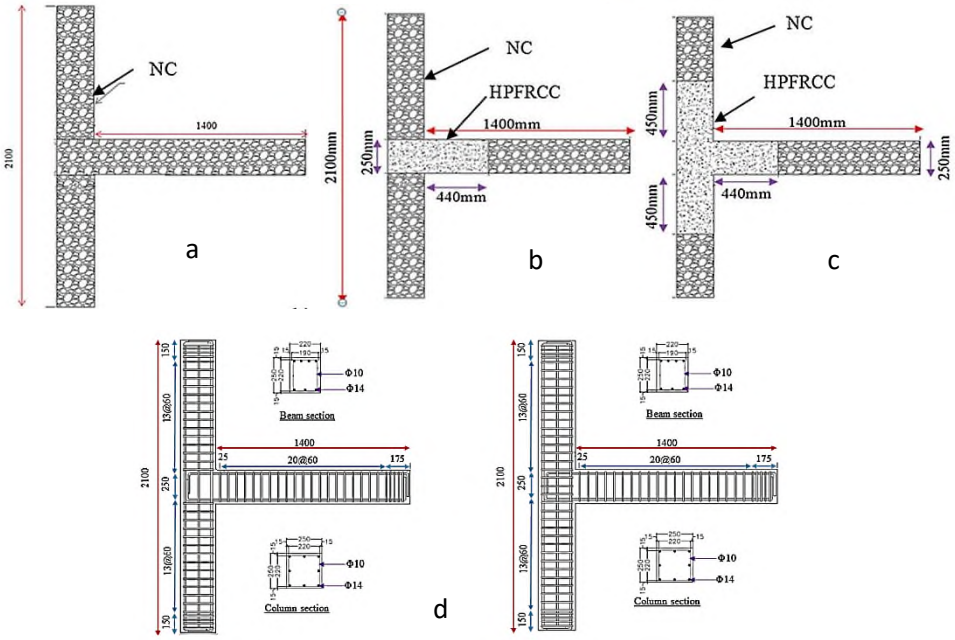

Figure 2.22 Details of the examined specimens, a) reference specimen, b) hybrid pattern C1, c) hybrid pattern C2 and d) reinforcement details [172].

The behavior of corner beam-column joints using ECC material instead of conventional concrete in the joints region was investigated by **Hosseini et al.** [173]. Two specimens of 1/4 scale were constructed and designed in accordance with ACI-318, chapter 21[132]. The first specimen was a reference specimen, while the second specimen constructed by using ECC instead of NSC in the joint region. The result indicated that the inclusion of ECC in the joints region enhanced the lateral strength by 15.7% while maintaining a general response closed to the reference specimen. Moreover, the reference specimen showed larger diagonal cracks and concrete spalling,

but damage in the ECC specimen was restricted to narrow diagonal cracks, as illustrated in Figure 2.23.

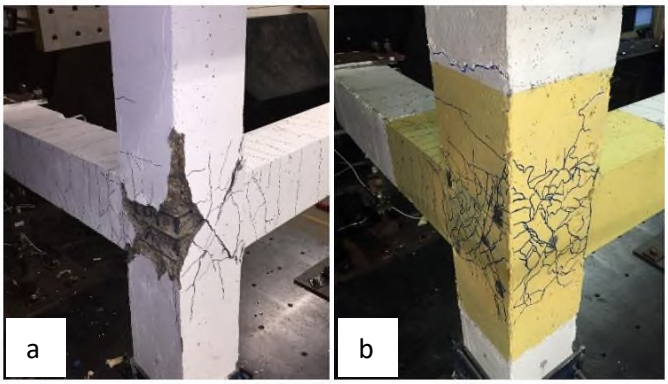

Figure 2.23 Crack patterns at the end of test, a) reference specimen, b) ECC specimen [173].

The application of ECC in the joint region of exterior and corner beam-column joints was examined by **Hosseini et al.** [174]. Eight 3D specimens were examined under biaxial cyclic load; five of them were corner joints, while the others were exterior joints. In addition to the joints type (corner or exterior), using of ECC or NSC in the joint region and the presence of transverse reinforcement in the joints were the key parameters. The results showed that all ECC specimens had relatively similar load-deformation responses. This is owing to the high shear strength of the ECC, which compensates for the loss in the shear strength caused by the elimination of the transverse reinforcement of the joint core. Moreover, ECC material changed the failure mode from shear crack to flexural yielding even when no transverse reinforcement was used. ECC specimens without the transverse reinforcement in joints core showed less damage level than the reference specimen. Also, exterior beam-column joint exhibit less damage due to significant confinement. Finally, owing to the confinement provided by ECC material and transverse beam, the absence of the transverse reinforcement in joints had no influence on the overall behavior of the exterior or corner beam-column joints.

Four half-scale exterior beam-column joints were examined by **Saghafi et al.** [175]. The first specimen was designed according to the seismic requirement recommended by ACI 318 [128], while the others were similar to the first specimen with no transverse reinforcement in the joins region. HPFRCC utilized instead of NSC in the joints region was manufactured using two types of fibers; the first involved 1% hooked end steel fibers plus 1% macro-synthetic fibre, the other used 2% hooked end steel fibers alone. The results demonstrated that all HPFRCC had sufficient shear strength to prevent local shear failure in the joints. Also, HPFRCC changed the failure to plastic hinge in the beam rather than shear failure at the joints in the reference specimen, as shown in Figure 2.24. Hybrid fibers showed better performance than single fibers in terms of energy dissipated capacity. Furthermore, during the loading process, HPFRCC specimens often exhibited lower damage tolerance at any drift than conventional specimens with/without seismic details.

Figure 2.24 Failure mode of the tested specimens, a) Reference specimen with full seismic detailed, b) Reference specimen with no transverse reinforcement in the joint core, c)HPFRCC specimen [175].

Dehghani et al. [176] developed a 3D finite element model to assess the influence of using ECC in the various patterns of beam-column connections, as shown in Figure 2.25. The validity of the model was developed based on the experimental work performed by **Yuan et al.** [165]. The results showed that ECC material improved the load-carrying capacity and ductility of the beam-column connections but had little impact on its initial stiffness. Furthermore, it was revealed that using ECC outside of the plastic hinge

regions was ineffective since most tensile and shear cracks exist throughout the joints. The results also demonstrated that ECC alone could not prevent the diagonal shear crack in the joint region.

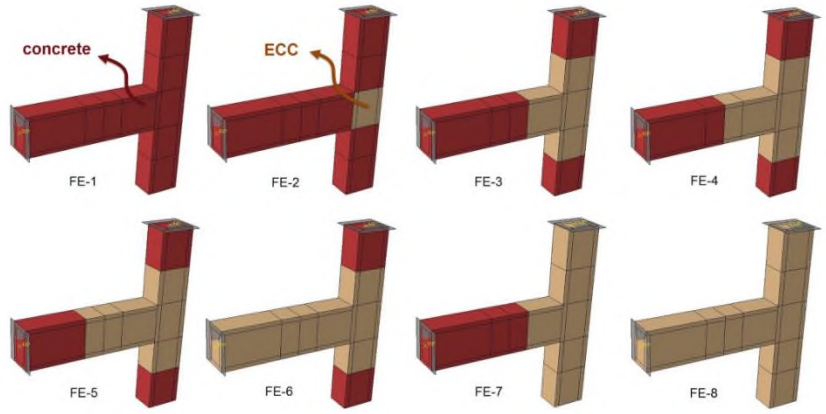

Figure 2.25 Different patterns to use ECC in beam-column joint[176].

Hybrid fibers which consisted of 1% hook end steel fibers plus 1% micro steel fibers, were used to produce HPFRCC [177]. A series of beam-column joints comprised of a reference specimen designed under the seismic requirements of ACI 318 [178] and three specimens had no transverse reinforcement in the joint core. Even though there was no transverse reinforcement in the joint core, the results indicated that HPFRCC material enhances ductility, energy dissipation, and the capacity to tolerate damage regardless of the spacing of the transverse reinforcements of the column and beam. Moreover, HPFRCC material was effective in controlling shear cracks in the joint core as well as preventing crack development in the core region. This was because of the significant improvement on bonding of the reinforcements and clear role of the bridging provided by fibers. Another reason is the strain hardening behavior of the of HPFRCC material in tension.

Zhang and Li [70] carried out an experimental and analytical investigation to study the performance of the beam-column joints by use ECC material in the joint core only. Six specimens (3 interior joints +3 exterior joints) were

examined with different joint transverse reinforcement amounts. In general, the shear strength of interior joints was 36% higher than that of exterior joints. Even with no transverse reinforcement in the joint core, both kinds of specimens showed ductile failure with the development of plastic hinges in the adjacent beams. The specimens without transverse reinforcement, on the other hand, have a larger diagonal crack and development that is earlier than the other specimens. In addition, for specimens without transverse reinforcements, joint deformation and its contribution to lateral displacement were greater than for other specimens.

In their study, Wang et al.[179] examined the performance of interior beam-column joints that utilized HPFRC in the joint region. A total of eight specimens were subjected to reversed cyclic loads to assess their behavior. The study focused on several key factors, including the transverse reinforcement ratio within the joint core (ranging from 0% to 2.9%), the level of axial compression load, the presence of web reinforcing bars, and the inclusion of vertical reinforcing bars across the joint zone. Despite the superior characteristics of HPFRC, the tested specimens experienced joint shear failure, except for those specimens that were reinforced with closely spaced transverse reinforcement, as depicted in Figure 2.26. This finding highlights the necessity of including transverse reinforcement to ensure structural integrity even with using HPFRC in the joint region.

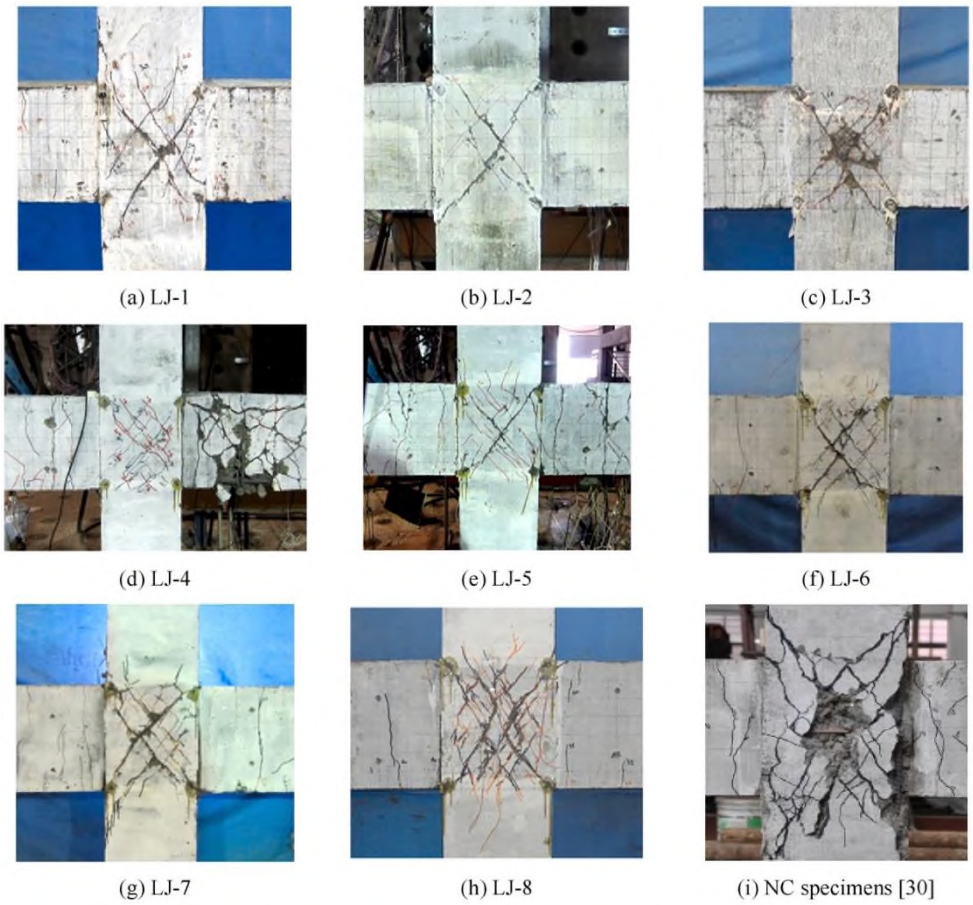

Figure 2.26 Failure mechanism of tested beam-column joint[179].

2.7 Summary and concluding remarks

Based on the extensive analysis of relevant literature, several conclusions can be drawn regarding the factors that impact the shear strength of confined beam-column joints. Additionally, these conclusions are supported by the findings obtained from experimental studies conducted over the past forty years, considering various materials used in hybrid beam-column joints:

1. The joint shear strength of the internal beam-column joint was proportional to the square root of concrete compressive strength ($\sqrt{f_c}$), while the concrete strength did not influence the exterior joint. This is attributed to the confinement given by transverse beams in the interior joint, which improves the diagonal compressive strut activity.

2. Torsional forces develop when the centerline of the beam is displaced from the centerline of the column, generating additional shear forces in the joint core. As a result, joint shear strength deteriorates. The inclusion of a slab was found to decrease the torsional effect of eccentric joints.
3. In contrast with unreinforced joints, the joint aspect ratio of reinforced joints had no effect on the joint shear strength.
4. According to the analysis of the database used in the present study, the column axial load has a positive effect on the joint shear strength of reinforced joints because of the increasing in the depth of compressive strut resulting from the increase in the axial load level on the column. Furthermore, lateral strain is reduced by transverse reinforcement in the joint core.
5. The concrete compressive strut cannot be adequately formed unless anchored at the end nodes. An adequate anchor for the diagonal strut may be created by bending the 90° hook of the longitudinal beam bar into the joint core.
6. There is currently no consensus on the function of transverse reinforcement in the joint core. However, the presence of the transverse reinforcement in the joint core improves the overall behavior of the beam-column joint, particularly the seismic performance.
7. Using SFRC in the joint region of a beam-column connection could enhance seismic performance considerably (ductility and energy absorption). However, for the most of reviewed studies and for their given dimensions and properties, it was found that SFRC did not change the failure mode from joint shear to flexural failure.
8. In comparison to NSC, the SFRC showed little or no concrete spalling and less damage in the joint region. The presence of SFRC, on the other hand, cannot prevent the development of diagonal cracks in the joint region.

9. It has been demonstrated that the large steel bar diameter was yielding in the SFRC joint core, meaning that adding steel fibers did not enhance the large bar diameter anchorage state. In addition, SFRC in the joint region alone cannot prevent the longitudinal bars in columns from buckling. For the reasons stated above, transverse reinforcement cannot be fully eliminated even using SFRC in the joint region.
10. The study revealed that utilizing HPFRCC in the joint area might completely eliminate transverse reinforcement in the joint core for internal beam-column joints.
11. Despite the superior improvement achieved by HPFRCC for non-seismic detailed exterior beam-column joints, the failure mechanism was still a joint shear failure. This proves that transverse reinforcement in the joint core cannot be totally eliminated in the external beam-column joint even when HPFRCC used in the joint region.
12. Both SFRC and HPFRCC manufactured with hybrid fibers (steel fiber+polypropylene fiber, steel fiber+ polyester, micro steel fiber+macro steel fiber, etc.) show better performance compared to those made from a single fibers type.
13. The use of HPFRCC outside plastic hinge regions (D- regions) has been shown to be ineffective because most tensile and shear cracks are observed across the joint region.

In general, HPFRCC improves the seismic performance of the beam-column joint and reduces the demand for closely spaced transverse reinforcement in the joint region. Despite HPFRCC's superior performance, transverse reinforcement in the joint core for the external beam-column joint is still required to prevent the formation of diagonal shear cracks. On the other hand, transverse reinforcement in the joint core of HPFRCC/NC (hybrid) internal beam-column joints can be reduced. Except for the studies

performed by Hosseini et al. [173][174], who investigate the performance of hybrid corner beam-column joints, most investigations in this field concentrated on the behavior of external/internal beam-column joints. Therefore, more experiments should be conducted to investigate the behavior of hybrid corner beam-column joints.

Chapter Three
Experimental Program

3.1 Introduction

This chapter presents the experimental program's details, including specimen design, material properties, mechanical properties, construction method, test setup, and loading protocols. The experimental program aims to achieve the following objectives:

1) Attempt to modify the failure mechanism from being brittle to ductile by using UHPC in the joint area.
2) Attempt to eliminate entirely the requirement for transverse reinforcement in the joint core.
3) Eliminate the necessity of employing closely spaced stirrups in the plastic hinge area of the adjacent members.
4) Rehabilitation the joint area by utilizing the UHPC in the form of a cold joint.
5) Reduce the recommended embedded length for the longitudinal bar of the beam that terminates through the joint core by utilizing UHPC in the joint region.
6) Conduct a study on the feasibility of employing GFRP as a hybrid reinforcement for the longitudinal bar of the beam.

3.2 Test Matrix

The names of the examined specimens were composed of five parts, each of which specified a variable. Figure 3.1 defines the designation of tested specimens.

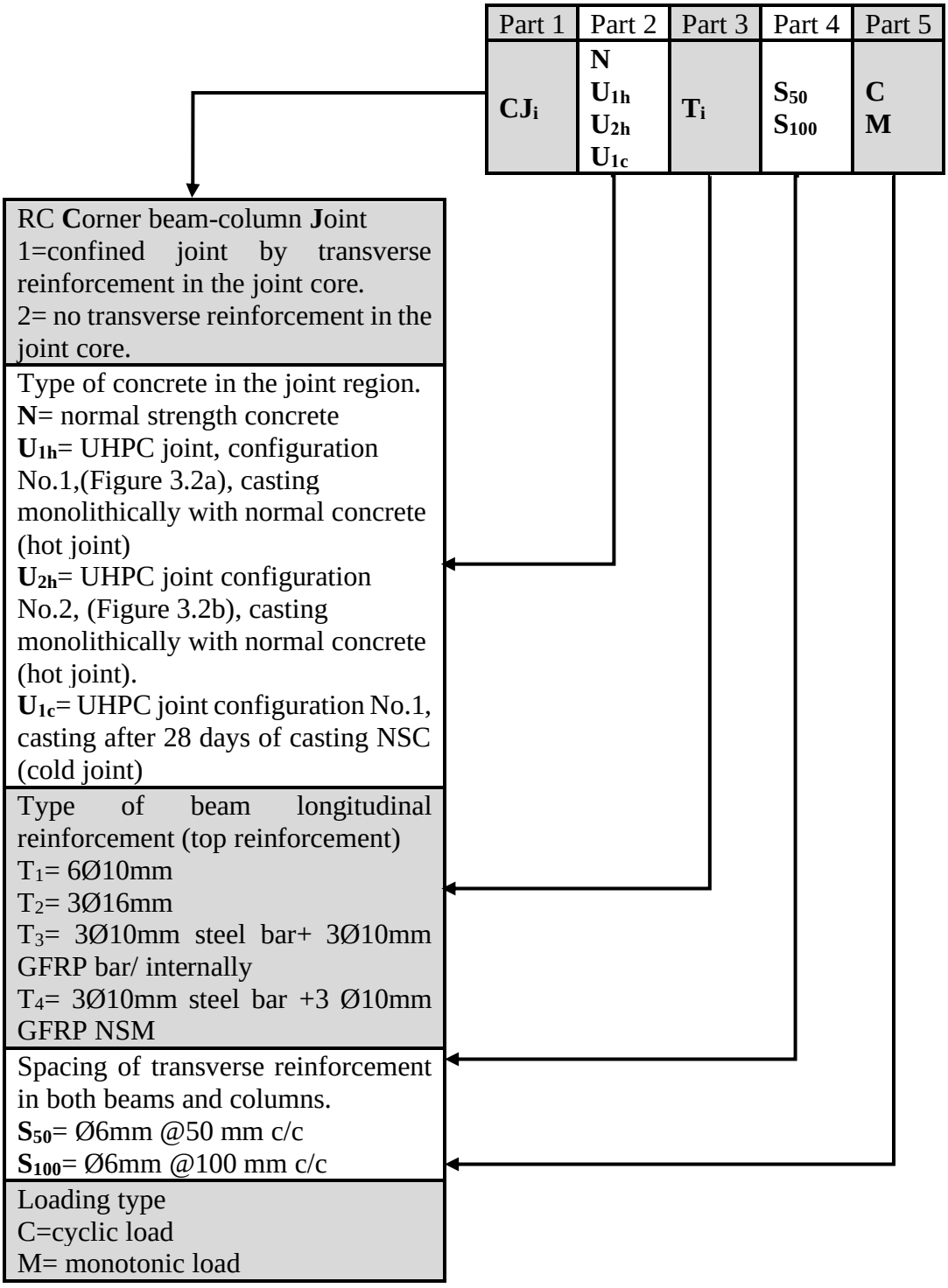

Figure 3.1 Detail of the designation of tested specimens.

For example, specimen **$CJ_2U_{1h}T_1S_{50}C$** represents a connection utilizing UHPC in the joint region, configuration No.1, the UHPC casting monolithic with normal concrete. The transverse reinforcement in the joint core was eliminated and the beams were reinforced by 6Ø10mm as tension reinforcement and Ø6mm @50 mm c/c as shear reinforcement for both beams and columns. The specimen was tested under cyclic load.

To investigate the aims stated above, twenty-two RC scalded corner beam-column joints were tested to failure under both monotonic and compression cyclic load, which were divided into five groups as presented in Table 3.1.

The first group consisted of seven specimens designed based on ACI 318 [17], chapter 18, and ACI-ASCE 352R [33]. The main variables considered in the experiment were the presence of transverse reinforcement in the joint core or not, the type of material used in the joint region (NSC or UHPC), the configuration of UHPC in the joint region, and the loading protocol (cyclic/monotonic). Hand calculations for the design control specimen are presented in Appendix B.

The second group consisted of five specimens that were similar to the first group, except that the spacing of transverse reinforcement in the adjoining beams and columns was duplicated to d/2 (designed to resist gravity load) instead of d/4 (designed to resist seismic load) in the first group.

The third group consisted of four specimens that simulated the rehabilitation of existing RC corner beam-column joints by removing and replacement techniques.

The fourth group consisted of four specimens that aimed to reduce the embedded length of longitudinal bars in beam that pass/terminated through the joint core by using UHPC in the joint region.

Finally, the fifth group utilized hybrid beam longitudinal reinforcement in the form of strengthening (NSM) or internal reinforcement.

The following sections will provide detailed information on the tested specimens.

Table 3.1 Specification of the tested specimens

No.	Group ID	Specimens ID	Joint Martial	Joint confinement	Transverse* reinforcement spacing	Beam longitudinal reinforcement	Loading type
1	I	$CJ_1NT_1S_{50}C$	NSC	Yes	Ø6@50mm	6Ø10mm	cyclic
2		$CJ_2NT_1S_{50}C$	NSC	No	Ø6@50mm	6Ø10mm	cyclic
3		$CJ_2U_{1h}T_1S_{50}C$	UHPC	No	Ø6@50mm	6Ø10mm	cyclic
4		$CJ_2U_{2h}T_1S_{50}C$	UHPC	No	Ø6@50mm	6Ø10mm	cyclic
5		$CJ_1U_{1h}T_1S_{50}C$	UHPC	yes	Ø6@50mm	6Ø10mm	cyclic
6		$CJ_2NT_1S_{50}M$	NSC	No	Ø6@50mm	6Ø10mm	monotonic
7		$CJ_2U_{1h}T_1S_{50}M$	UHPC	No	Ø6@50mm	6Ø10mm	monotonic
8	II	$CJ_2NT_1S_{100}C$	NSC	No	Ø6@100mm	6Ø10mm	cyclic
9		$CJ_2U_{1h}T_1S_{100}C$	UHPC	No	Ø6@100mm	6Ø10mm	cyclic
10		$CJ_2U_{2h}T_1S_{100}C$	UHPC	No	Ø6@100mm	6Ø10mm	cyclic
11		$CJ_2NT_1S_{100}M$	NSC	No	Ø6@100mm	6Ø10mm	monotonic
12		$CJ_2U_{1h}T_1S_{100}M$	UHPC	No	Ø6@100mm	6Ø10mm	monotonic
13	III	$CJ_2U_{1c}T_1S_{50}C$	UHPC	No	Ø6@50mm	6Ø10mm	cyclic
14		$CJ_2U_{1c}T_1S_{100}C$	UHPC	No	Ø6@100mm	6Ø10mm	cyclic
15		$CJ_2U_{1c}T_1S_{50}M$	UHPC	No	Ø6@50mm	6Ø10mm	monotonic
16		$CJ_2U_{1c}T_1S_{100}M$	UHPC	No	Ø6@100mm	6Ø10mm	monotonic
17	IV	$CJ_2NT_2S_{50}C$	NSC	No	Ø6@50mm	3Ø16mm	cyclic
18		$CJ_2NT_2S_{100}C$	NSC	No	Ø6@100mm	3Ø16mm	cyclic
19		$CJ_2U_{1h}T_2S_{50}C$	UHPC	No	Ø6@50mm	3Ø16mm	cyclic
20		$CJ_2U_{1h}T_2S_{100}C$	UHPC	No	Ø6@100mm	3Ø16mm	cyclic
21	V	$CJ_2NT_3S_{50}C$	NSC	No	Ø6@50mm	3Ø10 steel bar+3Ø10 GFRP bar	cyclic
22		$CJ_2NT_4S_{50}C$	NSC	No	Ø6@50mm	3Ø10 steel bar+3Ø10 GFRP bar	cyclic

*spacing of transverse reinforcement in adjoining members (beams+columns)

3.3 Specimens details

Based on the parametric study presented in this chapter, the specimens were designed considering the ACI 318[17] and ASCE-ACI 352R [33], as illustrated in Appendix B. The dimensions of the specimens were adjusted based on the capabilities of the testing equipment used in the study. All specimens had similar geometric properties. The beams' tension reinforcement was selected to produce substantial shear stresses on the joint core to ensure that the failure mode of NSC specimens is governed by joint

shear failure. The column dimensions were also chosen to provide the recommended development length of the longitudinal bar in the beam that terminated through the column. The strong column-weak beam principle was followed in the design of the specimens, with the flexural strength ratio exceeding 1.2 as recommended by ASCE-ACI 352R [33].

The beam-column joint is characterized as a discontinuity stress distribution region (D-region) because it creates complicated stresses due to the change in geometry of the structural member in this area. According to St. Venant's principle, the stresses in the D-region approach a linear distribution at a distance equivalent to the overall height of the member (h) away from the discontinuity region [128].

The high cost of UHPC makes it impractical to use it throughout an entire structural system. However, due to the fact that the joint region (D-region area) experiences the greatest tensile and shear stresses, it is practical to use UHPC in this area. This investigation employed two UHPC configurations in the joint area instead of NSC. In the initial configuration, UHPC was poured into the joint core and extended to a length equivalent to the beam depth through the adjoining beams, as shown in Figure 3.2a. This approach is more rational and cost-effective in terms of design. In the second configuration, UHPC was poured into the joint core and extended to a length equivalent to the depth of the components in the adjacent beams and columns, as depicted in Figure 3.2b. The following sections provide detailed descriptions of the specimens.

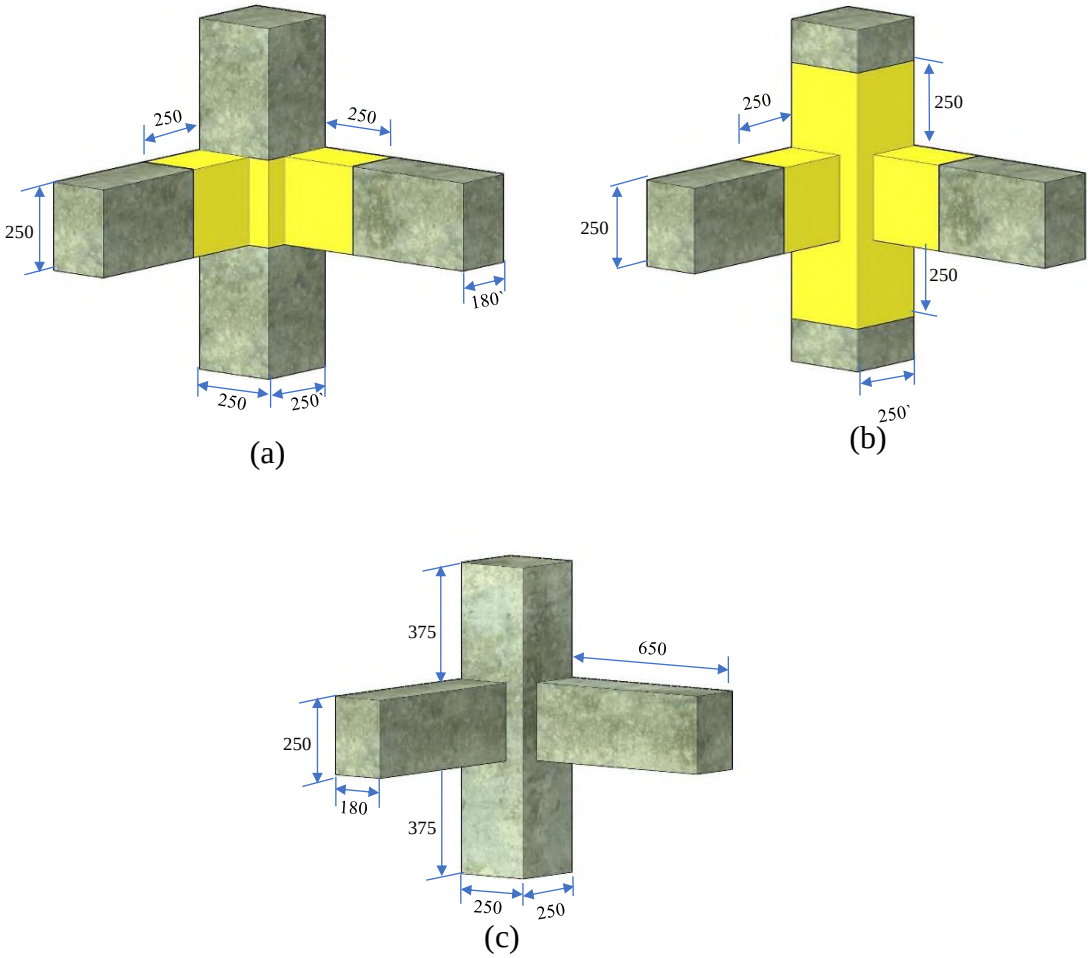

Figure 3.2 Configuration of UHPC in the joint region of the tested specimens, a) configuration type 1, b) configuration type 2, and c) NSC specimens.

3.3.1 Details of group I

The first group of specimens in this study consisted of seven specimens designed to investigate the use of UHPC to enhance the performance of corner beam-column joints and to totally eliminate transverse reinforcement in the joint core. The key variables examined in this group were the type of concrete used in the joint region, the presence of transverse reinforcement in the joint core or not, UHPC configuration and the loading protocol. Figure 3.3, presents detailed information on the geometry and reinforcement of the specimens used in this group.

The first specimen in the study was called **$CJ_1NT_1S_{50}C$**, and it served as a control specimen for comparison purposes. It was designed according to the guidelines provided by ACI-318 [17] and ACI-ASCE 352 [33]. To achieve this, the beams were reinforced with 6 bars of 10mm diameter at the top and 3 bars of 10mm diameter at the bottom, while the column was reinforced with 8 bars of 12mm diameter. This resulted in a longitudinal reinforcement ratio of 1.3% and 1.44% for beams and columns, respectively. Additionally, the specimen was reinforced with transverse reinforcement of 6mm diameter at a spacing of 50mm for beams and columns (including the joint core), which meets one of the seismic code requirements. These details are important to understand the design and construction of the control specimen and how it compares to the other specimens in the study.

The second specimen in group I was named **$CJ_2NT_1S_{50}C$** and was identical to the first one, except for the exclusion of transverse reinforcement within the joint core.

Two additional specimens were created for group I, which were similar to the second control specimen **$CJ_2NT_1S_{50}C$**, but with UHPC used in the joint region instead of NSC in two different configurations previously described. These specimens were labeled **$CJ_2U_{1h}T_1S_{50}C$** and **$CJ_2U_{2h}T_1S_{50}C$**. Another specimen, **$CJ_1U_{1h}T_1S_{50}C$**, had full seismic detail and used UHPC in the joint region instead of NSC. The last two specimens in group I, **$CJ_2NT_1S_{50}M$** and **$CJ_2U_{1h}T_1S_{50}M$**, were similar to **$CJ_2U_{1h}T_1S_{50}C$** and **$CJ_2U_{2h}T_1S_{50}C$** specimens but were subjected to a bidirectional monotonic load instead of a cyclic loading protocol. Figure 3.3 provides full details about the specimens in group I.

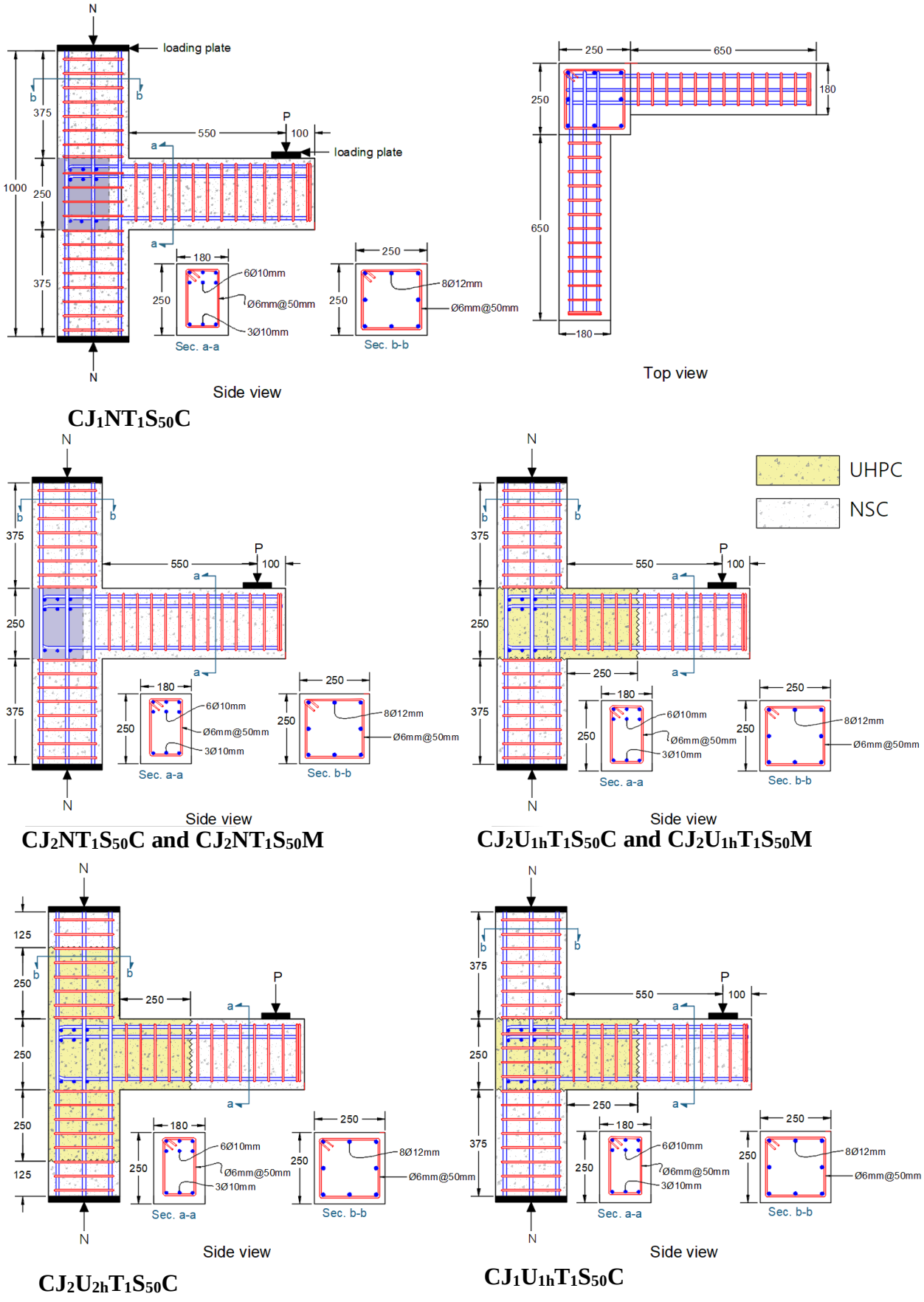

$CJ_1NT_1S_{50}C$

$CJ_2NT_1S_{50}C$ and $CJ_2NT_1S_{50}M$

$CJ_2U_{1h}T_1S_{50}C$ and $CJ_2U_{1h}T_1S_{50}M$

$CJ_2U_{2h}T_1S_{50}C$

$CJ_1U_{1h}T_1S_{50}C$

Figure 3.3 Specimens details of group I.

3.3.2 Details of group II

The second group included five specimens that were designed to resist non-seismic loads (gravity load). These specimens were similar to the ones in the first group, but the spacing between the transverse reinforcement was doubled to d/2 for both beams and columns. The objective of this group was to examine the effectiveness of UHPC in enhancing the behavior of a RC corner beam-column joint that was not designed for seismic loads, and to eliminate the requirement for tightly-spaced stirrups in the plastic hinge area of the adjacent members (beams and columns). The variables were the joint material, the configuration of UHPC in the joint region, and the loading protocol. Figure 3.4 shows the details of the specimens in this group. The first specimen served as a control specimen, labeled **$CJ_2NT_1S_{100}C$**. The other two specimens, labeled **$CJ_2U_{1h}T_1S_{100}C$** and **$CJ_2U_{2h}T_1S_{100}C$**, were similar to the control specimen in geometry and reinforcement detail, but the NSC in the joint region was replaced by UHPC in two different configurations. These specimens were tested under cyclic bidirectional load. The last two specimens in this group, labeled **$CJ_2NT_1S_{100}M$** and **$CJ_2U_{1h}T_1S_{100}M$**, were similar to the first and second specimens, but were tested under monotonic bidirectional loading.

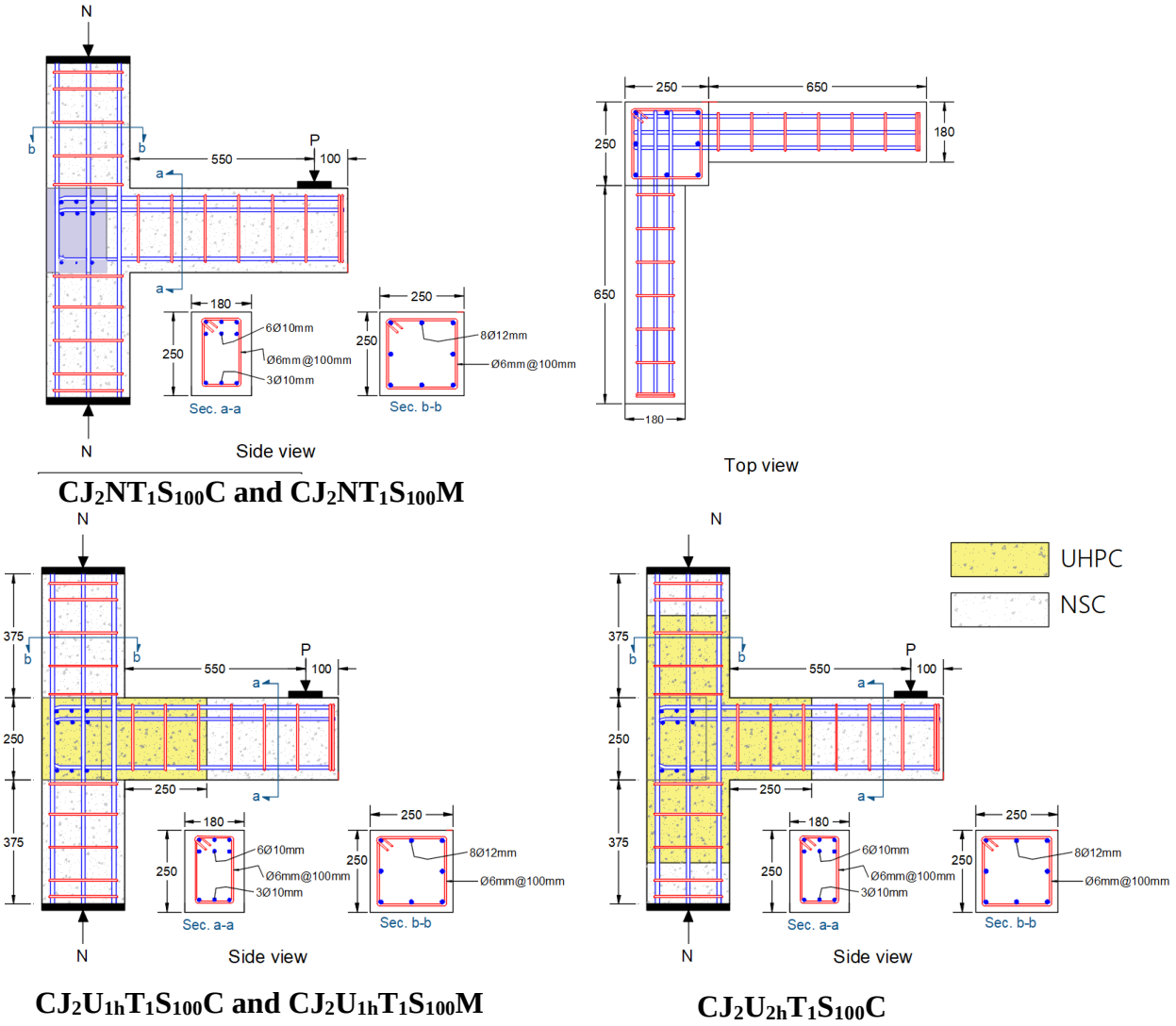

$CJ_2NT_1S_{100}C$ and $CJ_2NT_1S_{100}M$

$CJ_2U_{1h}T_1S_{100}C$ and $CJ_2U_{1h}T_1S_{100}M$

$CJ_2U_{2h}T_1S_{100}C$

Figure 3.4 Specimens details of group II.

3.3.3 Details of group III

According to the author's knowledge, no attempts have been made to use the UHPC as a repair the corner beam-column joints by removing and replacement techniques. To explore the potential of this technique, the study involved constructing four specimens in three stages to simulate the removal and replacement process. The study focused on two key factors: the transverse reinforcement in the adjoining members and the loading protocols.

All the specimens in this group had the same longitudinal reinforcement, consisting of 6Ø10mm reinforcement at the top of the beams and 3Ø10mm at the bottom, as well as 8Ø12mm reinforcement in the column. The transverse reinforcement in the adjoining member of the first two specimens consisted of Ø6mm@50mm, while the others had Ø6mm@100mm. The transverse reinforcement in the joint core was omitted, to simulate a severe case of joint damage. To repair the joint, UHPC was used as a replacement material in the joint region. Near-surface mounted (NSM) steel bars were added to each beam side to improve the bond between the old concrete and the new material used in the joint region. The subsequent section of this chapter will provide an in-depth discussion of the construction process. Figure 3.5 illustrates the details of the specimens in this group, highlighting the critical elements of the repaired joint, including the transverse reinforcement, NSM steel bars, and UHPC material.

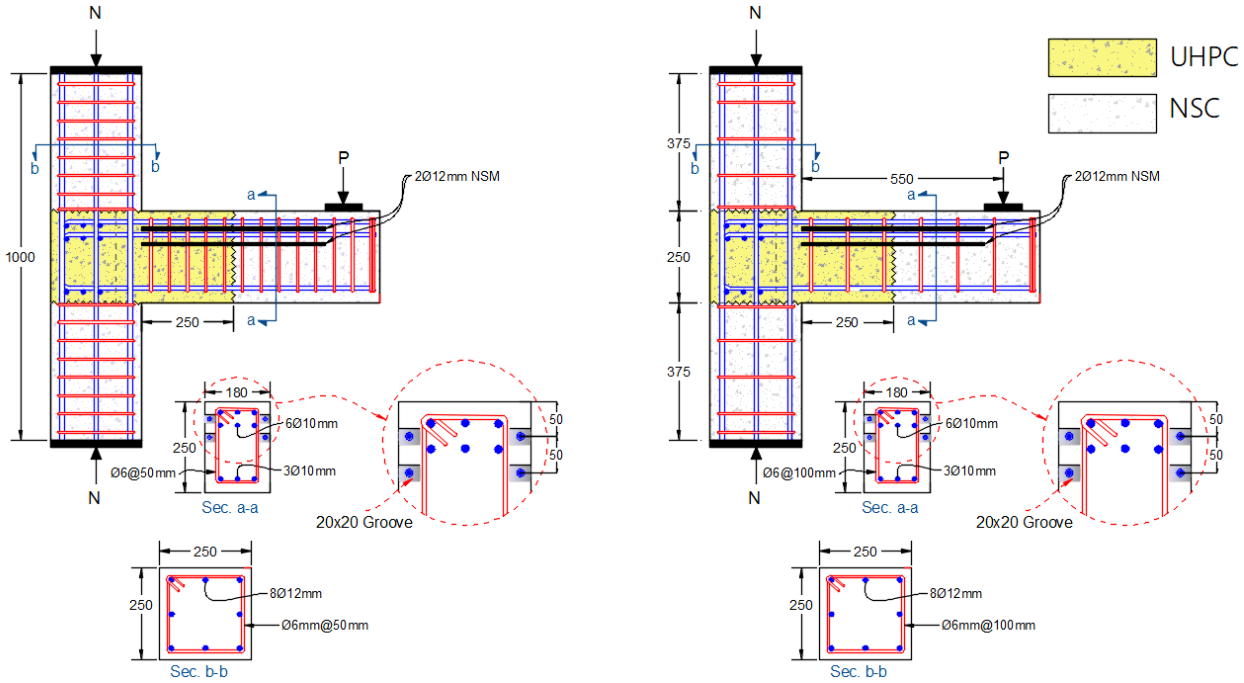

$CJ_2U_{1h}T_1S_{50}C$ and $CJ_2U_{1h}T_1S_{50}M$ **$CJ_2U_{1c}T_1S_{100}C$ and $CJ_2U_{1c}T_1S_{100}M$**

Figure 3.5 Specimens details of group III.

3.3.4 Details of group IV

As previously discusses in section 2.5.6, the modern building code recommends that the development length of longitudinal bars in beams that pass or terminate through the joint core be a crucial factor. This recommended length ensures the bond condition and helps prevent pullout or slip failure.

Table 3.2 displays the modern code provision for determining the necessary development length required to ensure the bond condition between the terminate/passes reinforcing bars in the beam and the joint core. According to Table 3.2, the total depth of the column (h_c) is not less than 25-28 times the diameter of the longitudinal reinforcing bar in beams. This requirement is crucial to ensure that the reinforcing bars can adequately bond with the concrete and avoid any potential bond failure, which could compromise the integrity and safety of the structure.

Designers have two solutions to satisfy this criterion: using many small diameter bars, which may cause reinforcement congestion in the connection region, or increasing the column size.

Table 3.2 Moderate code provision for calculating the development length passing/terminating through the joint core

Code provision	Recommendation for development length of beam bar pass through the joint core
ACI-ASCE 358R [33]	$l_{dh} = \frac{f_y d_b}{4.2\sqrt{f_c`}}$ Also, $\frac{h_c}{d_b} \geq 20\frac{f_y}{420}$
ACI 318 [17]	$l_{dh} = \frac{0.24 f_y d_b}{\lambda\sqrt{f_c`}}$, and the depth (h) of the joint (column) should be the greatest of: a) 20 d_b of the largest Grade 420 longitudinal bar. b) 26 d_b of the largest Grade 550 longitudinal bar.
NZS3101-1 [129]	$l_{dh} = 0.24 \propto_b \propto_1 \propto_2 \frac{f_y d_b}{\sqrt{f_c`}} \geq 8 d_b$ $f_c`$ = shall not be greater than 70MPa. $\propto_b$ = reinforcement provided in a flexural member in excess of that required $\propto_1$=0.7 for 32 mm bars or smaller with side cover normal to the plane of the hook ≥ 60 mm, and cover on the tail extension of 90° hooks equal to or greater than 40 mm and1.0 for all other cases $\propto_2$=0.8 where confined by closed stirrups and1.0 for all other cases
CSA A23.3 [102]	$l_{dh} = \frac{100\, d_b}{\sqrt{f_c`}} \frac{f_y}{400}$
BS EN 1998-1 [35]	$\frac{d_{bl}}{h_c} \leq \frac{7.5 f_{ctm}}{\gamma_{Rd} f_{yd}} (1 + 0.8 v_d)$ f_{ctm}=mean value of the tensile strength of concrete v_d= normalized design axial force in the column. γ_{Rd}=model uncertainty factor on the design value of resistances, taken as being equal to 1,2 or 1,0 respectively for DCH or DCM
AIJ [180]	$h_c/d_b \leq \frac{1+\gamma}{6\left(1+\frac{P}{A_g f_c`}\right)\frac{f_c`^{2/3}}{f_{yu}}}$

The aim of this group was to reduce the development length of the bar in the beam required to terminate through the joint core of corner beam-column joint by utilizing UHPC. Four specimens were constructed with a column depth to beam bar diameter ratio of 15.6, which was 40% less than that recommended by ACI318 ($25d_b$). The specimens had similar geometrical

properties, with beams reinforced with 3Ø16 mm as tension reinforcement and 3Ø10 mm as compression reinforcement, and columns reinforced by 8Ø12mm resulting in a longitudinal reinforcement ratio of 1.55% and 1.44% for beams and columns, respectively. It is worth mentioning that the transverse reinforcement in the core of the joint was eliminated in this group. Joint material (NSC/UHPC) and the spacing of transverse reinforcement in both beams and columns were the key variables considered in this study. The first specimen served as the control specimen, labeled **$CJ_2NT_2S_{50}C$**, while the second specimen was identical but with duplicated the spacing of transverse reinforcement in the beam and column (Ø6 mm @ 100 mm, equivalent to d/2). UHPC was utilized in the joint region of specimens **$CJ_2U_{h1}T_2S_{50}C$** and **$CJ_2U_{h1}T_2S_{100}C$** due to its high bond strength, which may be resulting in a reduced development length required to pass through the joint core. Figure 3.6 illustrates the geometrical and reinforcement details of the specimens in this group.

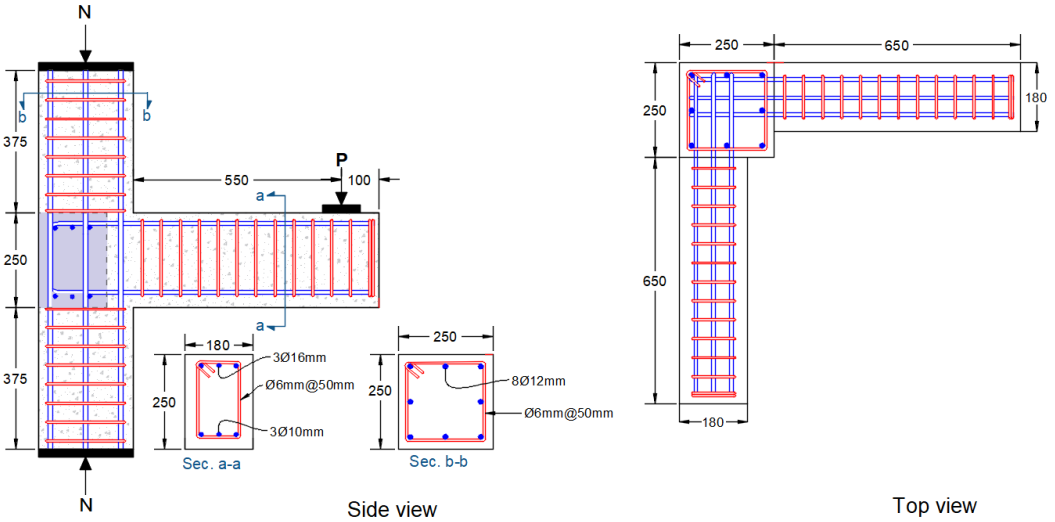

$CJ_2NT_2S_{50}C$

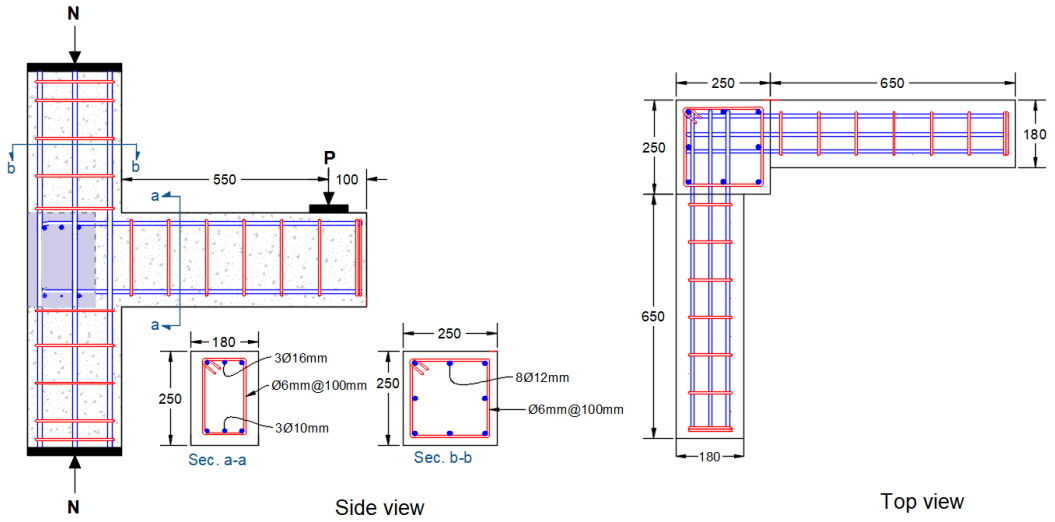

$CJ_2NT_2S_{100}C$

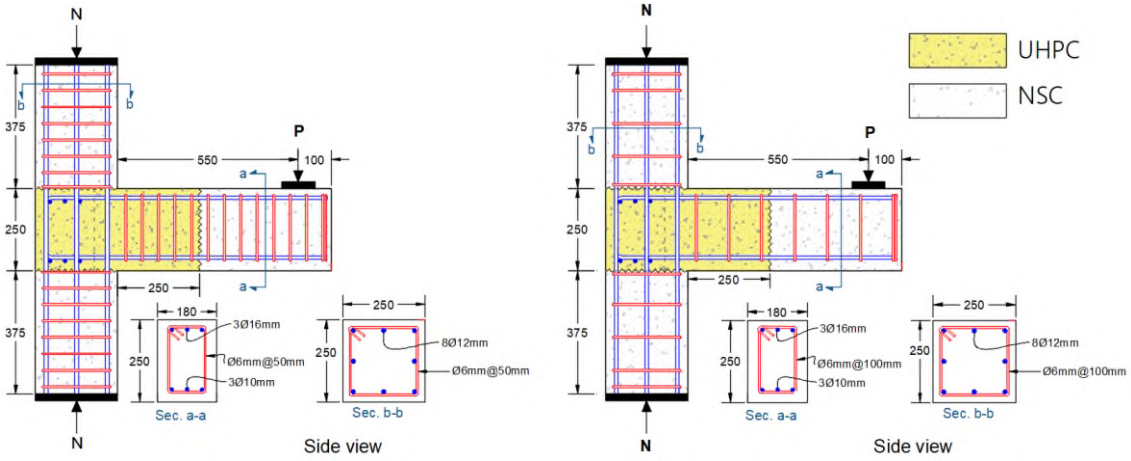

$CJ_2U_{1h}T_2S_{50}C$ **$CJ_2U_{1h}T_2S_{100}C$**

Figure 3.6 Specimens details of group IV.

3.3.5 Details of group V

In this group, an attempt was made to use hybrid reinforcement in the tension side of beams, comprising of 50% steel reinforcement and 50% Glass Fiber Reinforced Polymer (GFRP) reinforcement. To this end, two specimens were cast: the first specimen, labelled **$CJ_2NT_3S_{50}C$**, had beams reinforced with 3Ø10 mm steel bars and 3Ø10mm GFRP bars. The second specimen, labelled **$CJ_2NT_4S_{50}C$**, represented a strengthening case achieved by adding 3Ø10mm GFRP bars to each beam through a near-surface mounted (NSM) technique, while the initial specimen was reinforced with 3Ø10 mm steel bars at the top and bottom of the beam. Figure 3.7 illustrates the geometry and reinforcement details for each specimen in this group.

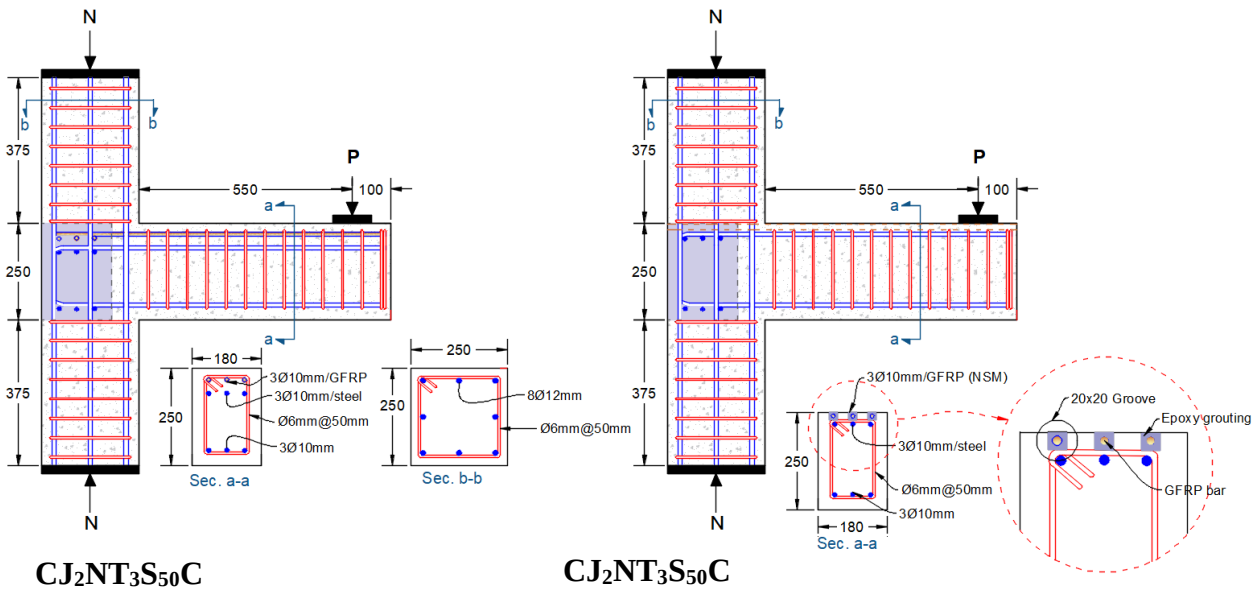

Figure 3.7 Specimens details of group V.

3.4 Material properties

3.4.1 Ultra-high performance concrete (UHPC)

To create an extremely compact matrix for UHPC, it is crucial to use a particle combination with a high density. UHPC is typically made up of a large proportion of cement, silica fume, fine sand, a superplasticizer, water,

and micro steel fiber. A considerable amount of cementitious materials and fine sands are required to achieve the desired strength, with a very low water to cementitious material ratio. As a result, a high dosage of superplasticizer is needed to ensure the desired workability and self-consolidation of the mixture. In UHPC, fine sand with a diameter of less than 0.6 mm is commonly used to enhance the performance of the final product, since it results in lower porosity and permeability [181]. Silica fume is an important component in UHPC, as it serves two primary purposes. Firstly, it enhances the hydration products, which contributes to the overall strength of the final product. Secondly, it helps to increase the density of the concrete. In addition to the use of silica fume, coarse aggregate is typically omitted from UHPC mixtures in order to maintain dense microstructures and enhance homogeneity. This approach allows the UHPC to be treated as a homogenous material [182]. Micro steel fibers are added in large quantities to enhance tension strength, as well as to provide excellent post-cracking performance by preventing crack opening through a bridging mechanism. Through a comprehensive study, it was demonstrated that the 2% volume fraction of micro steel fibers offers an excellent balance of cost, strength, ductility, and workability in UHPC mixtures. Additionally, the research showed that using a higher volume fraction did not significantly improve the material's properties, while using a lower volume fraction resulted in a weaker and less ductile material [181][183].

According to the above discussion, 48 trial mixes were carried out in the laboratory of the Engineering College at AL-Qasim Green University to achieve the fresh and mechanical properties of UHPC defined in the previous section. The main variables were the type of constituents, proportion percentage, and particle size. Table 3.3 presents the mix proportions of

UHPC adopted in the present study, and Figure 3.8 illustrates the constituent materials and their percentage by total weight of the mix.

Table 3.3 Mix proportions of UHPC

Constituents	The proportion by weight (kg/m^3)
Cement	950
Fine sand	1050
Silica fume	190[a]
Water	171[b]
Superplasticizer	39.9[c]
Micro steel fiber	157[d]

[a] silica fume=20% of cement weight, [b] w/b =15%, [c] sp/b=3.5% and [d] micro steel fiber=2% of total volume

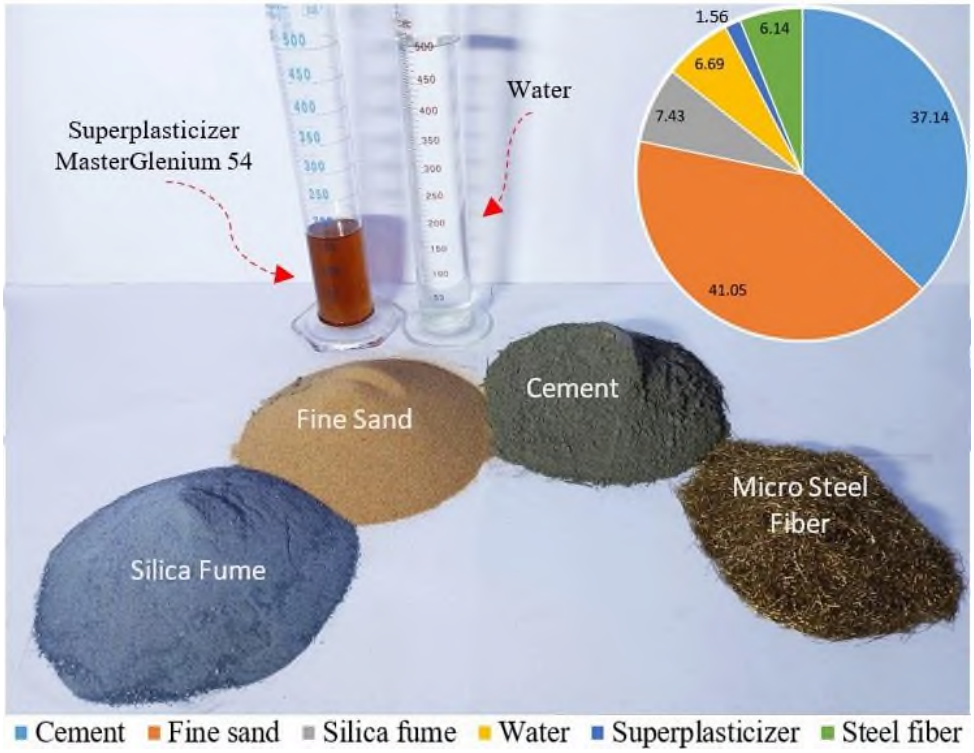

Figure 3.8 The UHPC constituent material and its percentage by total mix weight.

The UHPC was mixed using a high-shear mixer with a capacity of 325 L. The dry materials, including cement, sand, and silica fume, were mixed first for 1-2 minutes. Next, the liquid mixture of water and superplasticizer was added gradually and left to mix for about 12-15 minutes until the UHPC paste became flowable. Steel fibers were then added gradually to the UHPC

paste and mixed continuously for 3-5 minutes until they were well distributed throughout the paste. The UHPC was then ready to be poured into the specimens or molds for examining the mechanical properties. Figure 3.9 provides a summary of the mixing procedures. At the same time, the flowability of the UHPC was evaluated using the flow test, which was conducted according to ASTM C230 standard [184] and ASTM C1437 [185]. The ASTM C1856 [47] recommended that the flow of UHPC range between 200 and 250 mm. Based on trail mixes mentioned above, the present study adopted 230 to 240 mm UHPC flow. Figure 3.10 illustrate the flow test procedure.

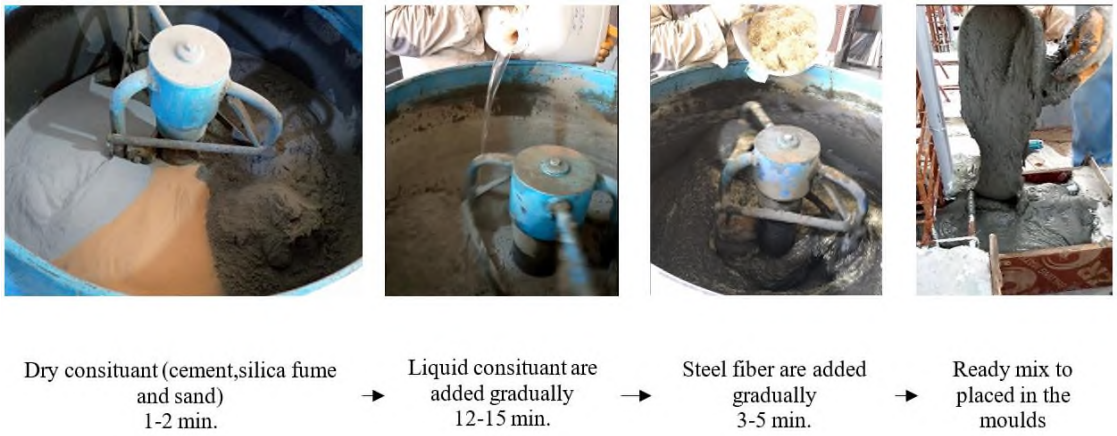

Figure 3.9 UHPC mixing procedure.

Figure 3.10 Flow test procedure for UHPC.

3.4.2 UHPC constituents material

3.4.2.1 Cement

Based on the results of the trial mixes, the best combination of compressive strength and flowability was achieved using Type V Portland cement (AL-JESR), which is manufactured by Lafarge Iraq- Al Sulaymaniyah. Appendix C presents the physical and chemical characteristics of Type V Portland cement.

3.4.2.2 Fine sand

Local natural sand was used to produce UHPC after passing it from a sieve 0.6 mm, as recommended by the previous study mentioned above. Appendix C provides details regarding the physical and chemical characteristics.

3.4.2.3 Silica fume (SF)

Micro silica, also known as silica fume, is generated as a by-product of silicon and ferrosilicon alloys. Its particle size is significantly smaller than that of cement particles. When mixed, silica fume plays two roles. Firstly, it reacts with calcium hydroxide to create calcium silicate hydrate (C-S-H). Secondly, the fine particle size of the remaining silica fume helps fill the microvoids between the components [186]. Therefore, the use of silica fume results in decreased porosity and permeability of the concrete, leading to improved strength and durability. A brand of high-quality silica fume called MasterRoc MS 610 [187], produced by BASF construction chemicals, was utilized in this study.

3.4.2.4 Superplasticizer (SP)

Carboxylic ether polymer high range water reducing admixture, commercially called MasterGlenium 54 [188] provided by BASF construction chemicals, was used in producing UHPC and achieving the required workability. Based on the trail mix mentioned above, the present study used a 3.5% superplasticizer to cementitious material.

3.4.2.5 Steel fiber

Copper-coating micro steel fibers with a straight shape (as shown in Figure 3.11) were utilized in the production of UHPC that was used in the present study. These fibers were obtained from Hebei Yusen Metal Wire Mesh [189]. Based on previous recommendations and the trial mix results, 2% of the UHPC mix's volume was composed of steel fibers. The physical properties of the steel fibers, as provided by the manufacturer's datasheet, are presented in Table 3.4. These properties meet the requirements of the ASTM A820 standard test [190].

Table 3.4 Physical properties of micro steel fiber

Parameter	Value
Description	Micro copper coated straight steel fiber
Length, l_f(mm)	13
Diameter d_f (mm)	0.2
Aspect ratio l_f/d_f	65
Tensile strength (MPa)	3005
Specific gravity (kg/m^3)	7800

Figure 3.11 Photo of copper-coated micro steel fiber.

3.4.3 Normal strength concrete (NSC)

Ready mix concrete with a maximum aggregate size of 19 mm, a slump of 120 mm, and a target compressive strength of 35 MPa at 28 days was used to cast the specimens sections. All the constituent materials were tested based on IQS specifications, as shown in Appendix C.

3.5 Mechanical properties and testing method for concrete

3.5.1 Mechanical properties of UHPC

3.5.1.1 Compressive strength

Standard testing methods for evaluating concrete compressive strength involve the use of either cylinder or cube specimens. While the cylinder is the standard specimen for many countries, including North America, France, Japan, Australia, and New Zealand, much of Europe relies on the cube specimen [191], [192]. However, the use of these standard procedures presents two main issues, namely the capacity of the testing machine and cylinder end preparation, which become especially problematic for high-strength concretes. In an attempt to address these issues, small specimens may be used to mitigate the first problem, while a cube specimen can be utilized to address the second issue. However, deviating from standard tests raises concerns regarding the accuracy and reliability of test results [193]. In the case of UHPC, extensive research has been conducted to investigate the size effect on compressive strength, and it has been found that the compressive strength produced by the cube specimen is comparable to that produced by the cylinder specimen. Therefore, the compressive strength obtained from both cube and cylinder specimens for UHPC is quite similar [181], [182], [193]–[195]. Grybeal [196] has presented a conversion factor for determining the cylinder compressive strength, which is shown in Table 3.5.

Table 3.5 Conversion factor to determine the UHPC cylinder compressive strength [196]

Tested specimens	Multiply by	Result
75 mm diameter cylinder	0.99	100 mm diameter cylinder
100 mm cube	1.00	
70.7 mm cube	0.93	
50 mm cube	0.96	
100 mm diameter cylinder	1.01	75 mm diameter cylinder
100 mm cube	1.00	
70.7 mm cube	0.94	
50 mm cube	0.96	

Based on the preceding discussions, the UHPC's compressive strength was assessed by ASTM C109 [197], utilizing a cube with a side length of 50 mm, and this was equivalent to the strength determined by cylinders through ASTM C1856 [45]. The compressive strength of UHPC was assessed using a universal testing machine that had a capacity of 2000 kN, as depicted in Figure 3.12. Table 3.6 presents the results of the test, indicating that the average compressive strength of UHPC was 132.18 MPa. On the other hand, the standard deviation and coefficient of variation were 4.125 MPa and 3.12%, respectively.

Figure 3.12 Compressive strength test and failure mode of tested specimen.

Table 3.6 Test results of UHPC compressive strength

Type of test	Test method	Values (MPa)		
Compressive strength	ASTM C109 [197] ASTM C1856 [47]	133.34	140.28	138.4
		130.78	133.08	130.2
		131.98	127.25	135.28
		132.07	127.7	132.34
		129.72	126.53	132.79
		130.63	132.95	133.72
		130.03	140.85	129.62
		128.1	132.27	130.17
		140.7	127.63	132.16
		126.2	138.7	130
Average		132.18 MPa		
St. Deviation (SD)		4.125 MPa		
Coefficient of Variation (COV)		3.12 %		

3.5.1.2 Splitting tensile strength

In the current study, the splitting tensile test, based on ASTM C496 [198], was performed to evaluate the tensile strength of UHPC in terms of splitting tensile strength. A cylinder with a diameter of 100 mm and a length of 200 mm was utilized to measure the splitting strength, as illustrated in Figure 3.13. The test findings revealed an average splitting tensile strength of 14.16 MPa with a standard deviation of 0.23 MPa. Table 3.7 outlines the specific results of the splitting tensile test.

Figure 3.13 UHPC splitting tensile strength test and failure mode of tested specimen.

Table 3.7 Test results of UHPC splitting tensile strength

Type of test	Test method	Values (MPa)
Splitting tensile strength	ASTM C496 [198]	14.15
		14.07
		14.6
		14.1
		14.09
		13.93
Average		14.16 MPa
St. Deviation (SD)		0.23 MPa
Coefficient of Variation (COV)		1.62 %

3.5.1.3 Flexural strength (Modulus of rupture)

The modulus of rupture is a form of indirect tensile strength testing. In this study, two different methods were used to assess the modulus of rupture as follows:

1) Third point loading method

This approach involved conducting the testing procedure in accordance with ASTM C78 [199]. Specimens with dimensions of 100mm × 100mm × 400mm were subjected to a flexural strength test using a universal testing machine that had a capacity of 1000 kN. The test was conducted under a four-point load configuration.

2) Center point loading method

The flexural strength of cement mortar was evaluated using this technique, which is based on ASTM C348 [200]. A center point load was applied to a specimen measuring 40mm × 40mm × 160mm, as depicted in Figure 3.14. The test outcomes for the modulus of rupture determined using both testing methods are presented in Table 3.8.

Figure 3.14 Flexural strength test under center point load, and failure mode of tested specimen.

Table 3.8 Test results of UHPC flexural strength based on ASTM C78 and ASTM C348

Type of test	Test Method	Value (MPa)	Method of test	Value (MPa)
Flexural strength (modulus of rupture)	ASTM C78 [199]	17.68	ASTM C348 [200]	20.352
		17.41		20.968
		18.08		20.244
		16.84		18.568
		17.82		18.68
		19.01		21.316
		17.45		21.364
		16.76		18.724
		17.35		18.284
		18.12		19.32
		17.23		19.68
		16.93		18.704
Average		17.56 MPa		19.68 MPa
St. Deviation (SD)		0.64 MPa		1.13 MPa
Coefficient of Variation (COV)		3.65%		5.76%

3.5.1.4 Direct tensile strength

This study evaluated the direct tensile strength of UHPC. Standard test methods for direct tensile strength have not been established, as it is difficult to guarantee uniform distribution of uniaxial stress throughout the specimen.

To address this issue, Zhou and Qiao [201] made a significant effort to create a design specimen for UHPC direct tensile strength testing. The study showed that the created specimen is efficient in describing the tensile strength of high-performance fiber cementitious concrete.

As mentioned in the study, a dog-bone shaped specimen with a cross-section of 50.8x50.8 mm and a gauge length of 152.4 mm was utilized to assess the direct tensile strength of UHPC. The specimen's details and dimensions, along with the fabricated mold and casted specimens, are shown in Figure 3.15. As depicted in the figure, two Ø16 mm threaded steel bars were embedded at both ends to connect the specimen with the testing machine. To ensure that the tensile strength was tested under quasi-static conditions, a low loading rate was employed during the test, as recommended by Zhou and Qiao [201].

At AL-Mustaqbal College, a universal testing machine with a capacity of 1000 kN was used to perform the UHPC direct tensile strength test. An LVDT was installed at the center of the dog-bone specimen along the loading path to measure the change in length. Two cameras recorded the applied load and change in length simultaneously, as shown in Figure 3.16, which depicts the test preparation.

A total of 12 dog-bone specimens were tested, and Figure 3.17 indicates that the crack localized within the gauge length after strain hardening. The UHPC tensile stress-strain curves are presented in Figure 3.18, and Table 3.9 summarizes the results of the direct tensile strength test.

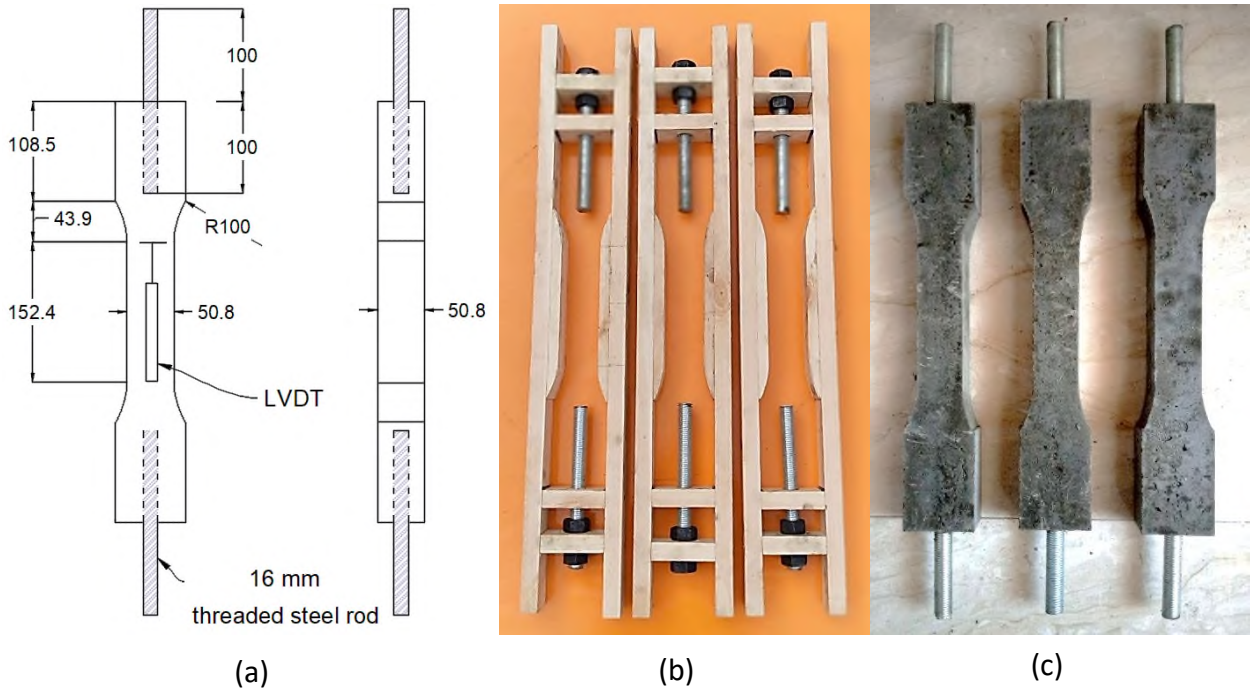

Figure 3.15 Direct tensile strength specimen, a) specimen detail, b) mold, c) specimens.

Figure 3.16 Setup and preparation for direct tensile strength test of UHPC.

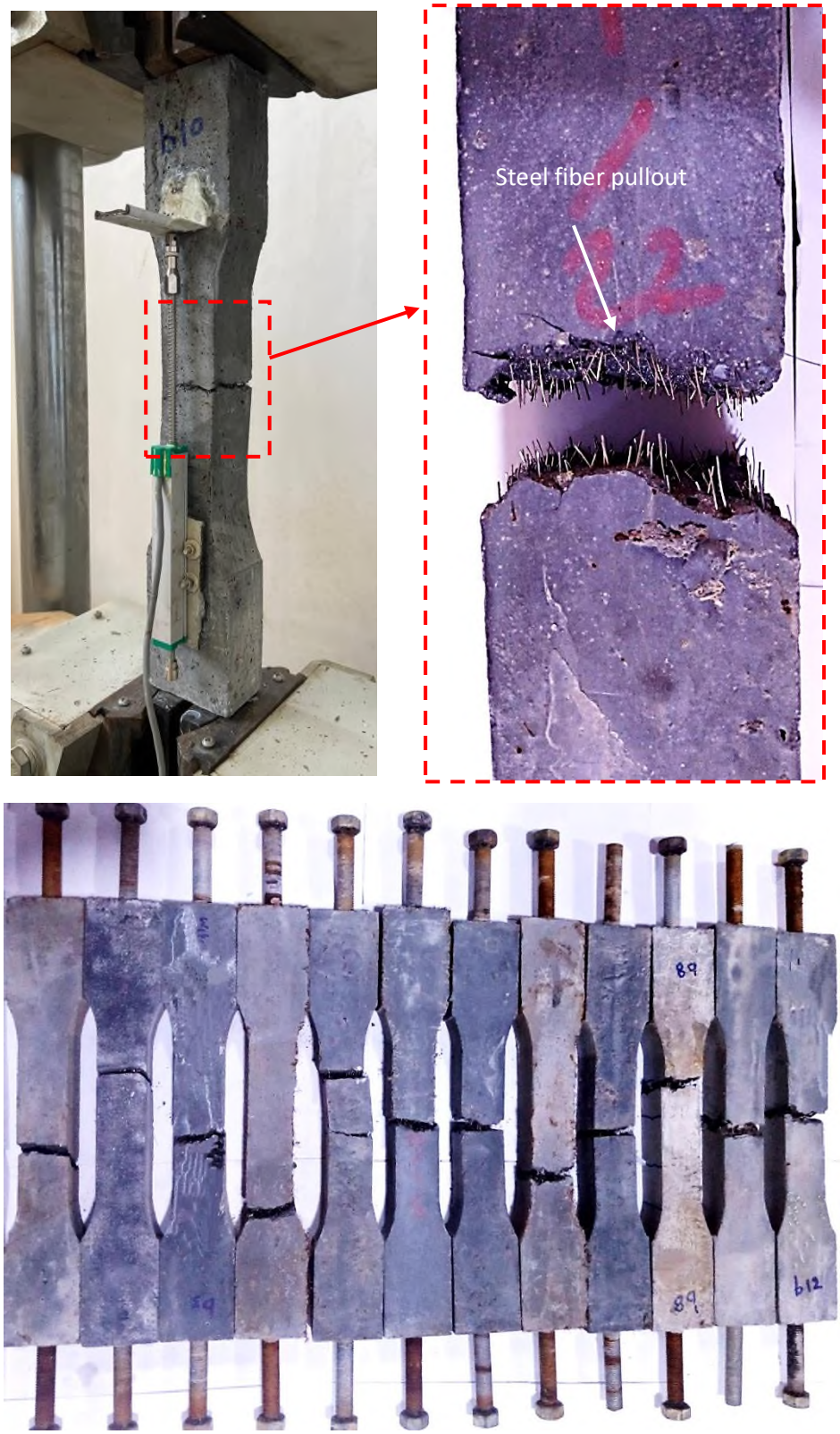

Figure 3.17 Failure mode of UHPC dog-bone specimens under direct tension.

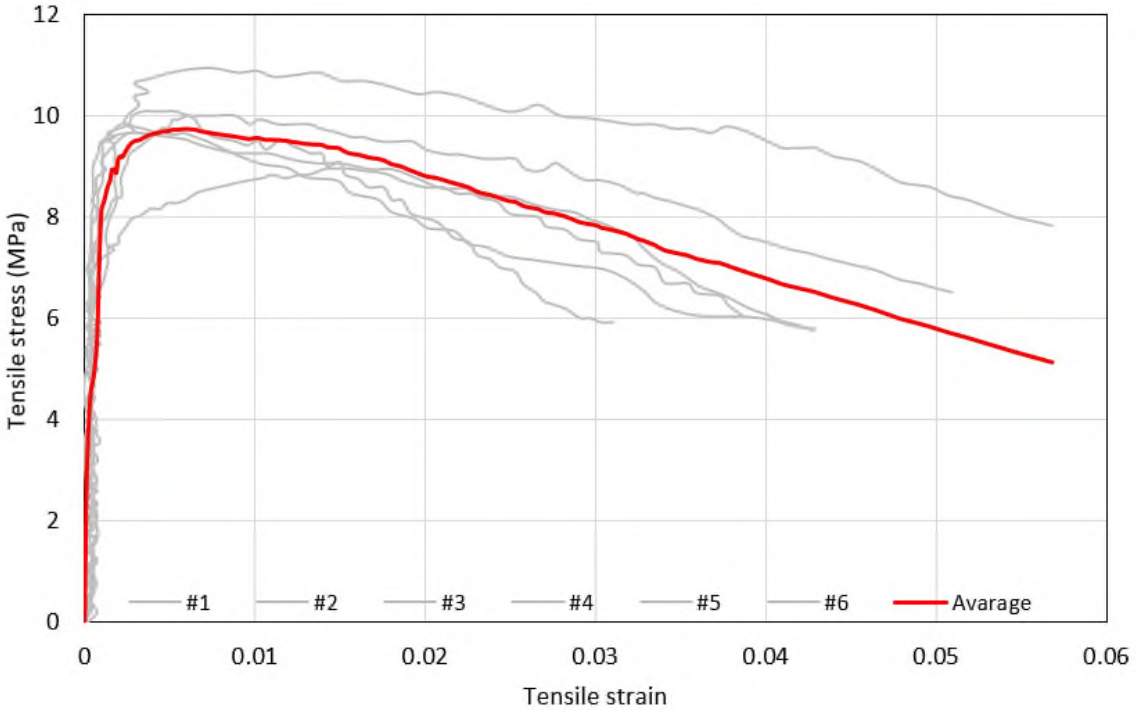

Figure 3.18 Tensile stress-strain curve for UHPC used in the present study.

Table 3.9 Test result of UHPC direct tensile strength

Type of test	Test Method	Value (MPa)
Direct tensile strength	Zhou and Qiao [201]	9.46
		9.66
		9.88
		9.83
		8.40
		9.15
		10.16
		10.82
		8.80
		9.37
		10.02
		9.88
Average		9.62 MPa
St. Deviation (SD)		0.62 MPa
Coefficient of Variation (COV)		6.68%

The splitting tensile strength and flexural strength tests generally overestimate the tensile strength compared to the direct tensile strength test, by approximately 47% and 100%, respectively. This difference in results is consistent with the behavior of NSC that has been extensively discussed by Mehta [202].

3.5.2 Mechanical properties of NSC

3.5.2.1 Compressive strength

A cube with a side length of 150 mm was used to evaluate the compressive strength of NSC (f_{cu}) based on BS EN 12390-3 [203]. The evaluation was performed using a universal testing machine with a 2000 kN capacity, as illustrated in Figure 3.19. As per the Federal Highway Administration (FHWA) recommendation [191], a conversion factor of 0.8 was used to convert cube compressive strength (f_{cu}) to cylinder compressive strength ($f_c^{`}$). The results of the concrete cube compressive strength test and their corresponding cylinder compressive strength are shown in Table 3.10. The average cylinder compressive strength was 36.98 MPa, with a standard deviation of 1.2 MPa.

Figure 3.19 Compressive strength test of NSC.

Table 3.10 Test result of NSC compressive strength

Type of test	Test Method	f_{cu} (MPa)		$f_c^{`}$ (MPa)	
Concrete compressive strength	BS EN 12390-3[203]	45.60	46.50	36.48	37.20
		47.40	48.40	37.92	38.72
		46.40	43.60	37.12	34.88
		45.80	44.40	36.64	35.52
		47.90	45.20	38.32	36.16
		46.30	46.10	37.04	36.88
		45.60	46.87	36.48	37.50
		46.52	48.76	37.22	39.01
		43.79	48.93	35.03	39.18
		45.12	47.47	36.10	37.98
		44.93	47.23	35.94	37.78
		44.00	46.47	35.20	37.18
Average		46.22 MPa		36.98 MPa	
St. Deviation (SD)		1.51 MPa		1.20 MPa	
Coefficient of Variation (COV)		3.26%		3.26%	

3.5.2.2 Splitting tensile strength

The splitting tensile strength of concrete is an indirect method for determining its tensile strength. A universal testing machine with a capacity of 2000 kN was utilized to determine the splitting tensile strength of cylindrical concrete specimens with dimensions of 150×300 mm. The test was performed in accordance with ASTM C496 [19]. Table 3.11 presents the test results for splitting tensile strength, with an average value of 3.25 MPa and a standard deviation of 0.3 MPa. The splitting test and failure mode are shown in Figure 3.20.

Table 3.11Test result of splitting tensile strength of NSC

Type of test	Test method	Values (MPa)
Splitting tensile strength	ASTM C496[198]	3.41
		3.28
		3.62
		2.78
		3.38
		3.00
Average		3.25 MPa
St. Deviation (SD)		0.30 MPa
Coefficient of Variation (COV)		9.38 %

Figure 3.20 NSC splitting tensile strength test and failure mode of tested specimen.

3.5.2.3 Flexural strength (modulus of rupture)

As mentioned previously, it represents another method to evaluate the tensile strength of concrete. The testing method was carried out based on ASTM C78 [199]. The specimen's size was $100mm \times 100mm \times 400mm$ tested under the third point using a universal test machine, as shown in Figur 3.21. The average value of the modulus of rupture is shown in Table 3.12.

Figure 3.21 Modulus of rupture test and failure mode for NSC.

Table 3.12 Test results of modulus of rupture test for NSC

Type of test	Test Method	Value (MPa)
Flexural strength (modulus of rupture)	ASTM C78 [199]	4.45
		4.62
		4.53
		4.46
		4.22
		4.45
		4.76
		5.81
		5.31
		5.54
		5.59
		5.44
Average		4.93 MPa
St. Deviation (SD)		0.65 MPa
Coefficient of Variation (COV)		11.36%

3.5.3 Mechanical properties of reinforcing bars

Deformed steel bars of diameters 16,12, 10 and 6 mm are used to construct the tested specimens. Table 3.13 presents the mechanical properties of the steel bar used in the present study, obtained from tensile tests for each diameter based on ASTM A615 [204]. A universal test machine with a

capacity of 1000 kN was used to examine the steel bar, as shown in Figure 3.22. However, the mechanical properties of GFRP bars were adopted as per the manufacturer's datasheet.

Table 3.13 Mechanical properties of steel and GFRP bars used in the present study

Material	Diameter (mm)	Yield strength (MPa)	Ultimate strength (MPa)	Modulus of elasticity[1] (GPa)
Steel	6	617	620	200
Steel	10	596	671	200
Steel	12	589	657	200
Steel	16	507	688	200
GFRP[2]	10	—	827	46

[1] assumed value, [2] as per manufacturer

Figure 3.22 Steel bar test and failure mode.

3.6 Construction method

Firstly, the process of fabricating steel reinforcement was initiated by following the detail provided for each group, as can be observed in Figure 3.23a. To simplify the construction process and eliminate the need for support under the beams, the beam-column joint was rotated 90° allowing for the two column segments and one of the beams to rest naturally on a flat surface. This resulted in a horizontal casting setup for the column segments,

one beam, and the joint, while the remaining beam was cast vertically. It is unlikely that the direction of casting to have a significant impact on the uniform properties of concrete in the specimens due to their relatively small size and the random fiber distribution in UHPC, as shown in Figure 3.23b.

To make the design more economical, UHPC was used only in the joint zone due to its higher cost. NSC was used in the other parts of the members. Two casting techniques were employed to achieve the objectives of the study: a hot joint and a cold joint. The construction process is illustrated in Figure 3.23.

For the hot joint, three wooden valves were created and inserted into the mold to separate the area containing UHPC and NSC, as shown in Figure 3.23c. Both types of concrete were poured and compacted simultaneously, as depicted in Figures 3.23d and e. The wooden valves were then removed, and the boundary zone between the two mixes was vibrated again, as shown in Figures 3.23f and g. Then, the vertical mold was installed and cast the UHPC part, followed by the normal concrete part, Figure 3.23h. After one day, the mold was removed, and the specimens were wrapped with burlap layers and wetted daily until 28 days.

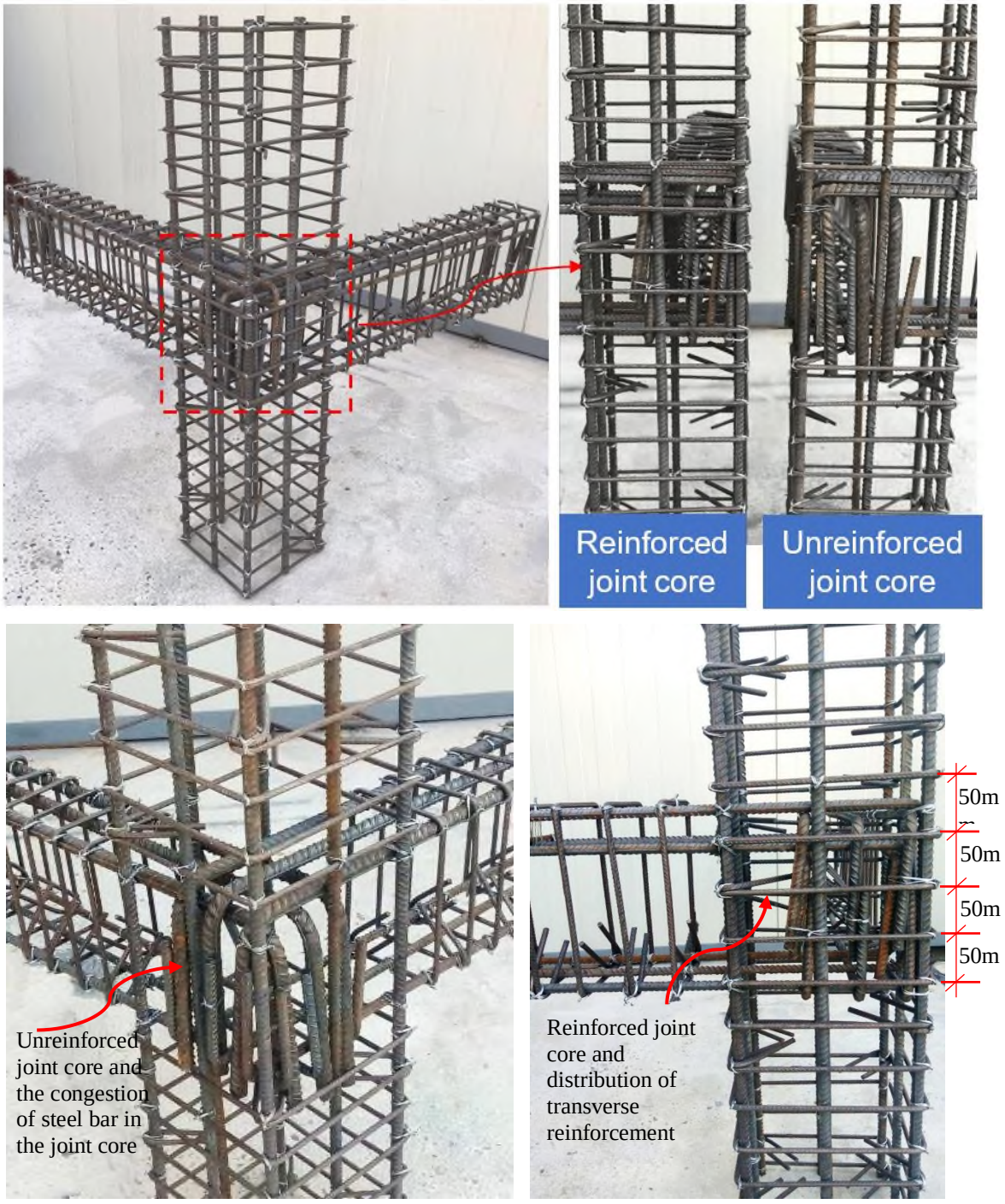

(a)

Figure 3.23 Casting specimens process (hot joint); a) prefabricated steel reinforcement.

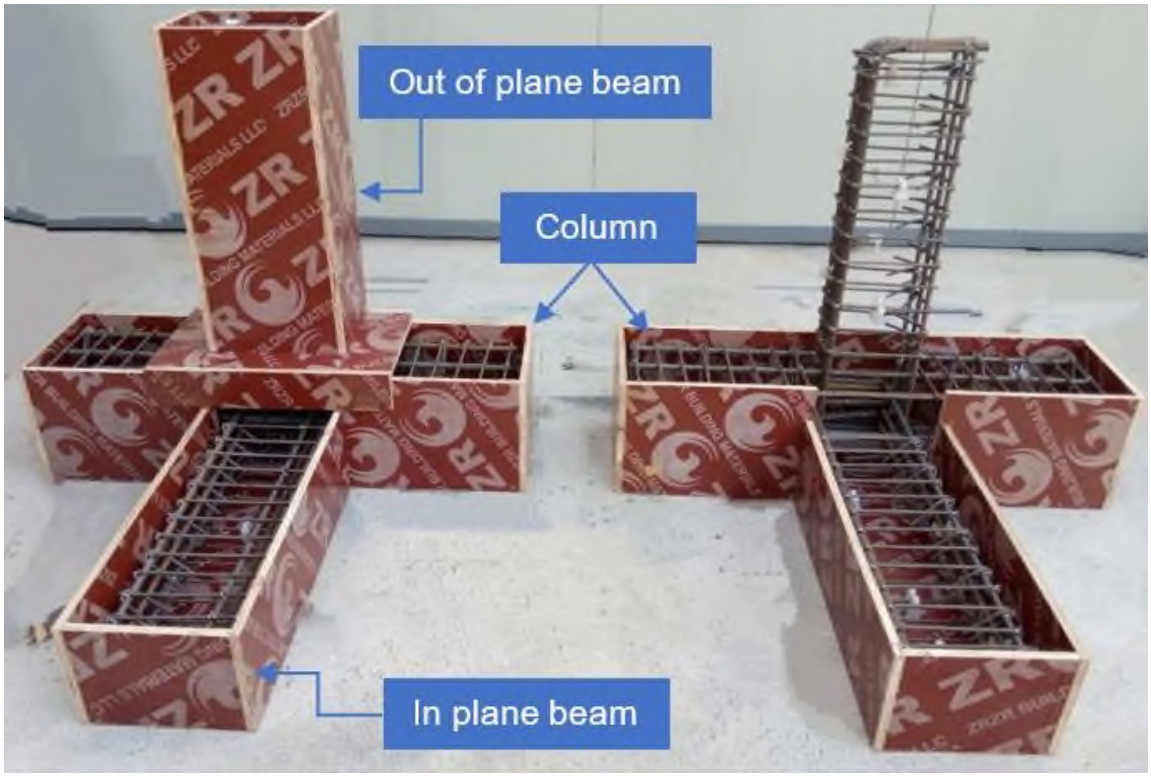

(b)

Figure 3.23 Continued, b) install the mould and reinforcement.

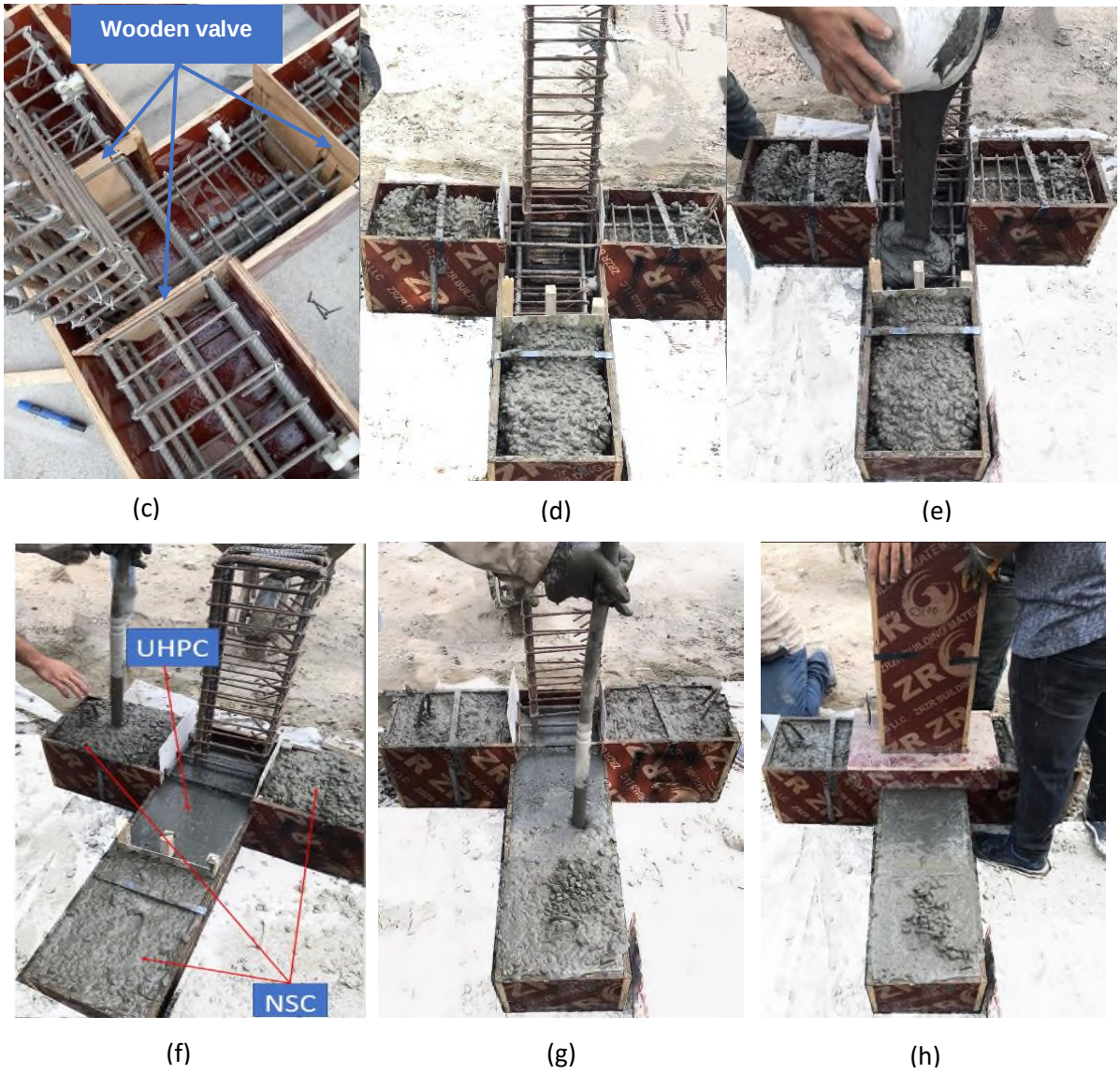

Figure 3.23 Continued; c) install wooden valves, d) pouring NSC, e) pouring UHPC, f) compacting both types of concrete, g) compact the boundary, h) install the vertical part.

In the cold joint technique, the plastic hinge region was filled with compacted wet sand (Figure 3.24a), and NSC was poured into the rest parts, and then moist cured for 28 days. After that, the sand (filler) in the joint region was removed and the joint interface was roughed to enhance the UHPC-NSC bond using a mechanical drill, Figure 3.24b. The specimens were then cleaned with high water pressure to remove all the dust particles and left until dry, Figure 3.25a. The cleaned specimens were then placed in

the wooden mold to cast the joint core, Figure 3.25b. An epoxy bonding agent, commercially named Quickmast 108 [205], was applied for the joint interface to improve the bonding between the old NSC and the new UHPC, Figure 3.25c. The epoxy was applied to the joint surface using a short-haired paint brush and left until the surface become tacky (typically after 1hr. as recommended by the manufacturer datasheet). Then, the UHPC was poured over the plastic hinge region and compacted well, Figures 3.25 d,and e. The wooden mold was removed after a day and moist cured for 28 days.

To improve the performance and reduce the effect of the cold joint, 2 Ø 12 mm was added on each side of the beam to connect the NSC and UHPC using the near surface mounted technique (NSM).

Grooves of length 500 mm (250 mm in the UHPC side and 250mm in the NSC side) and depth of 20 mm were made by a mechanical grinder and then cleaned with high water pressure to remove the dust. Half of the grooves depth were filled with the epoxy bonding agent, commercially named Polypoxy NF[206], and then steel rebars were placed and pushed. After that, the grooves were refilled with epoxy to cover the steel bar. Figure 3.26 illustrates the steel bar bonding method.

(a)

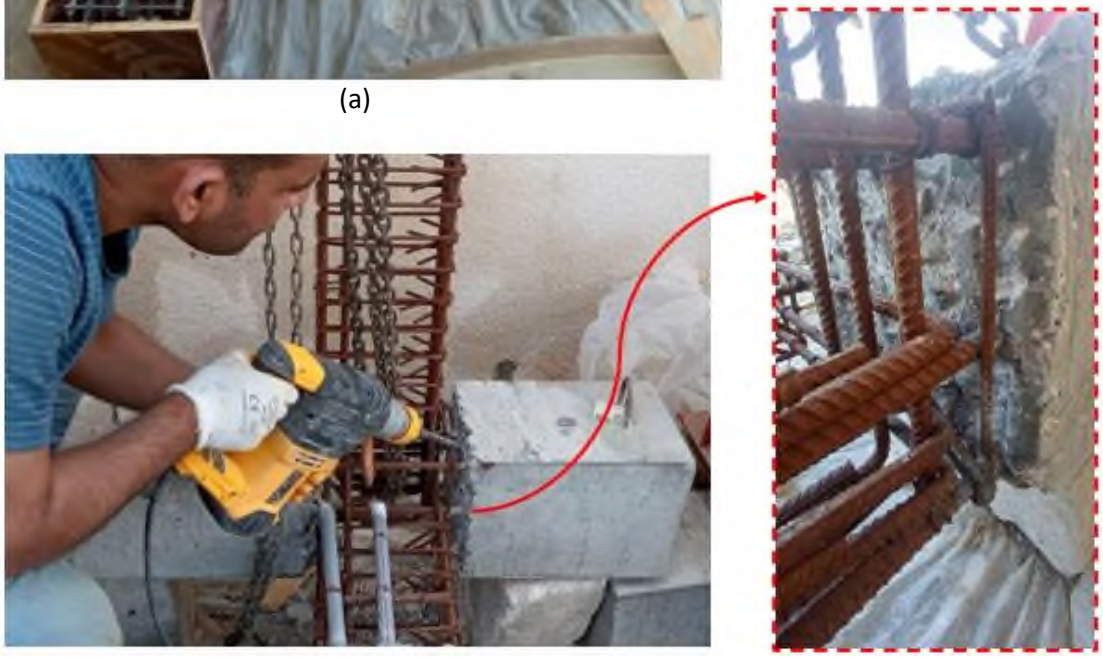

(b)

Figure 3.24 Preparing for construction of the cold joint, a) preparing the mould, b) roughing the joint interface.

Figure 3.25 Rehabilitation of specimens processing (cold joint), a) clean the specimens by high water pressure, b) install the specimens in the wooden mold, c) coating the joint interface with epoxy adhesive, d) pouring the UHPC in the joint region, e) compacting the UHPC.

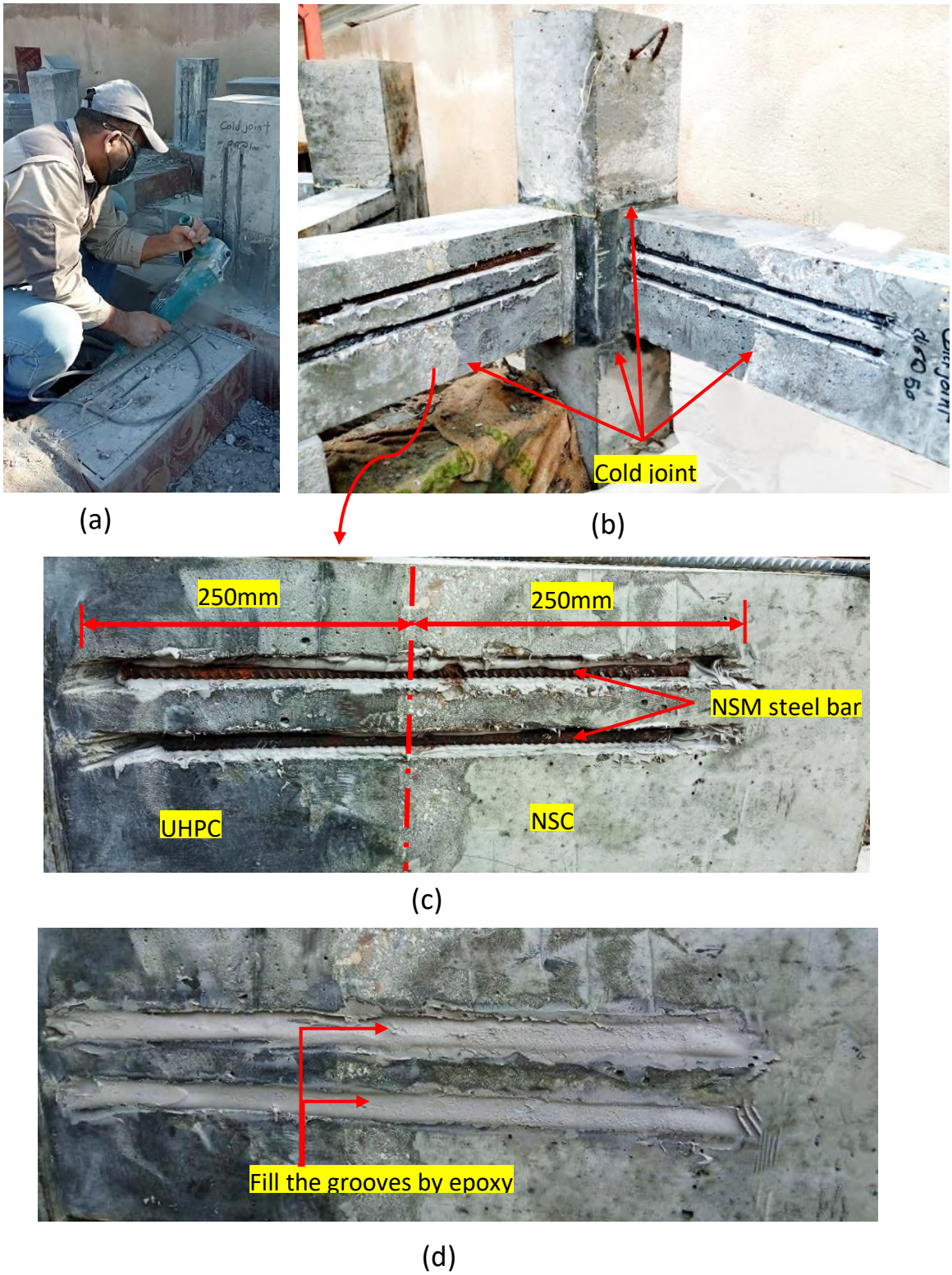

Figure 3.26 Process of bonging NSM steel bars, a) making grooved, b) and c) detail of NSM steel bar, d) fill the grooves by epoxy.

The specimen $CJ_2NT_3S_{50}C$ casted in a similar way to NSC specimens. However, the tension reinforcement of the beams was hybridized by steel bar and GFRP bar as discussed 3.3.5. Three GFRP bars were used as tension reinforcement in the beams in place of steel bar without any spatial details. Figure 3.27 illustrate the reinforcement details.

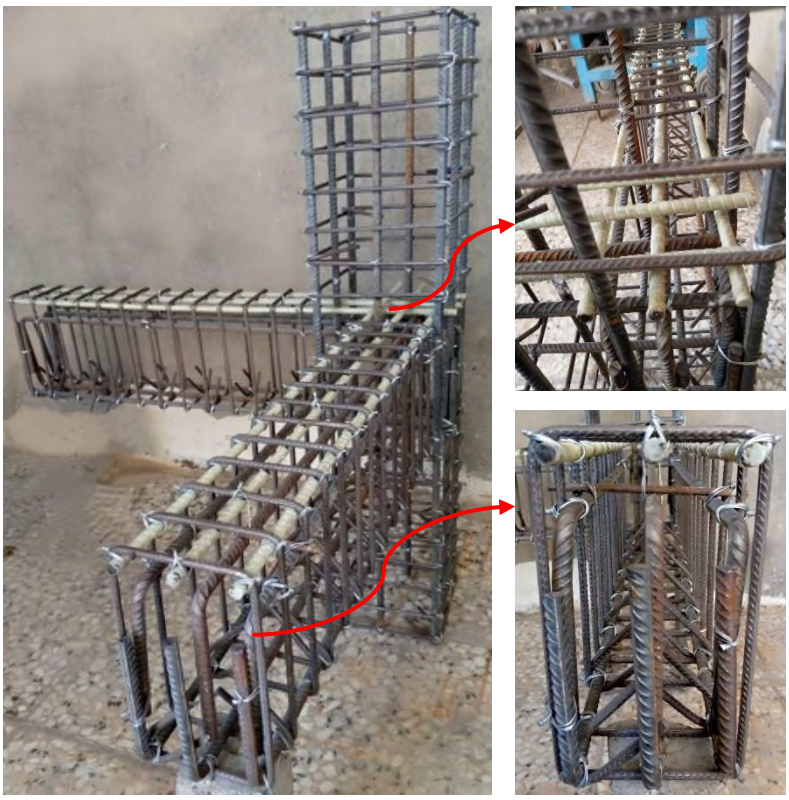

Figure 3.27 Reinforcement detail of specimen $CJ_2NT_3S_{50}C$.

Finally, the specimen $CJ_2NT_4S_{50}C$ was prepared by making grooves of 20×20mm in the tension side using a mechanical grinder and drilling the column following these grooves, as shown in Figure 3.28 a,b. After was cleaned by high water pressure, these grooves were filled with epoxy bonding commercially named Sikadur®-330 [207]. Then GFRP bars were installed in these grooves, and epoxy bonding was injected from the holes marked in the column until it appeared from the other side, Figure 3.28c. The GFRP bars were pushed inside the grooved and the remained of grooves were filled with epoxy, Figure 3.28 d,e.

Figure 3.28 Flexural strengthening of specimen $CJ_2NT_4S_{50}C$ using NSM-GFRP bars, a) making grooves in the tension side of beams, b) drilling the column in accordance to grooves, c) injecting epoxy through the holes, d),e) filling the grooves with epoxy.

All of the examined specimens were cleaned and painted with a white color for the NSC region and a yellow color for the UHPC region after 28 days of curing. The test was carried out at the engineering college's structural laboratory at the University of Karbala.

3.7 Test setup

Figure 3.29 illustrates the test setup and support conditions used to furnish the combined constant axial and increasing bidirectional bending test. The beam-column joint was held vertically at the bottom and top ends of the column, using a custom-made jig made of welded hollow steel sections. The jig fully collars the column ends and attaches to the strong testing frame via threaded bars.

A constant axial load of 150 kN was firstly applied onto the top face of the column using a 250 kN vertical hydraulic jack installed on a steel plate connected to the column top face. The load was chosen to be equal to the commonly used ratio of $(N/f_c^{`}A_g)$ =0.07, where N is the axial load and A_g is the column cross-sectional area (gross). Once the axial load stabilized, an increasing vertical load was applied to the ends of the beams, using 2000 kN hydraulic jack. A spreader beam was used to distribute the increasing load equally to the two beams, Figure 3.30. The vertical load on each beam was applied at 100 mm away from its free edge.

A load cell with a capacity of 2000 kN was used to monitor the force applied to the beams. The vertical displacements of the beams were measured using vertical linear variable differential transducers (LVDTs) with a gage of 100 mm. The LVDT was located 50 mm from the beam free end, Figure 3.31. The drift ratio (Δ/l) which is discussed later in the results section was obtained by dividing the vertical displacement (Δ) from the LVDT measurement by the distance between the LVDT and the face of column. Additionally, one side of each specimen was speckled with black and white inks to monitor the deformations and strains by a digital image correlation (DIC), Figure 3.32. Unlike conventional devices such as LVDTs and strain gages that produce limited results at targeted locations, the DIC technique can accurately detect the deformations of the whole specimen's surface. The

DIC approach may be used to get insight into the performance of the joints in terms of joint shear deformation, strain fields of the joint zone, and crack development.

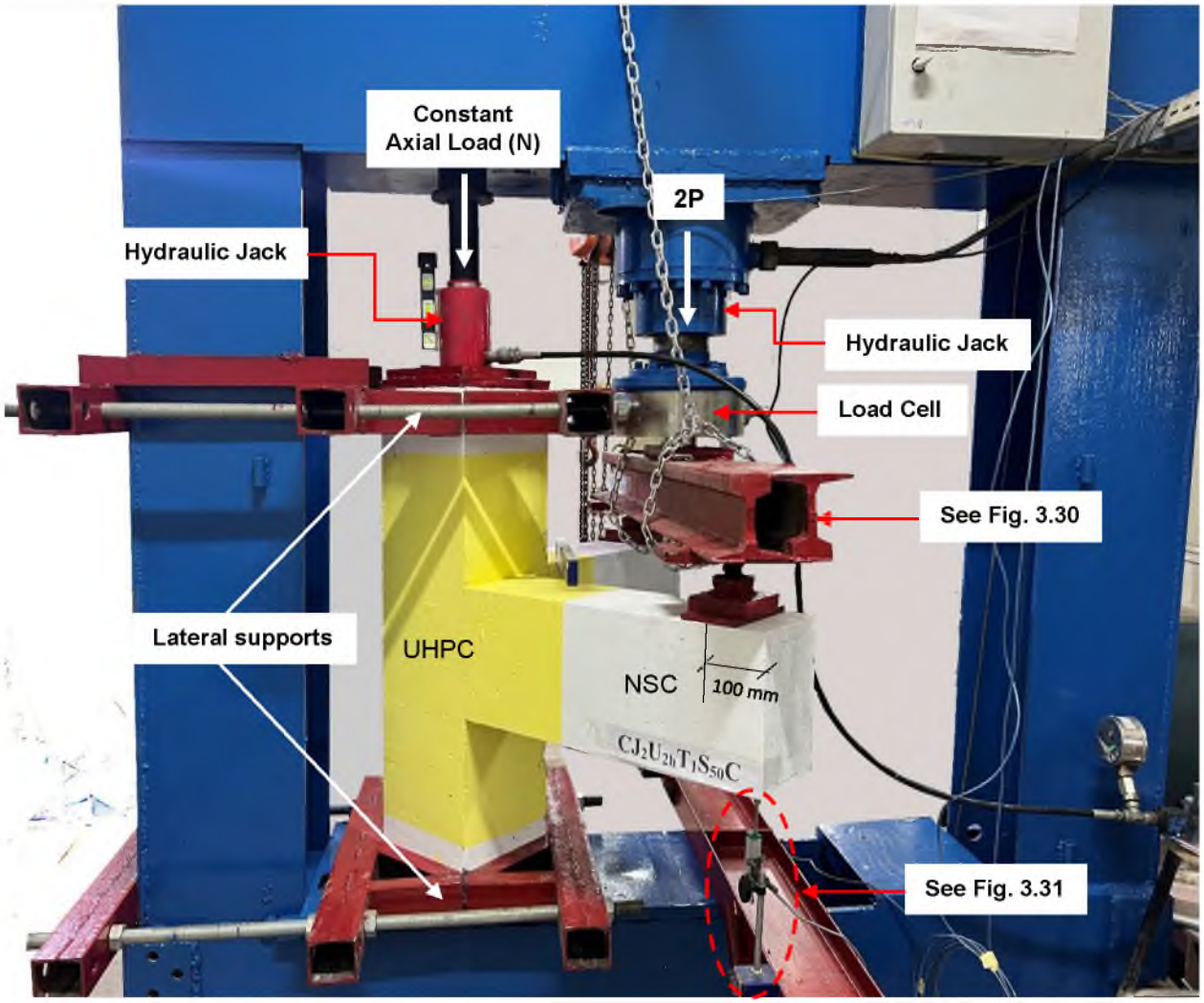

Figure 3.29 Test setup and instrumentation.

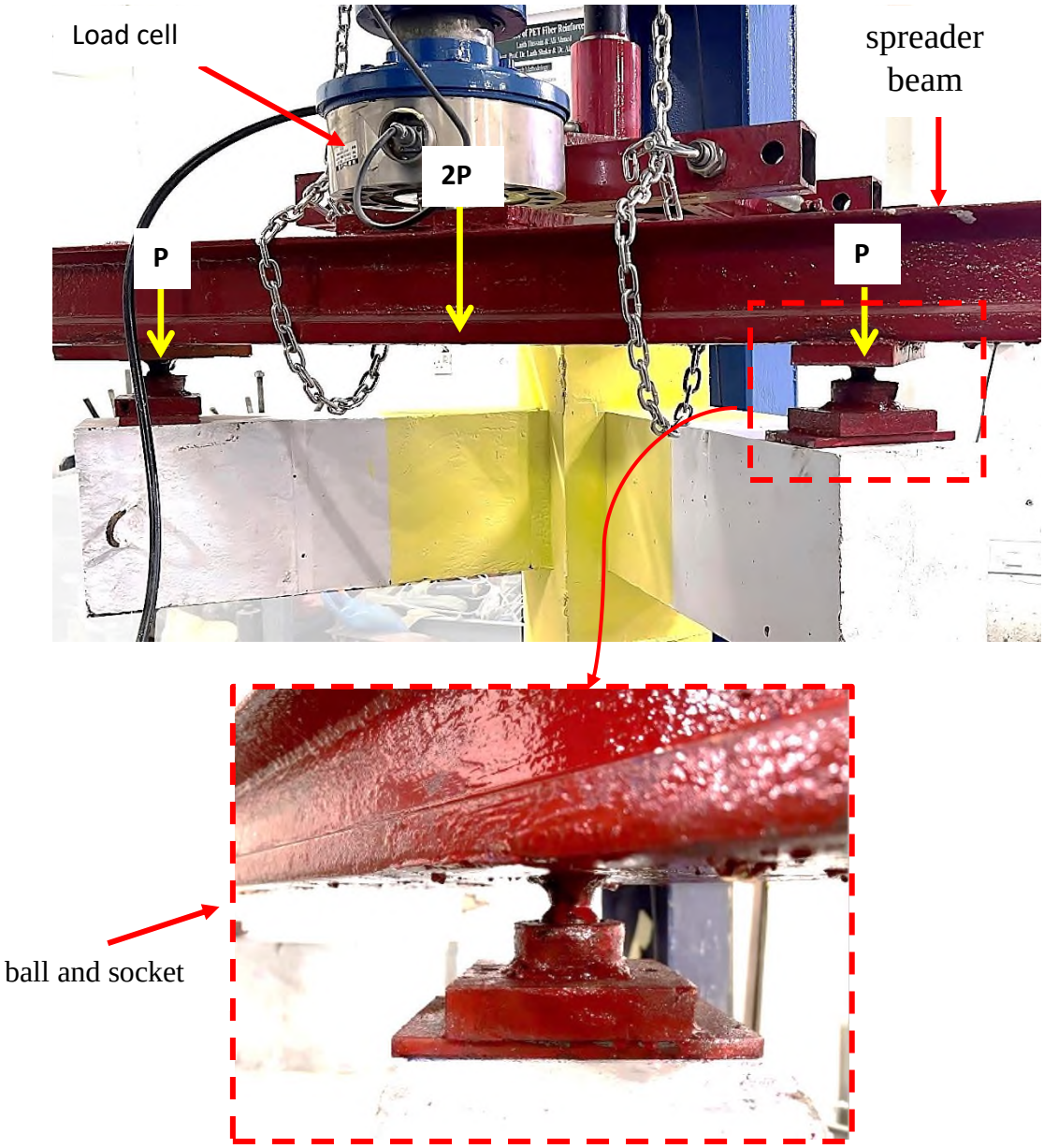

Figure 3.30 Loading condition.

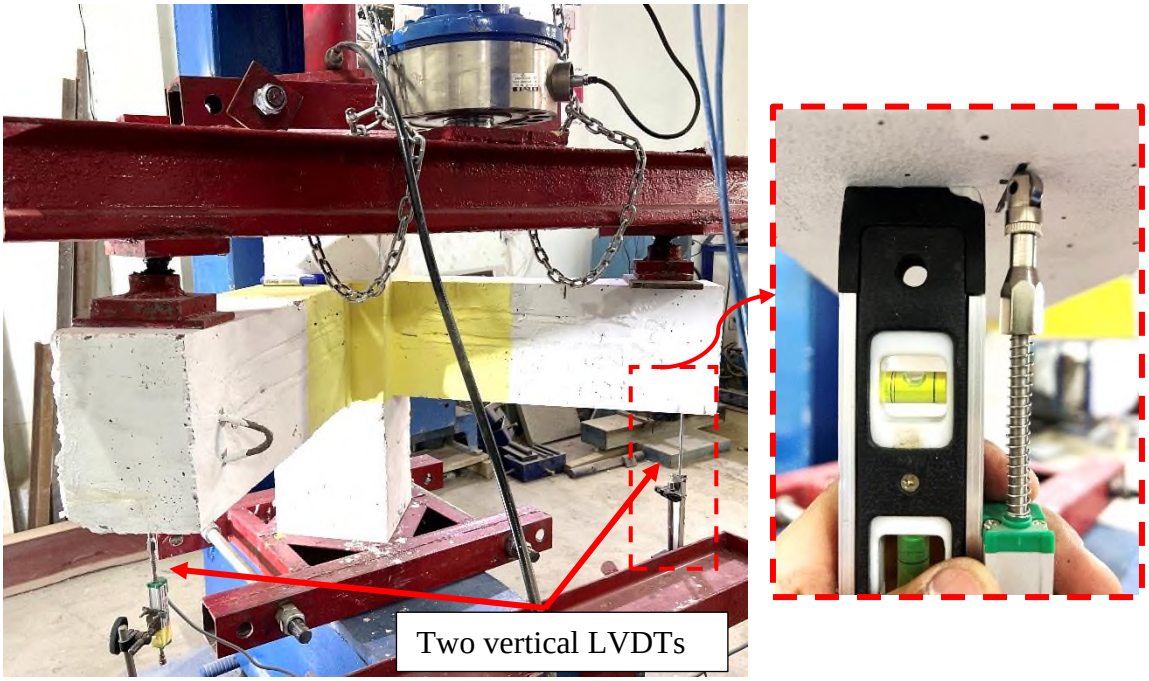

Figure 3.31 Installation the vertical LVDTs.

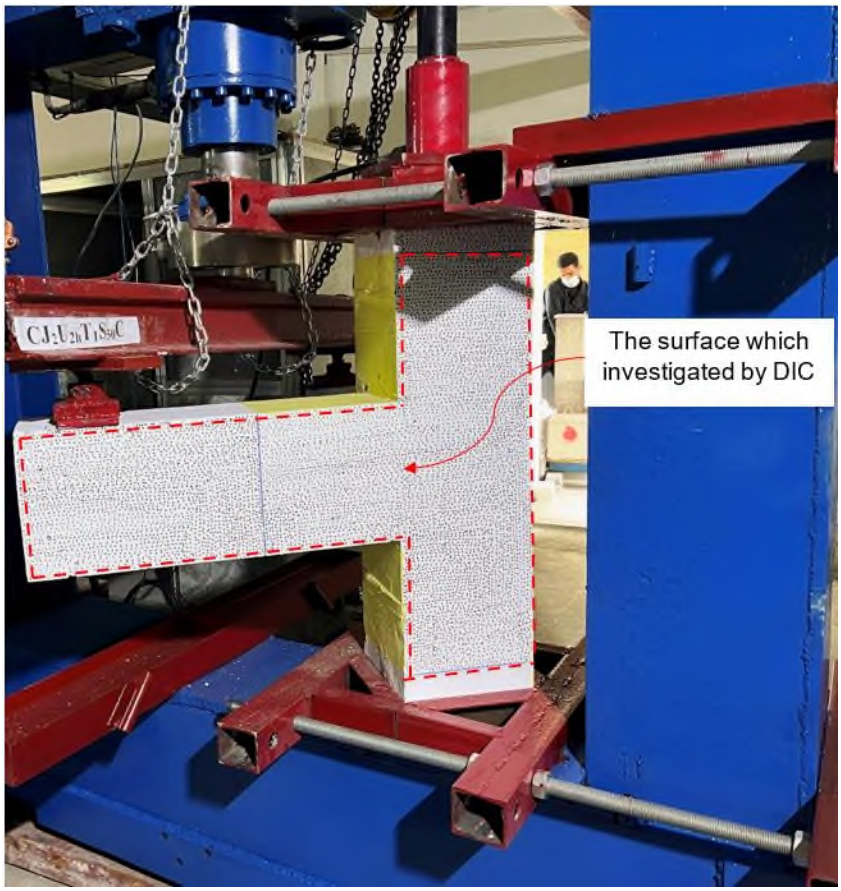

Figure 3.32 The side of the specimen monitored by DIC.

3.8 Loading protocol

The first investigation on cyclically loaded RC beam-column joints was carried out by Hanson and Connor [208] in 1967. The study revealed that subjecting a specimen to a horizontal load on the column ends with the beam restrained produced the same results as when the column ends were restrained and the beam was loaded vertically, as depicted in Figure 3.33.

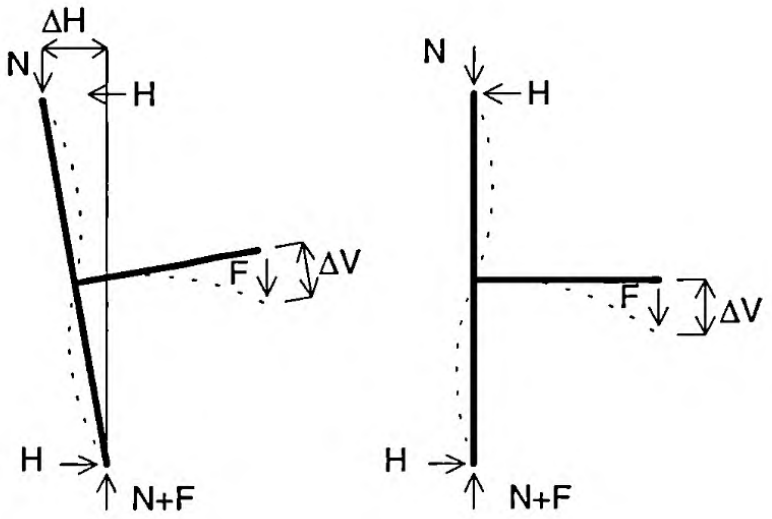

Figure 3.33 Ends restrained condition [208].

In the present study, the column ends were restrained and the load was applied on the orthogonal beam in two loading methods, namely monotonic and compression cyclic loading, both of which were force-controlled.

For monotonic loading, the load was gradually increased linearly with time at a constant rate until the specimen failed.

Takemura and Kawashima [209] investigated the behavior of identical RC bridge piers under six different cyclic loading protocols, as shown in Figure 3.34. The study revealed that the envelope curve of the tested specimens depended on various factors such as the number of cycles, the amplitude of each cycle, and the sequence of loading cycle [210]. Figure 3.35 illustrates the envelope curves of the tested specimens.

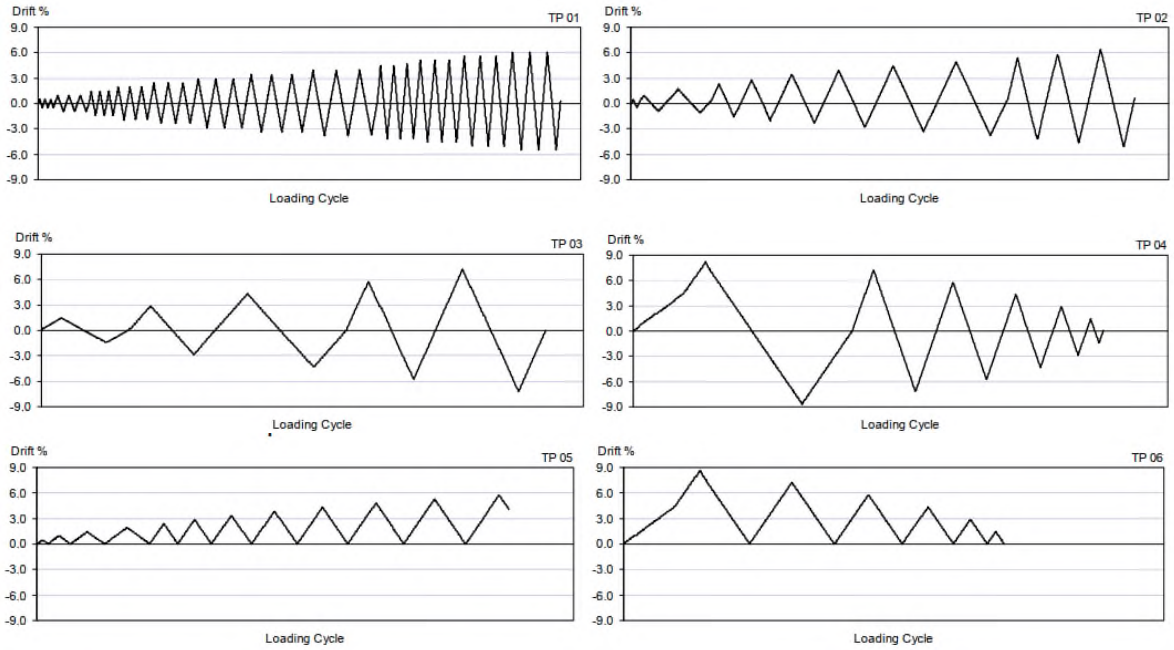

Figure 3.34 Cyclic load protocols examined by Takemura and Kawashima [209]

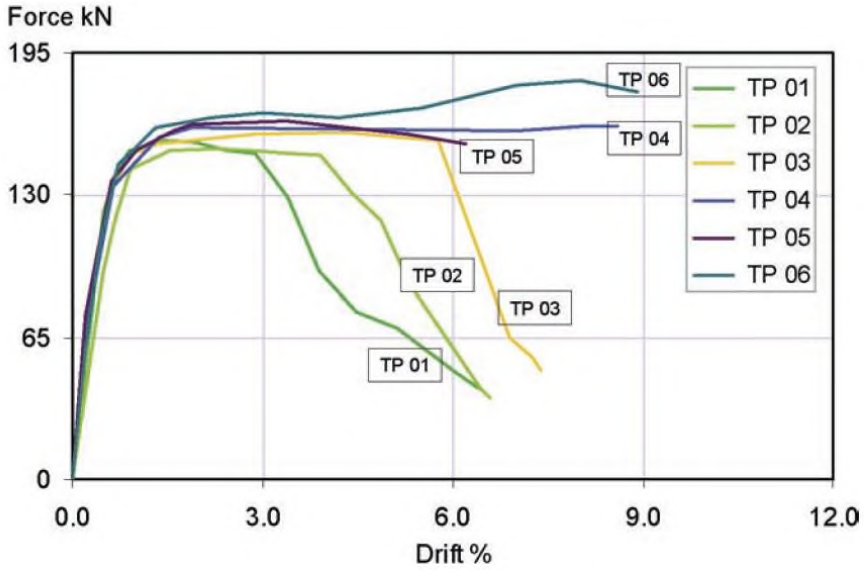

Figure 3.35 Comparison of load-drift response under six different loading protocols [209].

According to above discussion and available equipment, the cyclic load protocol TP05 shown in Figure 4.34 was adopted in the present study.

Figure 3.36 present the load history adopted in the testing the specimens under compression cyclic load protocol. The maximum applied load ($P_{max.}$) was adopted based on specimens tested under monotonic load and divided into multi-load steps as presented in Figure 3.36. Three load cycles for each

load step were applied. In each cycle, the load was increased at a constant rate until it reached the maximum step load, then unloaded to zero. This process was repeated for each load step till failure. At the end of each load cycle, the specimen was monitored and marked cracks and deformations. A computer software program connected with the hydraulic jack, load cell and LVDTs was recorded and saved the data automatically.

Before starting the test, all the LVDTs were calibrated and the specimen was loaded by 10 kN to check the specimen installation, software system and whether the instruments work properly.

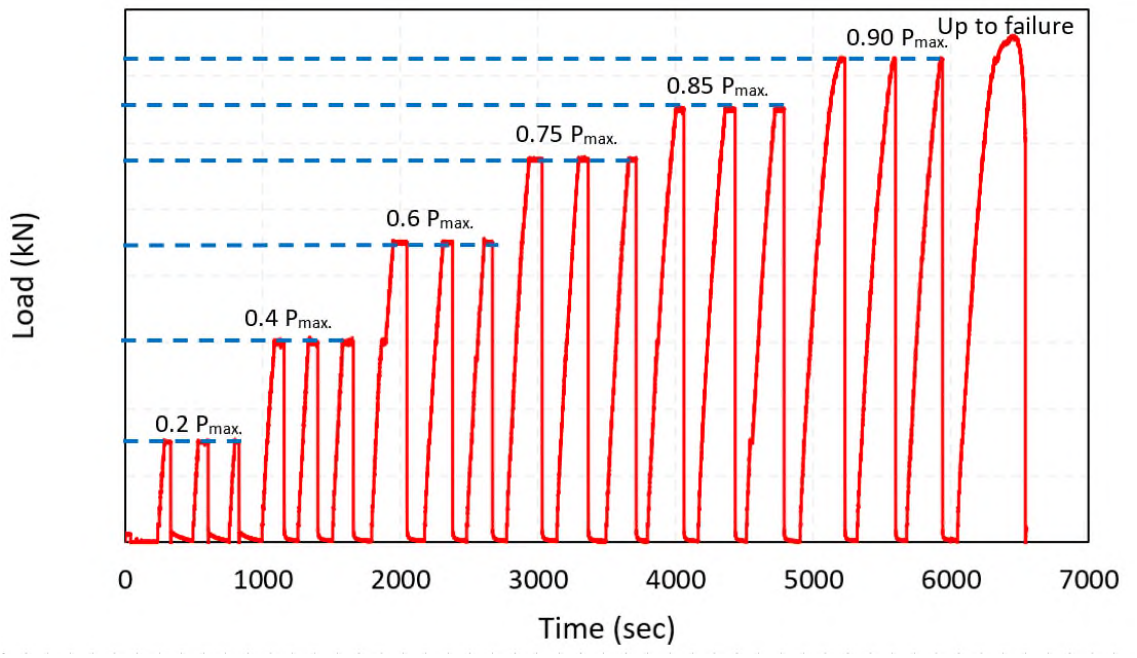

Figure 3.36 Cyclic load protocol history.

Chapter Four

Experimental Results and Discussions

4.1 Introduction

In this chapter, the test results of tested specimens will be presented. The response of each specimen will be discussed and analyzed using key performance measures that characterize their behavior. These performance measures include modes of failure, joint shear strength, joint cracking patterns and progression, force-drift relationships, ductility capacity, cumulative energy dissipation, and principle stresses. This performance was used to measure the effects of test parameters on unconfined corner beam-column joints. As discussed previously in section 3.3, the investigated factors include the effect of transverse reinforcement in the joint core, joint region material (NSC/UHPC), the configuration of UHPC, spacing of transverse reinforcement in adjoining members, embedded length passing through the joint core, joint casting method (hot/cold), and the use of GFRP bar as hybrid longitudinal reinforcement.

4.2 Specimens Tested under Cyclic Load

4.2.1 Cracks pattern and failure mode of the tested specimens under cyclic load

It is generally observed that shear failure patterns occur in the joint core of NSC unreinforced beam-column joints. This is due to the complex stress state caused by the combined effects of axial stress, bending moment, shear force, and torsion force resulting from the eccentric beam-to-column connection, as well as the total elimination of transverse reinforcement in the joint core. In contrast, UHPC specimens failed in flexural mode by developing a plastic hinge at the joint-beam interface. This is attributed to the high shear resistance of UHPC. Table 4.1 presents the main experimental results and failure modes. The following sections describe the experimental behavior of the tested specimens under cyclic load.

Table 4.1 Cracking load, ultimate load, and failure mode of the tested specimens

Group No.	Specimen ID	Flexural cracking load (kN)	Diagonal cracking load (kN)	Ultimate load (kN)	Inc. in ultimate load** (%)	Failure mode
I	$CJ_1NT_1S_{50}C$	30 (1)*	50 (4)	104.3 (10)	…….	B-F
	$CJ_2NT_1S_{50}C$	25 (1)	40 (4)	102.7 (9)	…….	BJ-F
	$CJ_2U_{1h}T_1S_{50}C$	30 (1)	90 (7)	152.3 (19)	48.3	B-F
	$CJ_2U_{2h}T_1S_{50}C$	45 (4)	-------	153.9 (16)	49.9	B-F
	$CJ_1U_{1h}T_1S_{50}C$	40 (4)	-------	154.0 (16)	50.0	B-F
II	$CJ_2NT_1S_{100}C$	20 (1)	45 (4)	98.5 (9)	……	BS-F
	$CJ_2U_{1h}T_1S_{100}C$	30 (3)	90 (7)	125.7 (12)	27.6	B-F
	$CJ_2U_{2h}T_1S_{100}C$	45 (3)	-------	1140 (16)	42.1	B-F
III	$CJ_2U_{1c}T_1S_{50}C$	45 (4)	90 (7)	148.9 (16)	45.0	B-F
	$CJ_2U_{1c}T_1S_{100}C$	30 (3)	90 (7)	147.3 (16)	49.5	B-F
IV	$CJ_2NT_2S_{50}C$	20 (1)	60 (4)	118.1 (12)	……	JS-F
	$CJ_2NT_2S_{100}C$	20 (1)	55 (4)	115.0 (12)	……	JS-F
	$CJ_2U_{1h}T_2S_{50}C$	35 (4)	75 (8)	182.8 (19)	54.8	B-F
	$CJ_2U_{1h}T_2S_{100}C$	35 (4)	75 (8)	175.8 (19)	52.2	B-F
V	$CJ_2NT_3S_{50}C$	20 (1)	40 (4)	81.0 (7)	-21.1	P-F
	$CJ_2NT_4S_{50}C$	20 (1)	55 (4)	115.4 (10)	12.0	JS-F

*the value between two brackets represents at which load cycle the crack or failure occurs.

**Percent of increase/decrease $= \frac{P_u - P_c}{P_c} \times 100$;

$P_u, P_c = ultimate\ load\ for\ UHPC\ and\ control\ specimens\ respectivilly,$ noting that group I, V, and $CJ_2U_{1c}T_1S_{50}C$ compared with control specimen $CJ_2NT_1S_{50}C$, while group II, and specimen $CJ_2U_{1c}T_1S_{100}C$ compared to control specimen $CJ_2NT_1S_{100}C$. in the case of group IV, the UHPC joint compared to corresponding NSC specimens.

Table 4.1 presents the five failure modes observed in the experimental work, which can be defined as follows:

- Beam Failure (B-F): Failure is governed by the yield of tension or compression longitudinal reinforcement of the beam. This is an ideal failure mechanism because it is ductile, and the load transmission between the upper and lower columns is not disrupted.
- Beam Shear Failure (BS-F): In this mode, the failure is controlled by beam shear failure. This is a brittle failure and is not recommended.
- Joint Shear Failure (JS-F): This is a catastrophic failure because it occurs suddenly and causes the collapse or partial collapse of reinforced concrete (RC) buildings.
- Beam Failure Followed by Joint Shear Failure (BJ-F): This type of failure is more ductile than JS-F. It is governed by the yield of tension reinforcement of the beam at the face of the column, followed immediately by joint shear failure.
- Pullout Failure (P-F): The failure is governed by the pullout of the longitudinal reinforcement of the beam from the joint core.

All the codes recommend designing based on the B-F mechanism and avoiding the other failure modes because they are brittle failures and can contribute to the collapse or partial collapse of RC structures.

4.2.1.1 Cracks pattern and failure mode of group I tested under cyclic load

The first specimen in this group was **$CJ_1NT_1S_{50}C$**, which was designed based on seismic requirements to serve as a control specimen. During the first load cycle at a load of about 30 kN, equivalent to a drift ratio of 0.26%, the first flexural crack was observed at the joint-beam interface, followed by a second flexural crack at a distance equal to d/2 from the first one. As the

load increased, more hairline flexural cracks were generated at a uniform distance (d/2). During the fourth load cycle, the first diagonal crack was observed in the joint core at a load of 50 kN. The flexural and diagonal cracks propagated and extended with continued load cycles, with no new cracks generated until the sixth load cycle. Additional diagonal cracks parallel to the first one were generated during the seventh load cycle at 75 kN. As the loading process continued, the number of cracks increased continuously, while the crack width had a slight increase. When the joint entered the failure stage, the number of cracks did not increase, while the width of cracks increased significantly due to opening and closing of the cracks at each cycle. However, it was observed that the concrete at the bottom face of the beams was crushed. Finally, the specimen failed due to the generation of a plastic hinge at the joint-beam interface with a severe diagonal crack in the joint core at the tenth load cycle with the ultimate load of 104.3 kN, corresponding to a 4.3% drift ratio. Figure 4.1 illustrates the failure process versus drift ratio of the specimen $CJ_1NT_1S_{50}C$ recorded by the DIC technique, and Figure 4.2 illustrate the failure mechanism of the tested specimen.

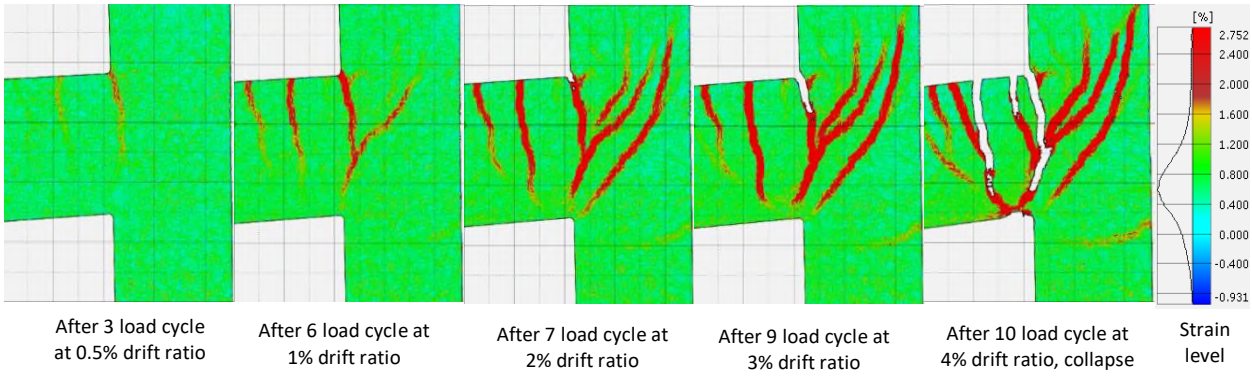

Figure 4.1 Damage process and crack pattern of specimen $CJ_1NT_1S_{50}C$ monitored by DIC.

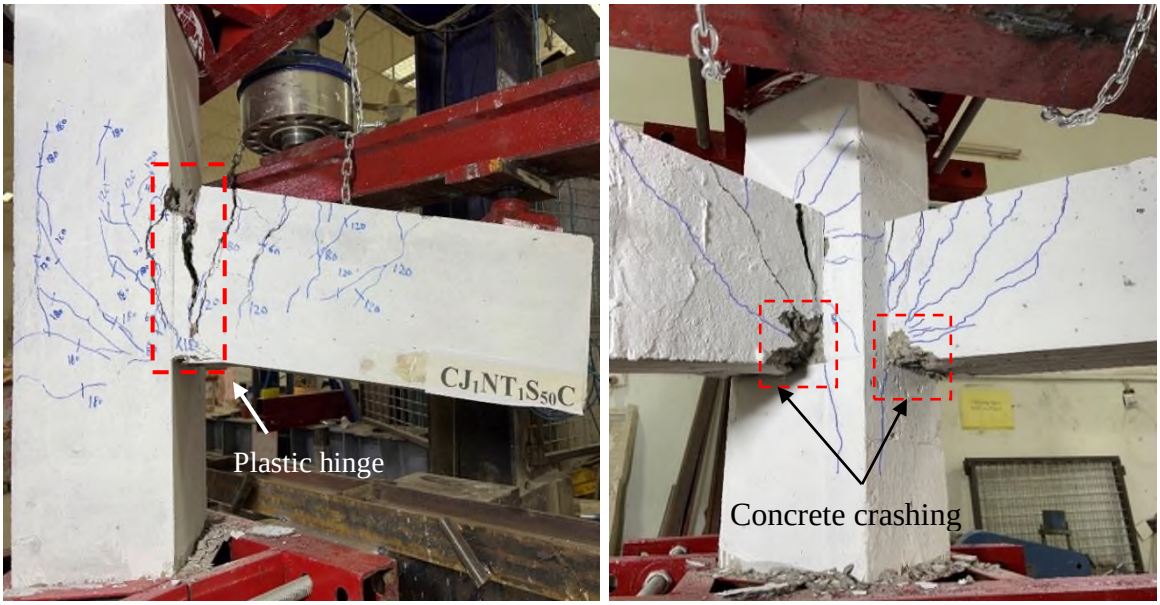

Figure 4.2 Failure mechanism and crack propagate at the end of test specimen $CJ_1NT_1S_{50}C$

The behavior of specimen **$CJ_2NT_1S_{50}C$** was similar to **$CJ_1NT_1S_{50}C$** in the initial stage of loading, with the first cracks observed at an earlier stage. The first visual flexural crack developed at joint-beam interface through the 1st load cycle at a load of 25 kN, while the first diagonal crack was observed in the joint core during the 4th load cycle at a load of 40 kN, followed by another diagonal crack at the end of the 4th cycle. As the load increased, multiple flexural cracks developed at a uniform distance of d/2, and the diagonal cracks extended to the corners. Residual cracks were observed after the 4th load cycle and were clearer after the 7th load cycle, where at a drift ratio of 1.93%, additional diagonal cracks developed rapidly in the joint core. These cracks extended along the outer edge of column. The joint lost its strength after nine load cycles at a load of 102.7 kN due to the formation of a plastic hinge at the joint-beam interface, followed simultaneously by joint shear crack and spalling of the concrete cover at the joint core. The damage process versus drift ratio is illustrated in Figure 4.3, while the failure mechanism and crack propagation at the failure are shown in Figure 4.4.

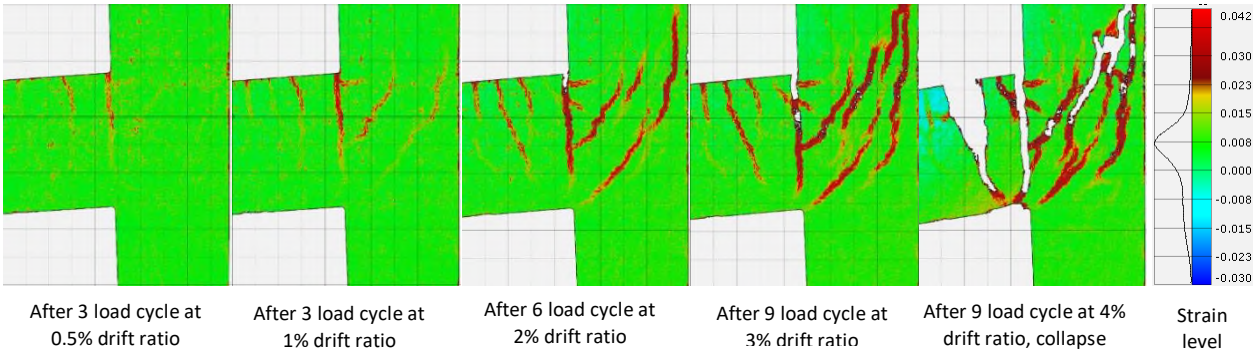

Figure 4.3 Damage process and crack pattern of specimen $CJ_2NT_1S_{50}C$ monitored by DIC.

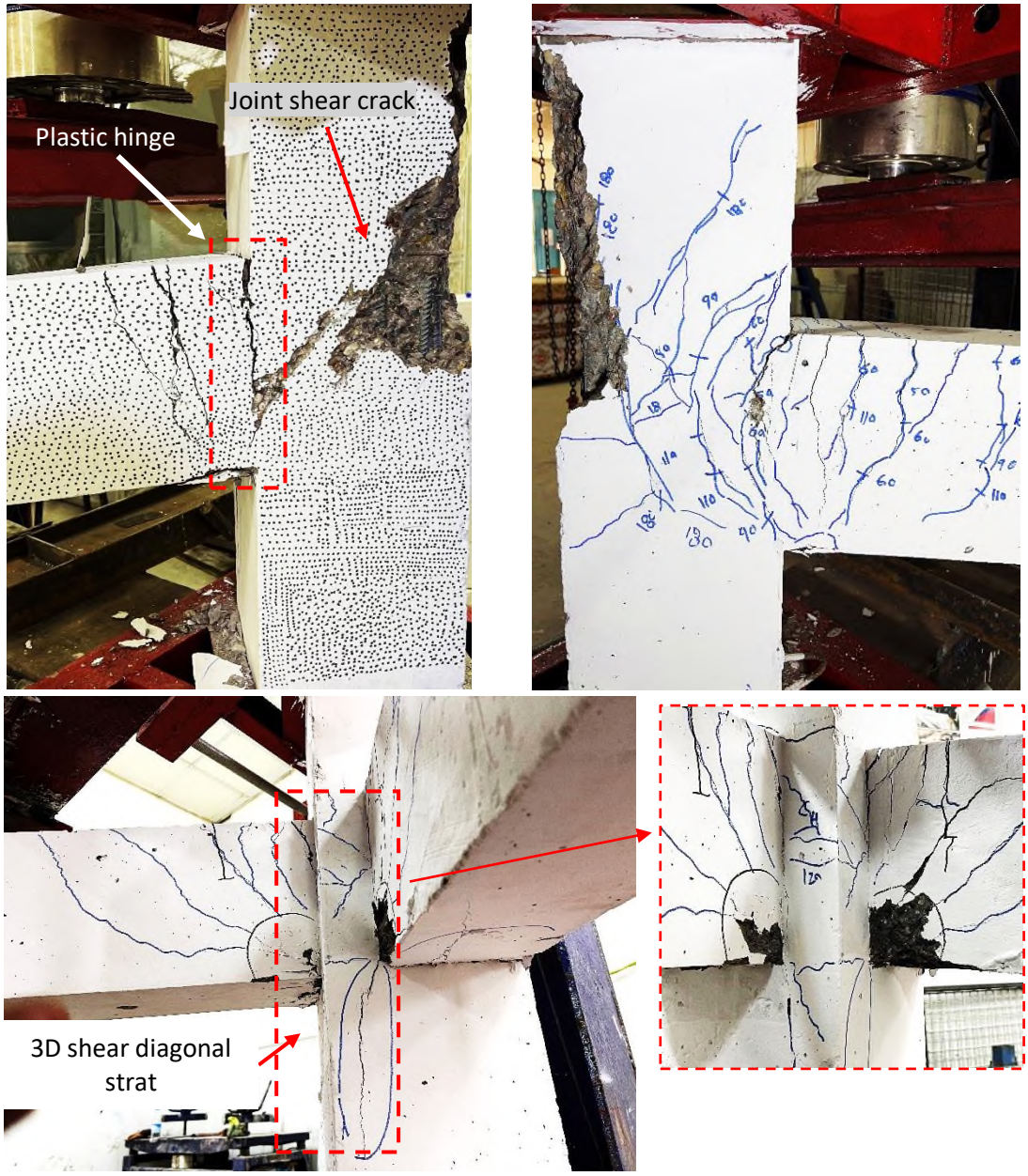

Figure 4.4 Failure mode and crack pattern at the end of the test specimen $CJ_2NT_1S_{50}C$.

It is worth mentioning that several cracks and damages were observed in the interior corner of the column below the joint, as illustrated in Figure 4.4. This may be attributed to the assumption that in a biaxially loaded joint, the primary strut is a three-dimensional strut that spans between the two outermost apexes of the joint, as recommended by Leon and Jirsa [211].

On the other hand, despite the complete removal of transverse reinforcement in the joint core, the UHPC specimens exhibit a distinct behavior, characterized by more stable hysteretic curves, less irreversible deformation, no severe diagonal cracks in the joint core, and no concrete crushing at the compression zone, when compared to NSC specimens. Furthermore, the failure mechanism of UHPC corner beam-column joints is governed by a flexural plastic hinge outside the joint core.

The specimen **$CJ_2U_{1h}T_1S_{50}C$** exhibited stable behavior until failure. The first visual crack was a flexural hairline crack that developed at the joint-beam interface after the first load cycle at a load of 30 kN. In contrast, the first diagonal hairline crack was observed at the peak of the seventh load cycle at a load of approximately 90 kN. At this stage, a horizontal crack also developed in the lower column at the joint-column interface. As the load cycles continued and load steps increased, flexural hairline cracks were generated in the plastic hinge region. Compared to NSC joints, the cracks in the UHPC region were still hairline and extended slowly, and residual flexural cracks were observed after removing the load following fifteen load cycles. This may be due to the bridging mechanism provided by steel fibers. After nine loading cycles, multiple diagonal hairline cracks developed in the joint core. These cracks did not persist after removing the load and remained hairline cracks until failure, while the flexural cracks at joint-beam interface widened. During the fourteenth load cycle at a drift ratio of 1.9%, additional horizontal cracks (flexural cracks) developed in the upper and lower column

due to tension stresses developed in this region. When the load (P) reached 152.3 kN, after nineteen load cycles, a flexural crack widened and concentrated at the joint-beam interface, and the steel fibers continued to pull out from the UHPC. At the peak load, the flexural plastic hinge widened significantly, and then the load dropped slightly. At this stage, the LVDTs were removed to avoid beam collapse and instrument destruction. The steel fibers continued to pull out from the UHPC, resulting in a slight load drop until the tension reinforcement fractured, as clearly shown in Figure 4.5.

The overall behavior of specimens **$CJ_2U_{2h}T_1S_{50}C$** and **$CJ_1U_{1h}T_1S_{50}C$** was quite similar to **$CJ_2U_{1h}T_1S_{50}C$**. However, the first flexural hairline crack was delayed in the initiation, and the diagonal crack in the joint core was restricted to extending in the diagonal path and changing its direction to propagate parallel to flexural cracks. Therefore, no diagonal cracks were observed in the joint core of these specimens. This may be due to extending the UHPC above and below the column in specimens $CJ_2U_{2h}T_1S_{50}C$ and providing transverse reinforcement in the joint core in addition to UHPC in specimen **$CJ_1U_{1h}T_1S_{50}C$**.

The **$CJ_2U_{2h}T_1S_{50}C$** specimen displayed the first visible flexural hairline cracks after undergoing three load cycles at 45 kN, corresponding to a 0.46 drift ratio. Notably, there were no horizontal cracks observed in the columns located above and below the joint, and no joint diagonal cracks were detected until the failure of the specimen. The absence of diagonal cracks may be attributed to the high tensile strength of UHPC utilized. Eventually, the specimen failed after 15 load cycles at a load of 153.9 kN due to the creation of a plastic hinge at the joint-beam interface.

The specimen **$CJ_1U_{1h}T_1S_{50}C$** represents a transitional stage between specimens **$CJ_2U_{1h}T_1S_{50}C$** and **$CJ_2U_{2h}T_1S_{50}C$**. The first hairline crack appeared at the joint-beam interface after three load cycles at 40 kN,

followed by a multi-flexural crack at 60 kN. After the ninth load cycle, a flexural crack was generated in the lower column and extended along the column depth at 115 kN. Similar to the other UHPC specimens, no severe damage, significant cracks, or joint diagonal cracks were observed until failure. However, failure occurred due to widening and concentration cracks at the joint-beam interface after 16 load cycles, with an ultimate load of 154 kN.

Figures 4.5 through 4.7 provide a visual representation of the crack patterns and failure mode observed at the test end of the UHPC specimens. A comparison with NSC specimens clearly shows that the joints in the UHPC specimens remained intact and free of severe damage and significant cracks. This can be attributed to the high tensile strength and shear resistance of UHPC, which prevents the occurrence of 3D diagonal strut damage at the interior corner of the lower column.

Furthermore, the figures illustrate the local fracture of all tension reinforcement at the joint-beam interface without yielding the tensile reinforcement inside the joint core. This is due to the high bond strength between UHPC and steel reinforcement. The presence of micro steel fibers in UHPC helps in gradually pulling them out without fracturing, thereby providing a warning before failure.

Figure 4.8 is an important representation of the damage process for the UHPC specimens monitored by DIC, providing a clear picture of the crack propagation and failure mode vs. drift ratio. Despite the similarity in behavior among all the UHPC specimens, it is worth noting that the column in specimen $CJ_2U_{2h}T_1S_{50}C$ did not show any flexural cracks until the failure, as illustrated in Figure 4.8(b). This behavior can be attributed to the additional reinforcement provided by the extension of UHPC above and below the joint core

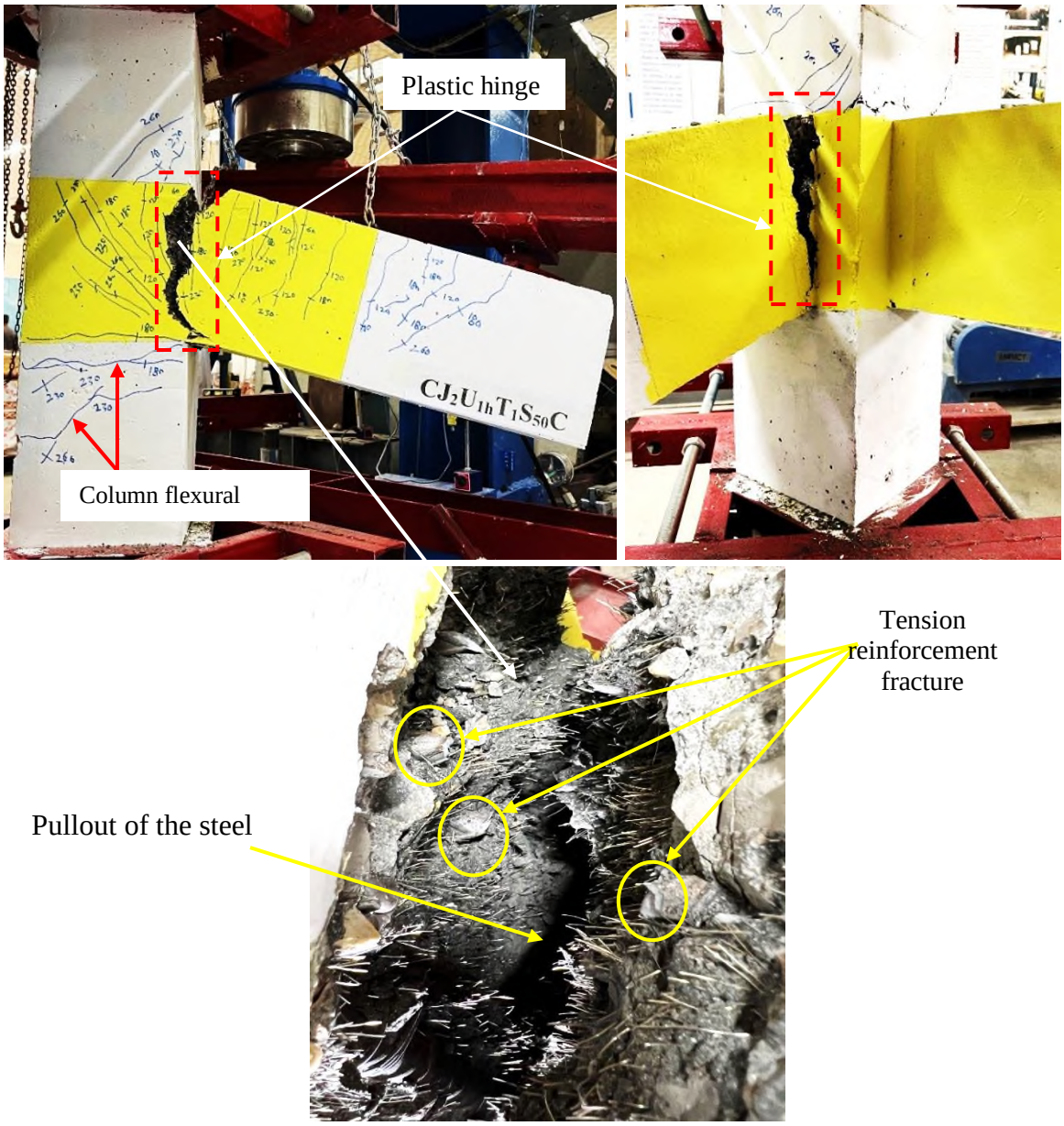

Figure 4.5 Failure mechanism and crack pattern at the end of the test specimen $CJ_2U_{1h}T_1S_{50}C$.

Figure 4.6 Failure mode and crack pattern at the end of the test specimen $CJ_2U_{2h}T_1S_{50}C$.

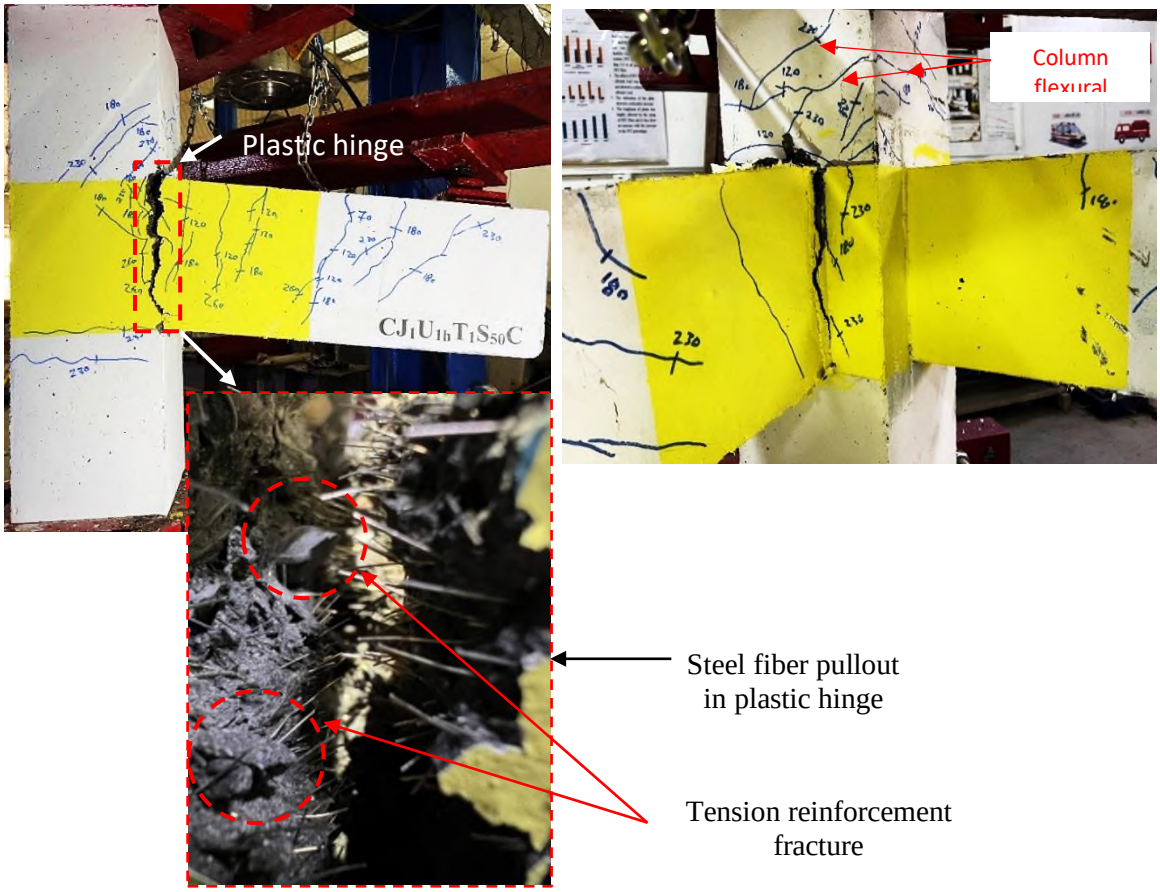

Figure 4.7 Failure mode and crack pattern at the end of the test specimen $CJ_1U_{1h}T_1S_{50}C$.

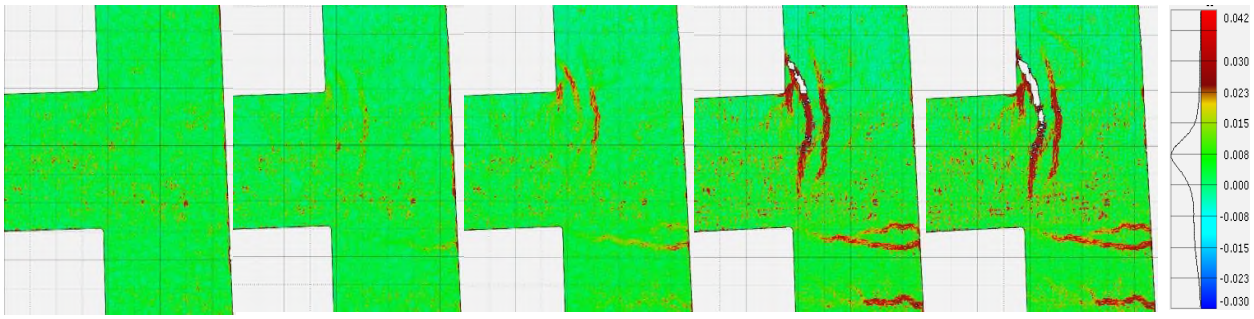

a) Specimen $CJ_2U_{1h}T_1S_{50}C$

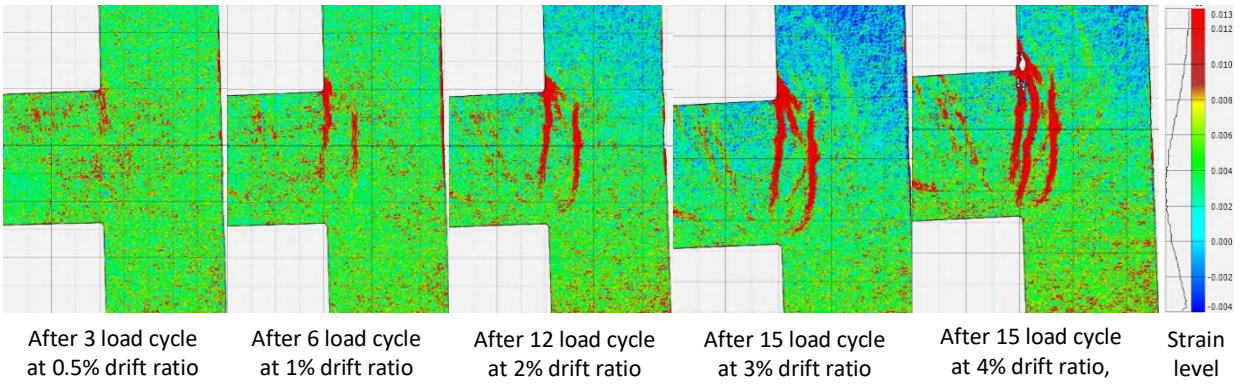

b) Specimen $CJ_2U_{2h}T_1S_{50}C$

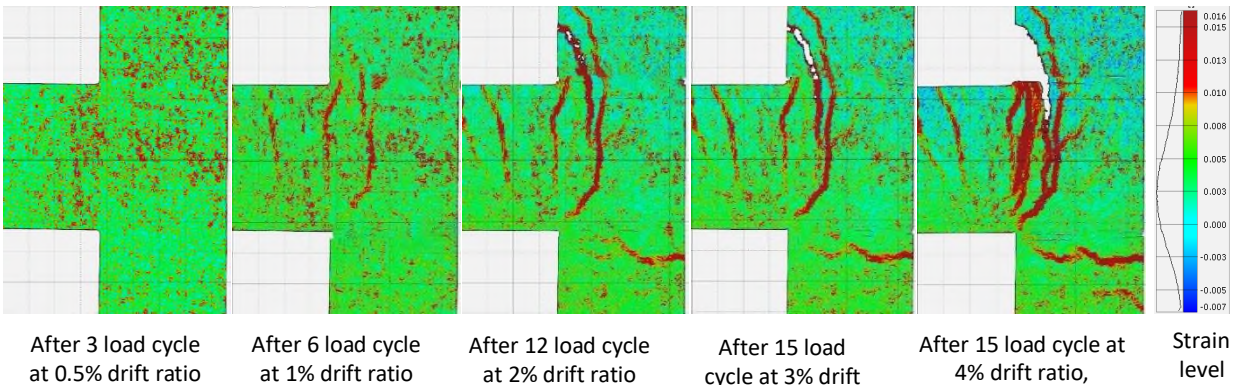

c) Specimen $CJ_1U_{1h}T_1S_{50}C$

Figure 4.8 Damage process and crack pattern of UHPC specimen monitored by DIC.

4.2.1.2 Cracks pattern and failure mode of group II tested under cyclic load

This group consisted of five specimens, with three of them being tested under cyclic load, and the remaining two were tested under monotonic load. In comparison to group I, the spacing of transverse reinforcement in both beams and columns was doubled in this group and was omitted from the joint core, while the other variables were kept similar. In this section, we will discuss the specimens tested under compression cyclic load, while the remaining specimens will be discussed in the second part of this chapter.

In the case of the first sample in this group (**$CJ_2NT_1S_{100}C$**), a flexural crack was observed at a distance of 70 mm from the column's face during the first load cycle at 20 kN. In the fourth cycle, at 45 kN, a diagonal crack formed in the joint core, which subsequently extended toward the ends of the joint. Multiple diagonal cracks developed in parallel to the initial crack as the load increased. After six load cycles, a rapid shear crack was observed in both orthogonal beams, and widened the diagonal crack in the joint core. A column flexural crack was also detected in the lower column at this stage. Thereafter, the specimens began to deteriorate and lose strength. The concrete cover at the tension side spalled, and the beam plastic hinge region was crushed due to shear cracks in the region, resulting in sudden failure. It was observed that the doubled spacing of the transverse reinforcement in the beam could not withstand the significant deformation capacity, leading to the sudden shear crack's failure. Additionally, the doubling of the transverse reinforcement spacing failed to prevent the buckling of the beam's longitudinal reinforcement, as shown in Figure 4.9. Despite reaching the beam flexural capacity, the specimen exhibited poor behavior and a brittle failure mode due to sudden shear cracks in both orthogonal beams, as depicted in Figure 4.9.

The use of UHPC in the joint region, as seen in specimens **$CJ_2U_{1h}T_1S_{100}C$** and **$CJ_2U_{2h}T_1S_{100}C$**, prevented concrete crushing and spalling. Furthermore, there were no significant diagonal cracks in the joint region or buckling of beam longitudinal reinforcement. UHPC generally compensates for the decrease in strength caused by the increased spacing of transverse reinforcement in both beams, column, and joint core.

In the case of specimen **$CJ_2U_{1h}T_1S_{100}C$**, a flexural crack appeared at the joint-beam interface after three load cycles at 30 kN. During the seventh cycle at a load level of 90 kN, the first hair diagonal crack emerged in the joint core, while additional flexural cracks appeared in the UHPC region of the beams, and shear cracks were noted in the NSC region of the beam. After 12 load cycles, multi diagonal hairline cracks emerged in the joint core, along with a horizontal crack below it. Similar to previous UHPC specimens, all the cracks in the UHPC region were hairline cracks and then concentrated at the face of the column to develop the plastic hinge. At a load level of 125.7 kN, after 12 load cycles, the load decreased slightly, and the flexural cracks concentrated at the joint-beam interface, widening due to steel fiber pullout. Subsequently, the tension reinforcement bars were ruptured. Figure 4.10 illustrates the crack patterns and failure mode at the end of the test for specimen **$CJ_2U_{1h}T_1S_{100}C$**.

In comparison to specimen **$CJ_2U_{1h}T_1S_{100}C$**, specimen **$CJ_2U_{2h}T_1S_{100}C$** exhibited stiffer behavior and resist more load cycles while displaying a similar crack pattern and failure mode. The first visual crack appeared after three load cycles at 45 kN, accompanied by multiple flexural hairline cracks distributed uniformly along the beam at a distance equal to d/2. No residual cracks were observed when the load was removed through cyclic loading until the 13th cycle. There were no significant joint diagonal cracks or damage. Similar to the other UHPC specimens, crack concentration and

widening occurred at the joint-beam interface, and then the load decreased gradually after reaching 140 kN. Figure 4.11 illustrates the failure mode and crack pattern at the end of the test for specimen **$CJ_2U_{2h}T_1S_{100}C$**.

Figure 4.12 summarizes the damage process with regard to the drift ratio for the specimens tested in group II, which were monitored by DIC.

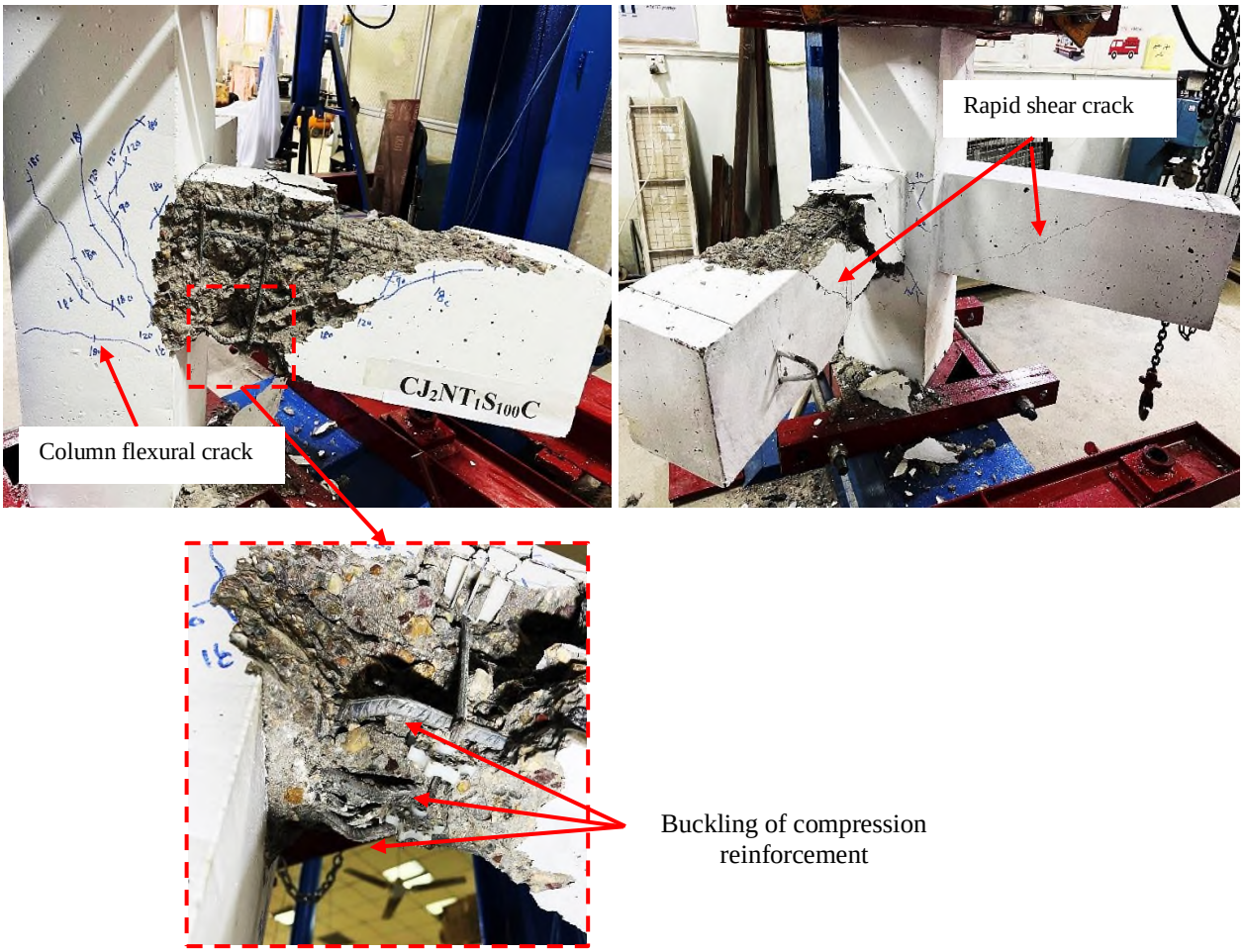

Figure 4.9 Failure mode and crack pattern at the end of the test specimen $CJ_2NT_1S_{100}C$.

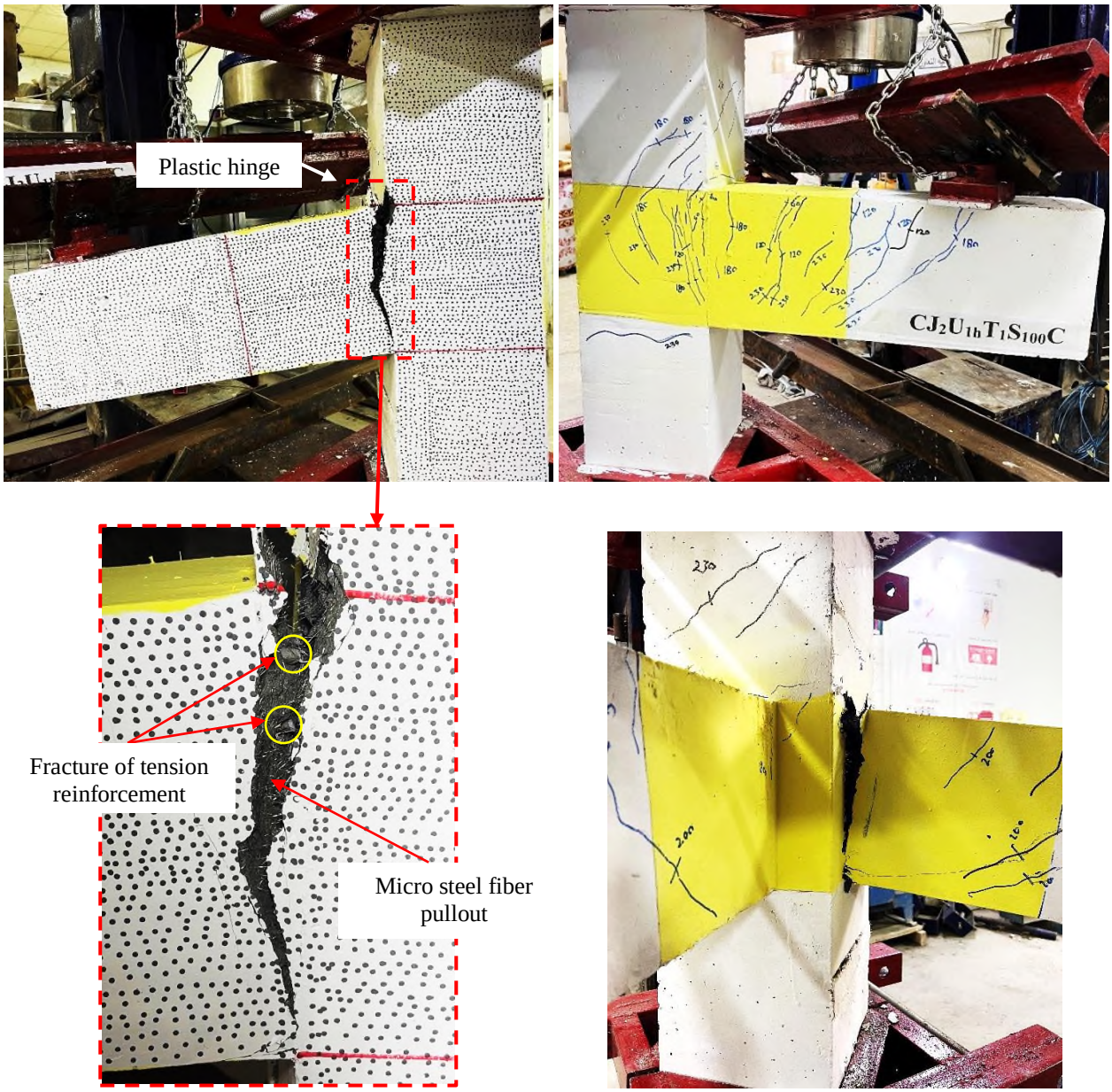

Figure 4.10 Failure mode and crack pattern at the end of the test specimen $CJ_2U_{1h}T_1S_{100}C$.

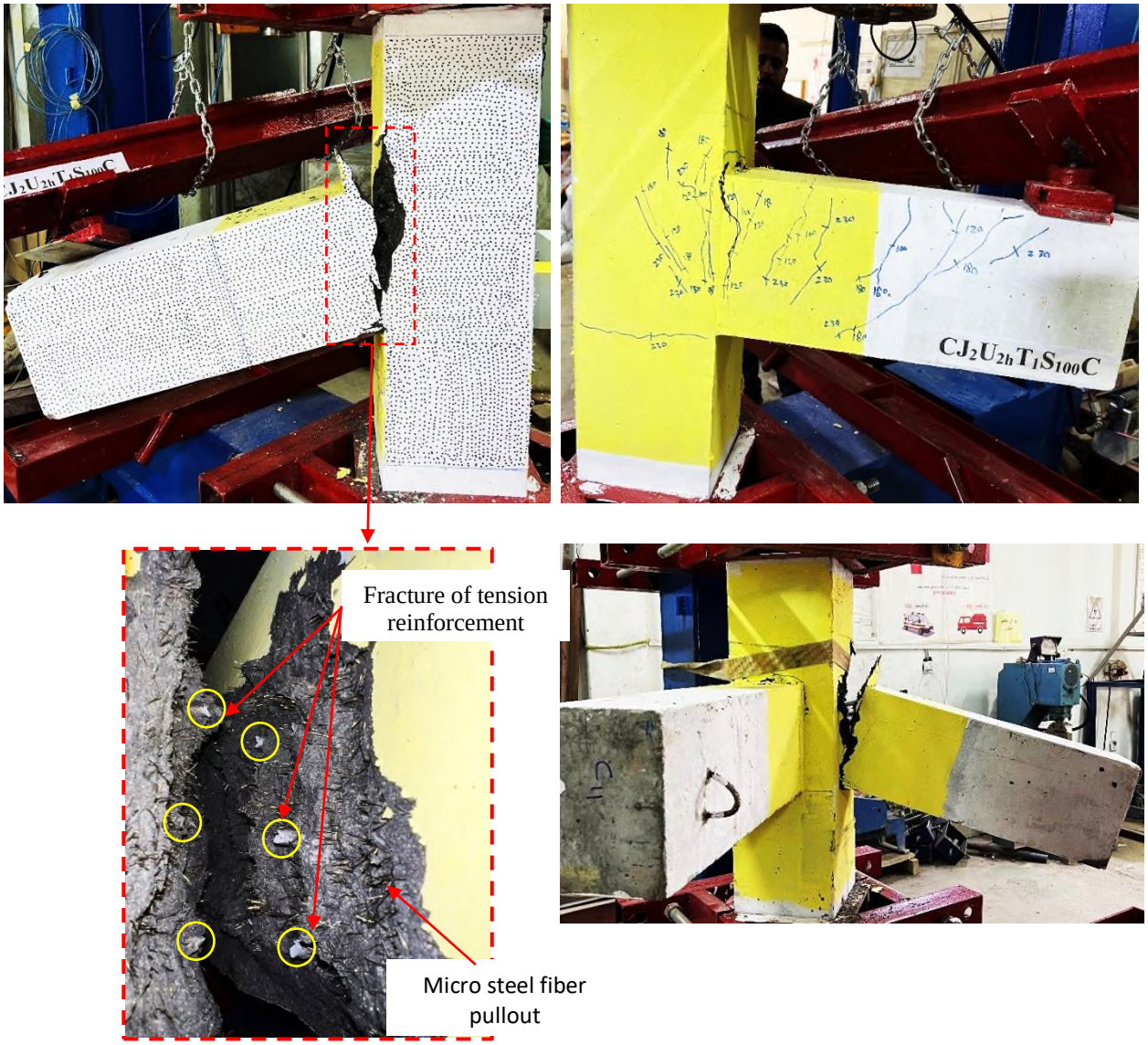

Figure 4.11 Failure mode and crack pattern at the end of the test specimen $CJ_2U_{2h}T_1S_{100}C$.

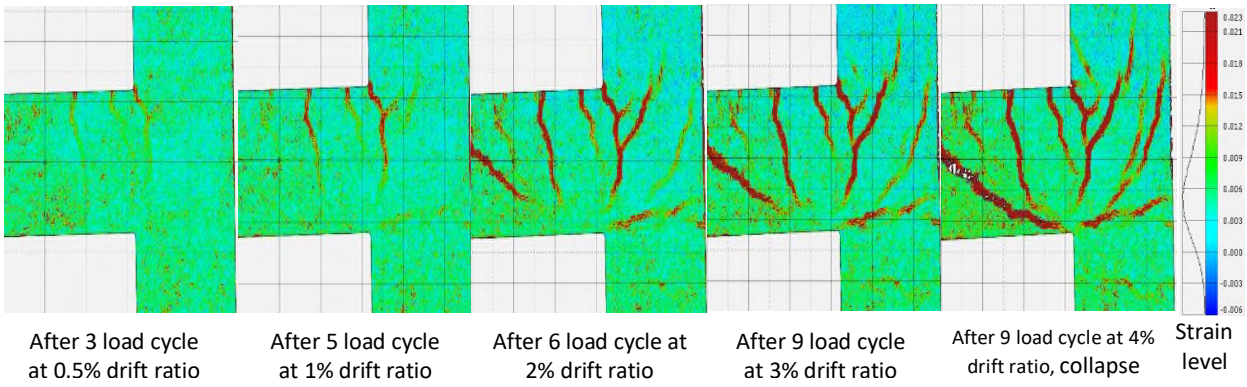

a) Specimen $CJ_2NT_1S_{100}C$

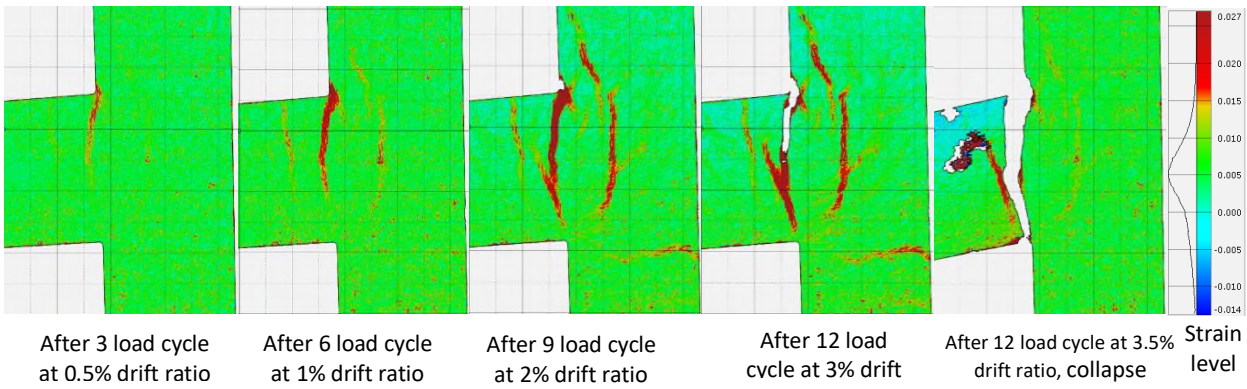

b) Specimen $CJ_2U_{1h}T_1S_{100}C$

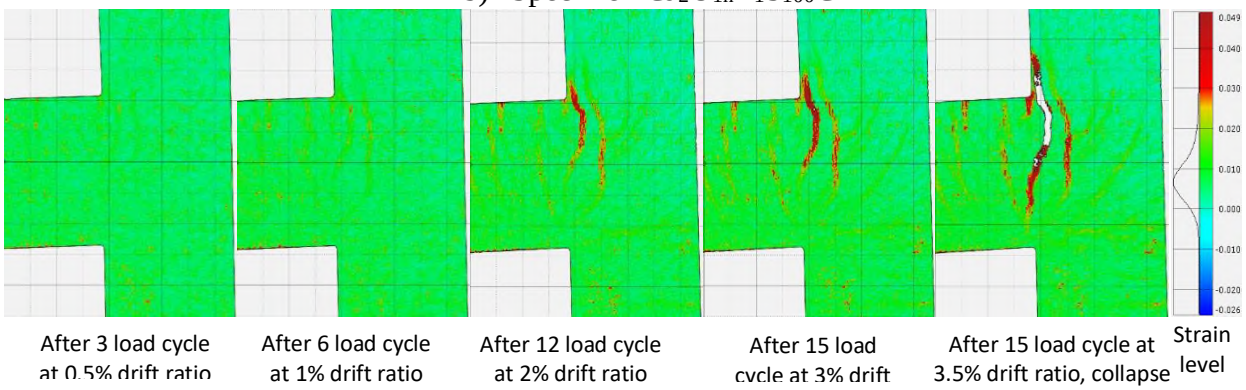

c) Specimen $CJ_2U_{2h}T_1S_{100}C$

Figure 4.12 Damage process and crack pattern of tested specimen in group II monitored by DIC.

4.2.1.3 Cracks pattern and failure mode of group III tested under cyclic load

All specimens in this group exhibited stable behavior, with no major cracks in the joint area. Even with eliminated transverse reinforcement in the joint's core, the presence of cold joint, and increased spacing of transverse reinforcement in both beams and the column, the failure mode observed was ductile, with a plastic hinge forming at the joint-beam interface. Additionally, incorporating NSM steel reinforcement on both sides of the beams helped to control cracks and delay their spread through the depth of the beams.

The first specimen in this group labeled **$CJ_2U_{1C}T_1S_{50}C$** was examined under cyclic load. At 45 kN after three load cycles, the first crack appeared at the joint-beam interface. At the same time, additional vertical cracks developed through the joint core. As the load increased and load cycles repeated, multiple flexural cracks were generated in the beams and stopped at the NSM steel bars. At the peak of the 7th load cycle, a hairline diagonal crack in the joint core was noted. After nine load cycles at a load of 115 kN, multiple hairline diagonal cracks were developed parallel to the first one, and the beam's flexural cracks across the NSM steel bars changed their path in the NSC region to shear cracks. During the 16th load cycle at 148.9 kN, the specimen lost its strength, and the load dropped slightly due to opening and extending the crack at the joint-beam interface. Until failure, no significant cracks were observed at the interface between NSC and UHPC. Based on the experimental observations, it is fair to say that the bond between UHPC and NSC was perfect, and the technique used in casting or removing and replacing the joint region was effective. Figure 4.13 illustrates the crack pattern and failure mode at the end of the test specimen **$CJ_2U_{1C}T_1S_{50}C$.**

The specimen **$CJ_2U_{1C}T_1S_{100}C$** shows approximately similar behavior to specimen **$CJ_2U_{1C}T_1S_{50}C$**. This means the UHPC joints are independent of the spacing of transverse reinforcement because of the high shear resistance of UHPC.

The first visible crack in specimen **$CJ_2U_{1C}T_1S_{100}C$** was observed after three load cycles at the joint-beam interface in a load level of 30 kN, followed by multi-flexural cracks developed in the beam at a uniform distance (d/2). In comparison, the first hairline diagonal crack in the joint core was observed at 90kN after six load cycles. As discussed in the previous specimen, the NSM steel bars restrict the propagation of cracks through the depth of the beam. During the 13th load cycle at 70 kN, a flexural crack was generated at the lower column between UHPC and NSC interface. Finally, the specimen failed at 147.3 kN due to the generation of a plastic hinge away from the joint core without severe cracks in the joint core or interface between NSC and UHPC, as shown in Figure 4.14.

In order to analyze the damage process of the examined joint in this group, the specimens were monitored by the DIC technique. Figure 4.15 illustrates the relationship between the drift ratio and the corresponding damage state of the specimens.

Figure 4.13 Failure mode and crack pattern at the end of the test specimen $CJ_2U_{1c}T_1S_{50}C$.

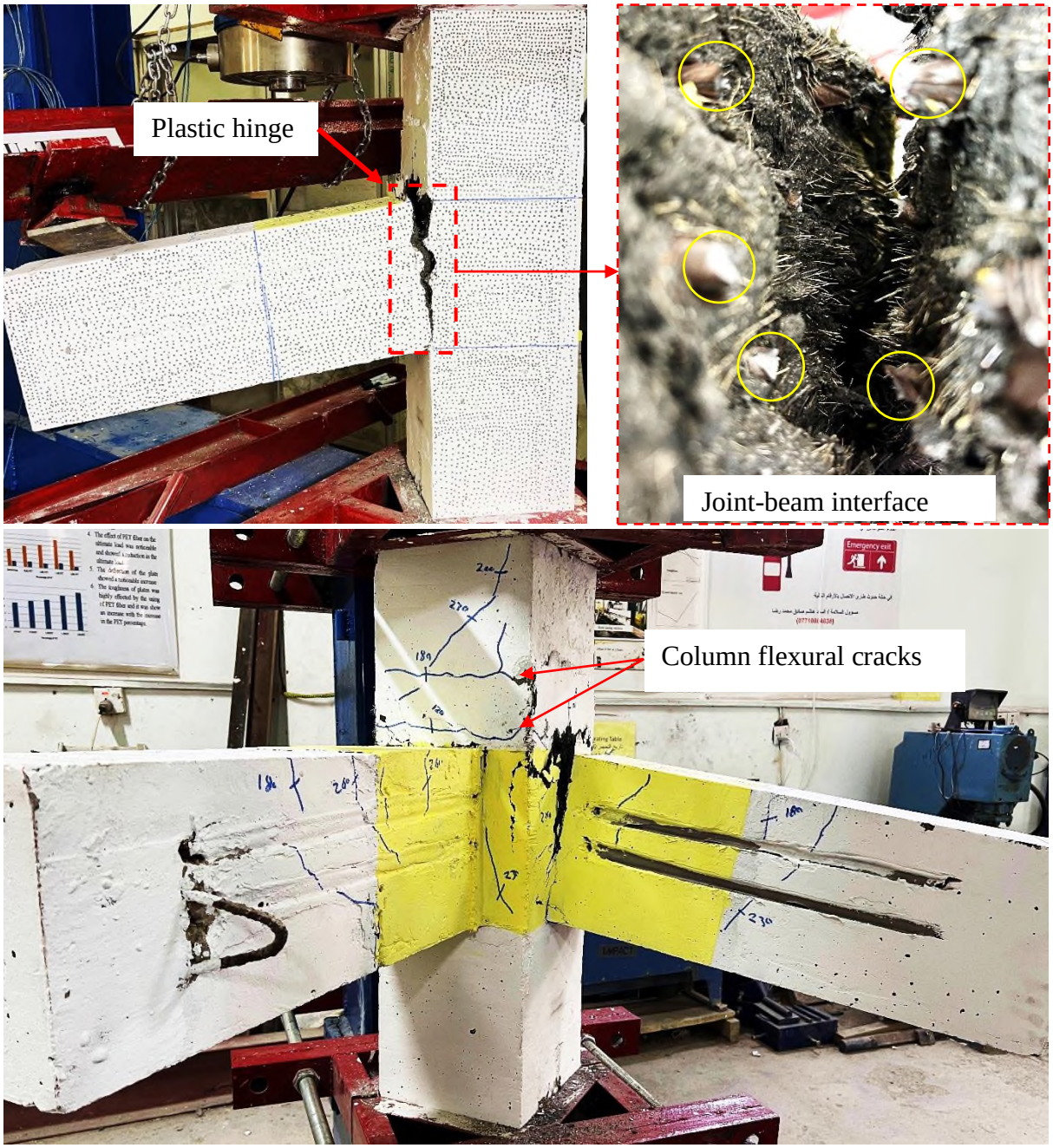

Figure 4.14 Failure mode and crack pattern at the end of the test specimen $CJ_2U_{1c}T_1S_{100}C$.

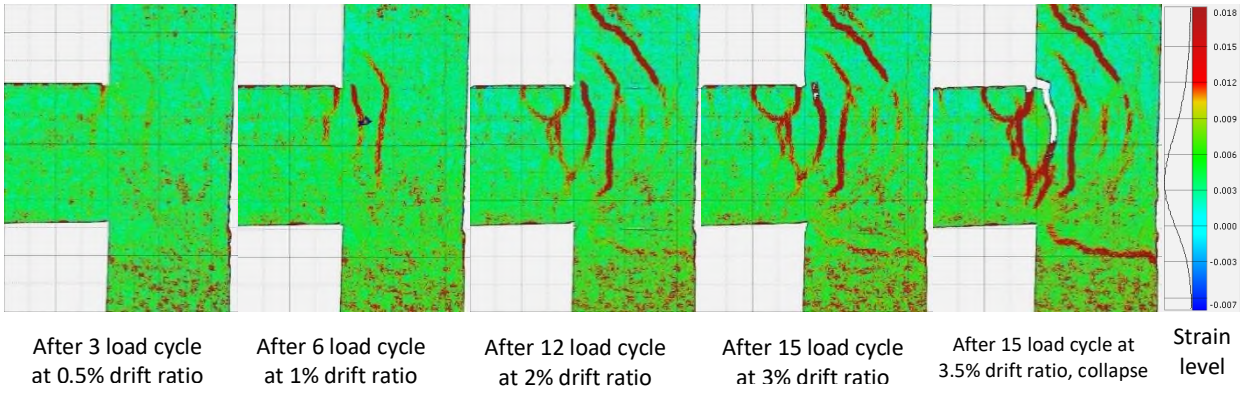

a) specimen $CJ_2U_{1c}T_1S_{50}C$

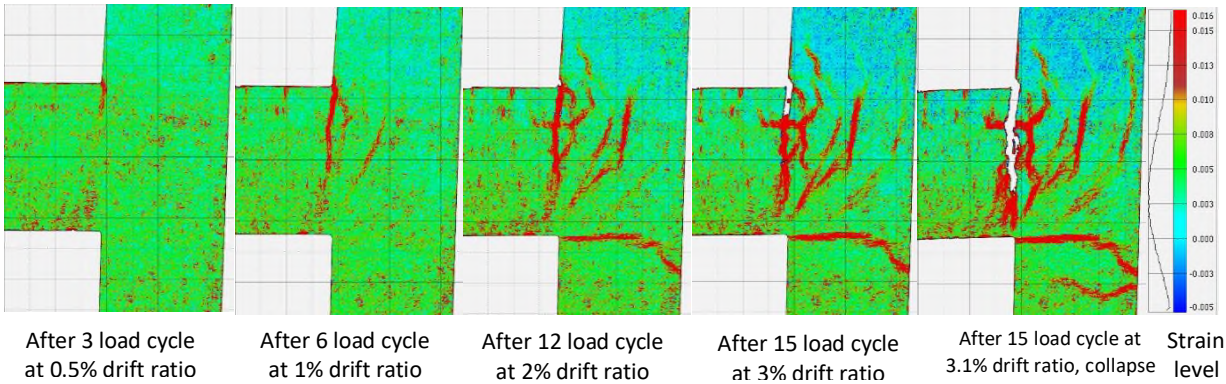

b) Specimen $CJ_2U_{1c}T_1S_{100}C$

Figure 4.15 Damage process and crack pattern of tested specimen in group III monitored by DIC.

4.2.1.4 Cracks pattern and failure mode of group IV tested under cyclic load

This group of specimens aimed to explore the use of UHPC in joint regions to enhance the behavior of RC corner beam-column joint. Specifically, the focus of this group was to investigate whether UHPC could be used to reduce the embedded length of longitudinal reinforcement in the beam required to pass through the joint core.

To test this hypothesis, four specimens were constructed with different arrangements of transverse reinforcement in both beams and columns. The

specimens were then subjected to cyclic loading to simulate seismic conditions and monitor their response.

The first specimen was NSC joint that served as a control specimen, labeled **$CJ_2NT_2S_{50}C$**. During the first load cycle at 20 kN, a flexural crack appeared at the joint-beam interface. In comparison, the first diagonal crack developed in the joint core at the peak of the 4th load cycle, which corresponds to the main diagonal strut supported by a hook of longitudinal reinforcement. The inclination of that crack matches the theoretical diagonal strut inclination of 45^{o}. Additionally, horizontal joint-column interface flexural cracking due to tensile action on the column was observed. Afterwards, a vertical crack was also initiated towards the outer edge of the joint, resulting from cover splitting action. As the load increased, the vertical cracks on both sides of the column were connected diagonally through the joint and connected to the vertical cover splitting crack, forming a large triangular concrete wedge that tended to separate from the outside corner of the column. The transverse reinforcement of the column prevented the separation of the concrete wedge. After nine load cycles, the vertical crack widened rapidly, and the specimen behavior deteriorated. Finally, the failure mechanism was governed by joint shear failure due crashing of the concrete at the joint core after 12 load cycles at a load of 118.1 kN.

After removing the crashed concrete, it was observed that the tile of hooks had moved out of the joint core, as illustrated in Figure 4.16. Movement of the hook of the beam longitudinal reinforcement and the development of multiple cracks in the joint core prove that the development length passing through the joint core was insufficient to prevent the slip of the beam longitudinal reinforcement.

The specimen **$CJ_2NT_2S_{100}C$** shows earlier cracks developing and more severe damage than **$CJ_2NT_2S_{50}C$**. This is due to the reduction of transverse reinforcement in the beams and columns. However, at the final stage, the specimen shows a similar failure mode to specimen **$CJ_2NT_2S_{50}C$**. Figure 4.17 illustrates the crack pattern and failure mode of the tested specimen.

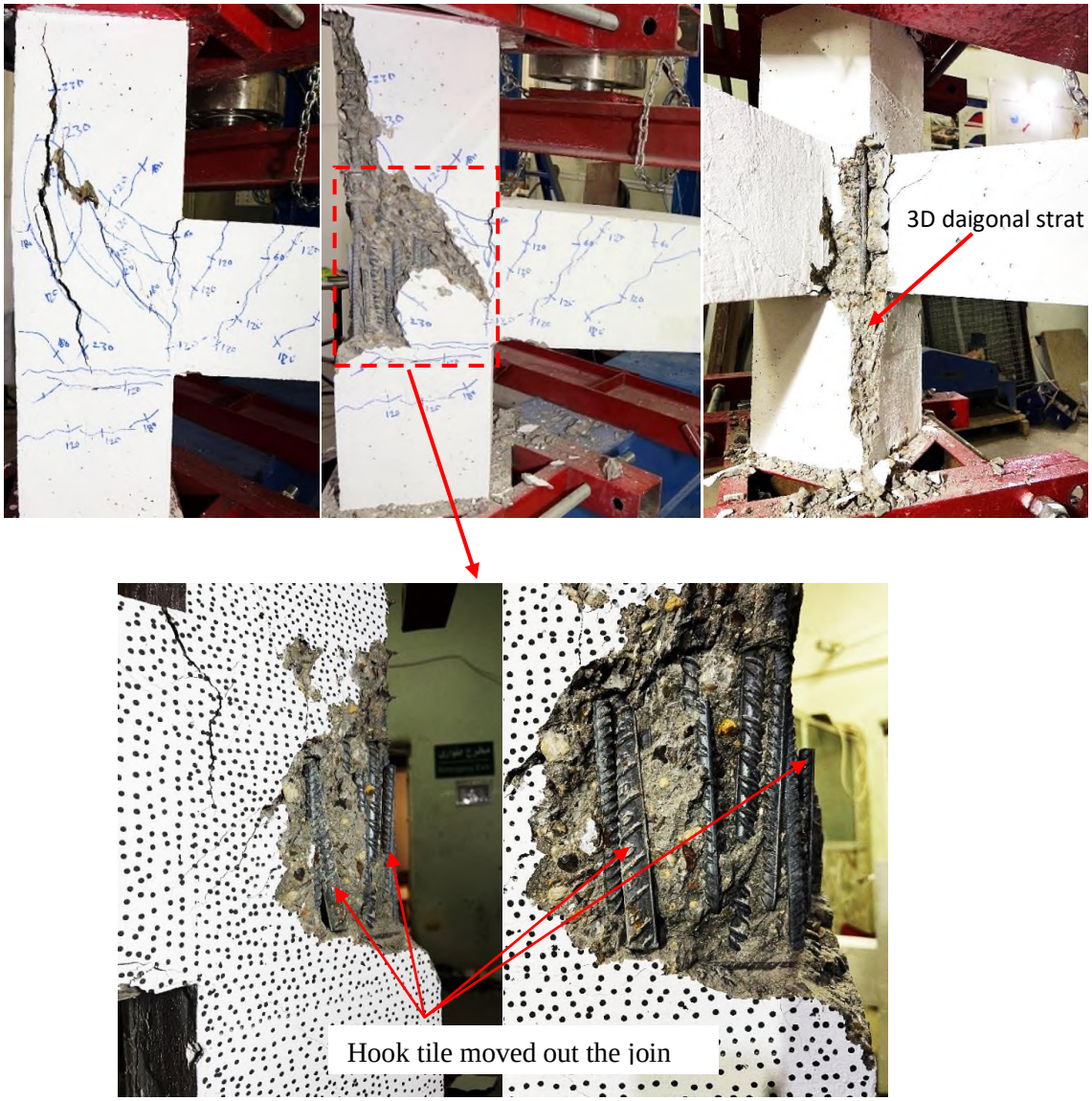

Figure 4.16 Failure mode and crack pattern at the end of the test specimen $CJ_2NT_2S_{50}C$.

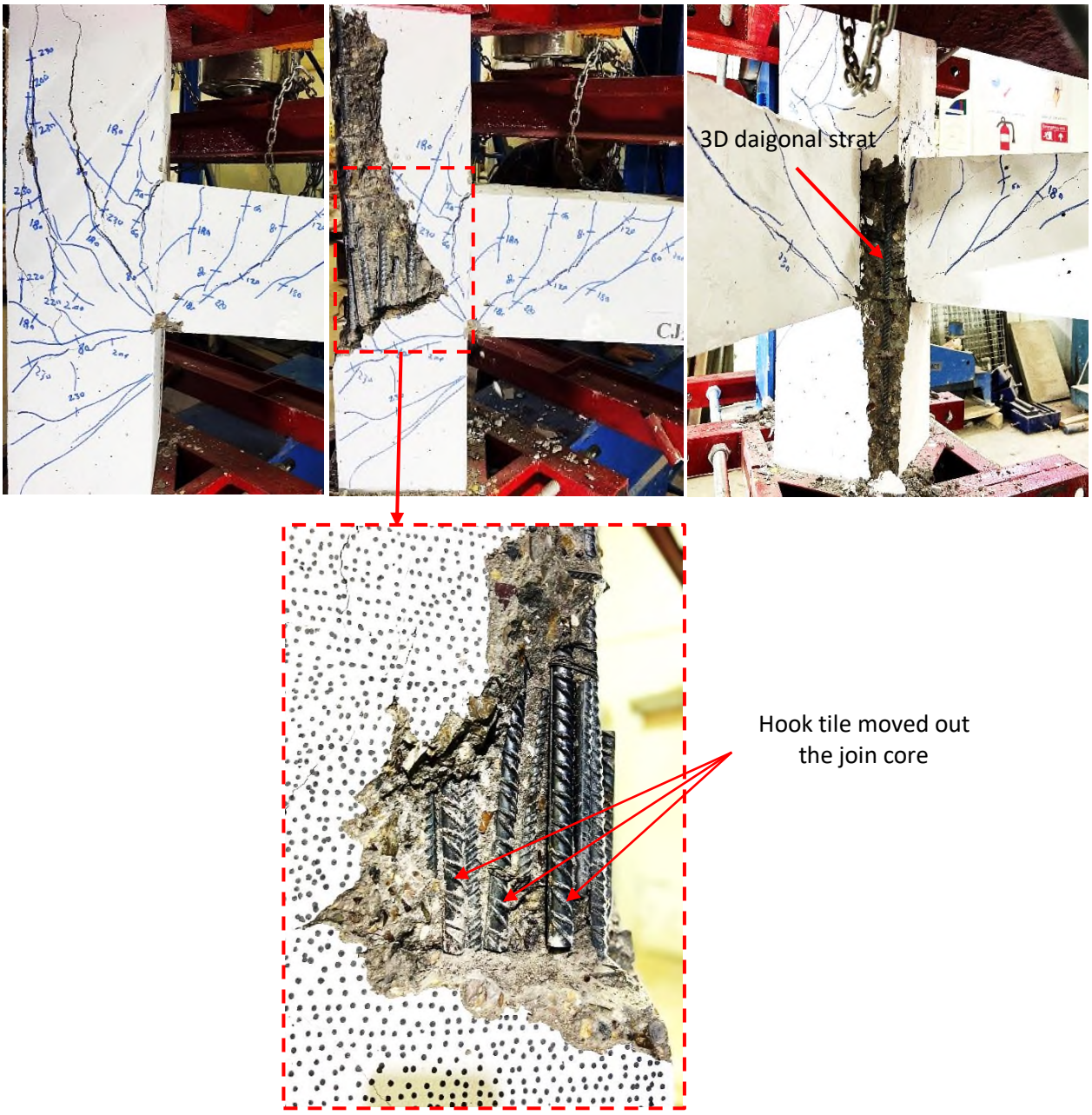

Figure 4.17 Failure mode and crack pattern at the end of the test specimen $CJ_2NT_2S_{100}C$.

Utilizing UHPC in the joint region in this group shows several advantages. One of these advantages is compensating for the reduction in anchorage length of the beam bar required to pass inside the joint core. Additionally, compensate for the reduction in transverse reinforcement in adjoining members. Furthermore, using UHPC in the joint region changes the failure mode from joint shear failure (brittle failure) to flexural failure (ductile failure). This is because UHPC has superior performance in terms of shear

resistance, bond strength, and tensile strength compared to traditional concrete.

For the specimen **$CJ_2U_{1h}T_2S_{50}C$**, the first hairline crack was observed at the joint-beam interface during the 4th load cycle in a load of 35 kN. At the peak of 6th load cycle, a horizontal crack was initiated at the joint-column interface due to the flexural stresses supported by the column. The first diagonal hairline crack was generated during the 10th load cycle at 75 kN. The inclination of that crack matches the theoretical diagonal strut inclination of 45^{o}. It's worth to mention when the load was removed through the cyclic loading protocol, there were no residual cracks observed till the 10th load cycle. After that, the residual cracks appeared clearly. The flexural cracks developed at a uniform distance (d/4) along the UHPC zone in the beam, while the cracks in the NSC changed their path to shear cracks. A diagonal crack was initiated in the column near the top support in addition to multi horizontal cracks below the joint after 12 load cycles at 130 kN. After 18 load cycles, the crack at the joint-beam interface widened, and steel fiber started to pull out. Similar to the other UHPC specimens, the failure occurs due to developing a plastic hinge at the joint-beam interface with no severe damage in the whole of the specimens at load equal to 182.9 kN. Except for the crack developed at the joint-beam interface, most of the cracks developed in the UHPC region still hairline until failure, whereas the cracks in NSC widened and extended as the load increased. Figure 4.18 illustrate the crack pattern and failure mode at the end of the test specimen.

The crack progression for specimen **$CJ_2U_{1h}T_2S_{100}C$** was almost identical to specimen $CJ_2U_{1h}T_2S_{50}C$. The first viable crack was a hairline crack away 100 mm from the face of the column at 30 kN during the 4th load cycle, flowed by crack joint-beam interface. After six load cycles, multi hairline flexural cracks were generated along the beams. During the 7th load cycle at 75 kN a

nearly vertical crack was developed through the joint core in addition to a sudden shear crack out of the beam UHPC region. as the load cycles repeated the vertical crack in the joint core propagated in a radial form. Except for this, the crack pattern and failure mode were similar to specimen **$CJ_2U_{1h}T_2S_{50}C$**. Figure 4.19 illustrate the crack pattern and failure mode at the end of the test. Figure 4.20 illustrate the damage process of tested specimens in this group that was monitored by DIC with respect to drift ratio till failure.

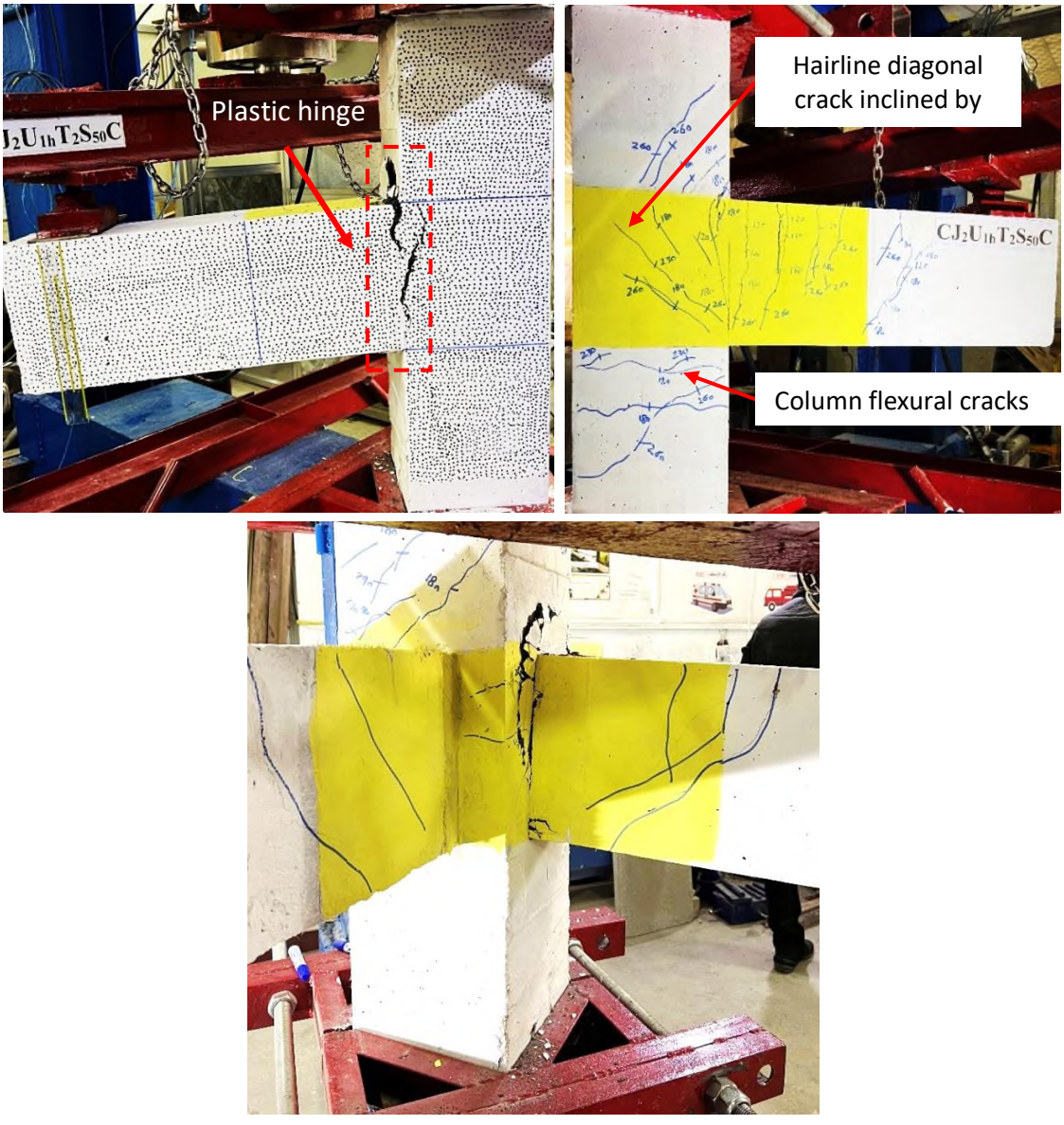

Figure 4.18 Failure mode and crack pattern at the end of the test specimen $CJ_2U_{1h}T_2S_{50}C$.

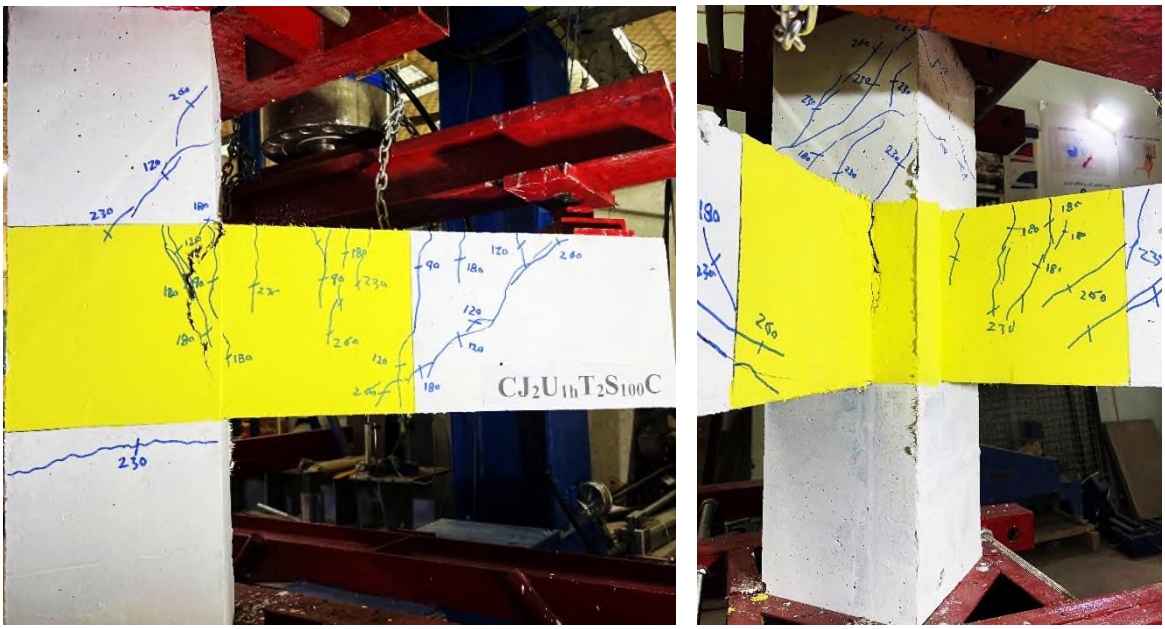

Figure 4.19 Failure mode and crack pattern at the end of the test specimen $CJ_2U_{1h}T_2S_{100}C$.

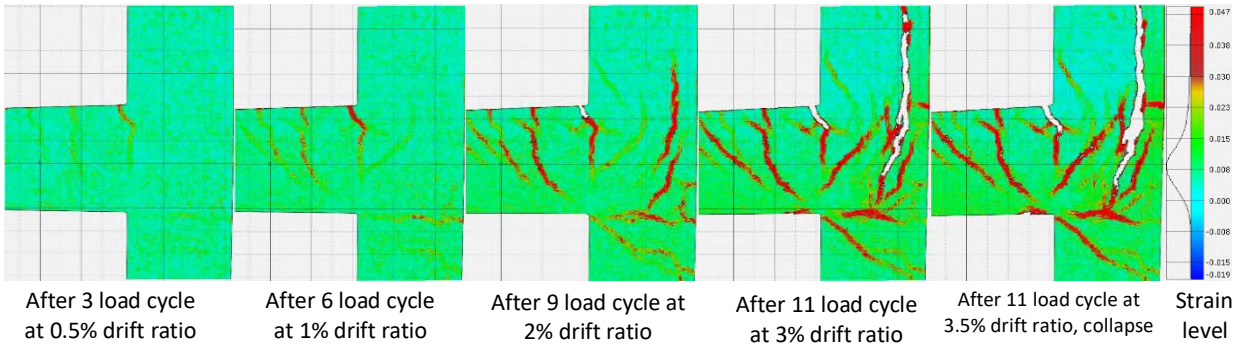

a) specimen $CJ_2NT_2S_{50}C$

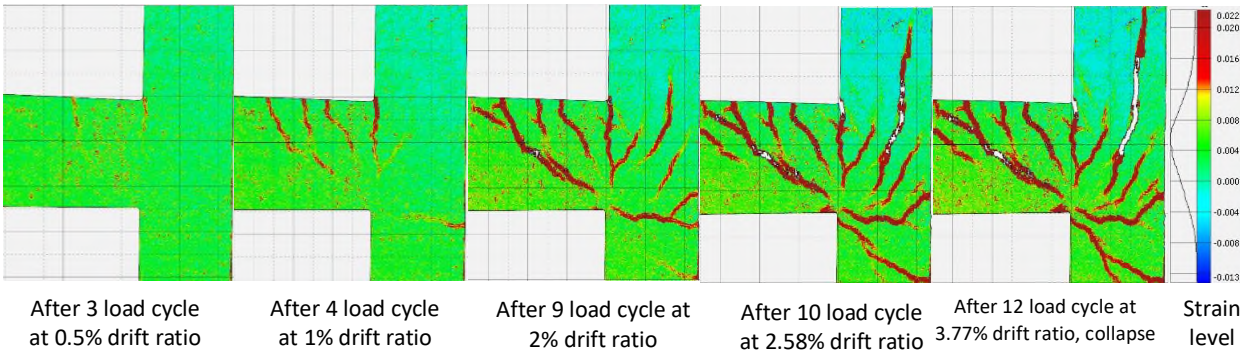

b) specimen $CJ_2NT_2S_{100}C$

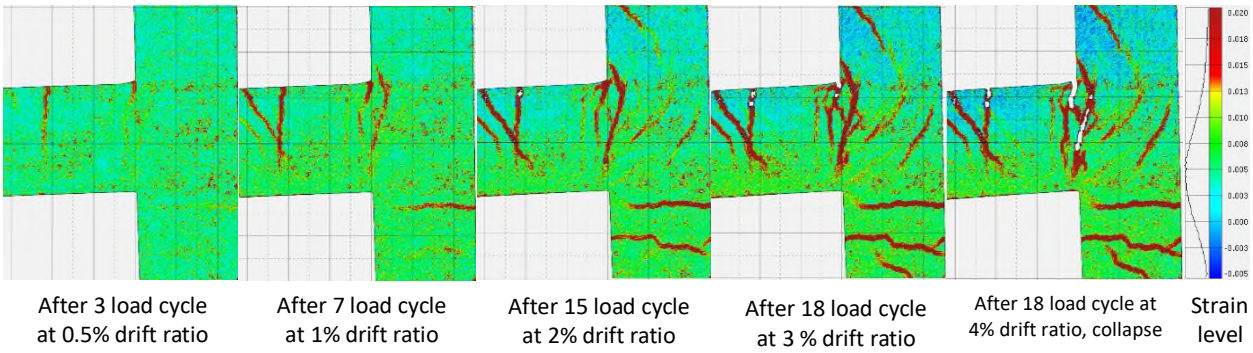

c) Specimen $CJ_2U_{1h}T_2S_{50}C$

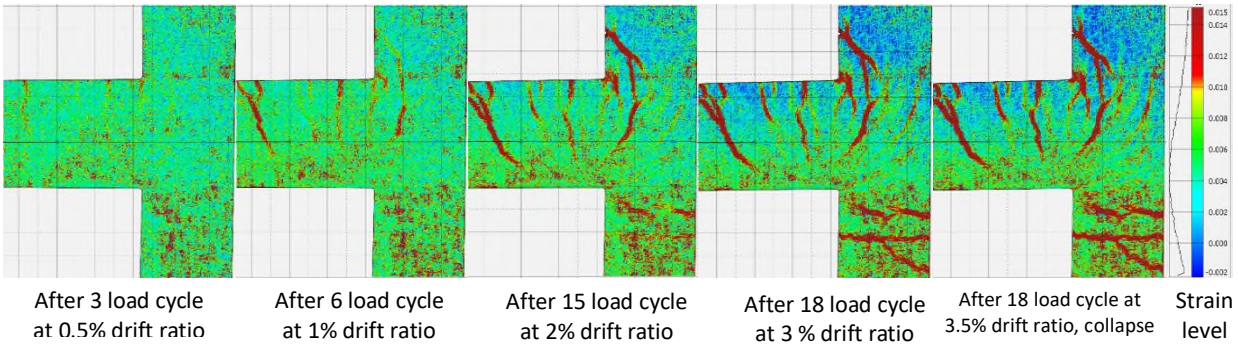

d) Specimen $CJ_2U_{1h}T_2S_{100}C$

Figure 4.20 Damage process and crack pattern of tested specimen in group IV monitored by DIC.

4.2.1.5 Cracks pattern and failure mode of group V tested under cyclic load

Two specimens in this group used the GFRP bar as hybrid reinforcement of the longitudinal bar in beams. Two methods were used to place the GFRP bars, internally reinforced and externally reinforced (NSM).

The first specimen in this group was labeled **$CJ_2NT_3S_{50}C$**; 50% of beam tension reinforcement was replaced with GFRP bars without special details. The specimen shows poor behavior. The first crack was a flexural crack at the joint-beam interface visible during the first load cycle at 20 kN, followed by another flexural crack at a distance of 200 mm. At the peak of the 1st load cycle, the cracks extended to 0.75 of the beam depth. After the first load cycle, residual cracks were observed. The first diagonal crack appeared during the 4th load cycle at 40 kN. At the end of 4th stage, another diagonal crack was developed parallel to the first one in addition to a flexural crack at a distance of 350 mm from the face of the column. Until failure, no additional cracks were generated. However, as the load repeated, the crack widened and propagated. Finally, the specimen failed after six load cycles at a load of 81.0 kN, which is less than beam flexural capacity (90.23kN), due to the slipping of the GFRP bars completely from the joint core; thus, the tension stresses were transformed into remaining steel bars, causing a sudden rupture in steel reinforcement. Figure 4.21 presents the crack pattern and failure mode at the end of the specimen test.

In comparison, the specimen **$CJ_2NT_4S_{50}C$** shows a different crack pattern and failure mode behavior due to a good bond between the GFRP bars and NSC in the joint core. The first crack appeared at the join-beam interface during the first load cycle at 20 kN. After 3 load cycles, at 55 kN the first diagonal crack was observed, followed by a horizontal crack at the joint-column interface. During the loading process, multi flexural cracks

developed at the tension face of the beam and extended through the depth. No slip was noted in NSM GFRP bars. The flexural cracks widened significantly and extended through the depth with generation of multi diagonal cracks in the joint core that matches the theoretical diagonal strut inclination of 45°. Finally, the main diagonal crack widened, and the concrete spalled from the joint region, causing a joint shear failure at a load of 115.4 kN, as shown in Figure 4.22. Although epoxy bonding fractured, no severe damage or slip of GFRP bars from the joint core was observed. On the other hand, the externally strengthened method by NSM technique show good performance and can be used to increase the flexural capacity of beams if needed. Figure 4.23 presents the crack pattern and strain level in the tested specimen of group V which is monitored by DIC.

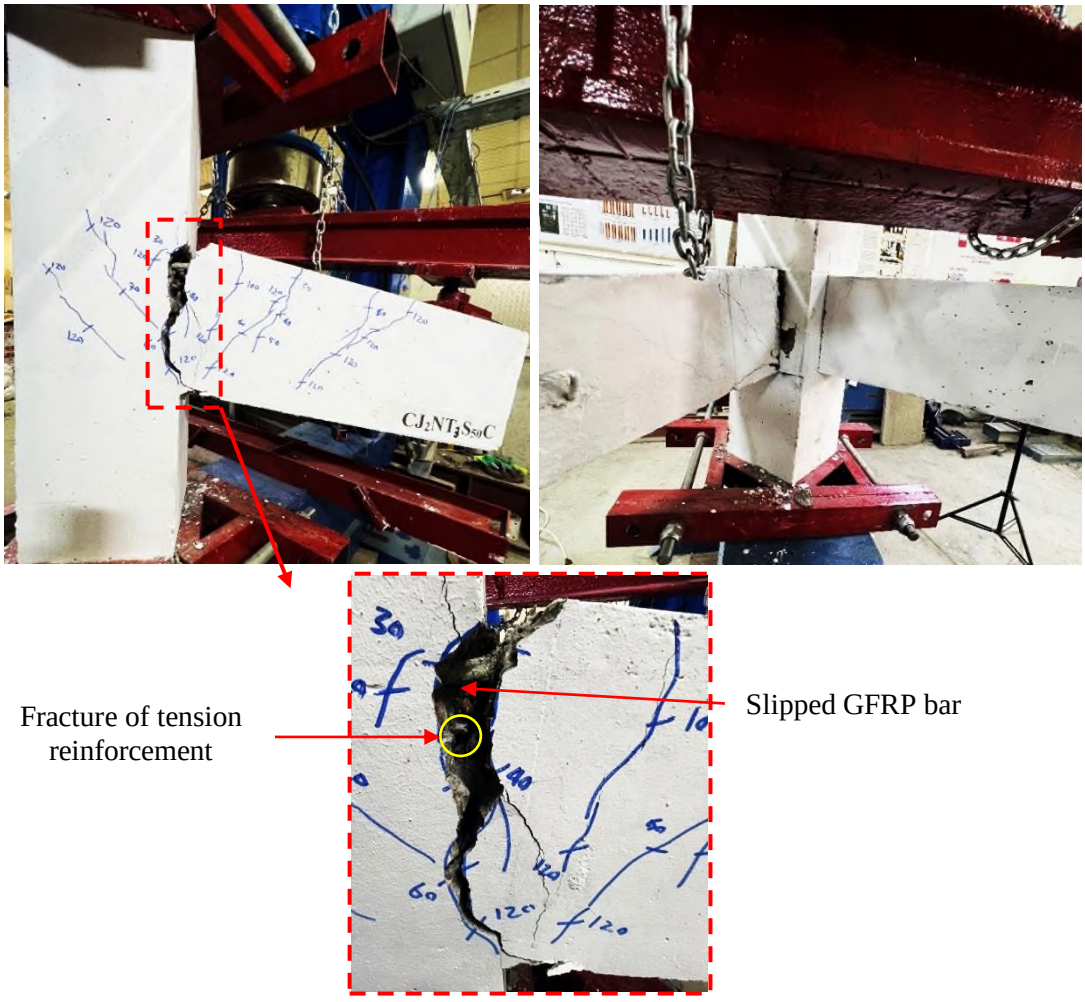

Figure 4.21 Failure mode and crack pattern at the end of the test specimen $CJ_2NT_3S_{50}C$.

Figure 4.22 Failure mode and crack pattern at the end of the test specimen $CJ_2NT_4S_{50}C$.

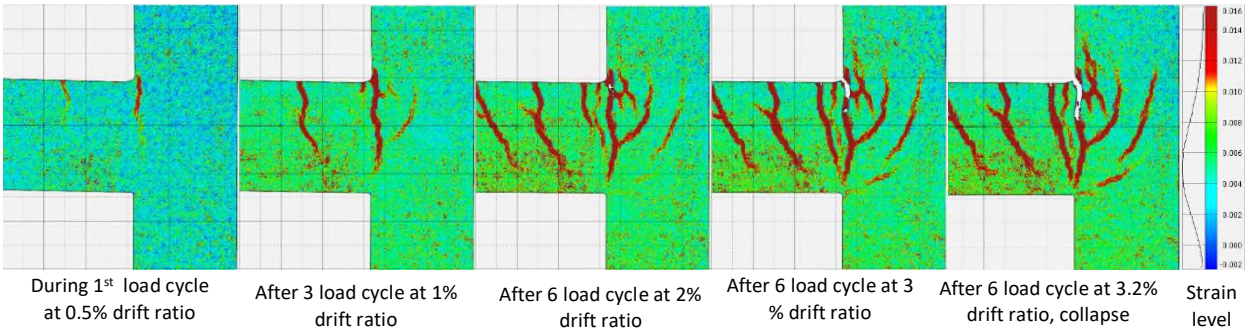

a) specimen $CJ_2NT_3S_{50}C$

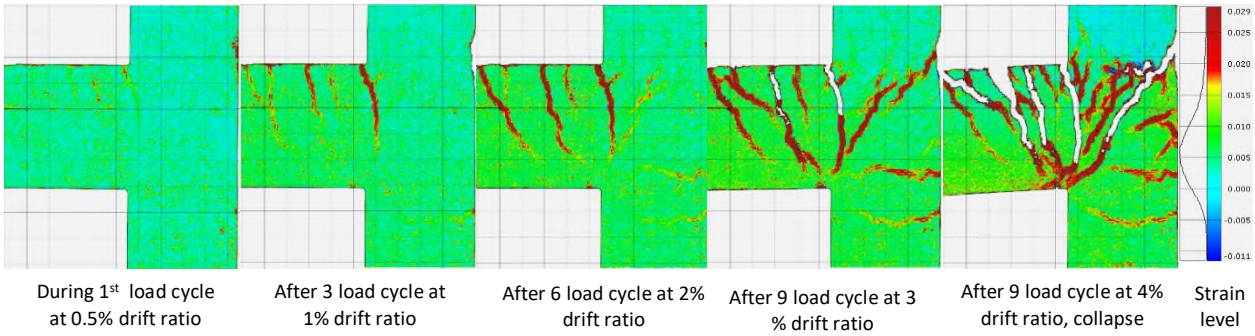

b) specimen $CJ_2NT_4S_{50}C$

Figure 4.23 Damage process and crack pattern of tested specimen in group V which was monitored by DIC.

4.2.2 Load-drift response

In order to study the shear capacity of RC corner beam-column joints, the load-displacement angle curves (drift ratio) of the joints were investigated. The drift ratio represents the relative rotation angle of the beam to the column. In the present study, the drift ratio is defined as the average recorded vertical deflection of the orthogonal beams divided by the distance between the location of LVDT and the face of the column, as shown in Figure 4.24.

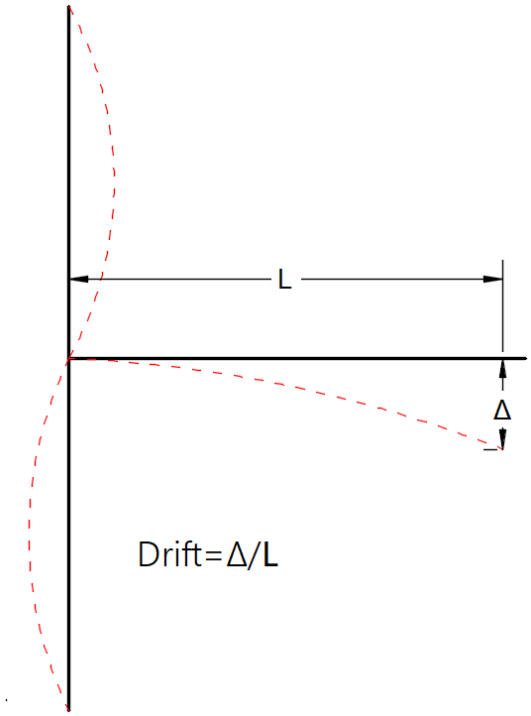

Figure 4.24 Drift response measurement.

4.2.2.1 Load-drift response of group I tested under cyclic load

In general, when specimens were subjected to cyclic compression loading, they initially showed elastic behavior. However, as the load increased, the specimens entered the elastic-plastic stage, resulting in irreversible plastic deformation. During this stage, the NSC specimens experienced a larger residual deformation, and their cracks developed rapidly, leading to a rapid degradation of their stiffness. In the final stage, the diagonal cracks widened, the core region concrete spalled off, and joint shear failure occurred. In contrast, the UHPC specimen remained stable until failure, which occurred due to the development of a plastic hinge at the joint-beam interface, without significant concrete spalling or severe crack development.

The control specimen **$CJ_1NT_1S_{50}C$**, shows stable behavior till the drift ratio is about 2%; as the load increases, the stiffness is degraded because of the opening and closing of the diagonal cracks in the joint region. Finally, the

specimen lost its strength due to the formation of a vertical crack at the face of the column, followed by the widening of the diagonal cracks with an ultimate load of 104.3 kN. Figure 4.25a shows the load-drift response of specimen **$CJ_1NT_1S_{50}C$**. Noting that the red dashed line represents the beam flexural capacity.

Despite the **$CJ_2NT_1S_{50}C$** specimen failing with a comparable ultimate load (102.7 kN) to that of **$CJ_1NT_1S_{50}C$**, its behavior differed significantly. The stiffness of **$CJ_2NT_1S_{50}C$** decreased earlier than **$CJ_1NT_1S_{50}C$**, and the joint area's diagonal cracks formed rapidly because the transverse reinforcement was entirely absent from the joint core. Additionally, Figure 4.25 b illustrates that **$CJ_2NT_1S_{50}C$** demonstrated less stiffness than **$CJ_1NT_1S_{50}C$** after a drift ratio of 0.5%. However, after a drift ratio of 2.5%, the two NSC specimens showed similar stiffness.

The incorporation of UHPC in other specimens resulted in an increase in their load-bearing capacity, and the formation of loops was more stable, without any noticeable decrease in strength and stiffness, as evidenced in Figures 4.25c,d,e. The improvement in behavior can be attributed to the superior properties of UHPC, such as shear resistance, bonding strength, and confinement effect.

The behavior of all UHPC specimens, regardless of the presence of transverse reinforcement or the configuration of UHPC in the joint region, was observed to be similar up to the point of failure. Furthermore, the load-bearing capacity of the UHPC specimens, namely specimens **$CJ_2U_{1h}T_1S_{50}C$**, **$CJ_2U_{2h}T_1S_{50}C$**, and **$CJ_1U_{1h}T_1S_{50}C$**, was increased by approximately 48.3%, 49.9%, and 50%, respectively, when compared to **$CJ_2NT_1S_{50}C$** specimen. The load-drift response of UHPC specimens remained stable until failure at a drift ratio of approximately 4% due to the lack of damage in the joint core, no slippage in the tension beam longitudinal bar, and no significant diagonal

cracks observed in the joint core. Additionally, the failure mode was changed to ductile failure with no substantial cracks or damage in the joint core.

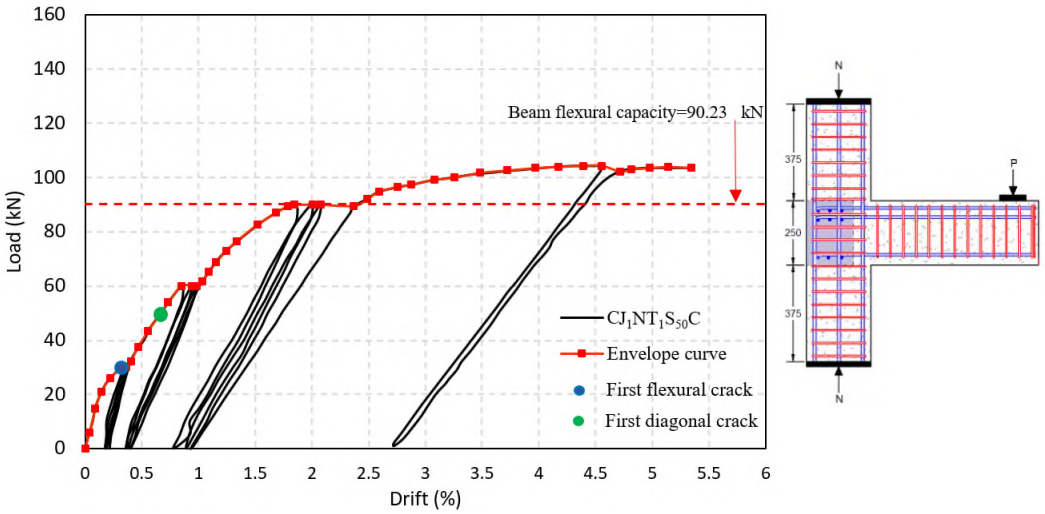

a) specimen $CJ_1NT_1S_{50}C$

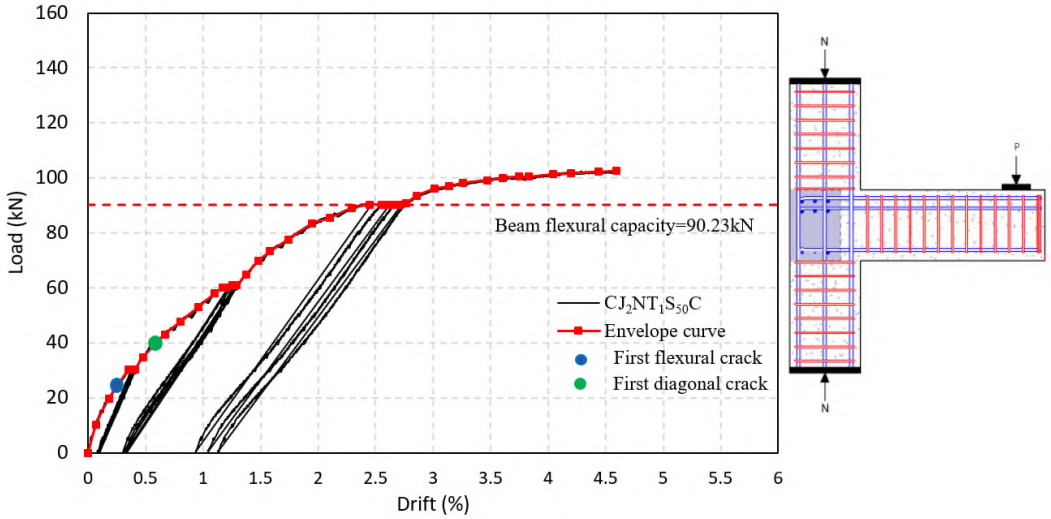

b) specimen $CJ_2NT_1S_{50}C$

Figure 4.25 Load-drift response of the tested specimens in group I; a) specimen $CJ_1NT_1S_{50}C$,and b) $CJ_2NT_1S_{50}C$.

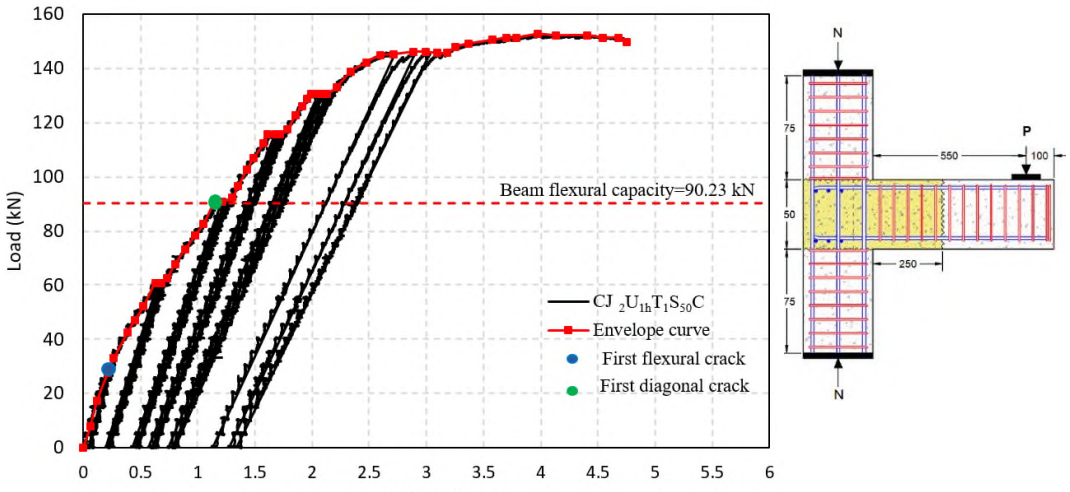

c) specimen $CJ_2U_{1h}T_1S_{50}C$

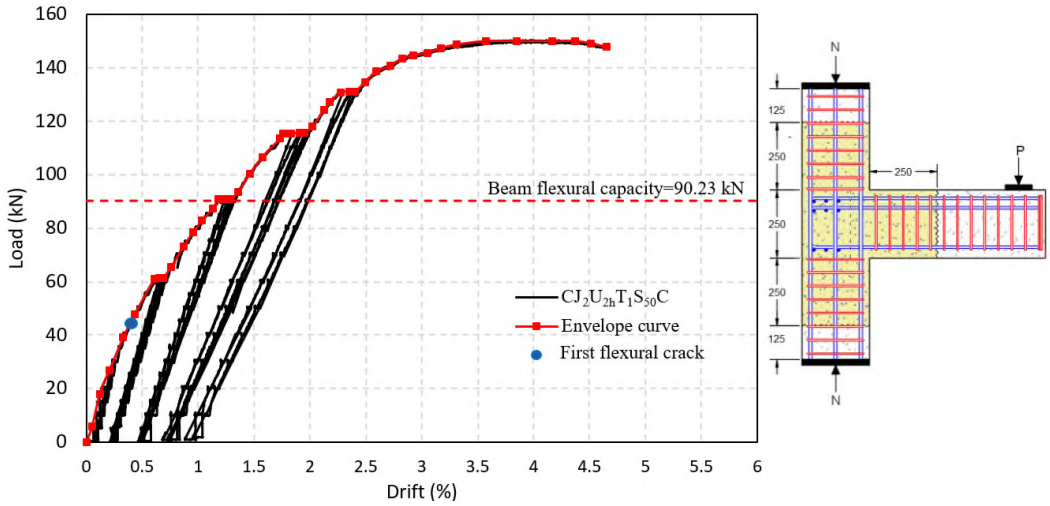

d) specimen $CJ_2U_{2h}T_1S_{50}C$

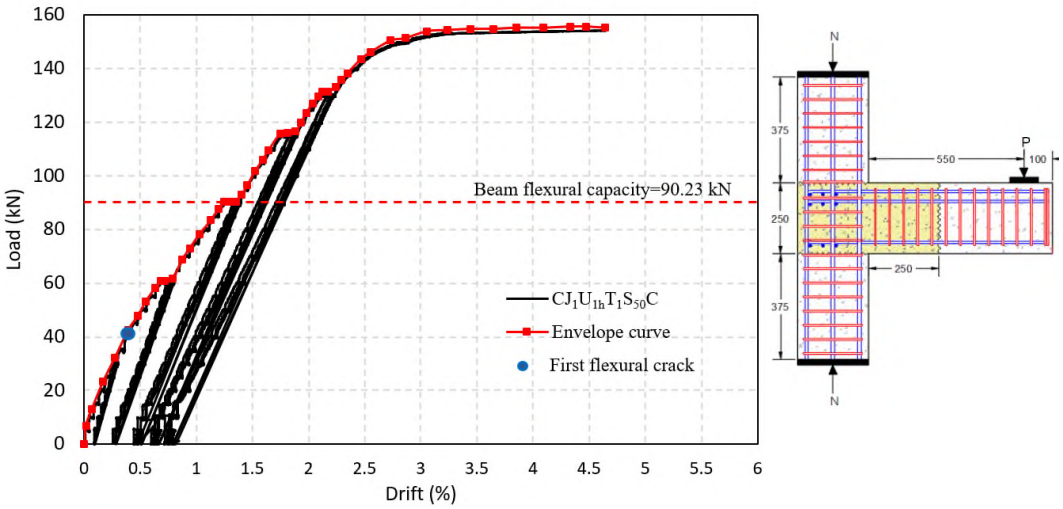

e) specimen $CJ_1U_{1h}T_1S_{50}C$

Figure 4.25 **continued**;c) specimen $CJ_2U_{1h}T_1S_{50}C$ d) specimen $CJ_2U2_hT_1S_{50}C$ and e) specimen $CJ_1U_{1h}T_1S_{50}C$.

The load-drift envelope of the specimens in this group, tested under compression cyclic load, is presented in Figure 4.26. It is evident that all UHPC joints exhibit similar behavior, indicating that the use of transverse reinforcement in the joint core, in addition to UHPC, does not significantly improve joint behavior. Furthermore, extending UHPC in the adjacent column and beams demonstrates behavior similar to the specimen that only extends UHPC in the adjacent beams. In addition, it is observed that transverse reinforcement in the joint core can be entirely eliminated without compromising the joint behavior.

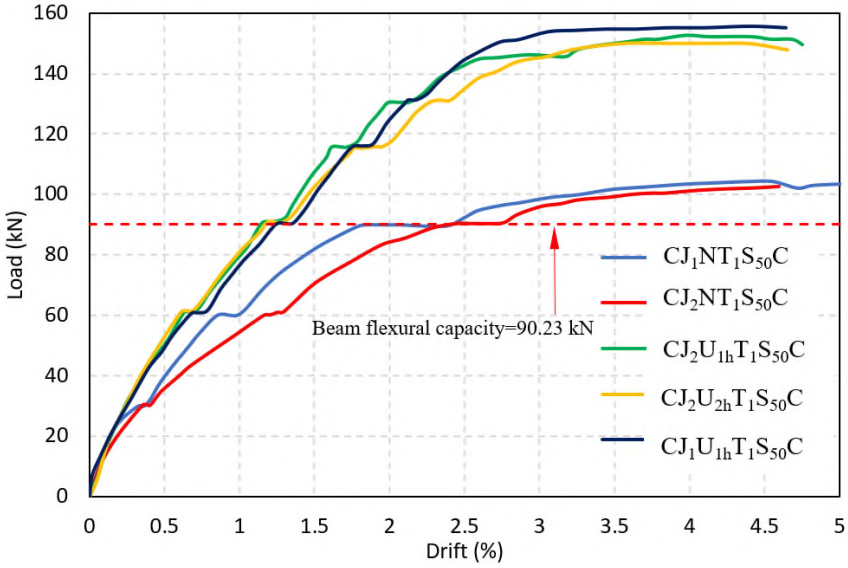

Figure 4.26 Load-drift envelopes curves for specimens tested under compression cyclic load in group I.

4.2.2.2 Load-drift response of group II tested under cyclic load

Figure 4.27 displays the load-drift response of the specimens in group II that were subjected to compression cyclic load testing. The NSC specimen exhibited stable behavior during the initial stage of loading. However, after the load step of 60 kN, the specimen experienced significant irreversible deformation due to the rapid development of shear cracks in both the joint and beam. At a drift ratio of approximately 2 %, the specimen lost its strength

and was unable to withstand additional loading cycles, as demonstrated in Figure 4.27 (a). This can be attributed to two factors: 1) reduction in confinement by increasing the spacing of transverse reinforcement in both beams and columns, and 2) omission of transverse reinforcement in the joint core. In contrast, the UHPC specimens exhibited stiffer behavior, less irreversible deformation, high load-carrying capacity, and a ductile failure mode, as shown in Figure 4.27 (b), (c).

Figure 4.28 displays the load-drift envelope curves of specimens in group II subjected to bidirectional compression cyclic load. The control specimen **$CJ_2NT_1S_{100}C$** is compared to UHPC specimens **$CJ_2U_{1h}T_1S_{100}C$** and **$CJ_2U_{2h}T_1S_{100}C$**. The results show that UHPC significantly increases the load carrying capacity, with ultimate load increases of approximately 28% and 42% for **$CJ_2U_{1h}T_1S_{100}C$** and **$CJ_2U_{2h}T_1S_{100}C$**, respectively, compared to the control specimen. Additionally, as illustrated in Figure 4.28, after the load reaches 90 kN, **$CJ_2U_{2h}T_1S_{100}C$** exhibits stiffer behavior and higher load carrying capacity than **$CJ_2U_{1h}T_1S_{100}C$**. This may be attributed to the confinement effect extending UHPC in columns both above and below the joint.

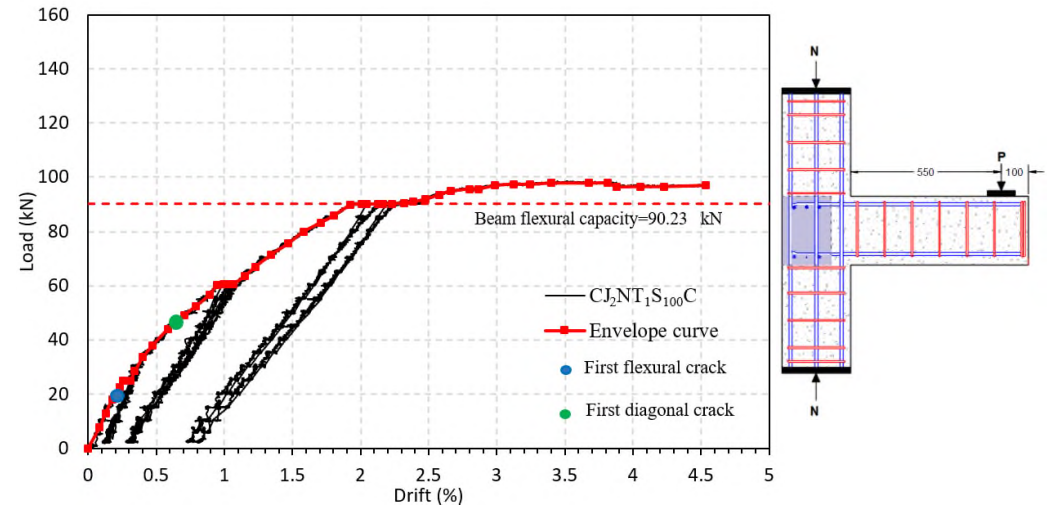

a) specimen $CJ_2NT_1S_{100}C$

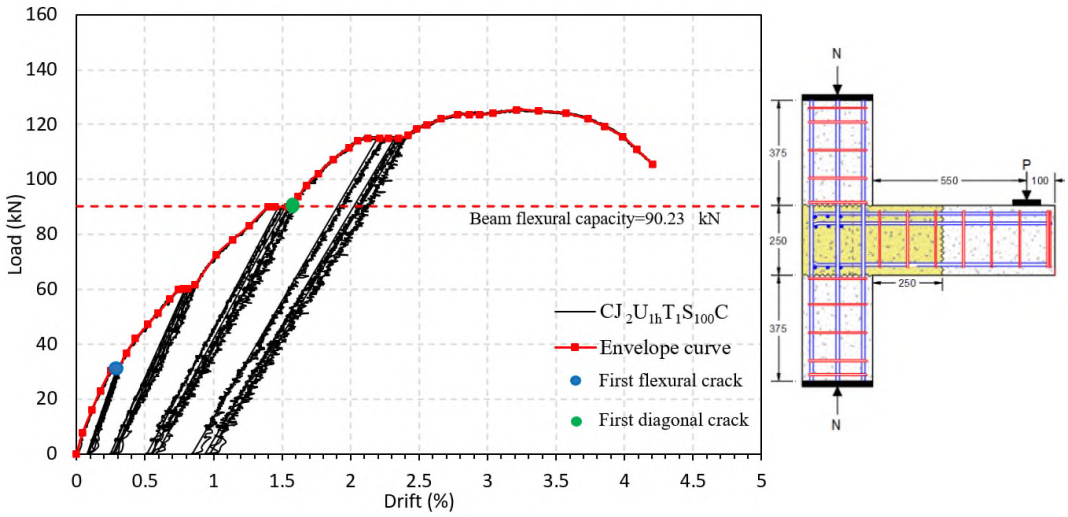

b) specimen $CJ_2U_{1h}T_1S_{100}C$

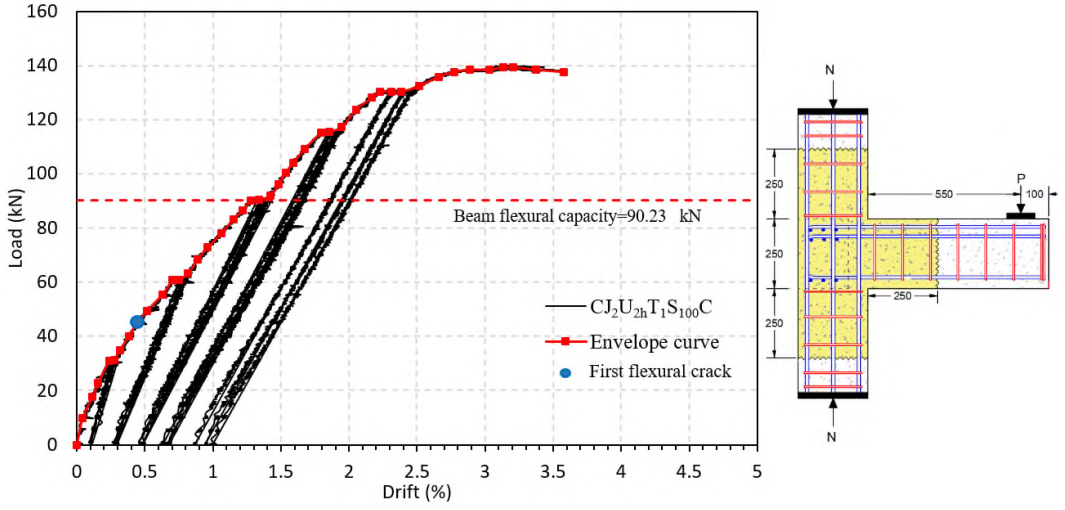

c) specimen $CJ_2U_{2h}T_1S_{100}C$

Figure 4.27 Load-drift response of the tested specimens in group II; a) specimen $CJ_2NT_1S_{100}C$, b) $CJ_2U_{1h}T_1S_{100}C$ and c) $CJ_2U_{2h}T_1S_{100}C$.

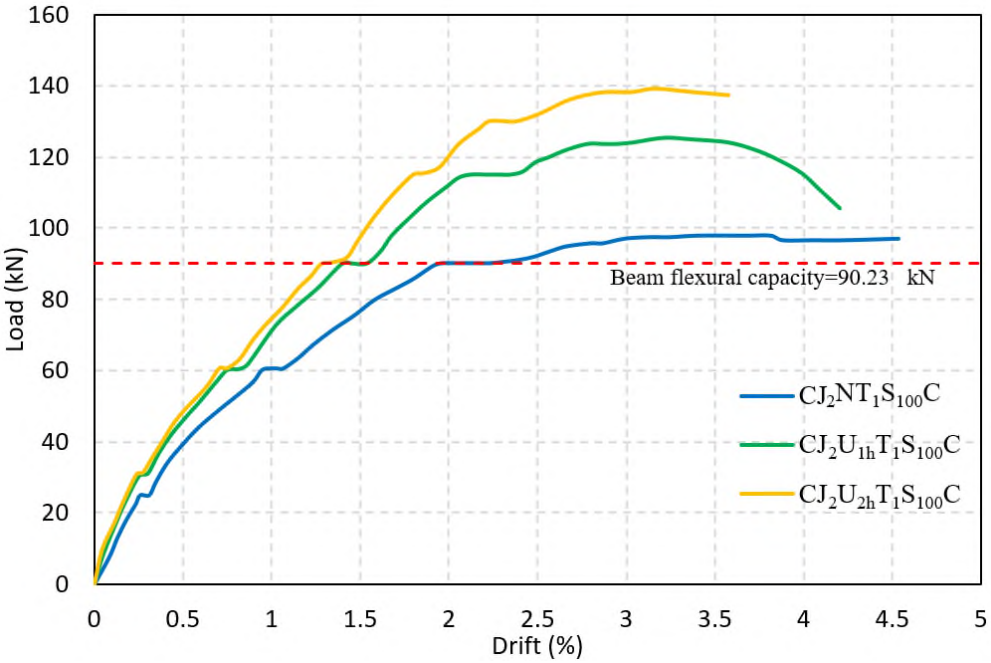

Figure 4.28 Load-drift envelopes curves for specimens tested under compression cyclic load in group II.

4.2.2.3 Load-drift response of group III tested under cyclic load

Figure 4.29 displays the cyclic response of RC corner beam-column joint that was rehabilitated using UHPC in the joint region in comparison to the control specimen made of NSC. It is evident that the UHPC joint exhibits superior performance compared to the NSC specimen. Although UHPC was primarily used in the joint core to enhance the failure mode and damage tolerance, the UHPC specimens show a considerable improvement in load-bearing capacity of approximately 45% for **$CJ_2U_{1c}T_1S_{50}C$** and 49.5% for **$CJ_2U_{1c}T_1S_{100}C$** compared to the corresponding control specimen. Moreover, the UHPC specimens display a more rigid behavior and less irreversible deformation. It is worth noting that casting the joint using a cold form method results in a cold joint at the UHPC-NSC interface. However, the specimens exhibit behavior that is identical to those cast using the hot method, as demonstrated in Figure 4.30. This is due to the effective casting procedure described in subsection 3.6 and the strong bond between UHPC and NSC.

Envelope curves for cold joints are shown in Figure 4.30, along with a comparison to hot joints with the same parameters. Based on the load-drift envelope, it is evident that the behavior of the hot and cold joints with close transverse reinforcement is similar. After a drift ratio of 1.5%, the **$CJ_2U_{1c}T_1S_{100}C$** specimen is more stiffer than the **$CJ_2U_{1h}T_1S_{100}C$** specimen. This may be because NSM steel bars were inserted to both sides of the beams to strengthen the connection between the old and new concrete. Finally, a plastic hinge formed at the joint-beam interface, leading to the same failure mechanism in all UHPC joint specimens.

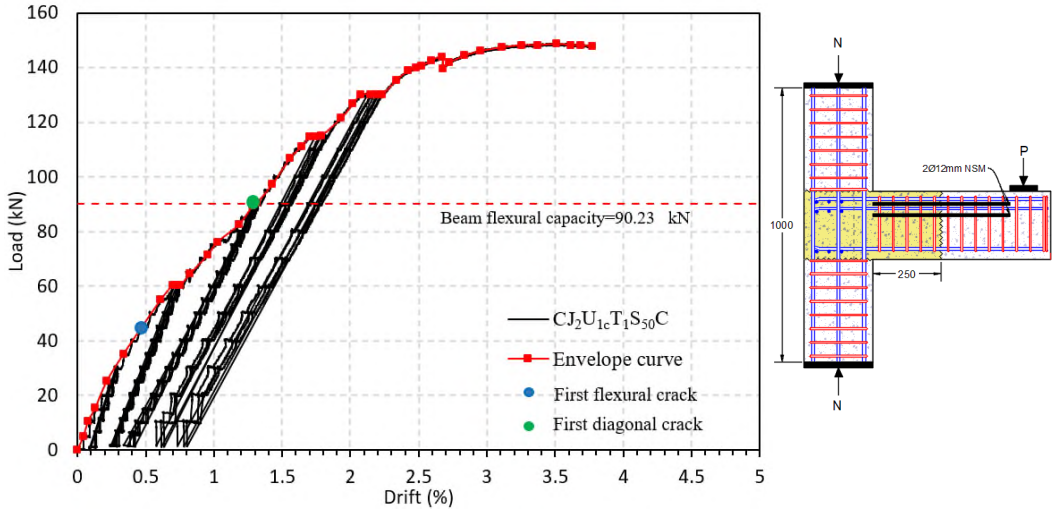

a) specimen $CJ_2U_{1c}T_1S_{50}C$

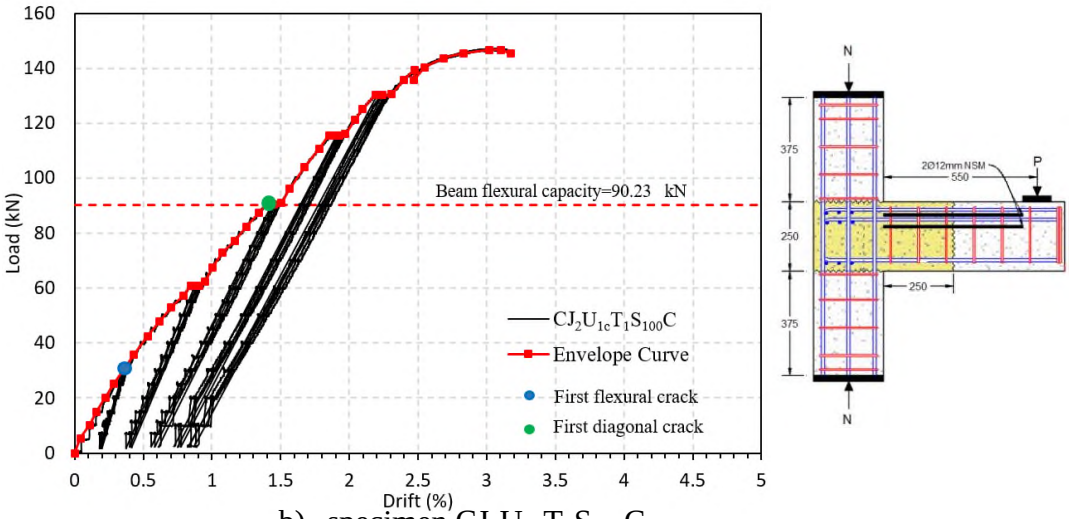

b) specimen $CJ_2U_{1c}T_1S_{100}C$

Figure 4.29 Load-drift response for cold joint specimens; a) specimen $CJ_2U_{1c}T_1S_{50}C$ and b) $CJ_2U_{1c}T_1S_{100}C$.

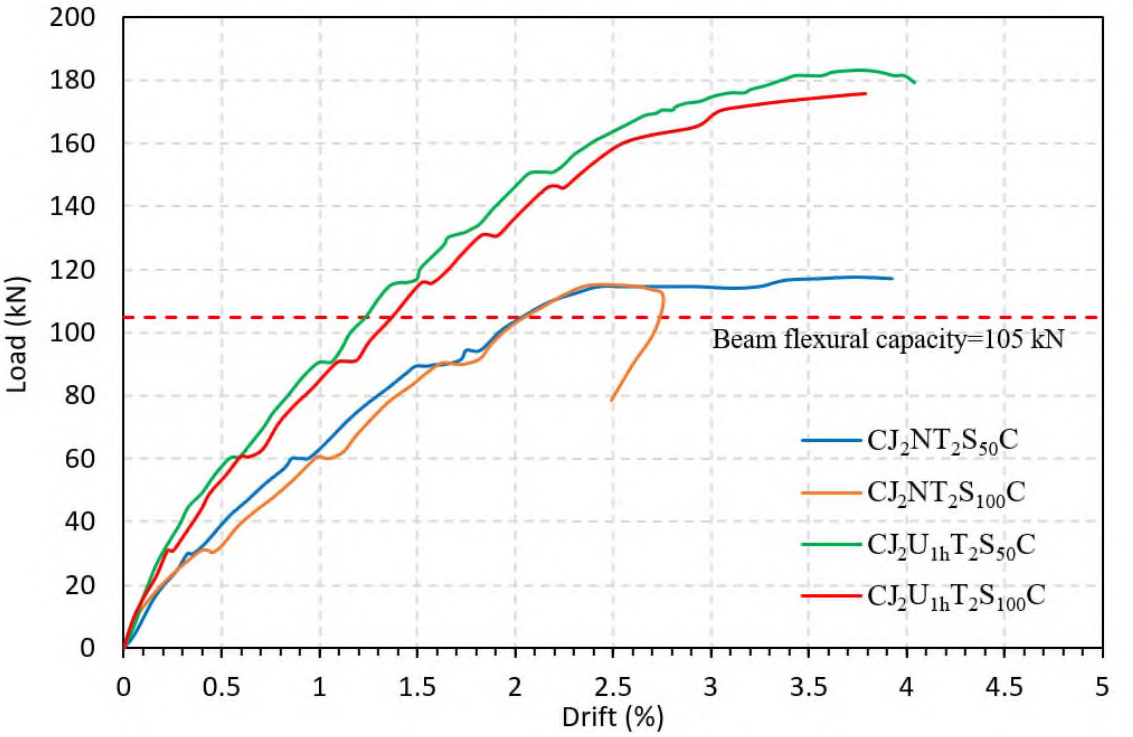

Figure 4.30 Compares the load-drift envelopes of cold joint and hot joint specimens.

4.2.2.4 Load-drift response of group IV tested under cyclic load

Figure 4.31 shows the load-drift response of the specimens in group IV. The NSC joint initially behaves stably but experiences large inelastic deformation after reaching a drift ratio of 1.5%. The NSC joint reinforced with transverse reinforcement spaced at 50 mm shows stiffer and more stable behavior than that reinforced with transverse reinforcement spaced at 100 mm. The specimen **$CJ_2NT_2S_{50}C$** failed at 118.1 kN after 12 compression cyclic loads, while the specimen **$CJ_2NT_2S_{100}C$** showed pinching at a load of 115.0 kN through the 10th cycle load. Both specimens ultimately failed due to spalling of concrete cover in the joint core, resulting from slipped beam longitudinal steel reinforcement and joint shear.

Figure 4.31 (c) and (d) indicate that the behavior of the UHPC joints differs from that of NSC joints. The UHPC specimens exhibit stable behavior with less inelastic deformation and no significant diagonal cracks, even though

the length of the steel longitudinal reinforcement passing through the joint core was 22% less than what is recommended in practical codes. Moreover, the joint core remains intact with no concrete spalling. The specimens **$CJ_2U_{1h}T_2S_{50}C$** and **$CJ_2U_{1h}T_2S_{100}C$** exhibit 54.8% and 52.2% higher load carrying capacity, respectively, compared to their corresponding NSC specimens. Ultimately, a plastic hinge forms at the joint-beam interface, leading to failure of the specimens.

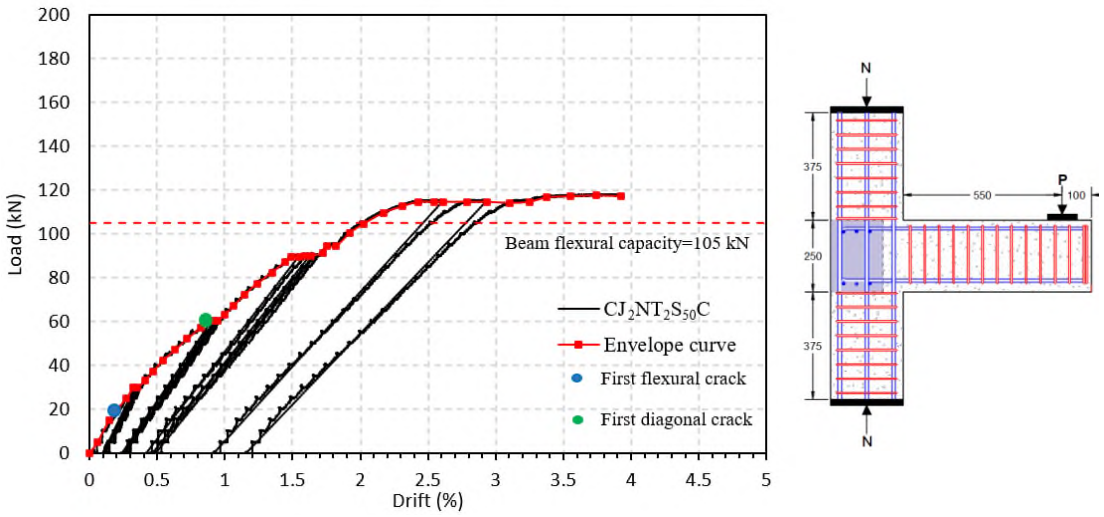

a) specimen $CJ_2NT_2S_{50}C$

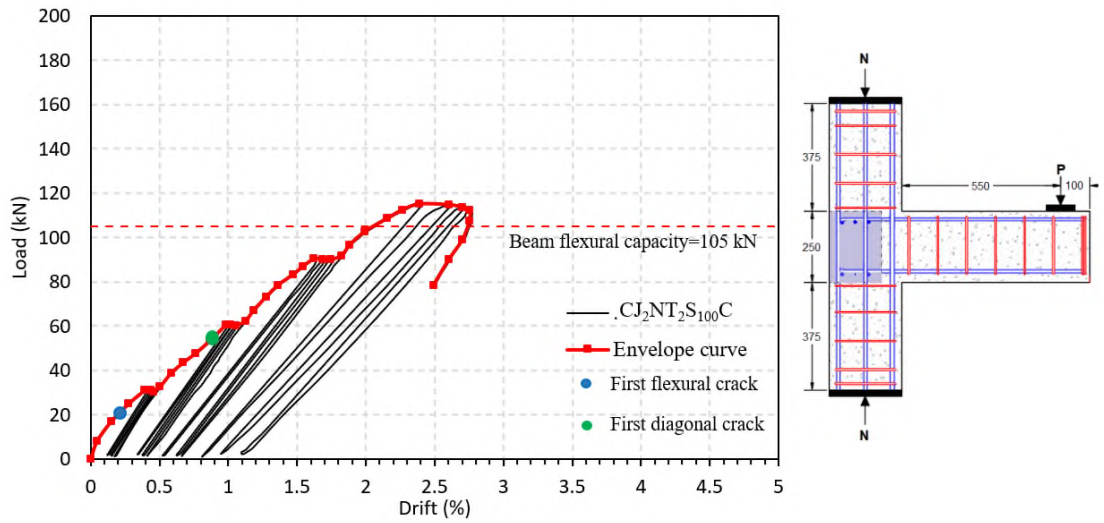

b) specimen $CJ_2NT_2S_{100}C$

Figure 4.31 Load-drift response of the tested joints in IV group; a) specimen $CJ_2NT_2S_{50}C$, and b) specimen $CJ_2NT_2S_{100}C$.

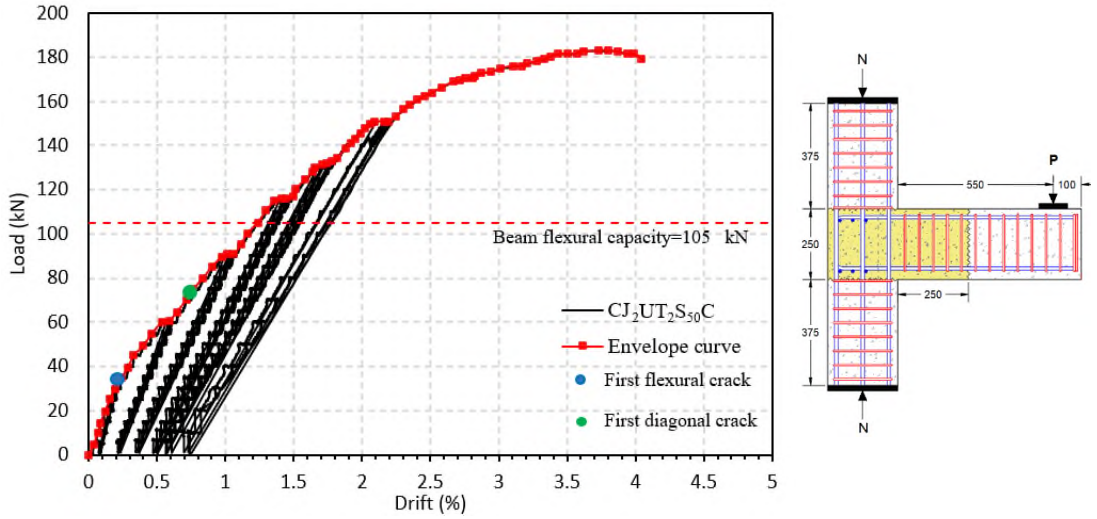

c) specimen $CJ_2U_{1h}T_2S_{50}C$

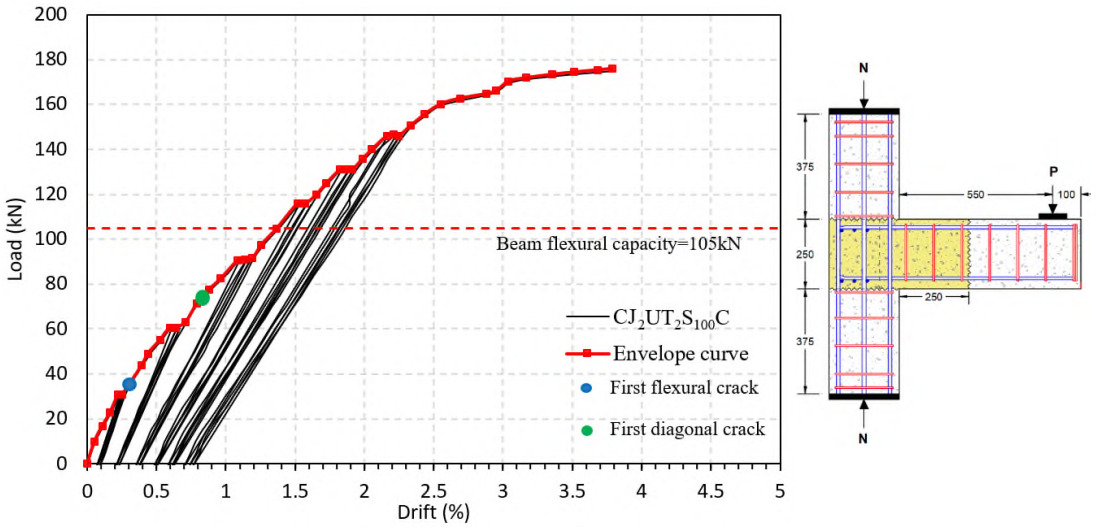

d) specimen $CJ_2U_{1h}T_2S_{50}C$

Figure 4.31 **continued**, c) specimen $CJ_2U_{1h}T_2S_{50}C$, and d) specimen $CJ_2U_{1h}T_2S_{100}C$.

Figure 4.32 present the envelopes curves for tested specimens in IV group. It is clear that the UHPC specimens show approximately similar behavior with slightly stiffer behavior for **$CJ_2U_{1h}T_2S_{50}C$**.

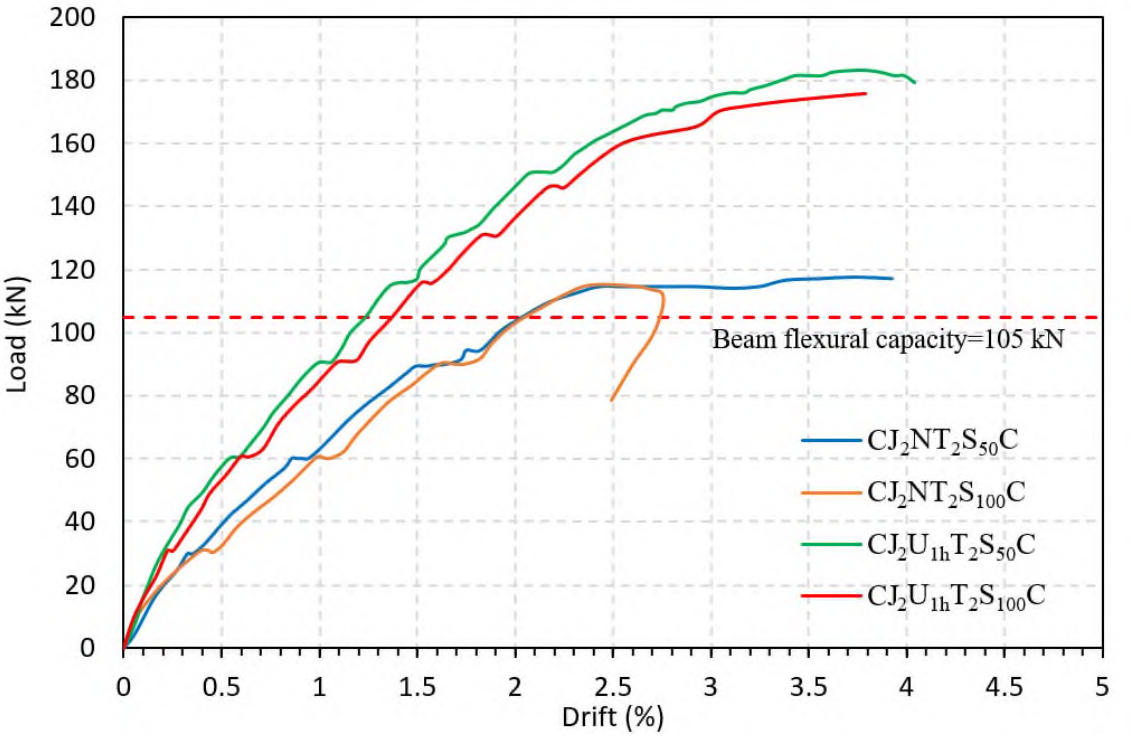

Figure 4.32 compares the load-drift envelopes of the tested specimens in group IV.

4.2.2.5 Load-drift response of group V tested under cyclic load

Figure 4.33 present the load-drift response of RC corner beam-column joint reinforced with hybrid reinforcement bars (50% steel bars with 50% GFRP bars). The specimen **$CJ_2NT_3S_{50}C$** shows poor behavior and large inelastic deformation. The specimen failed due to the pullout of the GFRP bars from the joint core at load level 81 kN in the seventh load cycle. In comparison, the specimen **$CJ_2NT_4S_{50}C$** shows stable behavior till load step 90 kN at an approximate drift ratio of 2.75%. After that, rapid diagonal cracks developed in the joint core causing large inelastic deformation, as shown in the load-drift response. Finally, the failure occurs due to joint shear crack at the 10th load cycle in a load equal to 115.4 kN, without observation slip of longitudinal GFRP bar. This may be attributable to the grooves' roughness, which helps to create a strong bond between the concrete and the composite made of epoxy resin and GFRP bar; thus, no slip was observed in specimen **$CJ_2NT_4S_{50}C$**.

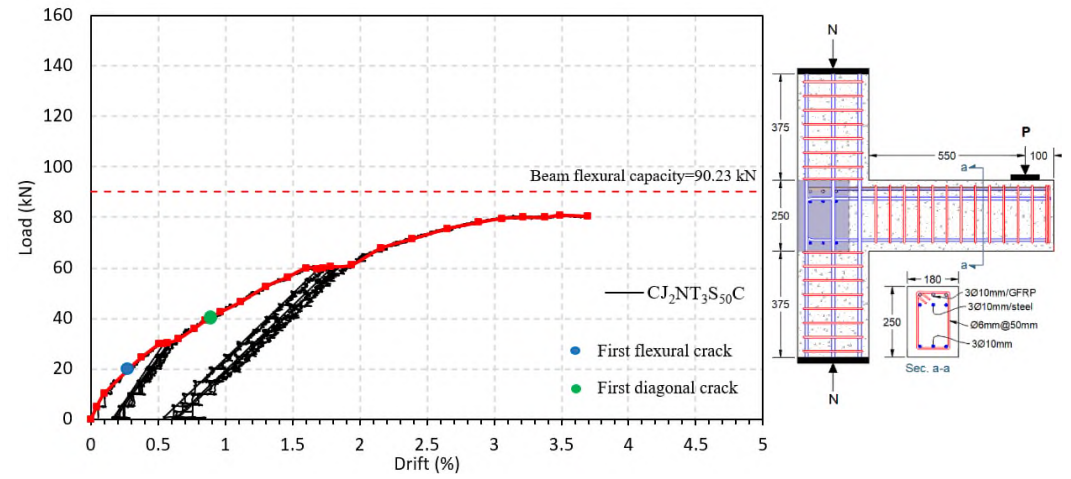

a) specimen $CJ_2NT_3S_{50}C$

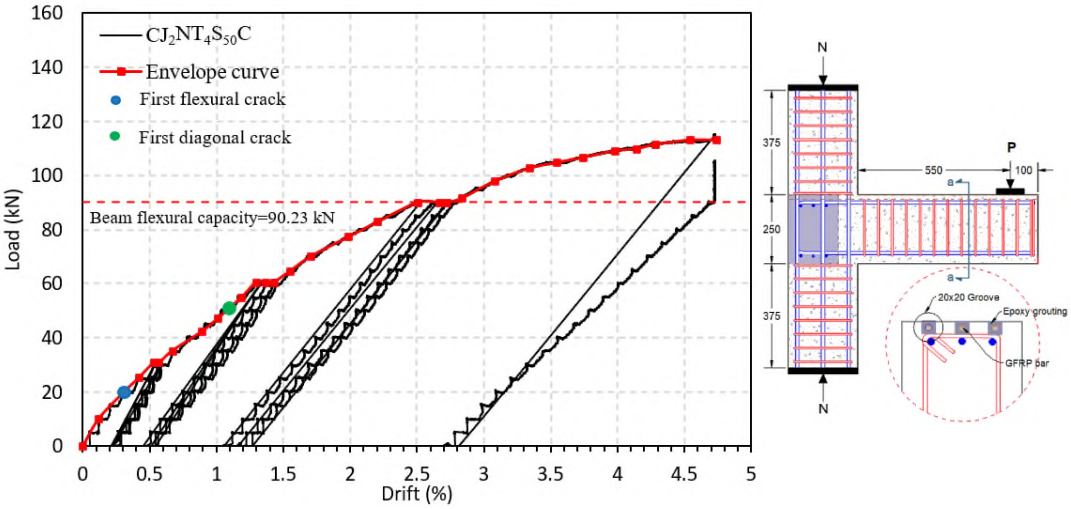

b) specimen $CJ_2NT_4S_{50}C$

Figure 4.33 Load-drift response of the tested specimens in group V; a) specimen $CJ_2NT_3S_{50}C$, and b) specimen $CJ_2NT_4S_{50}C$.

Finally, Figure 4.34 compares the envelope curves of the specimens that utilize hybrid beam longitudinal reinforcement with those that utilize regular steel reinforcement. One can note that the specimen **$CJ_2NT_3S_{50}C$** can't reach beam flexural capacity despite the high strength of the GFRP bar. Whereas the specimens **$CJ_2NT_4S_{50}C$** show load bearing capacity more than those reinforced by a deformed steel bar.

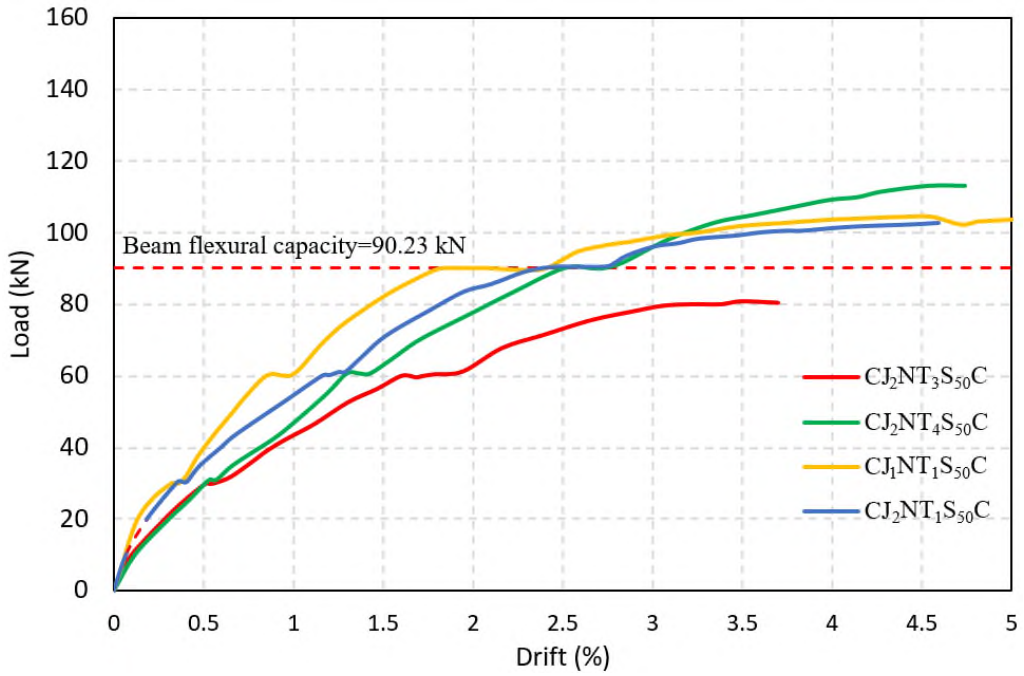

Figure 4.34 The envelope curves for the tested specimens in the V group compared to the control specimen.

4.2.3 Ductility of specimens tested under cyclic load

Ductility refers to the capability of a material or structure to experience significant deformation without losing its overall strength in crucial components. This quality indicates impending failure before it occurs and helps to decrease the demand for dynamic loads by enhancing energy dissipation [212], [213]. Ductile buildings have a higher level of resistance to sudden collapse because they can absorb a greater amount of the energy released during an earthquake.

For specimens that fail in shear, using the measure of energy dissipation or toughness is a more appropriate way to evaluate their ductility [214], [215]. The energy dissipation capacity of a structure is critical in reducing the impact of earthquake loads on the structure. The energy dissipated by an RC structure is a function of several factors, including the steel reinforcement, friction along existing cracks in concrete, and energy dissipated during the

formation of new cracks [216]. In the case of UHPC, the energy is also dissipated by steel fiber.

For the cyclic load, the area enclosed by a complete hysteretic loop at each cycle represents the energy dissipated by the specimen during the cycle. The cumulative hysteresis energy dissipation capacity is calculated by summating areas under the force-displacement hysteretic curve [217]. Since the cyclic load protocol used in the present study was compression cyclic load (not reverse cyclic load), thus the hysteretic loops are not interlocked. Therefore the cumulative energy dissipation calculated from the summation of each loop is very close to that calculated from envelop curve of the force-displacement hysteretic curve.

In the present study, the cumulative energy dissipation was calculated based on the area under the envelope of the force-displacement hysteretic curve.

4.2.3.1 Energy dissipation capacity of group I tested under cyclic load

Figure 4.35 presents the energy dissipation with respect to the drift ratio for the tested specimen under cyclic load. Utilizing the UHPC in the joint region significantly improves energy dissipation. The UHPC specimens (**$CJ_2U_{1h}T_1S_{50}C$**, **$CJ_2U_{2h}T_1S_{50}C$** and **$CJ_1U_{1h}T_1S_{50}C$**) show quite similar behavior despite the UHPC configuration and presence of transverse reinforcement in the joint core or not. The average energy dissipated by UHPC specimens at drift ratio of 2% is about 20% more than dissipated by **$CJ_1NT_1S_{50}C$** and about 37% more than by **$CJ_2NT_1S_{50}C$**. The increase becomes higher with proceeding the drift ratio; at a drift ratio of 4%, the dissipated energy by UHPC specimens is 40% compared to **$CJ_1NT_1S_{50}C$** and 50% compared with **$CJ_2NT_1S_{50}C$**.

At the ultimate load, the specimens **$CJ_2U_{1h}T_1S_{50}C$**, **$CJ_2U_{2h}T_1S_{50}C$** and **$CJ_1U_{1h}T_1S_{50}C$** show an increase of 47%, 35% and 40%, respectively,

compared to **$CJ_1NT_1S_{50}C$** and 54%, 42%, and 48% respectively, compared to **$CJ_2NT_1S_{50}C$**, as shown in Figure 4.36.

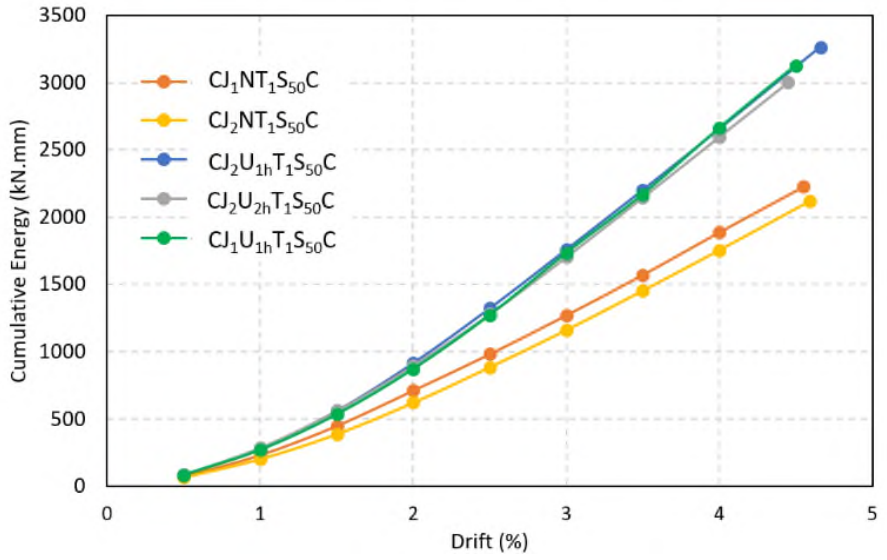

Figure 4.35 Cumulative dissipated energy with respect to drift ratio for the tested specimens in group I.

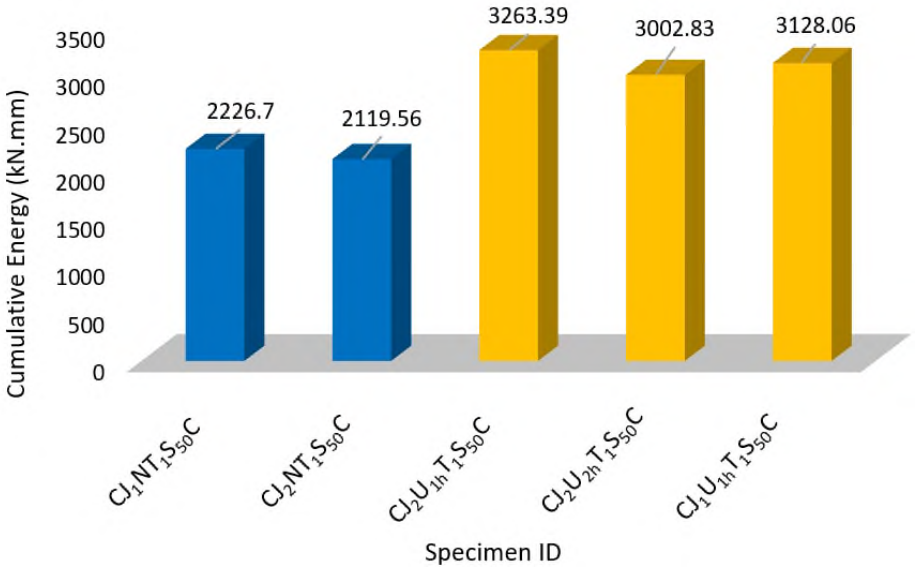

Figure 4.36 Cumulative energy of the tested specimens in group I at the ultimate load.

4.2.3.2 Energy dissipation capacity of group II tested under cyclic load

Figure 4.37 presents the dissipated energy with respect to the drift ratio for group II. Despite omitting the transverse reinforcement in the joint core and increasing the spacing of transverse reinforcement in adjoining members, using the UHPC in the joint region improves energy dissipation. Till drift ratio of 1.5%, the two UHPC specimens show an average increase of about 23% compared to NSC specimen. After that, as the drift ratio processing, the **$CJ_2U_{2h}T_1S_{100}C$** shows a higher increase in energy dissipation compared with **$CJ_2U_{1h}T_1S_{100}C$**. This may be due to extending the UHPC in the columns above and below the joint, compensating for the reduction in transverse reinforcement. At the ultimate load, the dissipated energy increased of 24% and 36% for specimens **$CJ_2U_{1h}T_1S_{100}C$** and **$CJ_2U_{2h}T_1S_{100}C$**, respectively, compared with **$CJ_2NT_1S_{100}C$**, as shown in Figure 4.38.

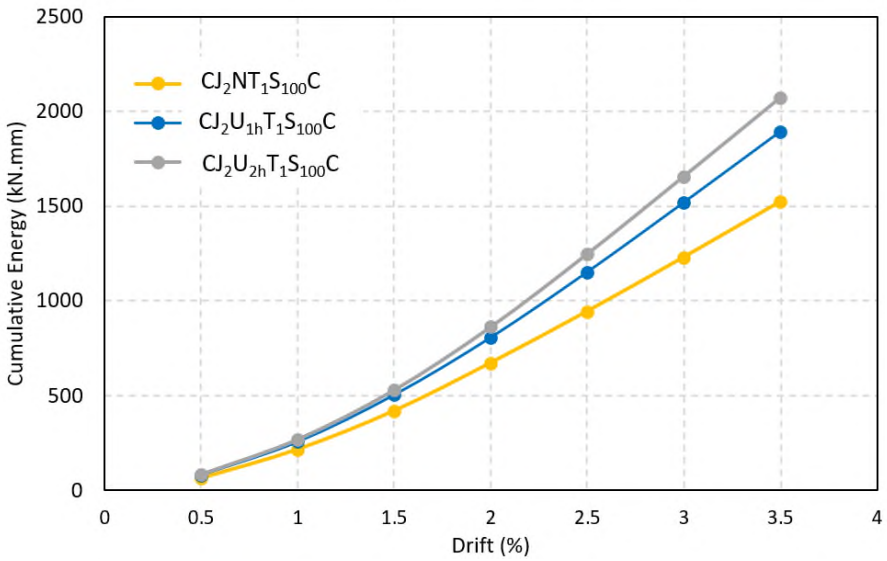

Figure 4.37 Cumulative dissipated with respect to drift ratio for the tested specimens in group II.

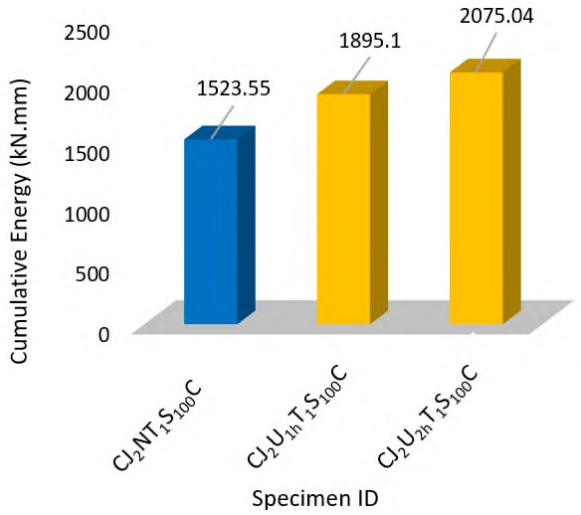

Figure 4.38 Cumulative energy of the tested specimens in group II at the ultimate load.

4.2.3.3 Energy dissipation capacity of group III tested under cyclic load

Figure 4.39 presents the energy dissipated by UHPC specimens cast in hot and cold methods. Compared to the hot joint, the dissipated energy by cold joints with respect to drift ratio are very close until the cold joint reaches the ultimate load. However, the hot joint shows more energy dissipation than the cold joint. Figure 4.40 shows the cumulative dissipated energy at the ultimate load. The specimen **$CJ_2U_{1c}T_1S_{50}C$** and **$CJ_2U_{1c}T_1S_{100}C$** shows an energy dissipation of 27% and 7% less than the corresponding hot joint.

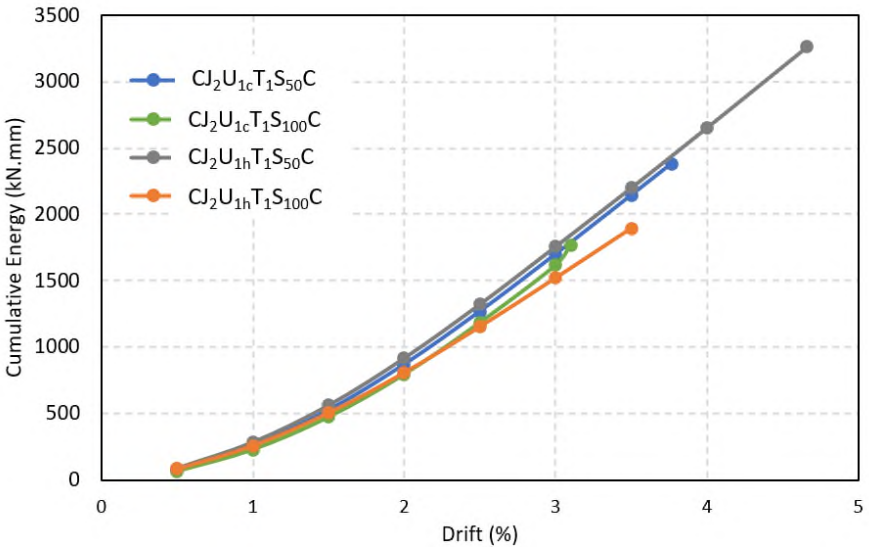

Figure 4.39 Cumulative dissipated with respect to drift ratio for the tested specimens in group III.

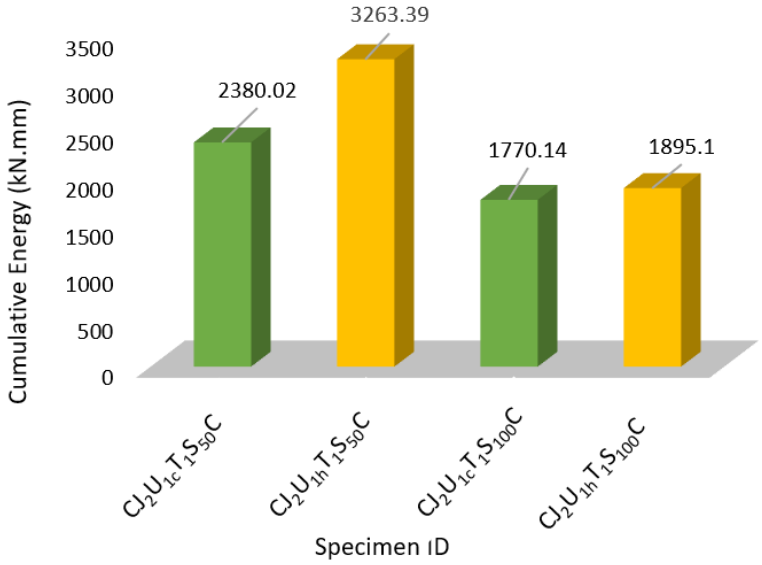

Figure 4.40 Cumulative energy of the tested specimens in group III at the ultimate load.

4.2.3.4 Energy dissipation capacity of group IV tested under cyclic load

Figure 4.41 presents the cumulative energy dissipation vs. drift ratio. The UHPC specimens show a significant improvement in energy dissipation. It is noted that for the same joint material, the dissipated energy improved as the transverse reinforcement increased for adjoining members. The specimen **$CJ_2NT_2S_{50}C$** dissipated energy 100% more than **$CJ_2NT_2S_{100}C$**, and **$CJ_2U_{1h}T_2S_{50}C$** dissipated energy 54% greater than **$CJ_2U_{1h}T_2S_{100}C$**.

Figure 4.42 illustrate the cumulative energy dissipation at the ultimate load. The specimens **$CJ_2U_{1h}T_2S_{50}C$** and **$CJ_2U_{1h}T_2S_{100}C$** show an increase in energy dissipation by about 103% and 163%, compared to **$CJ_2NT_2S_{50}C$** and **$CJ_2NT_2S_{100}C$**, respectively. Using the UHPC improves the energy absorbed due to the confinement effect, bond strength and shear resistance of the UHPC.

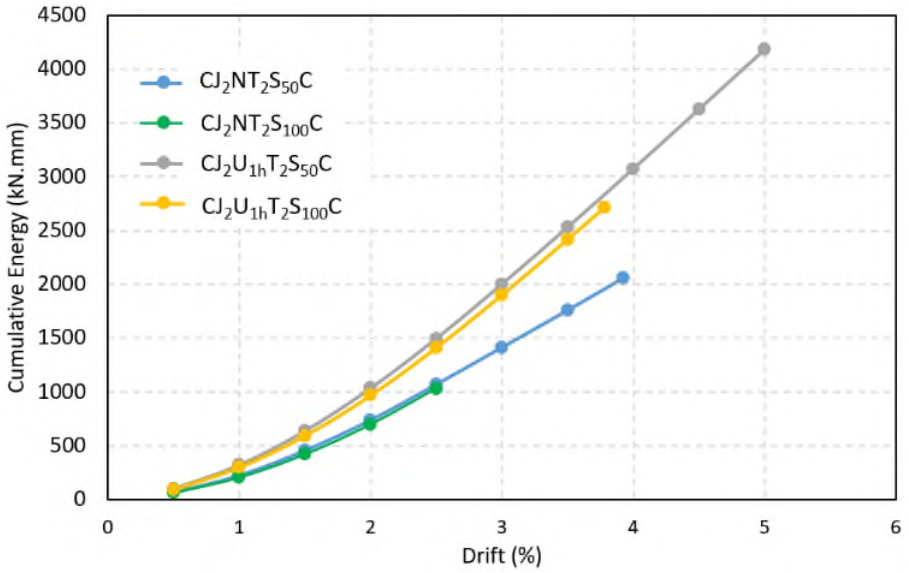

Figure 4.41 Cumulative dissipated with respect to drift ratio for the tested specimens in group IV.

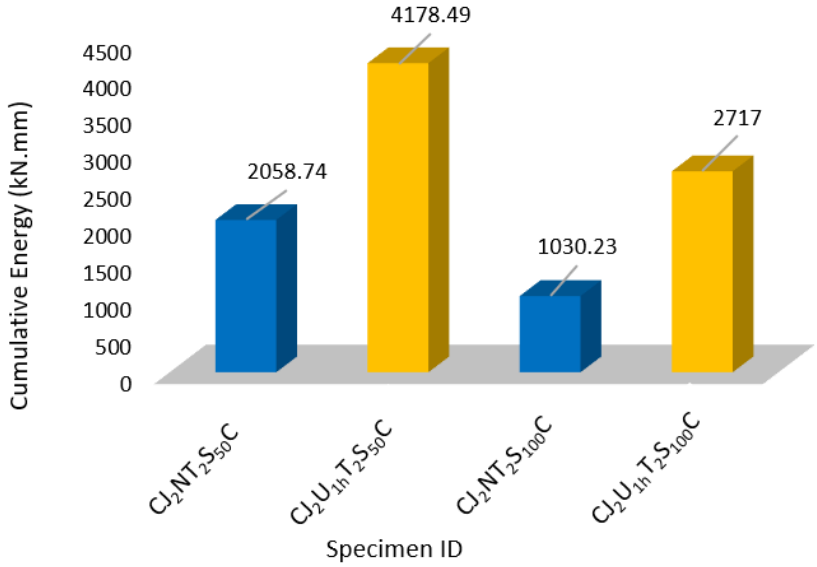

Figure 4.42 Cumulative energy of the tested specimens in group IV at the ultimate load.

4.2.3.5 Energy dissipation capacity of group V tested under cyclic load

It is clear from Figure 4.43 that the specimen **$CJ_2NT_3S_{50}C$** shows poor energy dissipation due to slippage of the GFRP bar before it reaches its strength capacity. On the other hand, the specimen **$CJ_2NT_4S_{50}C$** shows better behavior than **$CJ_2NT_3S_{50}C$**. At a drift ratio of 1%, both GFRP specimens show similar behavior and dissipated energy of 31% less than the

control specimen (**$CJ_1NT_1S_{50}C$**). Through proceeding the drift ratio, the specimen $CJ_2NT_4S_{50}C$ shows a constant decrease in energy absorption of 30% compared with the control specimen.

Figure 4.44 presents the energy dissipation of the tested specimens in group V at the ultimate load compared with those reinforced by steel bars. The specimen **$CJ_2NT_3S_{50}C$** and **$CJ_2NT_4S_{50}C$** show energy dissipation of 48% and 2% less than the control specimen.

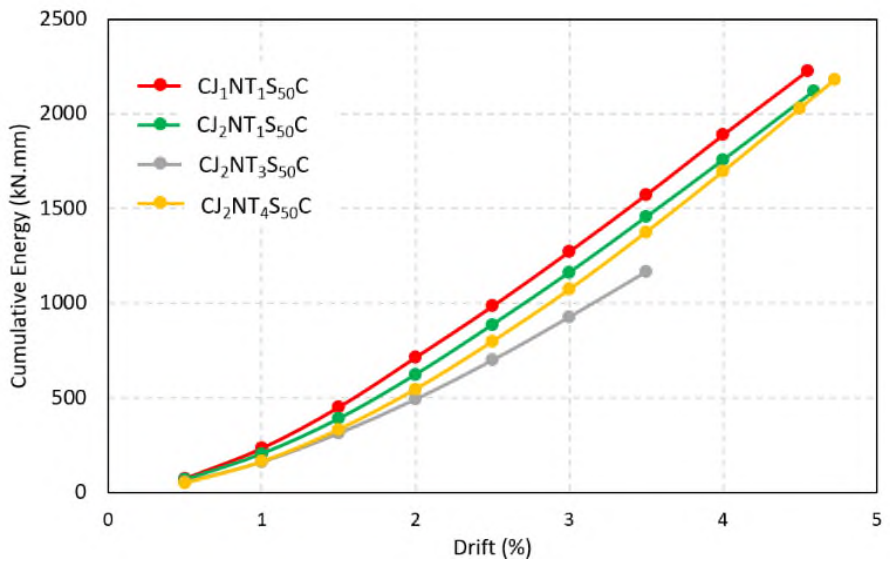

Figure 4.43 Cumulative dissipated with respect to drift ratio for the tested specimens in group V compared with that reinforced by steel bar.

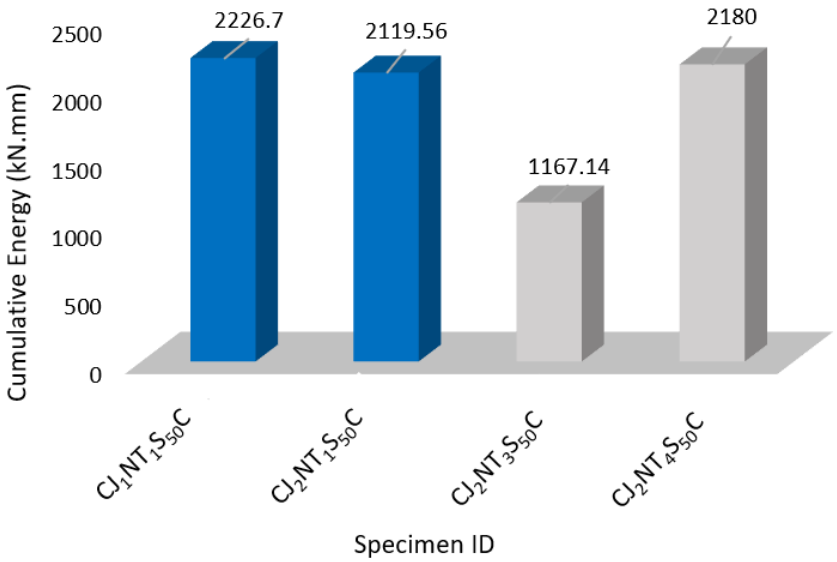

Figure 4.44 Cumulative energy of the tested specimens in group V at the ultimate load.

Figure 4.45 present the summary of energy absorbed by the tested specimens under cyclic load. Although the UHPC can compensate for the effect of increasing the spacing of transverse reinforcement in adjoining members, It is clear that transverse reinforcement had a significant effect on the absorbed energy beam-column joint.

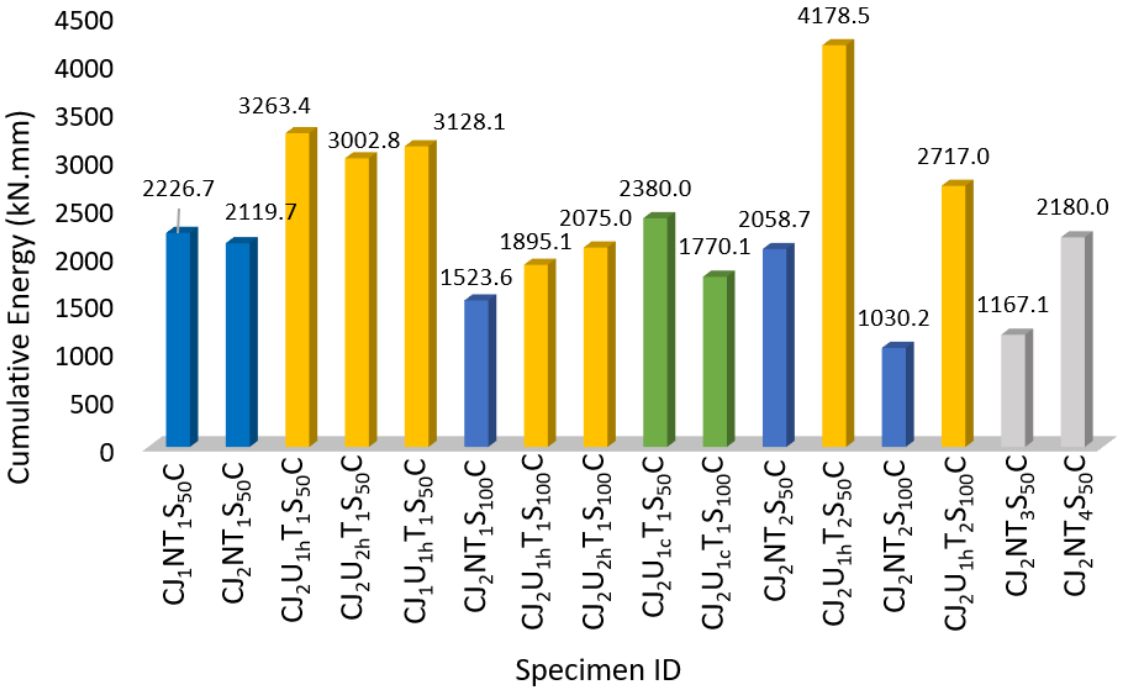

Figure 4.45 The energy absorbed by the tested specimens under cyclic load.

4.2.4 Stiffness

In the present study, the initial stiffness was used to evaluate the stiffness of the beam-column joint. The initial stiffness (K_i) is estimated by using the secant of the load-displacement envelope curve passing through the point at which the applied force reaches 75% of the ultimate load to the corresponding displacement, as shown in Figure 4.46 [215]. Thus, the initial stiffness can be calculated as follows:

$$K_i = \frac{0.75Pu}{\Delta_i} \qquad \text{.....4.1}$$

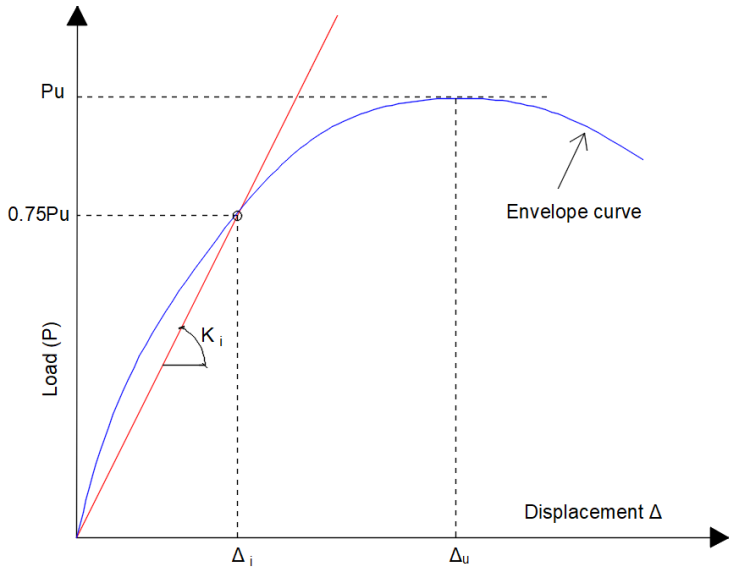

Figure 4.46 Determination of the initial stiffness[218].

4.2.4.1 The stiffness of group I tested under cyclic load

The total elimination of transverse reinforcement from the joint core (**$CJ_2NT_1S_{50}C$**) decreases the initial stiffness by about 23% compared to specimen **$CJ_1NT_1S_{50}C$**. This is due to the development and propagation of the cracks at early stage in the joint core as a result of omitting the transverse reinforcement from the joint core.

In addition to changing the failure mode to ductile failure through the formation of a plastic hinge at the joint-beam interface, reducing the damage tolerance and improving the load carrying capacity, utilizing the UHPC in the joint region improve the stiffness of the beam-column joint significantly. The initial stiffness of specimens **$CJ_2U_{1h}T_1S_{50}C$**, **$CJ_2U_{2h}T_1S_{50}C$** and **$CJ_1U_{1h}T_1S_{50}C$** were higher than **$CJ_1NT_1S_{50}C$** by about 21%, 14 and 22%, respectively. Moreover, these specimens were higher than **$CJ_2NT_1S_{50}C$** by about 56%, 47%, and 58%, respectively, as shown in Figure 4.47. This improvement is due to the superior performance of UHPC.

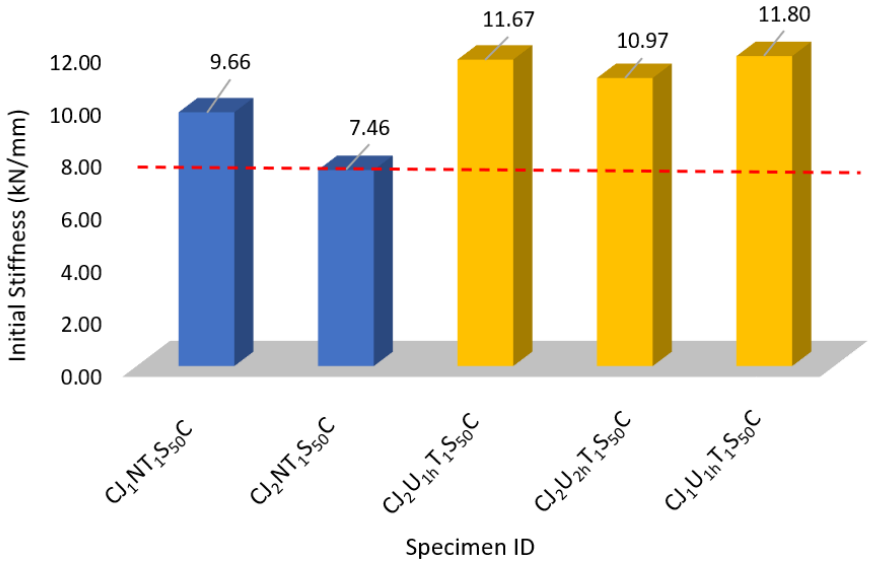

Figure 4.47 The initial stiffness of the tested specimens in group I.

4.2.4.2 The stiffness of group II tested under cyclic load

Figure 4.48 present the stiffness of tested specimens. The initial stiffness of these UHPC specimens were improved compared with corresponding NSC by about 11% and 25%, respectively.

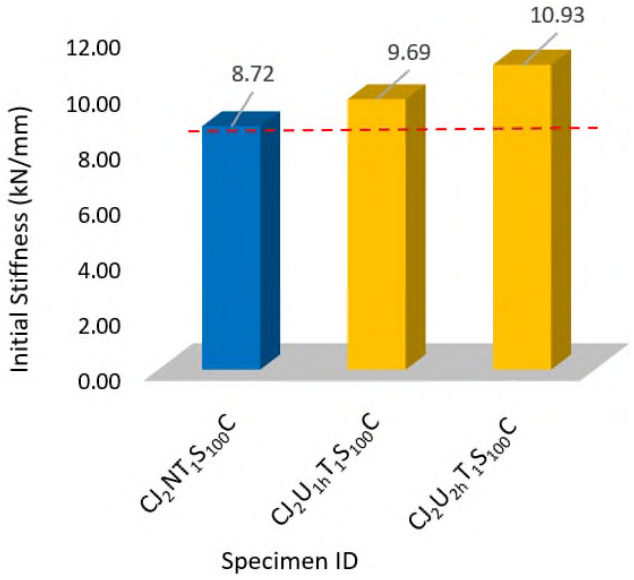

Figure 4.48 The stiffness of the tested specimens in group II.

4.2.4.3 The stiffness of group III tested under cyclic load

In this group, the cold joint's stiffness is measured and compared to that of its hot joint. Figure 4.49 demonstrates that the stiffness of both the hot and cold joints are comparable, providing assurance that the procedure used in the current investigation to remove and replace the joint region is effective.

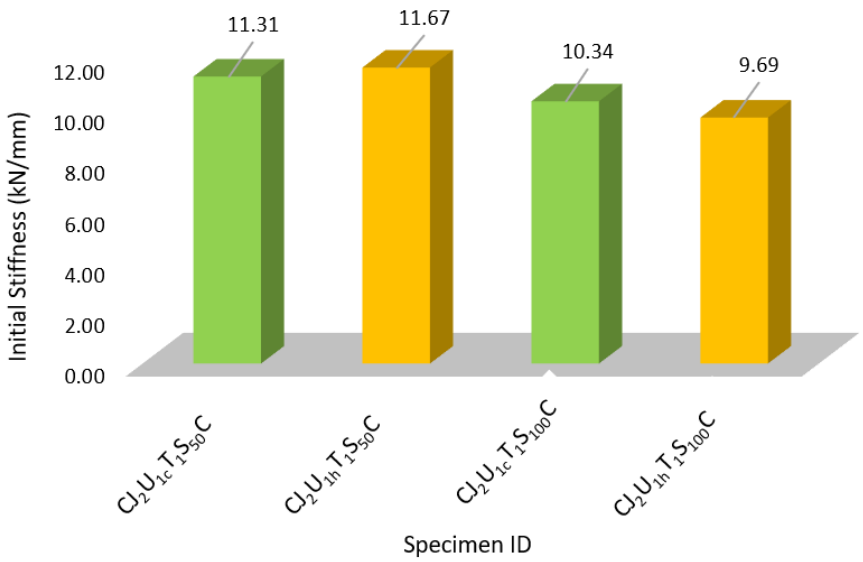

Figure 4.49 The initial stiffness of the tested specimens in group III.

4.2.4.4 The stiffness of group IV tested under cyclic load

Figure 4.50 present the initial stiffness of the tested specimens in this group. In addition to changing the failure mode to ductile failure regardless of the spacing of transverse reinforcement, omitting the transverse reinforcement from the joint core and decreasing the embedded length of beam longitudinal bar through the joint core, using the UHPC in the joint region improves the initial stiffness by about 17%.

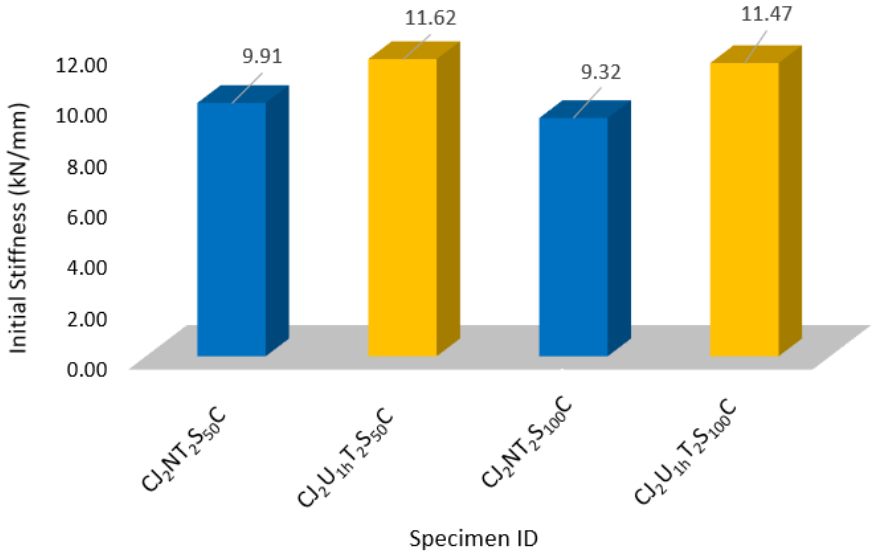

Figure 4.50 The initial stiffness of the tested specimens in group IV.

4.2.4.5 The stiffness of group V tested under cyclic load

The stiffness of the tested specimens in this group compared with those reinforced by traditional reinforcement. As shown in Figure 4.51, the initial stiffness of the GFRP specimens shows initial stiffness less than those reinforced by a steel bar. This may be due to the modules of elasticity of GFRP less than of steel bar.

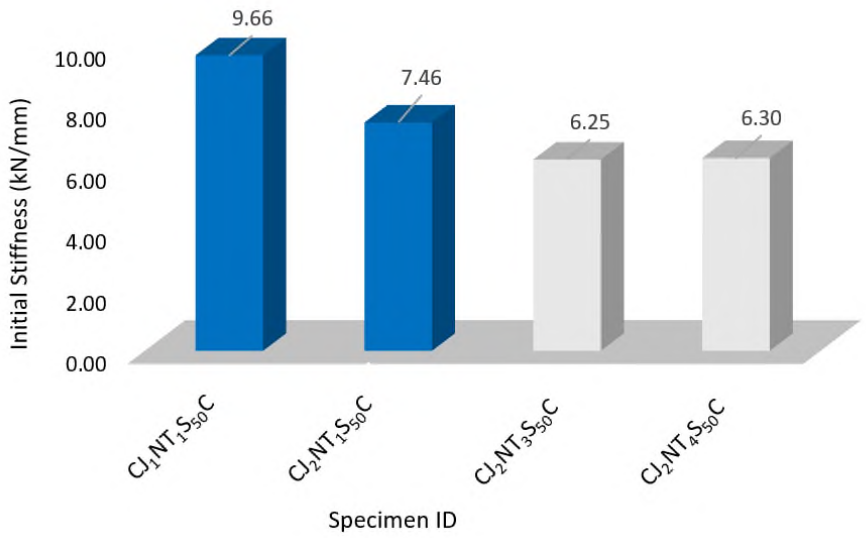

Figure 4.51 The stiffness of the tested specimens in group V.

Figure 4.52 summarises the initial stiffness of the tested specimens under cyclic load. It is clear that utilising UHPC in the joint region improve the behavior of beam-column joints in term of initial stiffness. However, duplicate the spacing of transverse reinforcement in adjoining members had a slight effect on the initial stiffness.

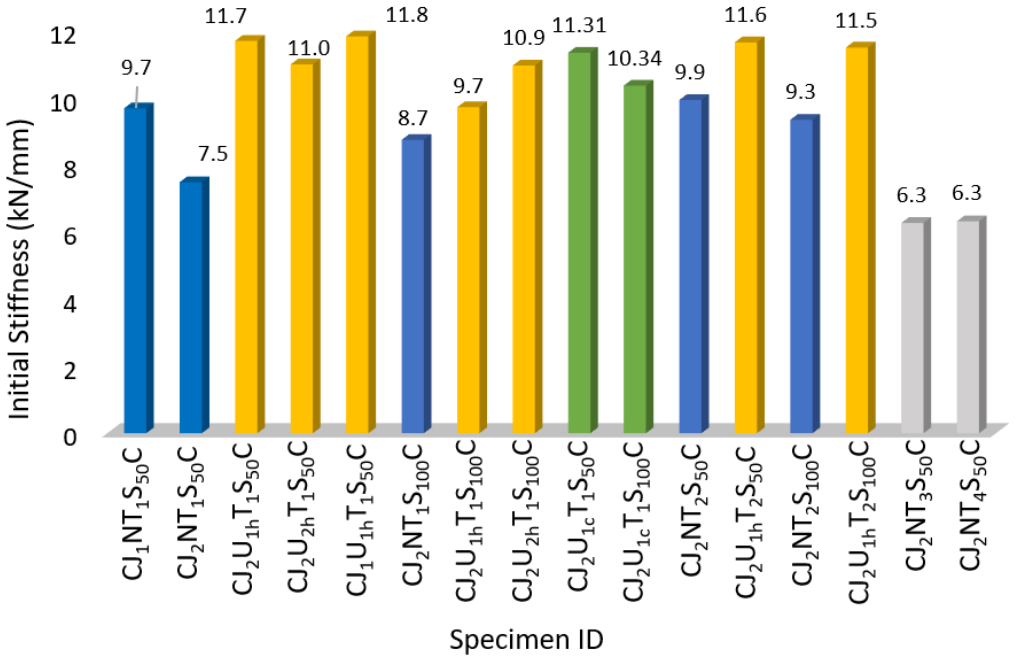

Figure 4.52 The initial stiffness evaluated from the tested specimens under cyclic load.

4.2.5 Joint principle stresses for the specimens that tested under cyclic load

The diagonal cracks in the joint core occur when the principal tension stress reaches the concrete tensile strength ($f_{t\text{-}max}$), indicating that the joint shear failure is a function of ($f_{t\text{-}max.}$) [175]. It should be noted that principal stresses are calculated from Eq. 4.2 according to Mohr circle principal, using normal and shear stresses. When the shear stress in the joint induces tensile stresses higher than $f_{t\text{-}max}$, cracking occurs in the joint. Based on the Mohr circle principle [219], the principle tensile and compressive stress at the mid-depth of the joint core is given by Eq.4.2:

$$\sigma_{1,2} = \frac{\sigma_x+\sigma_y}{2} \pm \sqrt{\left(\frac{\sigma_x-\sigma_y}{2}\right)^2 + (\tau_{xy})^2} \quad \text{.....4.2}$$

Where: σ_1= principle tensile stress (f_t), σ_2 = principle compressive stress (f_c), and σ_x= 0. While the normal axial compressive stresses on the column (σ_y) at the mid-hight of the joint core can be written as in Eq.4.3.

$$\sigma_y = \sigma_N = \frac{N}{h_c \times b_c} \quad \text{.....4.3}$$

Where N = axial load on column; h_c= total depth of column as illustrated in Figure 4.53, and b_c= total width of the column.

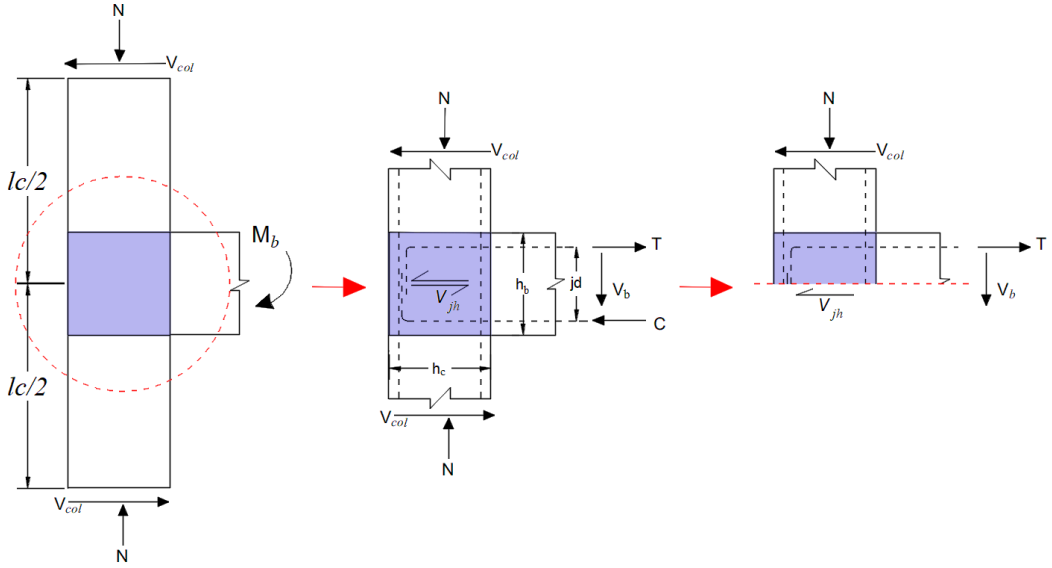

Figure 4.53 Free body diagram of the joint region.

Figure 4.53 illustrates the force acting on the joint and its free body diagram. The horizontal joint shear force (V_{jh}) can be estimated based on the equilibrium condition of a free body diagram at the mid-height of the joint [64], as shown in Figure 4.53. The shear strength can be calculated using Eq. 4.4.

$$V_{jh} = T - V_{col.} \quad \text{.....4.4}$$

Where T = tensile forces developed by longitudinal reinforcements of beams, and $V_{col.}$ = the column shear force.

The tensile forces developed in longitudinal reinforcement of the beam are calculated from the actual moment at the joint-beam interface, as follows:

$$M_b = T\ jd \quad \rightarrow \quad T = M_b/jd \qquad \text{.....4.5}$$

After that, the shear force in the column can be written as in Eq.4.6.

$$V_{col.} = M_b/l_c \qquad \text{.....4.6}$$

Sub. Eq.4.5 and Eq.4.6 in Eq.4.4 to get the joint shear force, as in Eq.4.7.

$$V_{jh} = \frac{M_b}{jd} - \frac{M_b}{l_c} \qquad \text{.....4.7}$$

Where: jd= the lever arm between the tensile force and centroid of compression force, and l_c= total length of the column.

The horizontal joint shear stress is then calculated by dividing the horizontal joint shear force to the joint area, as in Eq. 4.8.

$$\tau_{xy} = \tau_{jh} = \frac{V_{jh}}{h_c \times b_j} \qquad \text{.....4.8}$$

Where: b_j is the width of the joint, it is calculated based on ACI-ASCE 352 [16]. Then, the principle stresses at the mid-hight of the join can be written as shown in Eq. 4.19. Noting that The negative sign refers to compressive stress.

$$\sigma_1 = \frac{-\sigma_N}{2} + \sqrt{\left(\frac{\sigma_N}{2}\right)^2 + \left(\tau_{jh}\right)^2} \ , and \quad \sigma_2 = \frac{-\sigma_N}{2} - \sqrt{\left(\frac{\sigma_N}{2}\right)^2 + \left(\tau_{jh}\right)^2} \qquad \text{.....4.9}$$

Figure 4.54 illustrates the load condition, internal stresses, and principal stresses developed in the joint core.

Figure 4.55 plots the maximum principal tensile stress induced at the joint mid-height calculated based on the above methodology, for the fourteen specimens tested under cyclic load. In the figure, the dashed lines represent the maximum tensile strengths ($f_{t\text{-}max}$) for both materials. $f_{t\text{-}max}$ for NSC was

estimated as 85% of the splitting tensile strength as recommended by Mehata [202], while $f_{t\text{-}max}$ for UHPC was evaluated by direct tensile test mentioned in previous sections.

The max. Principal tensile stresses in the NSC joints exceeds the $f_{t\text{-}max}$ of NSC, explaining their sudden collapse with diagonal joint cracks. In contrast, the max. principal tensile stresses for UHPC joints were less than the $f_{t\text{-}max}$ of UHPC, reflecting the test observations where the specimens failed in a ductile manner without developing any significant joint diagonal cracks, which means that the joints can carry double the applied load in the joint to reach the failure.

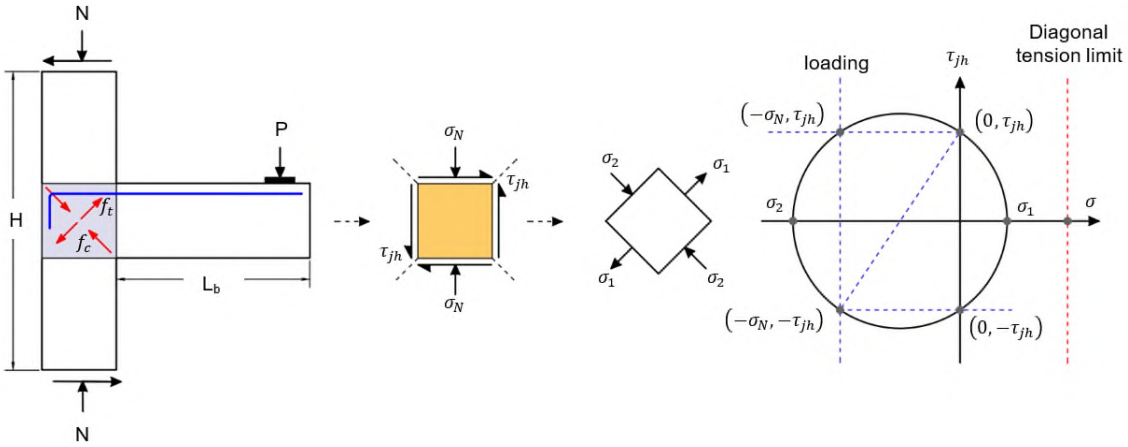

Figure 4.54 Principle stresses at mid-hight of the joint.

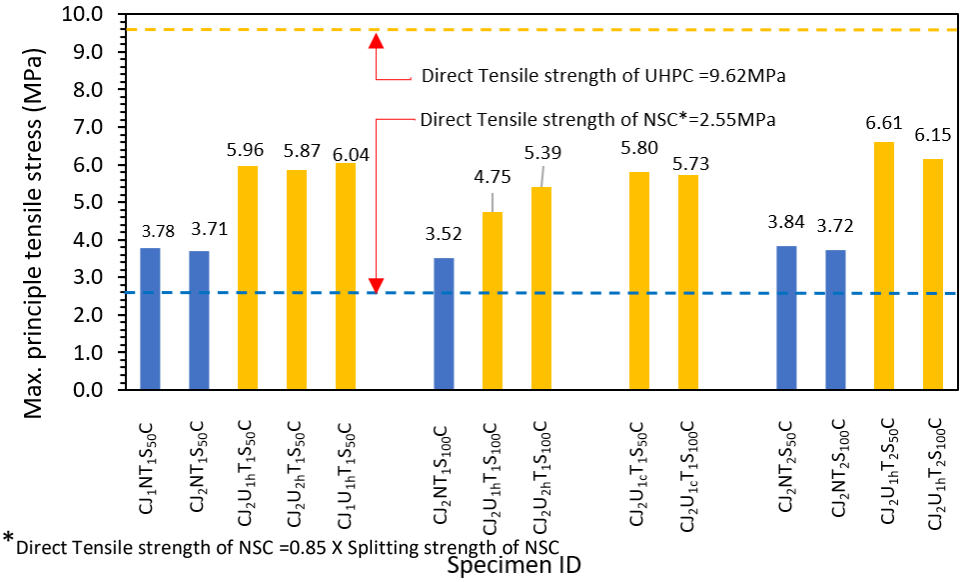

Figure 4.55 Comparison of maximum principal tensile stress induced in joint with the tensile strength of concrete.

Despite the specimen $CJ_1NT_1S_{50}C$ reinforced with seismic details, the maximum shear stress developed in the joint core was 4.83 MPa, corresponding to $0.79\sqrt{f_c`}$ , which is less than the ACI allowable limit ($1.0\sqrt{f_c`}$). At this stage, the tensile stress developed in the joint core (3.78 MPa) was higher than the tensile strength of NSC (2.55MPa), resulting in severe damage in the joint core. The unconfined NSC joint show approximately similar behavior. However, the diagonal cracks and damage were more severe than the confined joint, making the shear failure control the failure mode of the unconfined NSC specimens.

4.2.6 Joint shear strength of tested specimens under cyclic load

The utilization of UHPC in the joint region not only changes the failure mechanism to ductile failure but also leads to a notable improvement in the joint shear strength of groups I, II, and III. The joint shear strength of group I is observed to increase by approximately 48% to 50% and 27% to 42% for group II. While the UHPC specimens in group III show joint shear strength 45% to 50% in comparison to the control specimens. These findings demonstrate the exceptional effectiveness of UHPC in enhancing the shear strength of concrete joints.

Furthermore, specimens $CJ_2U_{1h}T_2S_{50}C$ and $CJ_2U_{1h}T_2S_{100}C$ exhibit even higher joint shear strength than their NSC counterparts by about 58% and 52%, respectively, as demonstrated in Figure 4.56. This significant increase in shear strength can be attributed to the high shear resistance and tensile strength of UHPC. This combination of properties makes UHPC an ideal material for reinforcing concrete structures in seismic regions, where the risk of failure due to shear stress is high.

Overall, the use of UHPC in concrete joints offers significant benefits in terms of improved shear strength, enhanced ductility, and increased

resistance to cracking and failure. This can help to ensure the structural integrity and safety of concrete structures in seismic regions, ultimately reducing the risk of damage and failure during earthquakes.

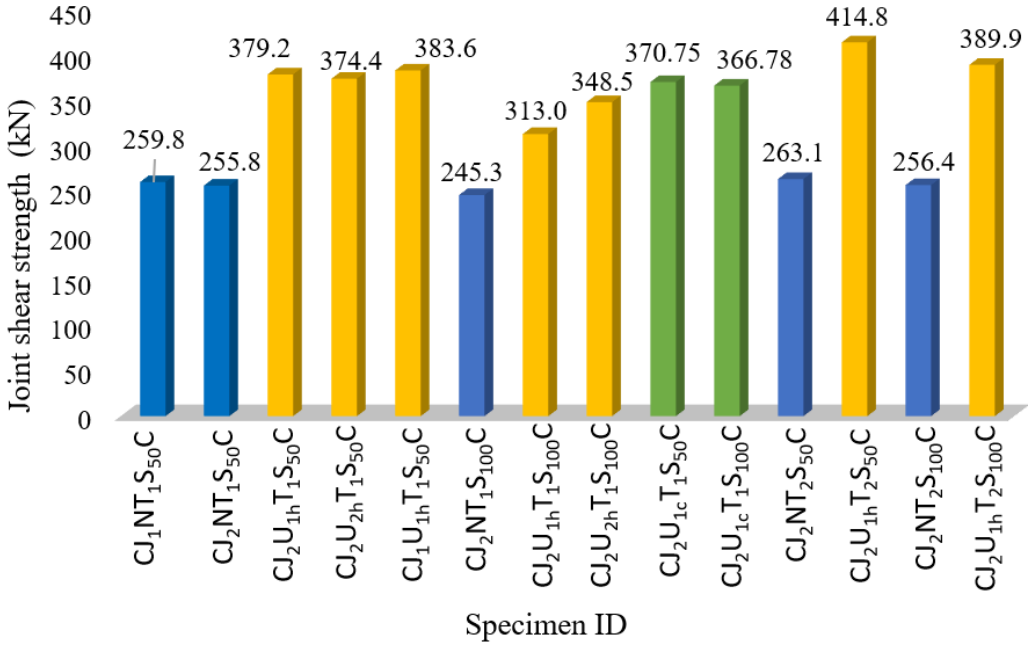

Figure 4.56 Comparison the joint shear strength for both types of concrete.

4.3 Specimens Tested under Monotonic Load

Most of the research in this field focuses on the behavior of beam-column joints under cyclic load that simulates the seismic load. However, little information exists in the literature on the behavior of beam-column joints under monotonic load compared to cyclically loaded joints. Even though the applied load was monotonic, Sarsarm [220] tested a series of exterior beam-column joints under a monotonic load. It was found that the utilize transverse reinforcement in the joint core can't prevent the formation of a diagonal crack in the joint core. Also, it was found that the joint with transverse reinforcement failed owing to beam yield, while the joint without transverse reinforcement collapsed due to the joint shear. A comparison between beam-column joints tested under both cyclic and monotonic loading showed that the deformation capacity of specimens under cyclic load is weaker and the failure mode is more brittle than that under monotonic loading. Nevertheless,

this is not changing the fact that the failure was a joint shear failure for both cyclic and monotonic loading [221] Thus, beam-column joints under monotonic load are not less severe than that under cyclic load.

The present subsections present the experimental results observed from the specimens tested under monotonic load. The result includes crack pattern and failure mode, ductility, energy dissipation, stiffness, and joint shear strength.

4.3.1 Cracking pattern and failure mode for specimens tested under monotonic load

Generally, the tested specimens under monotonic load show approximately similar behavior to that tested under compression cyclic load. Howeve, the NSC specimens show severe damage in the joint core and a brittle failure mode. On the other hand, UHPC specimens failed in flexural mode by forming a plastic hinge at the joint-beam interface. This is due to the high shear resistance of UHPC. Table 4.2 presents the main experimental results and failure modes. The following sections describe the experimental behavior of the tested specimens under monotonic load.

Table 4.2 Cracking load, ultimate load, and failure mode of the tested specimens under monotonic load

Group No.	Specimen ID	Flexural cracking load (kN)	Diagonal cracking load (kN)	Ultimate load (kN)	Inc. in ultimate load* (%)	Failure mode
I	$CJ_2NT_1S_{50}M$	25	30	103.5	…….	BJ-F
	$CJ_2U_{1h}T_1S_{50}M$	30	80	152.3	47.1	B-F
II	$CJ_2NT_1S_{100}M$	20	30	98.3	……	BS-F
	$CJ_2U_{1h}T_1S_{100}M$	30	90	145	47.5	B-F
III	$CJ_2U_{1c}T_1S_{50}M$	40	100	147.7	42.7	B-F
	$CJ_2U_{1c}T_1S_{100}M$	30	90	141.7	44.1	B-F

*Percent of increase/decrease $= \frac{P_u - P_c}{P_c} \times 100$;

$P_u, P_c = ultimate\ load\ for\ UHPC\ and\ control\ specimens\ respectivilly,$ noting that group I, and $CJ_2U_{1c}T_1S_{50}M$ compared with control specimen $CJ_2NT_1S_{50}M$, while group II, and specimen $CJ_2U_{1c}T_1S_{100}M$ compared to control specimen $CJ_2NT_1S_{100}C$. In the case of group III, the UHPC joint compared to corresponding NSC specimens.

4.3.1.1 Cracking pattern and failure mode of group I tested under monotonic load

For the specimen **$CJ_2NT_1S_{50}M$**, the first diagonal crack developed in the joint core when the applied load (*P*) reached 30 kN. As the load increased, the diagonal cracks extended towards the ends of the joint. The inclination of that crack matches the theoretical diagonal strut inclination of 45°. Then additional diagonal cracks were developed parallel to the initial one. It was found that the number of cracks and crack width both grew gradually during the loading process. As the joint progressed to failure, the cracks did not increase in number but widened considerably. After that, the vertical cracks on both sides of the column propagated diagonally through the joint and connected to forming a large triangular concrete wedge that tended to separate from the outside corner of the column. As the diagonal cracks widened, the joint's strength and stiffness rapidly deteriorated. Finally, the concrete in the joint core was crushed, as shown in Figure 4.57, and lost its load-carrying capacity at a load of 103.5 kN.

On the other hand, the other UHPC specimen show stable behavior with no significant damage/cracks. Moreover, all the cracks in the joint region were hair cracks till failure. The major benefit of using UHPC at the joint region is that it changes the failure mode from brittle failure due to joint shear crack to ductile failure by creating a plastic hinge at the joint-beam interface.

For the specimen **$CJ_2U_{1h}T_1S_{50}M$**, the first visual hairline crack was observed when the load reached 30 kN at the joint-beam interface. In contrast, the first diagonal hairline crack was developed when the load reached 80 kN with slight propagation and no widening until the ultimate stage, as shown in Figure 4.58. Additional flexural and diagonal hairline cracks were observed in the UHPC region as the applied load increased and still hairline till the ultimate stage. When the load (*P*) reaches 130 kN, a flexural crack widens

and concentrates at the face of the column, and steel fiber starts to pull out from the UHPC matrix. At the peak load, the flexural plastic hinge at the joint-beam interface widens significantly at a load of 152.5 kN, and then the load drops slightly. At this stage, the LVDTs were removed to avoid collapsing the beams and destroying the instruments. The steel fiber continues to pull out from the UHPC matrix with a slight load drop until tension reinforcement fractures, and this is clearly shown in Figure 4.58.

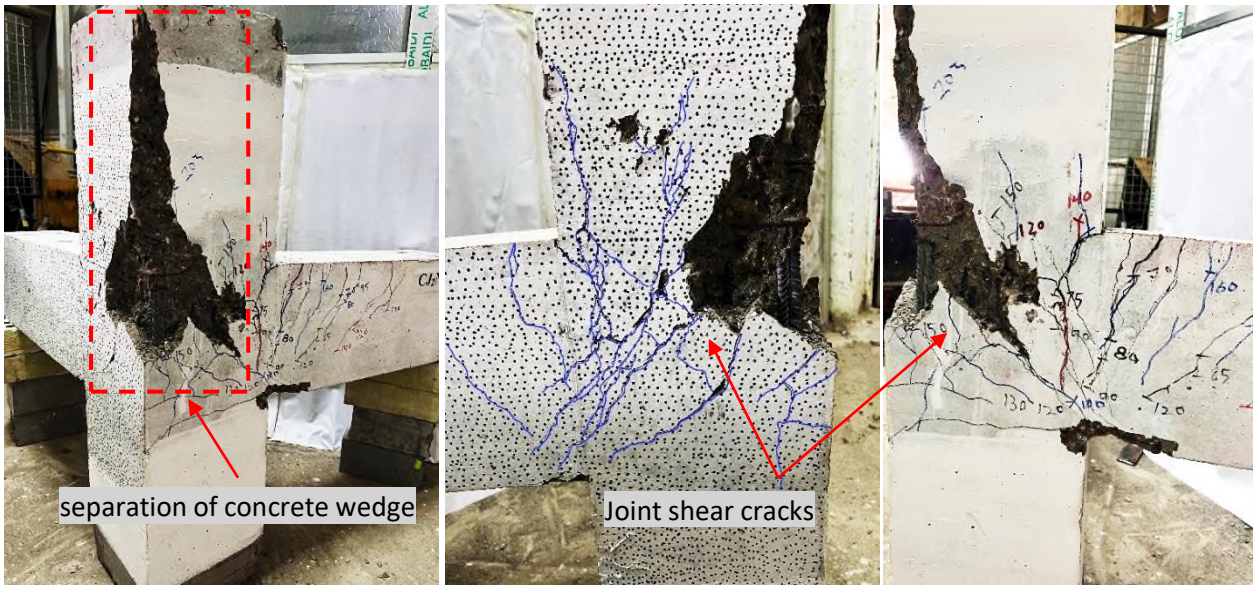

Figure 4.57 Failure mode and cracking pattern at the end of the test specimen $CJ_2NT_1S_{50}M$.

Figure 4.58 Failure mode and cracking pattern at the end of the test specimen $CJ_2U_{1h}T_1S_{50}M$.

4.3.1.2 Cracking pattern and failure mode of group II were tested under monotonic load

The specimen **$CJ_2NT_1S_{100}M$** was more severe damage than **$CJ_2NT_1S_{50}M$** at the same drift ratio level. In addition to diagonal shear cracks, a series of shear cracks were generated suddenly in both beams, columns and joint due to increasing the transverse reinforcement spacing from d/4 to d/2. The crack widens and extends rapidly when the load is increased. It was also observed that the bottom reinforcement was buckling after the concrete cover was crushed, as seen in Figure 4.59. Finally, the specimen collapsed suddenly due to a combination of severe damage in the joint core and beam shear failure at a load of 98.3 kN.

The UHPC region of specimen **$CJ_2U_{1h}T_1S_{100}M$** showed almost similar behavior to that of **$CJ_2U_{1h}T_1S_{50}M$**, meaning the UHPC compensates for the reduction in transverse reinforcement in this region. However, multiple diagonal cracks were generated in the NSC region of both beams and columns due to increasing the spacing of transverse reinforcement, as shown in Figure 4.60.

Figure 4.61 present the damage process of the tested specimens in group I and II with respect to the drift ratio. One can note from Figure 4.61 (a) and (b) the specimen **$CJ_2NT_1S_{100}M$** shows more severe damage compared to **$CJ_2NT_1S_{50}M$** at the same drift level. Moreover, flexural cracks developed in the lower column of specimen **$CJ_2NT_1S_{50}M$** whereas the cracks developed in a shear pattern for the specimen **$CJ_2NT_1S_{100}M$**. This is mainly due to increasing the spacing of transverse reinforcement in the joint region.

Despite the spacing of transverse reinforcement and total elimination of transverse reinforcement in the joint core, both UHPC specimens show similar behavior till failure, as shown in Figures 4.61 (c) and (d).

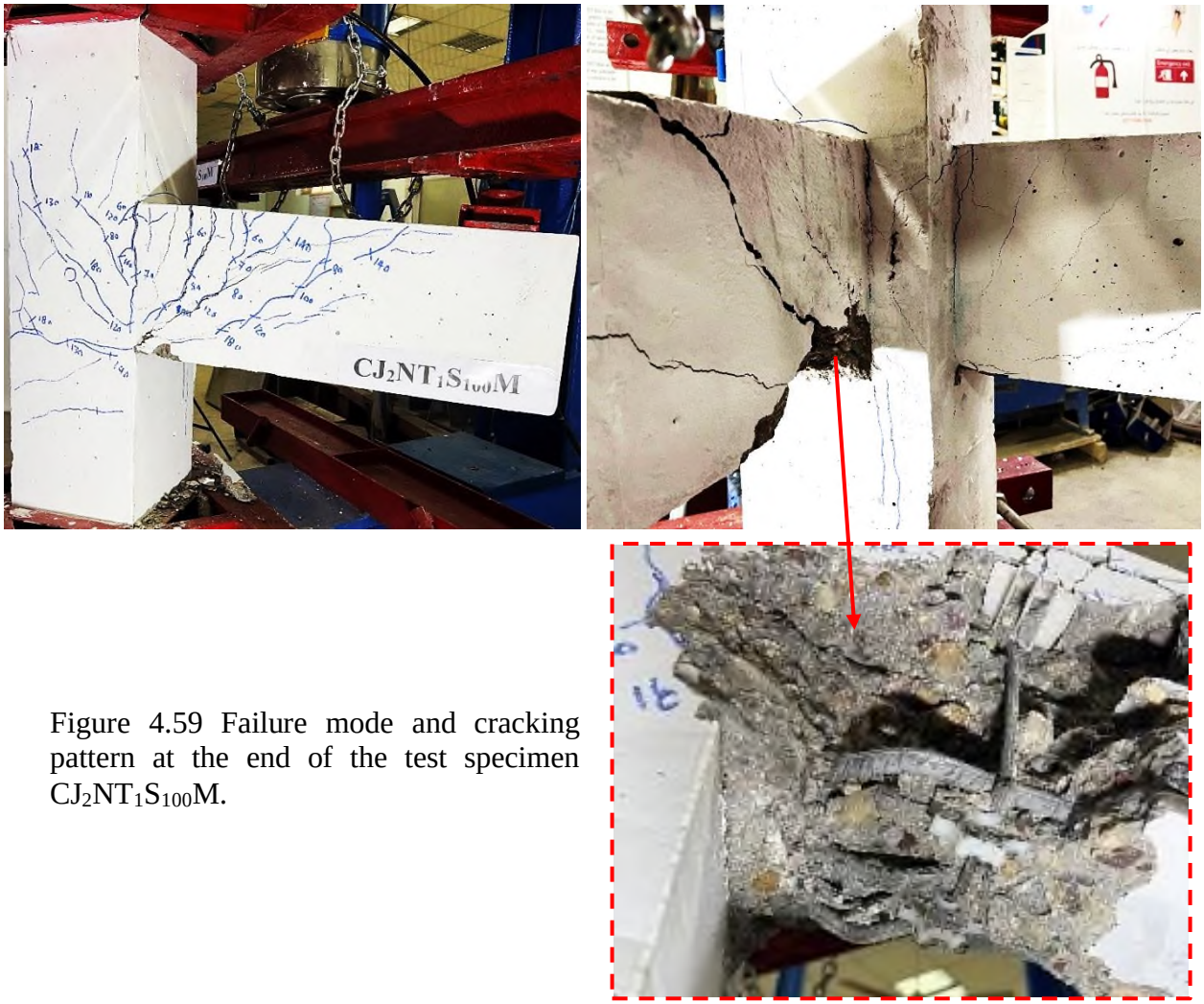

Figure 4.59 Failure mode and cracking pattern at the end of the test specimen $CJ_2NT_1S_{100}M$.

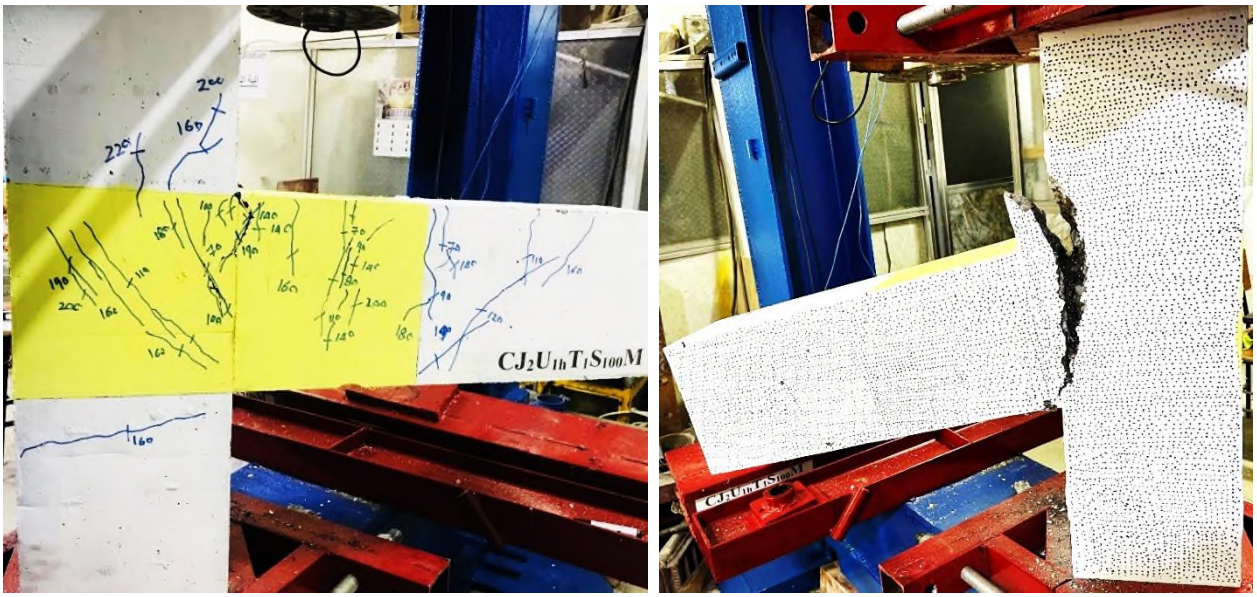

Figure 4.60 Failure mode and cracking pattern at the end of the test specimen $CJ_2U_{1h}T_1S_{100}M$.

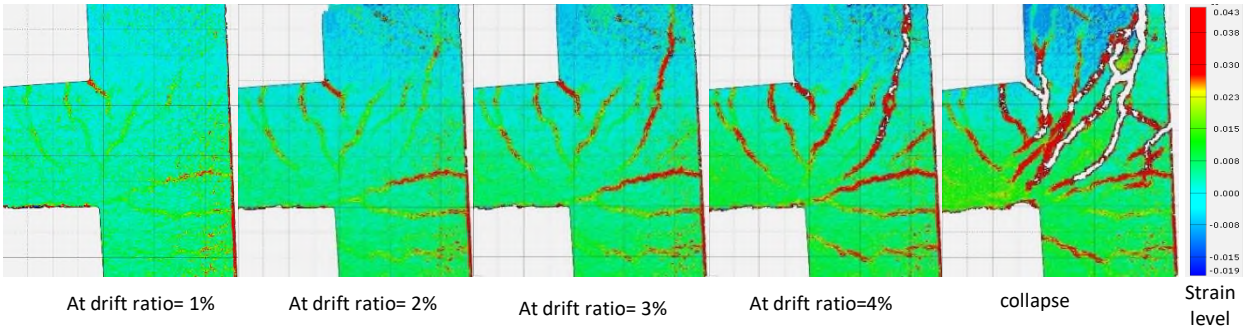

a) $CJ_2NT_1S_{50}M$

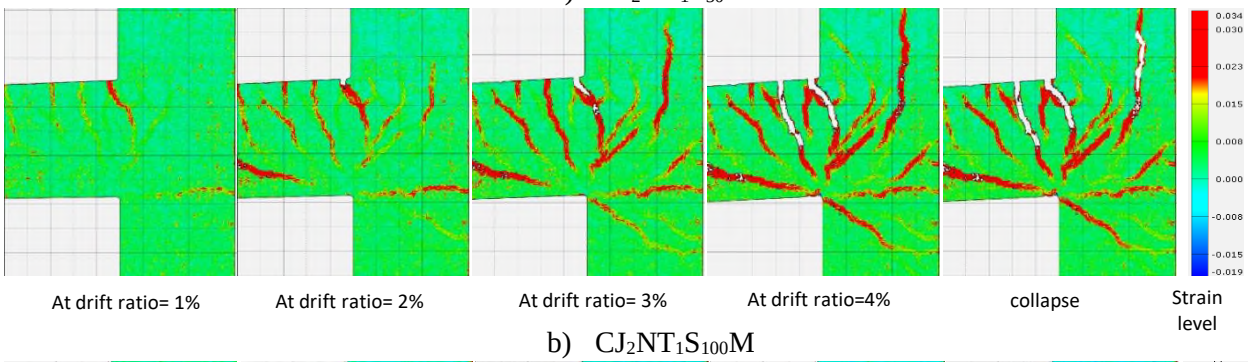

b) $CJ_2NT_1S_{100}M$

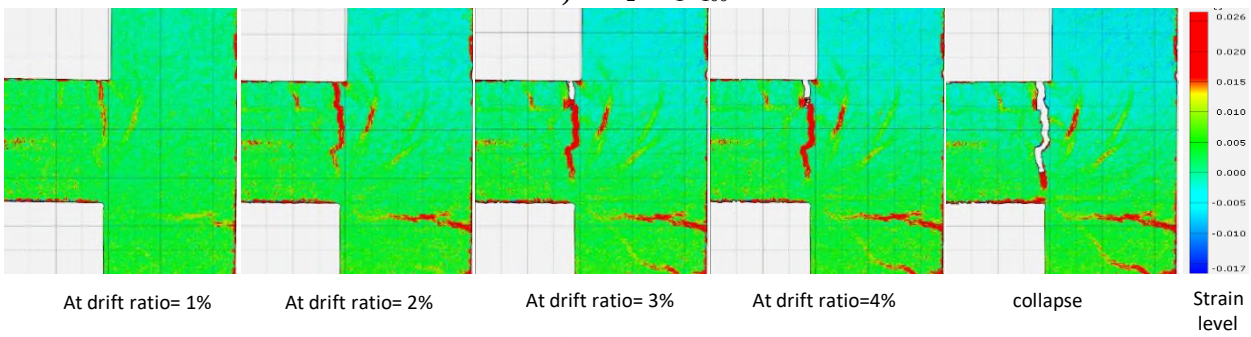

c) $CJ_2U_{1h}T_1S_{50}M$

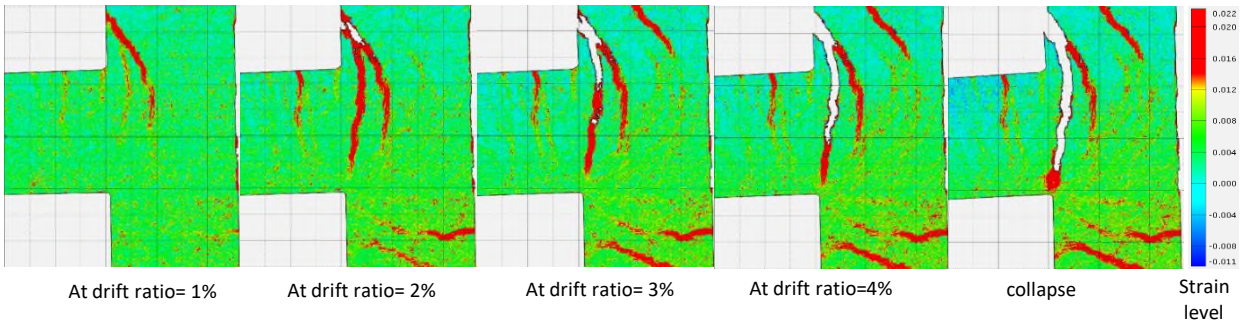

d) $CJ_2U_{1h}T_1S_{100}M$

Figure 4.61 Failure process of tested specimens in groups I and II that were monitored by DIC.

4.3.1.3 Cracking pattern and failure mode of group III were tested under monotonic load

This group contains two specimens cast in the cold procedure, and the variable is the spacing of transverse reinforcement (d/4 and d/2). In both

specimens, the transverse reinforcement was eliminated from the joint core. Despite the complete removal of transverse reinforcement from the joint core and the increase the spacing of transverse reinforcement in the joint region, the behavior of both specimens was quite similar because the shear resistance of UHPC compensated for the loss in confinement supplied by transverse reinforcement.

The first flexural crack was generated at 40 kN, 50 mm away from the face of the column for the specimen **$CJ_2U_{1c}T_1S_{50}M$**, followed by multi flexural cracks. The NSM steel bar on both sides of the beams restricted the propagation of flexural cracks through the depth of the beams. A flexural crack was initiated in the lower column at a load of 70 kN. Then as the load reached 100 kN, multi hairline cracks were initiated in the joint core and still hairline till failure. No significant cracks were observed at the NSC-UHPC interface. Similar to other UHPC specimens, the flexural cracks concentrated and widened at the joint-beam interface. Finally, the specimen failed at 147.7 kN due to the formation of a plastic hinge at the joint-beam interface. The specimen **$CJ_2U_{1c}T_1S_{100}M$** shows similar behavior to **$CJ_2U_{1c}T_1S_{50}M$**, and this is can clearly be noted in Figures 4.62 (a),(b), and 4.63 (a),(b).

a) Specimen $CJ_2U_{1c}T_1S_{50}M$

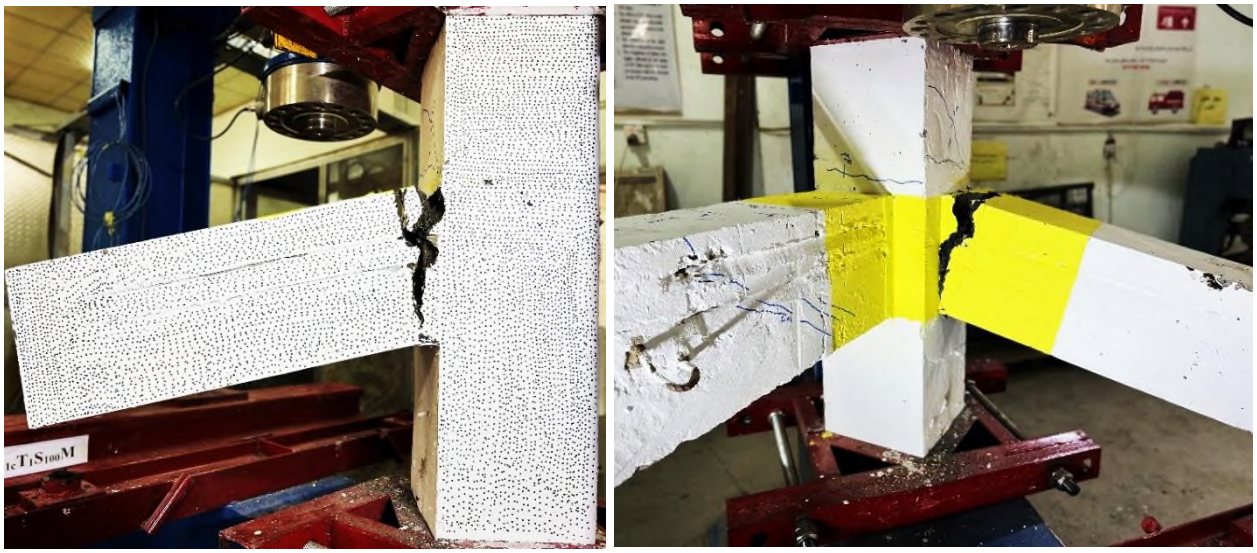

b) Specimen $CJ_2U_{1c}T_1S_{100}M$

Figure 4.62 Failure mode and crack pattern at the end of the test of the specimens in group III.

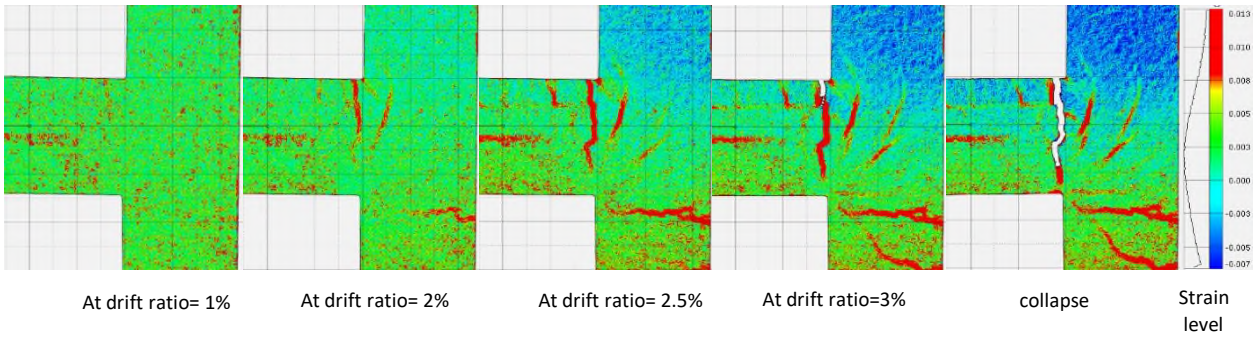

a) Specimen $CJ_2U_{1c}T_1S_{50}M$

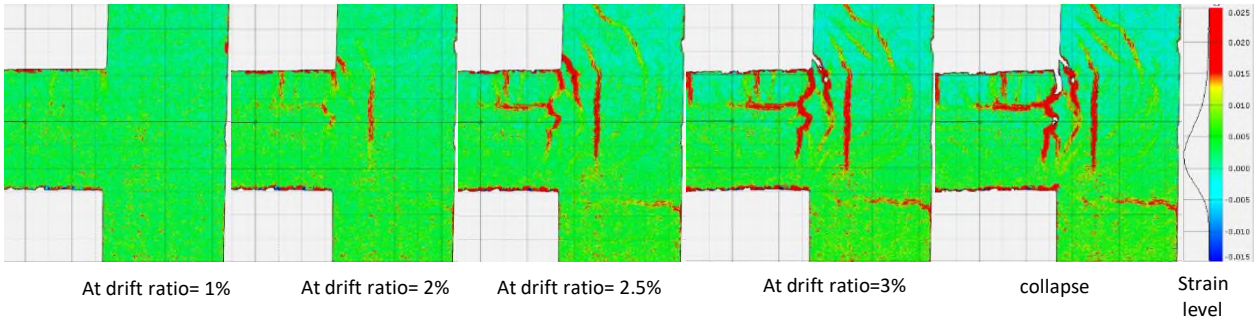

b) Specimen $CJ_2U_{1c}T_1S_{100}M$

Figure 4.63 Failure process of tested specimens in group III that were mentored by DIC.

Similar to specimens tested under cyclic load, no damage was observed at the NSC-UHPC interface. Therefore, its fare to say the bond between two materials is full bond.

In general, the above results show that using UHPC in the beam-column joint shifts the failure mode from a brittle joint shear (in conventional NSC joints) to a ductile flexural failure in the beam, even after removing the joint transverse reinforcement and halving the transverse reinforcement in the beams and column segments. This is likely due to UHPC's high tensile, shear, and bond strengths as well as its extraordinary compressive strength that impedes crushing and spalling failures and subsequent buckling of embedded longitudinal bars.

4.3.2 load-drift response of tested specimens under monotonic load

In order to study the behavior of reinforced concrete beam-column joints, the load-displacement angle curves (drift ratio) of the joints were investigated. At the drift equal to 2%, the NSC joints, especially the specimen **$CJ_2NT_1S_{100}M$** showed large deformation and multiple cracks developed rapidly, making stiffness degraded rapidly, as remarked in Figure 4.64. In contrast, the specimen **$CJ_2NT_1S_{50}M$** showed more stable behavior due to the confinement provided by transverse reinforcement. Finally, the NSC specimens lost their strength due to the widening of the diagonal joint crack and spalling of concrete at the joint core at a load level of 104.5 kN and 98.3 kN for specimens **$CJ_2NT_1S_{50}M$** and **$CJ_2NT_1S_{100}M$**, respectively. Although the NSC specimens reached their beam flexural capacity (90.23kN), but the failure was brittle (unrecommended failure mode). Regardless to transverse reinforcement spacing, both UHPC specimens show similar behavior. The load-drift response of the UHPC specimens can be divided into three stages; 1) liner response unit load reaches about 130 kN; 2) strain hardening response until the specimens reach the ultimate load; 3) strain softening response till collapse. The behavior of UHPC specimens is clearly governed by a linear overstrength response, as seen in Figure 4.64. The specimens **$CJ_2U_{1h}T_1S_{50}M$** and **$CJ_2U_{1h}T_1S_{100}M$** show an increase in the load-carrying capacity by about 47% compared to their corresponding NSC specimens.

For the UHPC cold joint, regardless of transverse reinforcement spacing, both specimens show similar behavior, as shown in Figure 4.64. Its clear that the cold joint is slightly stiffer than **$CJ_2U_{1h}T_1S_{100}M$**; this may be due to the addition of steel bars for both sides of beams in the form of NSM. However, the specimens **$CJ_2U_{1c}T_1S_{50}M$** and **$CJ_2U_{1c}T_1S_{100}M$** show an increase in load-

bearing capacity of about 44% and 45% with respect to corresponding NSC specimens.

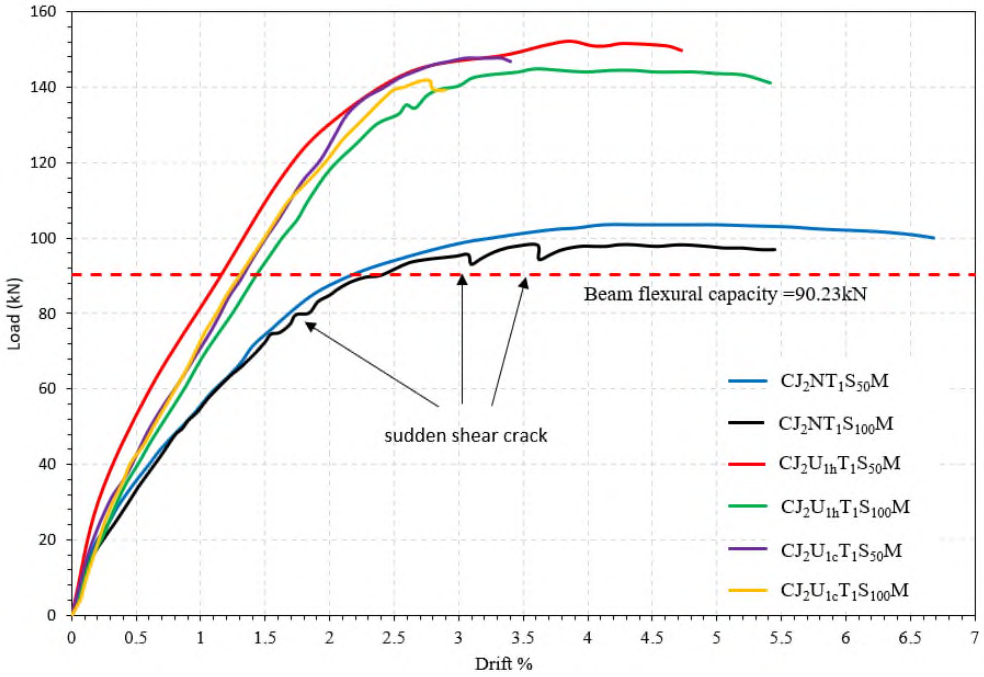

Figure 4.64 Load-drift response of the tested specimens in groups I,II, and III which tested under monotonic load.

4.3.3 Ductility of tested specimens under monotonic load

The ductility index is defined as the ratio of the ultimate deflection to the yield deflection [213]. Also, it can be found in accordance with toughness or energy absorption, which is defined as the area under the load-deflection curve up to the ultimate load [213]. Figure 4.65 presents the energy absorption of tested specimens, its clear that utilize UHPC in the joint region improves the energy absorption significantly. The energy absorption of specimen **$CJ_2U_{1h}T_1S_{50}M$** was 35% greater than that of **$CJ_2NT_1S_{50}M$**, whereas the energy increased 72% in the case of **$CJ_2U_{1h}T_1S_{100}M$** with respect to **$CJ_2NT_1S_{100}M$**. In contrast, the cold joint shows a slight decrease in energy absorption compared to the hot joint. The energy absorption of specimens **$CJ_2U_{1c}T_1S_{50}M$** and **$CJ_2U_{1c}T_1S_{100}M$** was greater than corresponding NSC specimens, about 5%, and 29%, respectively. However, it was found that the cold joint showed less energy absorption than those cast

in the hot method by about 20%. This means the UHPC material compensates for the lack of transverse reinforcement in the joint core as well as beams and columns.

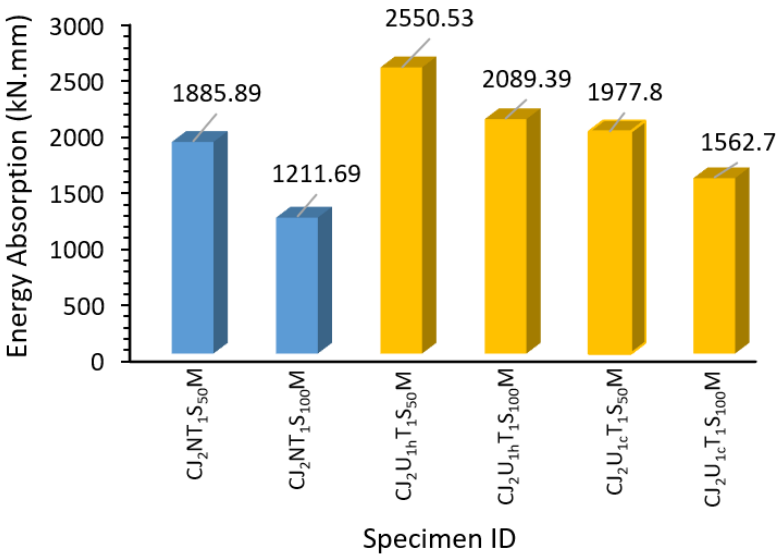

Figure 4.65 The Energy absorption for tested specimens under monotonic load.

4.3.4 Stiffness of tested specimens under monotonic load

As discussed in the previous part, the initial stiffness (Ki) is adopted in the present study to assess the stiffness of tested specimens. Utilizing the UHPC in the joint region of the corner beam-column joint increases the initial stiffness significantly. As shown in Figure 4.66, the specimens **$CJ_2U_{1h}T_1S_{50}M$** and **$CJ_2U_{1h}T_1S_{100}M$** shows an increase in initial stiffness by about 50% and 27%, corresponding to the control specimens **$CJ_2NT_1S_{50}M$** and **$CJ_2NT_1S_{100}M$**, respectively. However, both cold joints show similar behavior regardless of transverse reinforcement spacing. The initial stiffness of the cold joints was 36% greater than NSC specimens. This improvement was mainly due to the micro steel fiber that reinforced the UHPC matrix restricting cracks propagation and preventing stiffness degradation. In addition, NSM steel bars placed on both sides of beams also restrict the flexural and shear cracks.

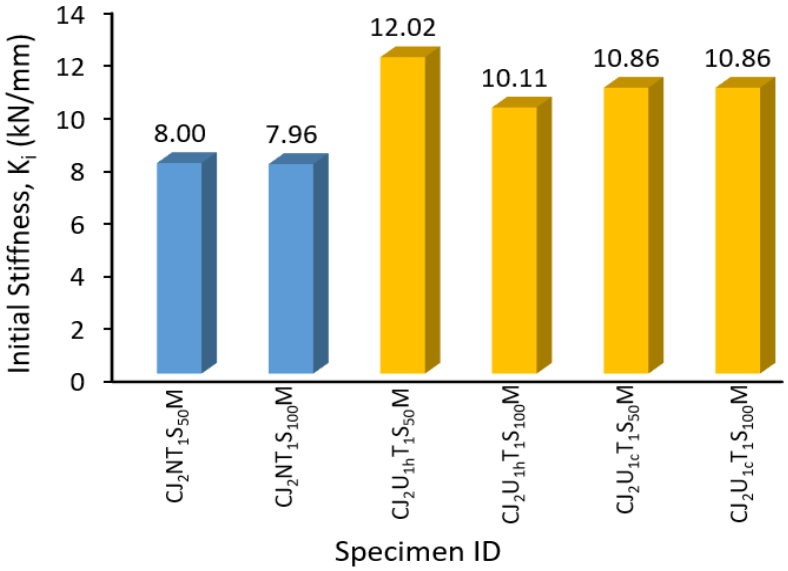

Figure 4.66 The initial stiffness of the tested specimens under monotonic load.

4.3.5 Joint principle stresses

According to section 4.2.5 discussed previously, the principle stress of both NSC/UHPC specimens are calculated. Figure 4.67 present a comparison of the maximum principal tensile stress induced at the mid-hight of the joint core with the maximum tensile strength of both concrete types. It is clear from Figure 4.67 that after the NSC specimens exceed the concrete tensile strength, the specimens strength drops, and the collapse occurs due to the development of diagonal cracks in the joint core of the NSC specimens. Contrary to NSC, the UHPC exhibits tensile strain hardening accompanied by multiple micro-cracks after the formation of first crack. The UHPC specimens collapsed without reaching their ultimate tensile, which explains why the joint core of the UHPC specimens was free of significant joint diagonal cracks.

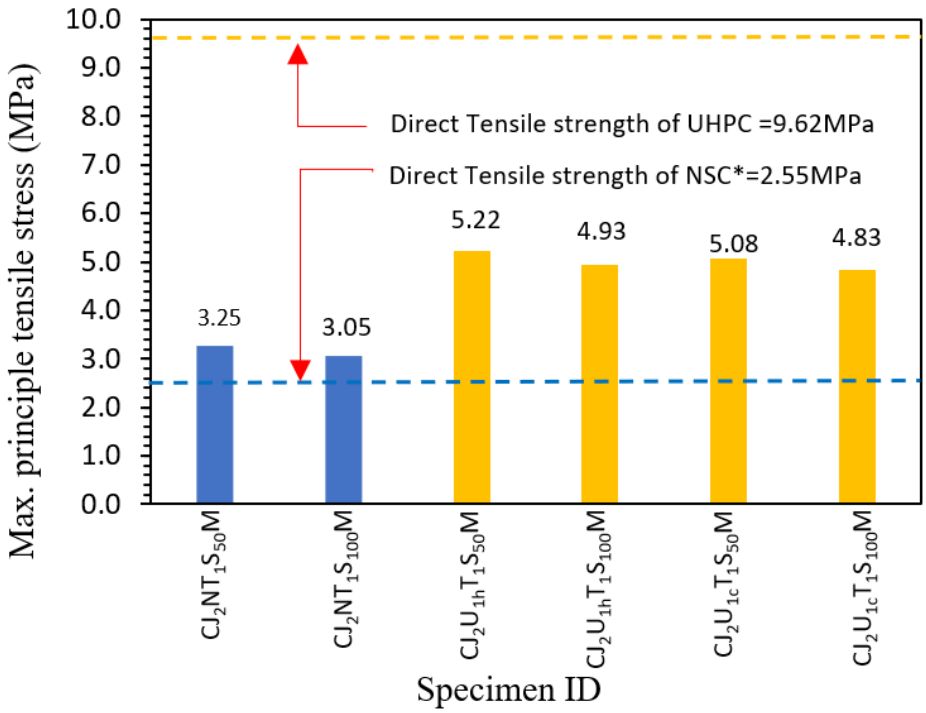

Figure 4.67 Comparison of maximum principle tensile strength of materials with the direct tensile strength of concrete.

Figure 4.68 demonstrates that incorporating UHPC in the joint region can result in a noteworthy improvement in the joint shear strength of the corner beam-column joint. Specifically, the use of UHPC can increase the joint shear strength by up to 47% compared to NSC specimens. This improvement is a substantial enhancement and highlights the effectiveness of UHPC in enhancing the mechanical properties of structures. It is worth noting that the application of UHPC in the joint region is a potent technique for achieving this benefit, as it can significantly increase the load-carrying capacity of the structure. Therefore, the use of UHPC in the joint region is a promising approach to improving the strength and durability of structures while ensuring their safety and reliability.

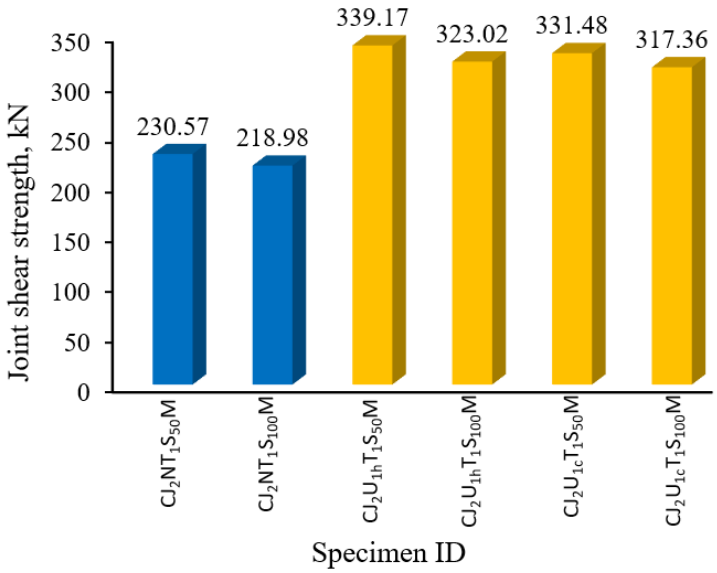

Figure 4.68 Comparison between the joint shear strength of conventional NSC specimens and that of UHPC specimens.

Chapter Five

Assessment of Codes Provision for Predicting Joint Shear Strength

5.1 Introduction

The presence of wide diagonal cracks in the beam-column joint during earthquakes cannot be eliminated, even when following the suggested building codes, as previously mentioned in section 1.3. In order to find the issues behind this problem, the predicted joint shear strength based on different national codes was examined and compared with the experimental joint shear capacity of reinforced beam-column joint collected from the literature. The experimental data collected from 46 references consist of 129 exterior joints, 115 interior joints, and 10 joints confined by all four sides, as mentioned in section 2.4.

5.2 Code provisions for predicting joint shear strength

The main code provisions for predicting joint shear strength are discussed in the sections below.

5.2.1 ACI-ASCE committee 352[16]

ACI-ASCE developed the first guideline for the beam-column joint in 1976. This guideline was revised many times till the final revision in 2010. Based on this code, the joint shear strength is calculated as follows:

$$V_j = \lambda\sqrt{f_c^`}h_c b_j \quad \ldots\ldots\ldots\ldots\ldots\ldots\ldots\ldots\ldots\ldots\ldots\ldots\ldots\ldots\ldots\ldots \quad 5.1$$

Where:

λ is the confinement factor depending on the confinement provided by transverse beams. The ACI-ASCE 352 classifieds the joint into three cases according to the beams framing to the column, as shown in Figure 5.1. Figure 5.1(a) presents the joint confined by all four sides. In contrast, the joints confined by three faces or two opposite faces are classified as interior joints, Figure 5.1(b). The joints are classified as exterior joints if confined by one face or two orthogonal faces, Figure 5.1(c). Most codes adopt this classification. Table 5.1 present the value of the confinement factor (λ).

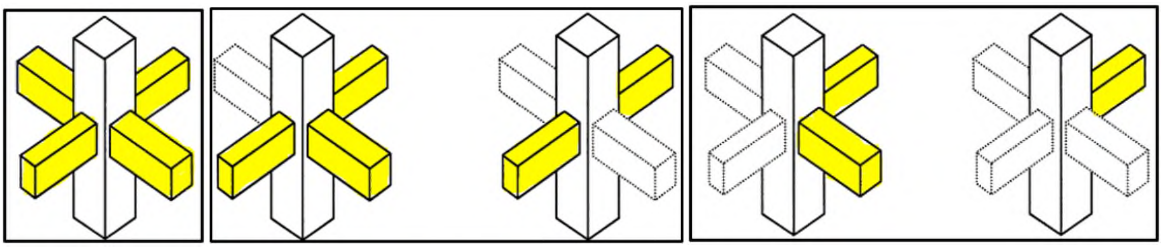

(a) (b) (c)

Figure 5.1 Confinement condition of beam-column joint by transverse beams, a) all four sides, b) three/two sides, and c) other cases.

Table 5.1 Confinement factor (λ) for different cases in ACI-ASCE

Confinement condition	All four sides	Three/two sides	Other cases
λ	1.66	1.25	1.0

b_j= Effective joint width can be calculated as follow

$$b_j \leq \begin{cases} \frac{b_c+b_b}{2} \\ b_b + \sum\frac{mh_c}{2} \\ b_c \end{cases} \quad \ldots\ldots\ldots\ldots\ldots\ldots\ldots\ldots\ldots\ldots\ldots\ldots\ldots\ldots.. \quad 5.2$$

Where: b_c= column width; b_b= beam width; h_c= total depth of column, and m= Slope to define the effective width of joint transverse to the direction of shear.

5.2.2 ACI 318-19 [17]

Chapter 15 in version 19 of ACI 318 focuses on the design requirements of the beam-column joint. The joint shear strength is estimated as in Eq. 5.3.

$$V_j = \lambda\sqrt{f_c`}h_c b_j \quad \text{.....5.3}$$

Where: λ= confinement factor, its clear define in Table 5.2; b_j=joint width can be calculated as follow:

$$b_c > b_b \rightarrow b_j = min.\begin{cases} b_b + 2x \\ b_b + b_c \end{cases}$$

$$b_c < b_b \rightarrow b_j = b_c$$

x= perpendicular distance from the longitudinal axis of the beam to the nearest side face of the column.

Table 5.2 Confinement factor (λ) for different cases in ACI 318-19

Confinement condition	All four sides	Three/two sides	Other cases
λ	1.7	1.2	1.0

Compared with ACI-ASCE, the joint width and value of the confinement factor are computed somewhat differently.

5.2.3 IS 13920:2019 [222]

The Indian Standard (IS 13920:2019) estimated the joint shear strength in the line of ACI 318-19, as shown in Eq. 5.4. All the variables in this equation define similarly as in 5.2.2, except the confinement factor for the case of the joint confined from all four sides is assumed to be 1.5 rather than 1.7 in ACI 318-19.

$$V_j = \lambda\sqrt{f_c`}h_c b_j \quad \text{.....5.4}$$

5.2.4 National Standard of Canada CSA A23.3:19 [102]

The National Standard of Canada for concrete structure (CSA A23.3:19) adopted a provision to calculate joint shear strength similar to that in ACI-ASCE, ACI 318 and IS 13920 with some different like the confinement factor, method to calculate joint width and limited the value of concrete compressive strength. Based on that, the joint shear strength can be estimated as follow:

$$V_j = \lambda \varphi \emptyset_c \sqrt{f_c`} h_c b_j \quad \text{.....5.5}$$

Where:

λ= density factor equal to 1.0 for normal concrete,0.85 for semi-loe dencity, amd 0.75 for low denncity concrete.

φ= confinement factor, its clear define in Table 5.3.

$\emptyset_c$= tensile strength factor equal to 0.65.

$f_c`$= concrete compressive strength.

h_c= column depth.

b_j=joint width can be calculated as follow:

$b_j = min.(h_c, 2b_b)$

Table 5.3 Confinement factor (φ) for different cases in CSA A23.3:19

Confinement condition	All four sides	Three/two sides	Other cases
φ	2.2	1.6	1.3

5.2.5 Architectural Institute of Japan AIJ:2010 Standard [180]

The nominal joint shear strength estimated by the AIJ is derived from large experiments conducted between 1988 and 1996 on interior and exterior joints. It is found that the compressive strength of concrete has a greater impact on the shear strength of beam-column joints than the amount of

transverse reinforcement, therefore, the nominal joint shear strength is estimated by considering the compressive strut mechanism [223]. Eq. 5.6 presents the joint shear resistance based on AIJ.

$$V_j = k\lambda F_j h_c b_j \quad \text{.....5.6}$$

Where

k= shape factor equals 1.0 for the exterior joint, 0.70 for the interior joint, and 0.40 for the knee joint.

λ= confinement factor, as defined in Table 5.4.

F_j= represent the concrete factor =$0.80(f_c^{`})^{0.70}$.

h_c=column depth.

b_j= joint effective width= $b_b + b_{a1} + b_{a2}$

b_b = beam width

$b_{a1}\ and\ b_{a2}$= minimum of $h_c/4\ \ and\ (b_c - b_b)$ on either side.

Table 5.4 Confinement factor (λ) for different cases in AIJ:2010

Confinement condition	All four sides	Three/two sides	Other cases
λ	1.0	0.85	0.85

5.2.6 NZS 3101-1[129]

The New Zealand Standard for concrete structures (NZS) assumes that the horizontal joint shear strength is a function of concrete compressive strength, depth of column, and width of joint as illustrated in Eq. 5.7. Its clear that Eq. 5.7 independent on the confinement provided by transverse beams.

$$V_j = min.\begin{cases} 0.2f_c^{`}h_c b_j \\ 10h_c b_j \end{cases} \quad \text{..... 5.7}$$

Where:

$$b_c > b_b \rightarrow b_j = min.\begin{cases} b_b + 0.5h_c \\ b_c \end{cases}$$

$$b_c < b_b \rightarrow b_j = min.\begin{cases} b_c + 0.5h_c \\ b_b \end{cases}$$

Where b_b is the beam width, h_c column depth, and b_c column width.

5.2.7 BS EN 1998-1:2004 [35]

BS EN 1998-1:2004 provides more detailed guidelines for the calculation of joint shear strength, including the determination of the joint type, material properties, and forces acting on the joint. The standard also provides design equations for the calculation of joint shear strength based on these factors, which may differ from the equations provided in other codes, as illustrated in Eq. 5.8.

$$V_j = \eta f_{cd} \sqrt{\frac{1-v_d}{\eta}} h_c b_j \qquad \text{.....5.8}$$

Where:

η = reduction factor on concrete compressive strength due to tensile strains in transverse direction = κ (1-f_{ck}/250).

The factor κ is 0.60 for the interior joint and 0.48 for the exterior joint

f_{cd}= Design strength of concrete from Eurocode =$\alpha_{cc}\, f_{ck}/\gamma_c$

Where: $\alpha_{cc} = 1.0\ for\ shear, \alpha_{cc} = 1.5,$

$\gamma_c =\ is\ the\ partial\ safety\ factor\ for\ concrete$

$and\ f_{ck} = concrete\ compresiive\ strength$

And the effective joint width bj:

$$b_c > b_b \rightarrow b_j = min.\begin{cases} b_b + 0.5h_c \\ b_c \end{cases}$$

$$b_c < b_b \rightarrow b_j = min.\begin{cases} b_c + 0.5h_c \\ b_b \end{cases}$$

5.3 Analysis of code provisions via experimental result

The study considered seven national code provisions that estimate the shear capacity of RC beam-column joints. These codes were ACI-ASCE 352, ACI 318-19, IS 13920, CSA A23.3, AIJ, NZS 3101-1, and BS EN 1998-1, and

their anticipated joint shear capacity was compared to experimental joint shear strength. The safety factor in these provisions can differ from one to another, based on several variables. To ensure a fair comparison between the various codes, all safety factors used in the codes that predict joint shear capacity were considered as one.

Figures 5.2 to 5.8 depict the correlation between the experimental joint shear capacity of 256 specimens and the corresponding predicted values obtained from the seven different code provisions discussed earlier. The reference line in these figures is represented by a dashed line, which indicates the point where the predicted shear strength equals the experimental shear strength. If the points for a particular code provision lie below this reference line, it signifies that the code formula is conservative, i.e., the actual shear resistance of the joint is more than what the code formula predicted. Conversely, if the points fall above the reference line, it means that the formula used in the code provides an overestimation of the shear resistance of the joint. By analyzing the data presented in these figures, researchers can determine the reliability of each code provision and compare the accuracy of the different formulae used to predict joint shear capacity.

Figures 5.2 to 5.8 were used to compare the joint shear strength estimated by different codes with the experimental joint shear strength. Unfortunately, a high degree of variability was observed between the predicted and experimental results, which indicates that none of the codes can be considered accurate for design purposes. To illustrate this variation more clearly, a statistical analysis was performed on the estimated joint shear strength compared to the experimental joint shear strength, and the results are presented in Table 5.5. This table shows the mean value (μ) of the ratio of predicted joint shear strength to experimental, standard deviation (SD), coefficient of variation (COV), and the mean absolute errors (MAE). The

elevated COV values indicate that the joint shear strength calculated by codes can be significantly inaccurate. After analyzing the data presented in Table 5.5, it has been observed that the code predictions exhibit considerable variability from the experimental results.

Table 5.5 Statistical analysis of predicted joint shear strength to experimental shear strength

Joint type	ACI-ASCE	ACI 318	IS 13920	CSA	AIJ	NZS	BS EN
			Exterior joints				
μ	1.03	1.14	1.14	0.96	1.19	1.43	1.86
SD	0.26	0.30	0.30	0.25	0.33	0.64	1.02
COV	25.33	26.74	26.74	25.98	28.22	44.65	54.91
MAE	41.92	93.10	93.10	1.23	140.68	290.06	622.88
			Interior joints				
μ	1.02	1.03	1.03	0.92	1.24	1.00	1.50
SD	0.55	0.57	0.57	0.48	0.77	0.59	1.18
COV	54.07	55.55	55.55	52.38	62.26	59.51	78.66
MAE	188.78	154.57	154.57	275.46	119.72	143.78	391.90
			Joint confined by all four side				
μ	0.92	1.03	1.16	1.28	1.04	1.26	0.80
SD	0.26	0.20	0.22	0.28	0.21	0.48	0.28
COV	28.07	19.32	19.32	21.72	19.73	38.36	35.48
MAE	302.50	99.76	332.37	514.77	40.87	661.94	654.15

(a)

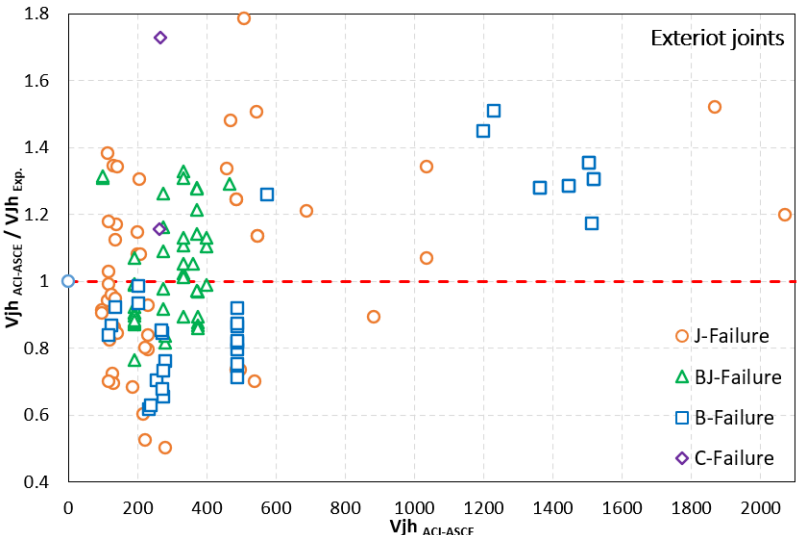

(b)

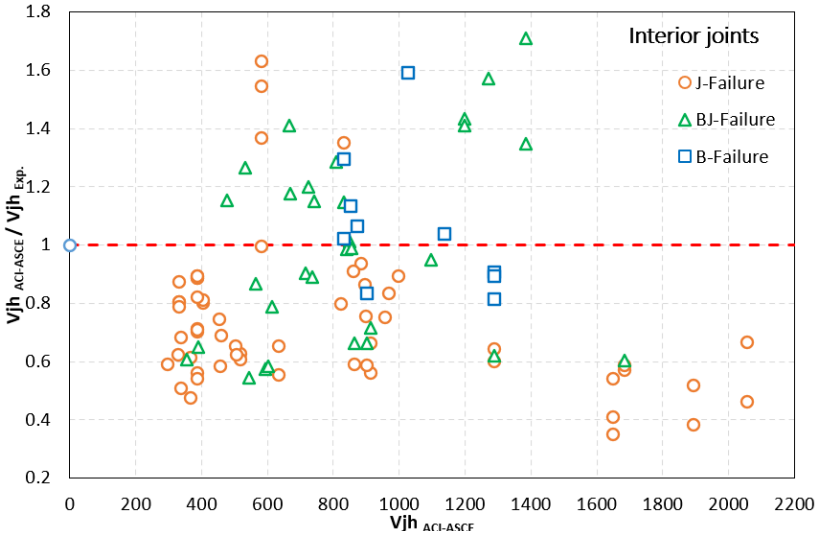

(c)

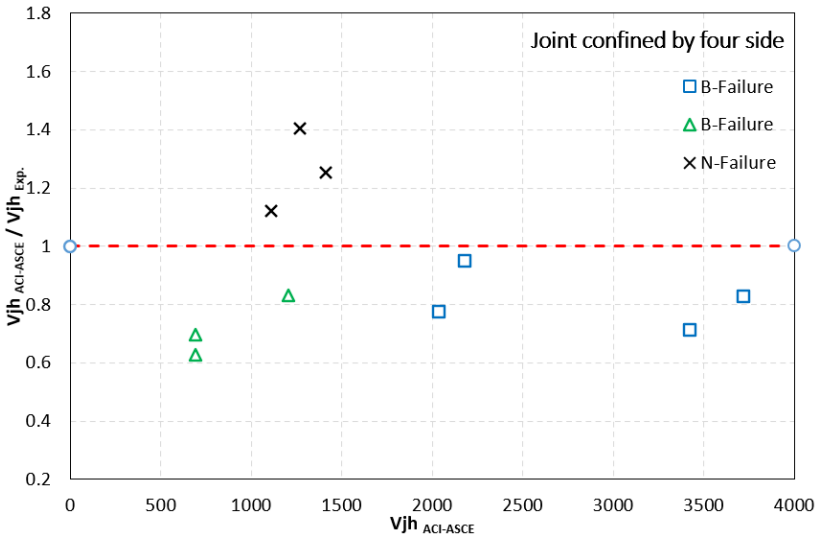

Figure 5.2 Predicted joint shear strength based on ACI-ASCE 354R vs experimental joint shear strength; a) exterior joints, b) interior joints, and c) joints confined by all four sides.

(a)

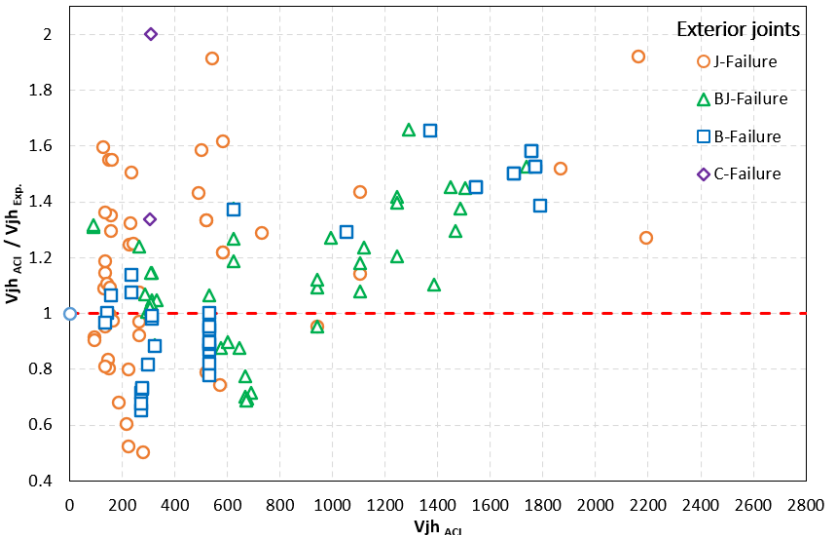

(b)

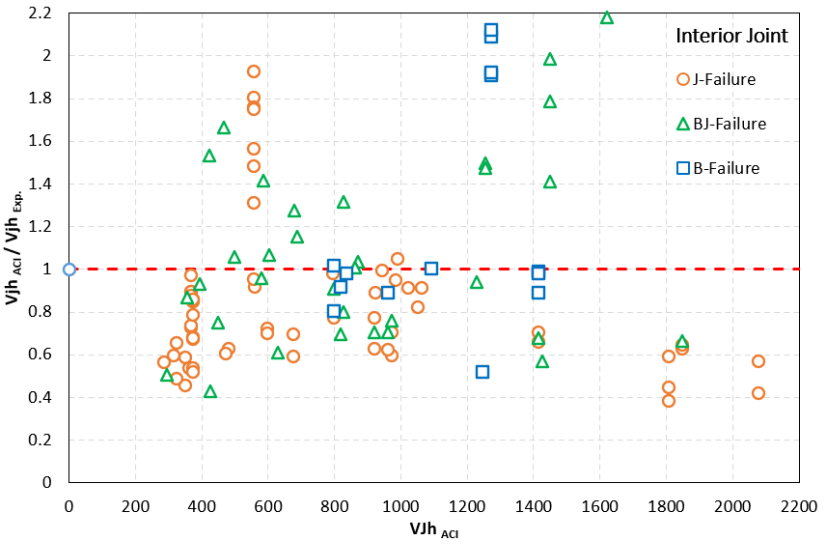

(c)

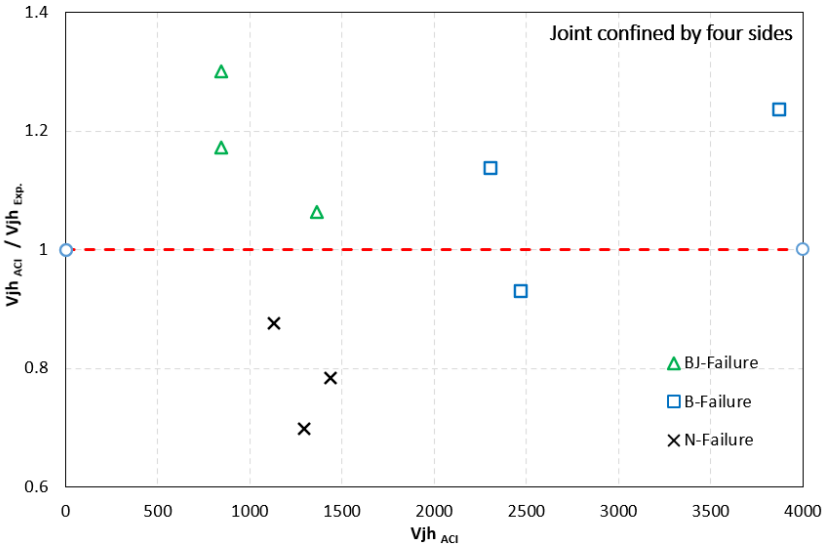

Figure 5.3 Predicted joint shear strength based on ACI 318-19 vs experimental joint shear strength; a) exterior joints, b) interior joints, and c) joints confined by all four sides.

(a)

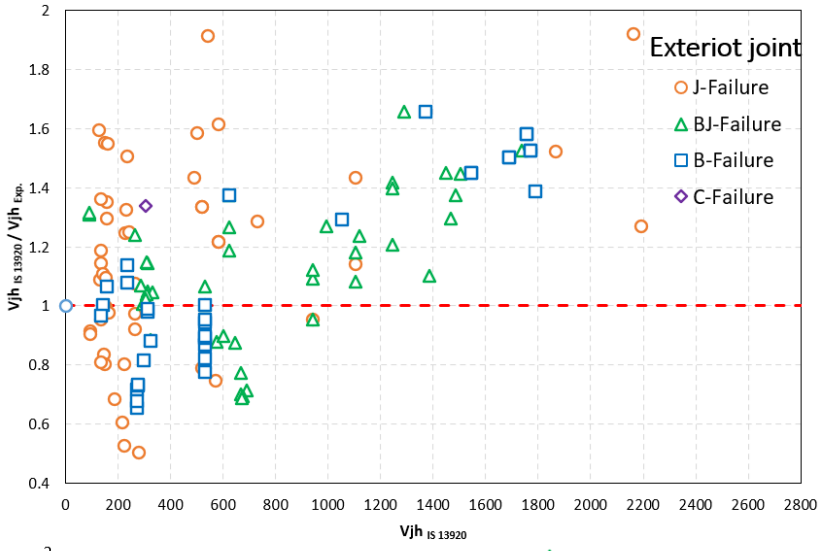

(b)

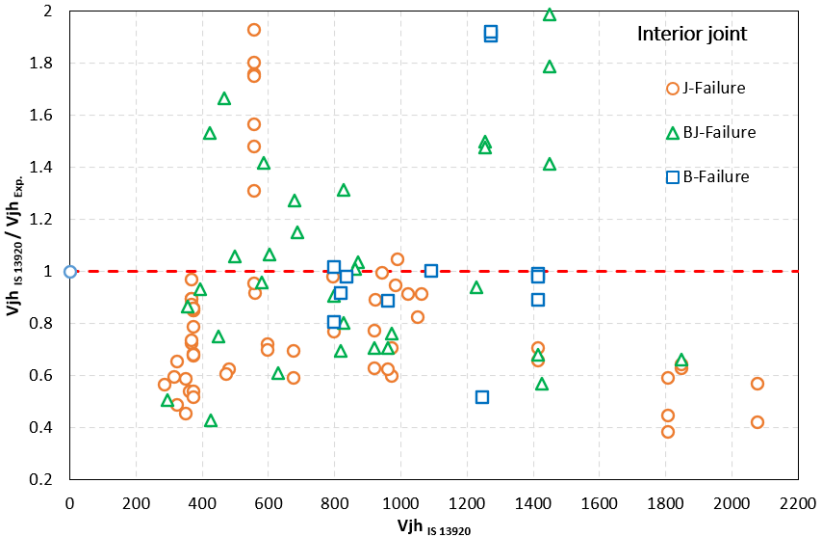

(c)

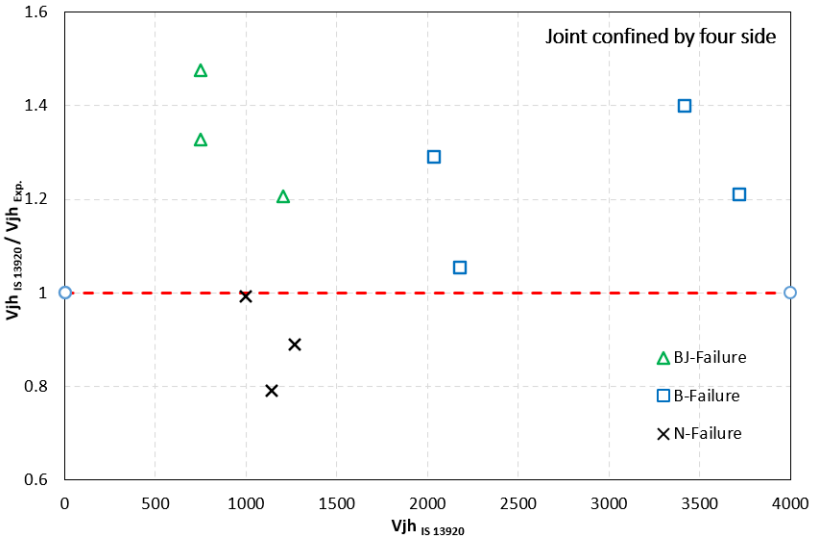

Figure 5.4 Predicted joint shear strength based on IS 13920 vs experimental joint shear strength; a) exterior joints, b) interior joints, and c) joints confined by all four sides.

(a)

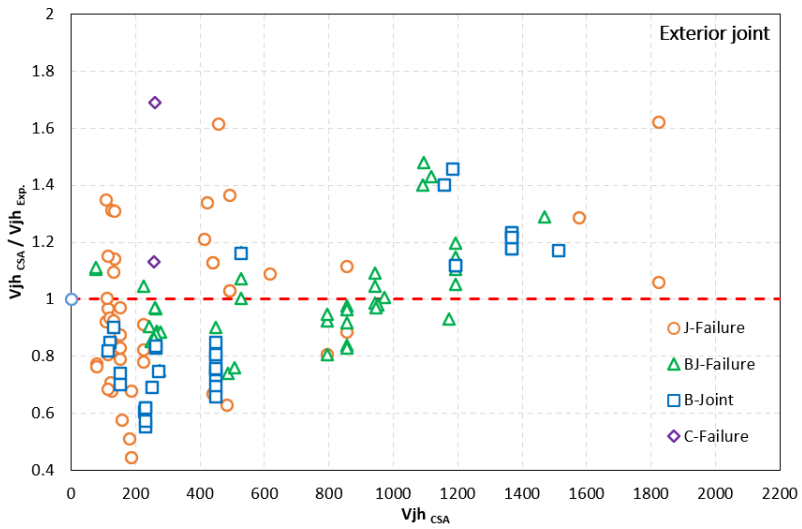

(b)

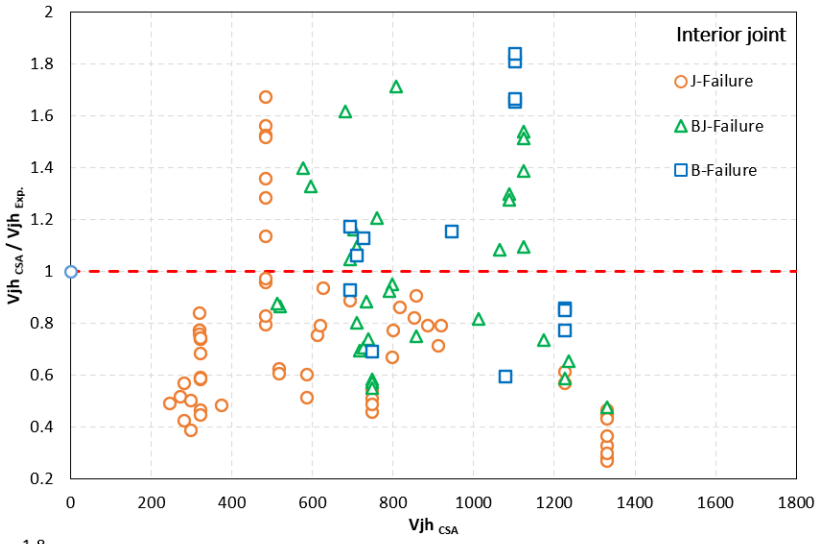

(c)

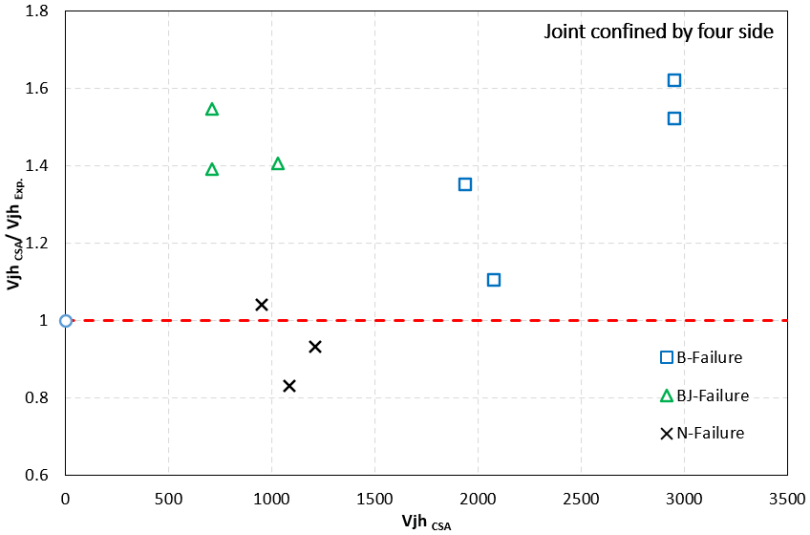

Figure 5.5 Predicted joint shear strength based on CSA A23.3:19 vs experimental joint shear strength; a) exterior joints, b) interior joints, and c) joints confined by all four sides.

(a)

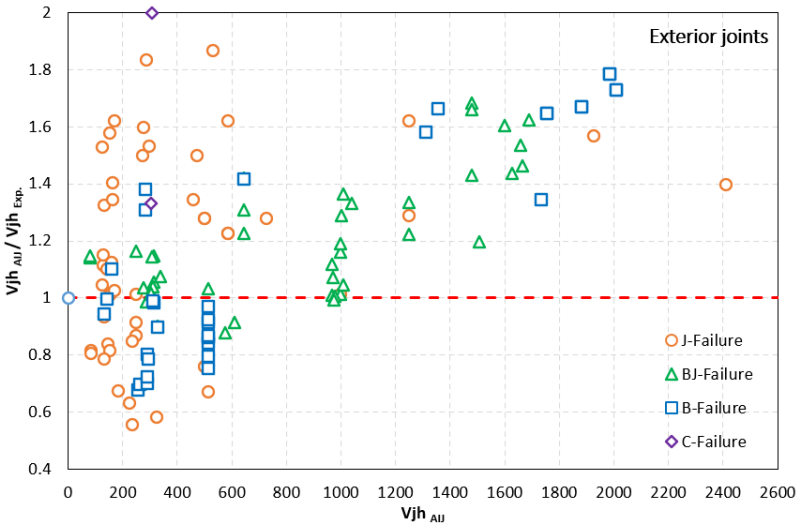

(b)

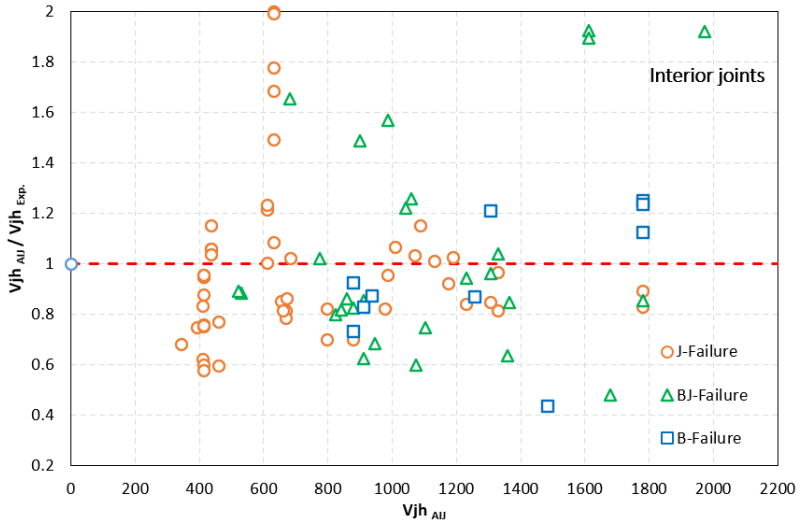

(c)

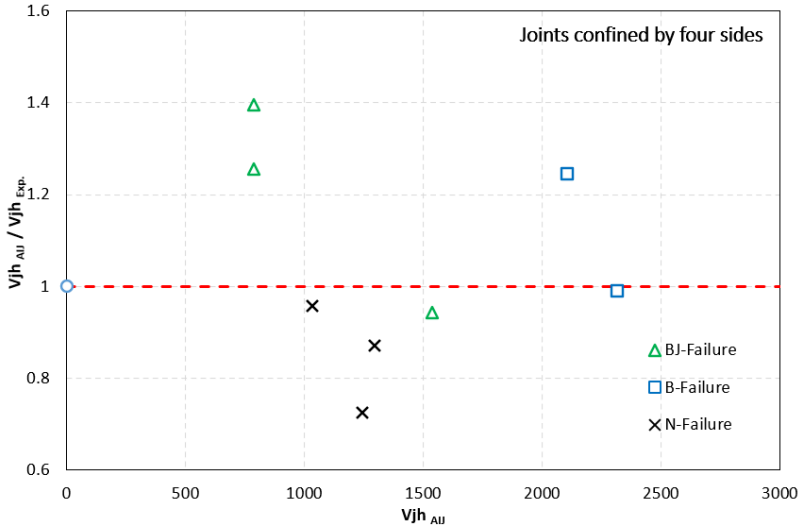

Figure 5.6 Predicted joint shear strength based on AIJ vs experimental joint shear strength; a) exterior joints, b) interior joints, and c) joints confined by all four sides.

(a)

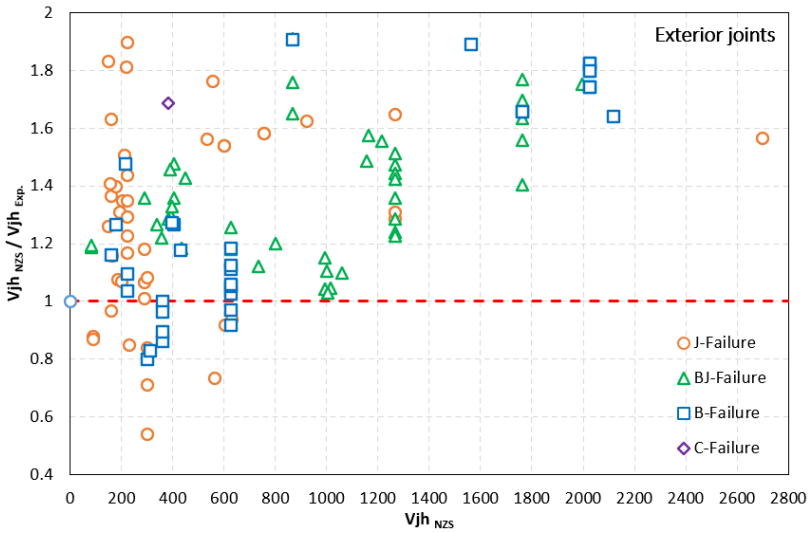

(b)

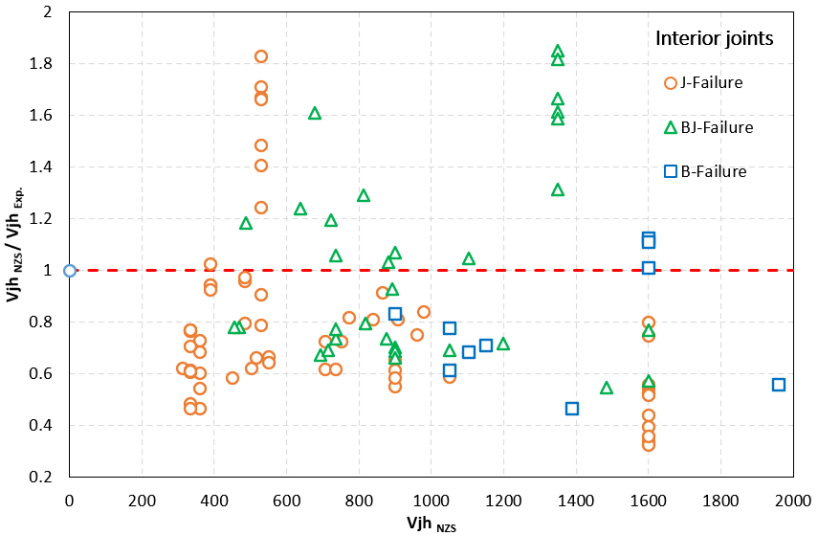

(c)

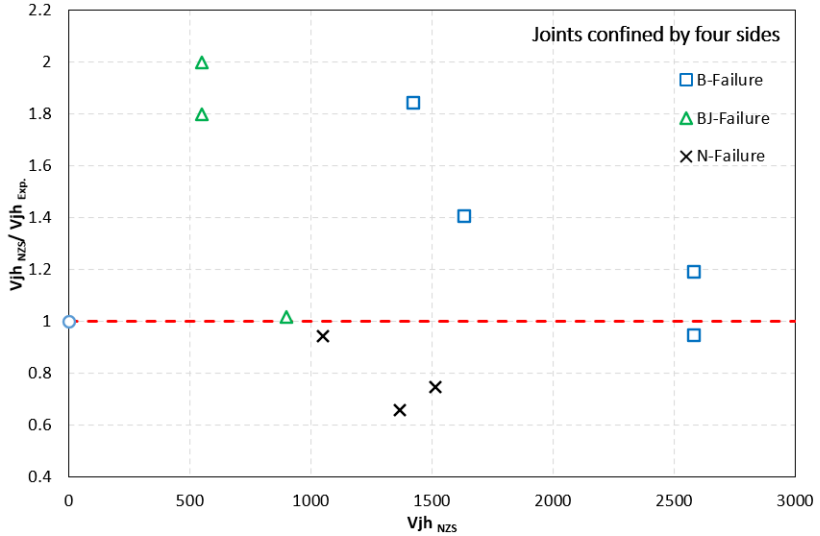

Figure 5.7 Predicted joint shear strength based on NZS 3101-1 vs experimental joint shear strength; a) exterior joints, b) interior joints, and c) joints confined by all four sides.

(a)

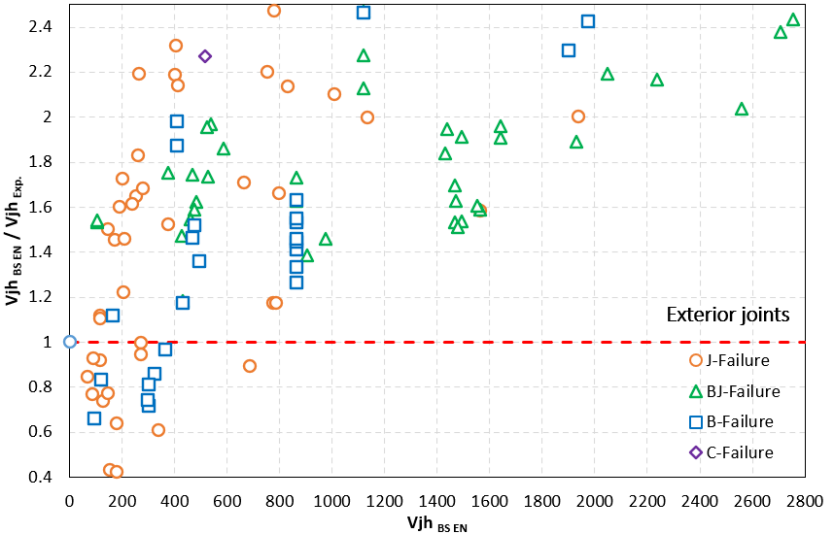

(b)

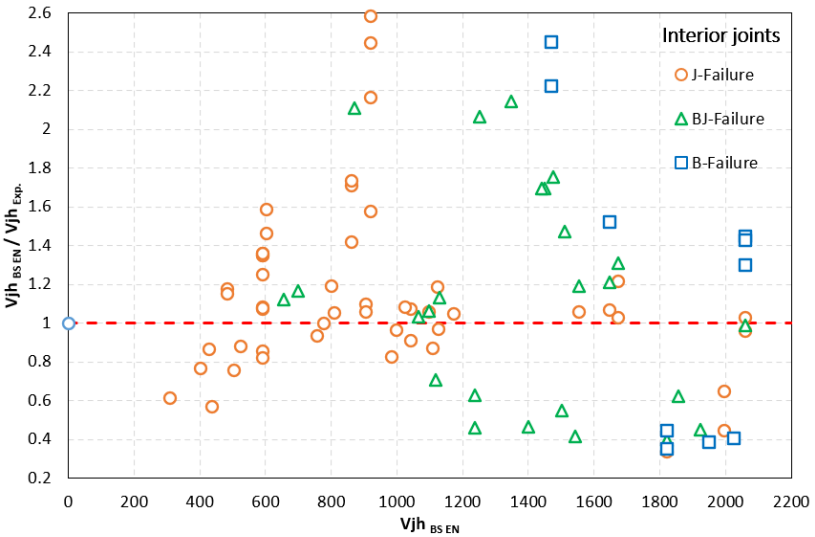

(c)

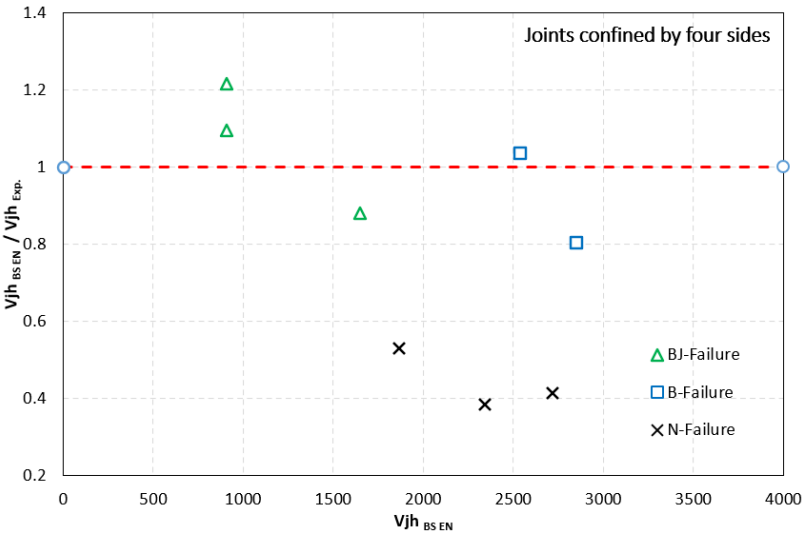

Figure 5.8 Predicted joint shear strength based on BS EN 1998-1 vs experimental joint shear strength; a) exterior joints, b) interior joints, and c) joints confined by all four sides.

For exterior joints, none of the seven codes can accurately estimate the joint shear strength of RC beam-column joints with confidence. While the ratio of predicted to experimental joint shear strength is near to one for ACI-ASCE and CSA, the scatter is still very high, indicating a lack of accuracy in these code provisions. In contrast, the joint shear strength predicted by AIJ, NZS, and BS EN shows high standard deviation (SD), coefficient of variation (COV), and mean absolute errors (MAE), suggesting that these codes cannot be relied upon for design purposes. The results indicate that current code provisions do not provide a satisfactory level of accuracy in predicting the joint shear strength RC beam-column joints. This could be because most codes base their provisions on limited parameters, such as the effective joint area and concrete compressive strength, while only a few codes consider the column axial load and the effect of joint confinement by adjoining beams.

For any model to fit data more accurately, the average values should be close to one, and the coefficient of variation should be as little as possible. However, a higher coefficient of variation value indicates a significant difference between the experimental data and the model's predictions. Additionally, the joints that are confined by all four sides show inconsistent results when compared to the experimental joint shear strength. The predicted value has a higher mean absolute error, indicating less accuracy in the model's predictions. Based on these findings, it is clear that none of the national codes mentioned above can be relied upon for safe design purposes. Therefore, it is crucial to improve the models' accuracy to ensure the safe design of structures.

Figures 5.9 to 5.11 present the percentage of specimens that show overestimated joint shear strength by different codes. For the exterior joint, it is clear that 39.5% - 86% of the investigated specimens show an overestimated joint shear strength, whereas the interior joint and joint

confined by all four sides show an overestimated joint shear strength of about 30%-61% and 30% -80% respectively.

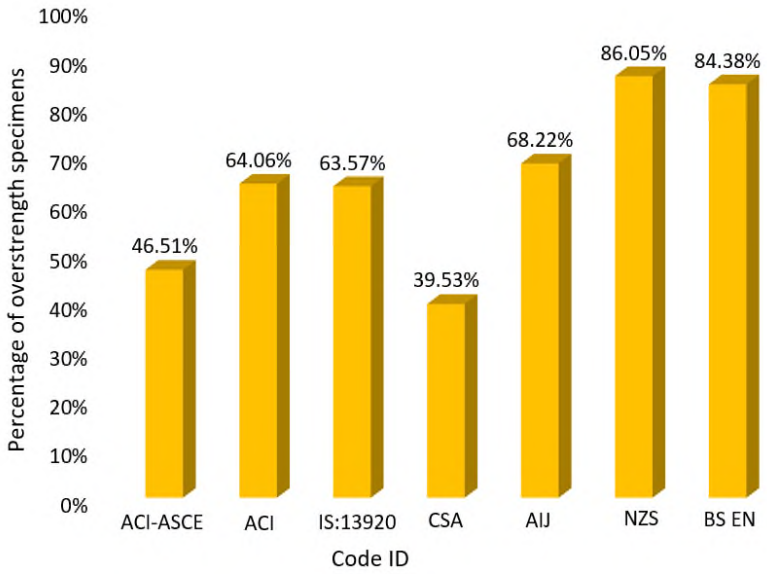

Figure 5.9 The percentage of exterior joints that shows overestimated joint shear strength based on different codes.

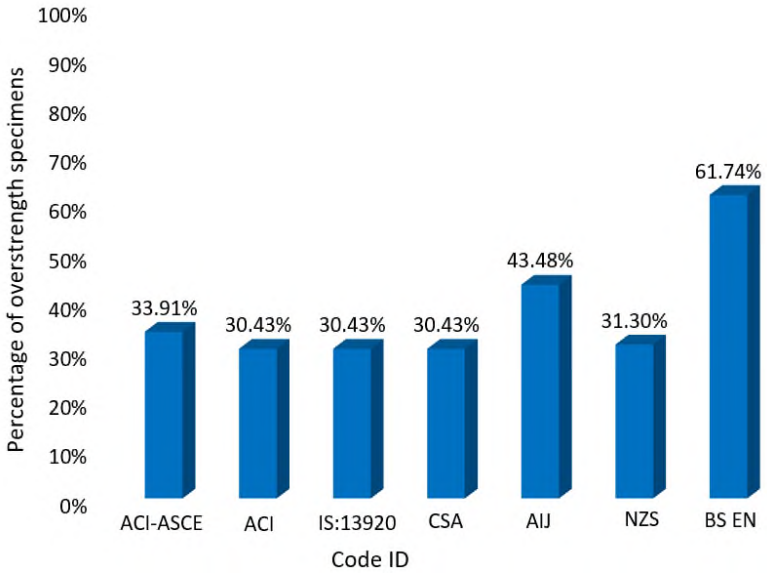

Figure 5.10 The percentage of interior joints that shows overestimated joint shear strength based on different codes.

Figure 5.11 The percentage of joints confined by all four sides that shows overestimated joint shear strength based on different codes.

There are significant differences in the shear strength predicted by various codes, and these discrepancies can be attributed to several reasons. Firstly, different codes use varying methods for determining the effective joint width. Secondly, most codes, except for ACI-ASCE, ACI, and IS 13920, do not account for the effect of eccentricities between the beam and column. Thirdly, the codes impose different limitations on the concrete compressive strength. Lastly, different codes adopt different confinement factors.

Based on the statistical analysis presented above, it is evident that none of the codes available in the literature can safely predict the shear capacity of RC beam-column joints. This raises the question of why beam-column joints can suffer significant damage despite being constructed in accordance with the code criteria.

5.4 Application of ACI 318 code on the experimental results of the present study.

The comparison presented in Table 5.6 demonstrates that the joint shear force calculated using ACI 318 [17] (based on Eq. 5.3) tends to overestimate the experimental results for both NSC and UHPC specimens tested under cyclic and monotonic load conditions. Specifically, the predicted joint shear force is overestimated by a range of 45% to 55% for NSC specimens and 73% to 130% for UHPC specimens tested under cyclic load. Furthermore, the variation is even higher for specimens tested under monotonic load. It is noteworthy that the anticipated joint shear strength of NSC specimens is observed to be 106%-117% greater than the experimental joint shear strength, whereas for UHPC specimens, it is notably higher at 165%-183%.

Figure 5.12 displays the correlation between the predicted joint shear strength and the experimental outcomes. The figure reveals a substantial discrepancy between the predicted and experimental joint shear strength values, suggesting that the ACI 318 code provision is not accurate in predicting the joint shear strength of the corner beam-column joint.

In summary, the comparison in Table 5.6 and Figure 5.12 indicates that the predicted joint shear strength using ACI 318 is significantly higher than the experimental joint shear strength. This can be attributed to several factors, including the limited variables considered in the code provision, the lack of consideration for the bidirectional load applied to the joint core, the effect of high-strength concrete, and the axial load supported by the column. The findings of this study highlight the need for further research to improve the accuracy of the code provision for predicting the joint shear strength.

The paragraph discusses the results of a study that compared the experimental joint shear factor ($\gamma_{Exp.}$) and the joint shear factor adopted by

ACI 318 (γ_{ACI}) for NSC and UHPC specimens tested under cyclic and monotonic loads. The comparison was conducted using Table 5.6, which presents the results for both factors in columns (6) and (7).

According to the results, the joint shear strength factor adopted by ACI 318 was overestimated for both NSC and UHPC specimens tested under cyclic and monotonic loads. The percentage of overestimation was found to 24% to 33% higher for NSC specimens tested under cyclic load, and ranged from 62% to 99% for UHPC specimens.

The overestimation percentages were found to be much higher for both NSC and UHPC specimens tested under monotonic load. The joint shear strength factor adopted by ACI 318 was overestimated by 77%-87% and 129%-145% for NSC and UHPC specimens, respectively.

To further illustrate the differences between the experimental joint shear factor and the joint shear factor adopted by ACI provision, Figure 5.13 was presented. This figure shows a comparison between the two factors for both NSC and UHPC specimens tested under cyclic and monotonic loads. Overall, the results of the study indicate that the joint shear factor adopted by ACI 318 may not be reliable for predicting the shear behavior of NSC and UHPC specimens, particularly under monotonic loading conditions.

Table 5.6 Experimental results of the tested specimens

Group ID (1)	Specimens ID (2)	$Vjh_{Exp.}$ kN (3)	Vjh_{ACI} kN (4)	$\frac{Vjh_{ACI}}{Vjh_{Exp.}}$ (5)	$\frac{\gamma_{Exp.}{}^{(1)}}{\sqrt{MPa}}$ (6)	$\frac{\gamma_{ACI.}{}^{(2)}}{\sqrt{MPa}}$ (7)	$\frac{\gamma_{ACI}}{\gamma_{Exp.}}$ (8)
Specimens tested under cyclic load							
I	$CJ_1NT_1S_{50}C$	259.76	381.17	1.47	0.79	1.00	1.26
	$CJ_2NT_1S_{50}C$	255.79	381.17	1.49	0.78	1.00	1.28
	$CJ_2U_{1h}T_1S_{50}C$	379.19	718.6	1.90	0.61	1.00	1.64
	$CJ_2U_{2h}T_1S_{50}C$	374.44	718.6	1.92	0.60	1.00	1.66
	$CJ_1U_{1h}T_1S_{50}C$	383.62	718.6	1.87	0.62	1.00	1.62
II	$CJ_2NT_1S_{100}C$	245.34	381.17	1.55	0.75	1.00	1.33
	$CJ_2U_{1h}T_1S_{100}C$	313.04	718.6	2.30	0.50	1.00	1.99
	$CJ_2U_{2h}T_1S_{100}C$	348.47	718.6	2.06	0.56	1.00	1.78
III	$CJ_2U_{1c}T_1S_{50}C$	370.75	718.6	1.94	0.60	1.00	1.68
	$CJ_2U_{1c}T_1S_{100}C$	366.78	718.6	1.96	0.59	1.00	1.70
IV	$CJ_2NT_2S_{50}C$	263.09	381.17	1.45	0.80	1.00	1.24
	$CJ_2NT_2S_{100}C$	256.35	381.17	1.49	0.78	1.00	1.28
	$CJ_2U_{1h}T_2S_{50}C$	414.80	718.6	1.73	0.67	1.00	1.50
	$CJ_2U_{1h}T_2S_{100}C$	389.85	718.6	1.84	0.63	1.00	1.59
Specimens tested under monotonic load							
I	$CJ_2NT_1S_{50}M$	230.57	475.2	2.06	0.71	1.25	1.77
II	$CJ_2NT_1S_{100}M$	218.98	475.2	2.17	0.67	1.25	1.87
I	$CJ_2U_{1h}T_1S_{50}M$	339.17	898.2	2.65	0.55	1.25	2.29
II	$CJ_2U_{1h}T_1S_{100}M$	323.02	898.2	2.78	0.52	1.25	2.41
III	$CJ_2U_{1c}T_1S_{50}M$	331.48	898.2	2.71	0.53	1.25	2.34
III	$CJ_2U_{1c}T_1S_{100}M$	317.36	898.2	2.83	0.51	1.25	2.45

(1)$\gamma_{Exp.} = Confinement\ factor\ based\ on\ exprimental\ results$

(2)$\gamma_{ACI} = Confinement\ factor\ based\ on\ ACI$

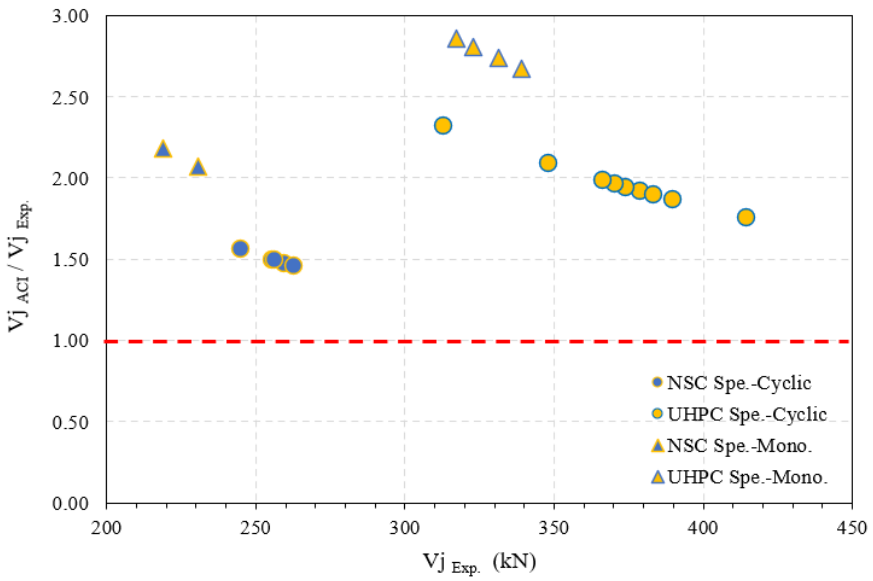

Figure 5.12 Relationship between the predicted and experimental joint shear strength.

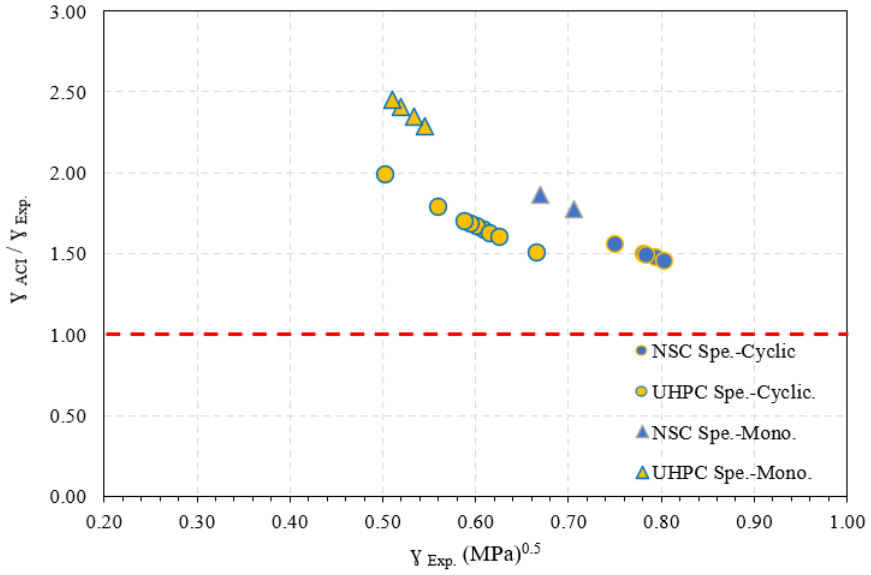

Figure 5.13 Relationship between the predicted and experimental joint shear strength factor.

In order to overcome the shortcomings of the existing code's provision, it is advised to develop a new model that can better capture the complexities of beam-column joints. This new model could be developed by either the strut and tie principle or machine learning techniques. To ensure the accuracy and reliability of this model, it should account for all the factors that have an impact on the behavior of the joint, even those that are currently overlooked by prevailing codes.

Upon conducting statistical analysis of the data gathered from both literature review and present experimental results, it is advisable to utilize the ACI 318 [17] code provisions for estimating the joint shear strength of exterior beam-column joints. This is due to the widespread use of the ACI 318 code and simple application for designing the exterior beam-column joint. However, it is recommended that modify the joint shear strength factor and joint width calculated according to ACI-ASCE in order to ensure a conservative and safe design, as the beam-column joint is a crucial element in maintaining the structural integrity of reinforced concrete structures.

Following a comprehensive statistical analysis of the literature database and experimental results of the present study, it has been recommended that the joint shear strength factor for the NSC joint be adjusted to 0.70, and 0.50 for UHPC specimens, and then the joint shear strength calculated based on Eqs. 5.9 and 5.10, respectively. Accurate estimation of joint shear strength is crucial for ensuring the safety and reliability of structural systems, making this finding particularly significant for the field of beam-column joint design. Figure 5.14 illustrates that modifying the ACI 318 provision led to a reduction in the number of specimens that exhibited overestimated joint shear strength to 6%. Additionally, Figure 5.15 demonstrates the correlation between experimental joint shear strength conductedin the present study and that predicted based on the modified ACI 318 provision.

$$V_{uj} = 0.70\sqrt{f_c^{`}}\, h_c b_j \quad \rightarrow \quad \text{for NSC} \qquad 5.09$$

$$V_{uj} = 0.50\sqrt{f_c^{`}}\, h_c b_j \quad \rightarrow \quad \text{for UHPC} \qquad 5.10$$

Where

$$b_j \leq \begin{cases} \dfrac{b_c + b_b}{2} \\ b_b + \sum_{b_c} \dfrac{m h_c}{2} \end{cases}$$

b_c: column width, b_b: beam width, h_c: total depth of column, and m: Slope to define the effective width of joint transverse to the direction of shear.

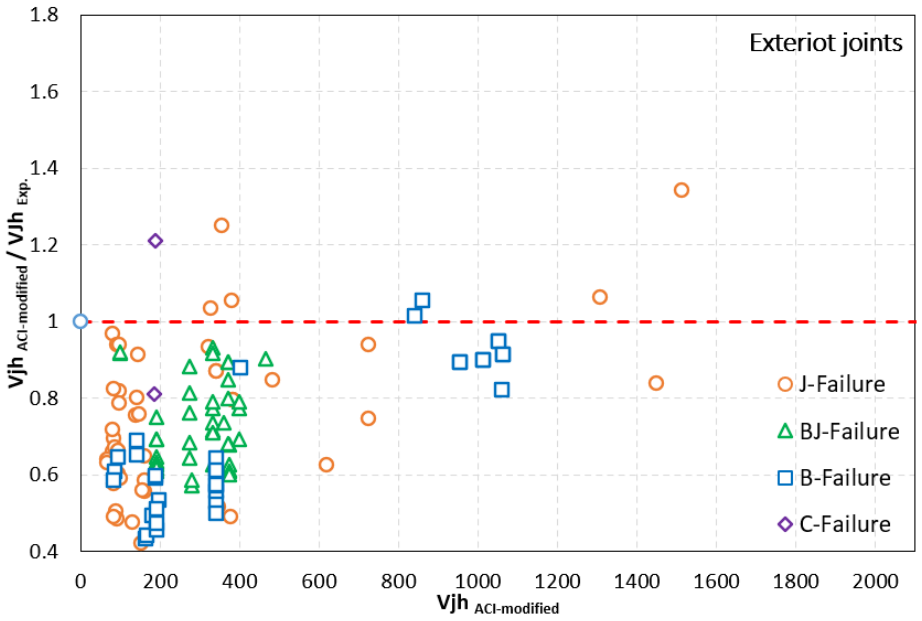

Figure 5.14 Predicted joint shear strength based on modified ACI vs. experimental joint shear strength for exterior beam-column joints.

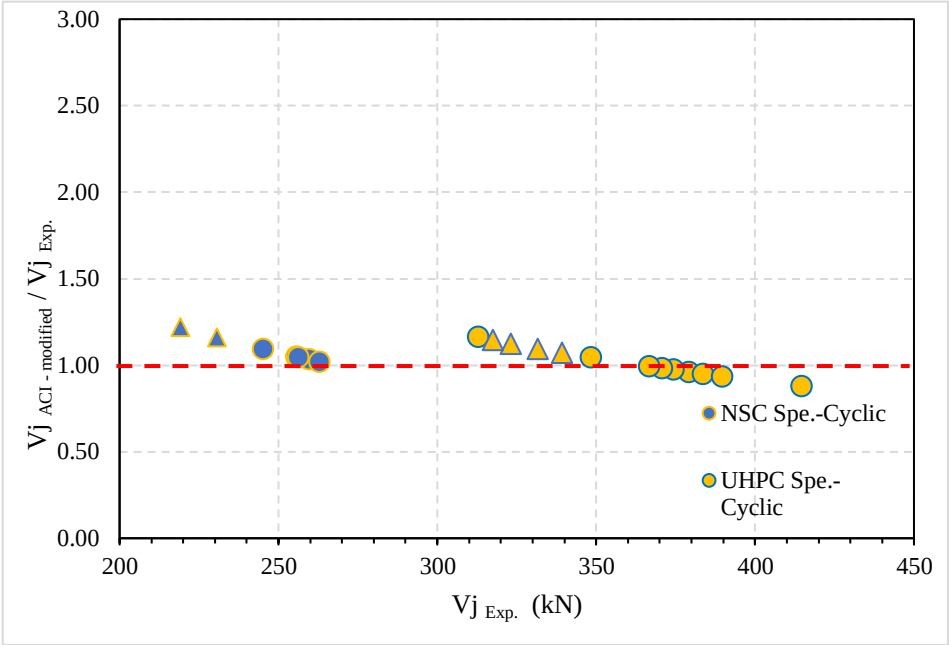

Figure 5.15 Relationship between the predicted joint shear strength based on modified ACI provision and experimental result of the present study.

Chapter Six

Conclusions and Recommendations

6.1 Introduction

In this study, an in-depth review and experimental investigation were carried out to examine the behavior of hybrid RC corner beam-column joints subjected to both cyclic and monotonic loads. The review summarized various studies that employed hybrid concrete techniques to enhance the seismic performance of beam-column joints and presented the significant factors that influence joint behavior. Additionally, the standard codes commonly used to determine joint shear strength were evaluated.

The experimental study had several objectives, including trying to shift the failure mode from joint shear failure (brittle failure) to flexural failure (ductile failure), eliminating the transverse reinforcement in the joint core, reducing the need to closely transverse reinforcement in adjoint members, and decreasing the embedded length of the longitudinal bar in the beam that passes through the joint core. To achieve these goals, twenty-two RC corner beam-column joints were tested under cyclic and monotonic loads, considering various factors such as the joint material, the UHPC configuration in the joint region, the casting method, the amount and spacing

of transverse reinforcement in the joint and adjoining members, and the type and diameter of the longitudinal bar in the beam.

Based on the results of the experimental study and the review, the following conclusions were made:

6.2 Experimental conclusions

1. Using transverse reinforcement in the joint core according to code requirements can't prevent the formation of severe diagonal cracks in the joint core.
2. The utilization of UHPC in the joint region modifies the failure mechanism from the typical joint shear failure observed in NSC specimens to flexural failure through the creation of a plastic hinge at the joint–beam interface.
3. In spite of the complete absence of transverse reinforcement in the joint core, the use of UHPC in the joint region is capable of preventing the formation of severe diagonal cracks in the joint core. This could be attributed to the elevated shear resistance of UHPC.
4. Utilizing the UHPC in the joint region compensates for the shear strength reduction of adjoining members due to increase the spacing of transverse reinforcement from d/4 to d/2.
5. The UHPC specimens show a significant improvement in the ultimate load capacity with stable behavior till failure. The ultimate load capacity increases by about 50%.
6. The UHPC improves the performance of beam-column joints in terms of damage tolerance, energy absorption, stiffness and joint shear strength.
7. The UHPC confined the beam longitudinal bars well and prevented it from buckling due to the increased spacing of transverse reinforcement.
8. Utilize UHPC in addition to transverse reinforcement in the joint core shows similar behavior to that with only UHPC in the joint core. This

confirms the efficiency of UHPC in resisting the shear force and compensates for the role of transverse reinforcement in the joint core.

9. Although most of the UHPC specimens show similar behavior in terms of cracking patterns, failure mode, stiffness and ultimate load regardless of transverse reinforcement spacing, the UHPC specimens with transverse reinforcement distributed at d/4 show an increase in energy absorption of about 20%-60% compared to those with transverse reinforcement distributed at d/2.
10. The rehabilitation of the corner RC beam-column joint has proven to be highly effective through the removal of the NSC in the joint region, which is then replaced by UHPC. This approach has been shown to exhibit superior performance in comparison to NSC joints, with significant improvements in both joint shear strength and initial stiffness by approximately 50% and 45% respectively. In summary, this method of rehabilitation demonstrates a promising solution for enhancing the overall structural integrity and resilience of corner beam-column joints.
11. Despite the presence of a cold joint at the interface NSC-UHPC, it has been shown that this type of joint exhibits similar behavior to those cast using hot methods. In fact, it is reasonable to assert that the bond between the NSC and UHPC is practically superior. This observation can be attributed to the outstanding mechanical properties of UHPC, including high strength, high ductility, and excellent bonding characteristics.
12. The bond between the beam longitudinal bar passing through the joint core has deteriorated for the NSC specimens when the development length of the tension bar in beams was reduced to 15 bar diameter.
13. Given the significant bond strength of UHPC, it is not necessary for longitudinal bars in beams that pass through the joint core to be developed to 25 times the bar diameter as required by most national codes. It was found that 15 times the diameter of the bar passing through the UHPC

joint was adequate to prevent the occurrence of the pullout failure mechanism.

14. Even though the transverse reinforcement was not included in the joint core and the spacing of the transverse reinforcement in the adjoint members was increased, while the development length of the longitudinal bar in the beam passing through the joint core was decreased to 15 bar diameter, the use of UHPC in the joint region compensated for these shortcomings. Additionally, the failure mode of the corresponding NSC specimens changed from joint shear failure to flexural failure.
15. The UHPC joints show about 50% higher joint shear force in comparison with NSC specimens.
16. Both configurations of UHPC in the joint region show similar behavior. However, columns in the second configuration of UHPC show no flexural cracks.
17. The addition of near-surface mounted steel bars at both sides of beams for the cold joint restricted the propagation of cracks through the depth of the beam.
18. Despite some hairline cracks, the joint core in the overall UHPC specimens remained intact. This is due to the fact that the tensile stress in UHPC is approximately 40% higher than the principal tensile strength of the specimens at the ultimate load.
19. Using UHPC in the joint core and extending it to cover a distance equal to the beam depth through the beam and a distance equal to the column depth above and below the joint core (known as the D-region) is a practical approach due to the high cost of UHPC. This is because the D-region experiences the greatest tensile and shear cracks, making it the most critical area to be reinforced with UHPC.
20. In the current study, specimens tested under monotonic load exhibited behavior similar to those tested under cyclic load. The joint core in NSC

specimens sustained severe damage and ultimately failed due to joint shear failure.

21. The use of GFRP bars as hybrid reinforcement for beams results in poor behavior, with failure occurring due to the pullout of GFRP bars from the joint core before they reach their ultimate capacity.
22. Strengthening the beam at the tension side by NSM GFRP bars show superior behavior and the specimen reaches its ultimate capacity without deboning or pullout of GFRP bars from the joint core.

6.3 Theoretical conclusions

According to the deep review in this field, the following conclusion can be drawn:

1. The ACI 318 provision show an overestimated joint shear strength. The predicted joint shear force shows overestimated value that ranges between 45% to 54% for NSC specimens and 73% to 130% for UHPC specimens. Therefore it can't be adopted for design purposes.
2. Extensive statistical analysis of experimental joint shear strength and that predicted according to various national codes (including ACI-ASCE 352, ACI-318, IS 13920, CSA A23.3, AIJ, NZS 3101, and BS EN) has revealed a significant discrepancy between predicted and actual joint shear strength. In fact, all of the examined national codes exhibited a tendency to overestimate joint shear strength, with a high degree of scatter in the data. This finding highlights a key challenge in designing concrete structures, where reliance on national codes alone may result in inadequate joint shear strength and expose the beam-column joint to severe damage.

3. Based on statistical analysis it was found that the modified ACI equations shown below for calculating joint shear strength were conservative and can be adopted for the design of the exterior beam-column joint.

$$V_{uj} = 0.70\sqrt{f_c^{`}}\, h_c b_j \quad \rightarrow \quad \text{for NSC}$$

$$V_{uj} = 0.50\sqrt{f_c^{`}}\, h_c b_j \quad \rightarrow \quad \text{for UHPC}$$

6.4 Recommendations

Generally, despite the large body of literature on the behavior of hybrid joints, and experimental work, there are still many challenges that need to be addressed. Based on the experimental results, several recommendations are made below, with further issues that need to be highlighted.

1. Develop a three-dimensional finite element model utilizing original software, taking into consideration the characteristics of UHPC, to verify the behavior of RC hybrid corner beam-column joints.
2. Investigate the behavior of the UHPC corner joint without special reinforcement detail under reverse cyclic load.
3. Beams with large diameters of 20 and 25 mm should be used in experiments to determine the optimal length of the longitudinal bar that must pass through the UHPC joint area and compare with the code requirement.
4. Repairing the integrity of an RC corner beam-column joint by replacing the deteriorated joint area with UHPC after yielding the beam longitudinal bar under varying degrees of damage.
5. Theoretically, a new provision should be driven to calculate the joint shear strength according to the strut and tie model or based on machine learning because most of the national shows over estimate joint shear strength and this can’t be adopted in the practical design.

[1] A. Ghobarah, M. Saatcioglu, and I. Nistor, “The impact of the 26 December 2004 earthquake and tsunami on structures and infrastructure,” *Eng Struct*, vol. 28, no. 2, pp. 312–326, 2006, doi: 10.1016/j.engstruct.2005.09.028.

[2] B. Zhao, F. Taucer, and T. Rossetto, “Field investigation on the performance of building structures during the 12 May 2008 Wenchuan earthquake in China,” *Eng Struct*, vol. 31, no. 8, pp. 1707–1723, 2009, doi: 10.1016/j.engstruct.2009.02.039.

[3] T. R. MCEER-00-0003, “The Chi-Chi, Taiwan, Earthquake of September 21, 1999: Reconnaissance Report,” 2000. [Online]. Available: http://nisee.berkeley.edu/elibrary/Text/S37336

[4] G. I. Kalogeropoulos, A. D. G. Tsonos, D. Konstandinidis, and S. Tsetines, “Pre-earthquake and post-earthquake retrofitting of poorly detailed exterior RC beam-to-column joints,” *Eng Struct*, vol. 109, pp. 1–15, 2016, doi: 10.1016/j.engstruct.2015.11.009.

[5] S. Pampanin, G. M. Calvi, and M. Moratti, “Seismic behaviour of RC beam-column joints designed for gravity loads,” *12th Europen Conference on Earthquake Engineering*, vol. 726, no. May 2014, pp. 1–10, 2002, [Online]. Available: ir.canterbury.ac.nz/bitstream/10092/173/1/12587505_Main.pdf%60

[6] C. Beschi, P. Riva, G. Metelli, and A. Meda, “HPFRC Jacketing of non seismically detailed RC corner joints,” *Journal of Earthquake Engineering*, vol. 19, no. 1, pp. 25–47, 2015, doi: 10.1080/13632469.2014.948646.

[7] CEB (Comite Euro-International du Beton), *Rc Frames Under Earthquake Loading:State of the art report*. Lausanne, Switzerland: Thomas Telford Services Ltd, 1996. doi: 10.1680/rcfuel.35478.

[8] M. Saatcioglu *et al.*, “The August 17, 1999, Kocaeli (Turkey) earthquake - Damage to structures,” *Canadian Journal of Civil Engineering*, vol. 28, no. 4, pp. 715–737, 2001, doi: 10.1139/cjce-28-4-715.

[9] H. Sezen, K. J. Elwood, A. S. Whittaker, K. M. Mosalam, J. W. Wallace, and J. F. Stanton, “Structural Engineering Reconnaissance of the August 17, 1999, Kocaeli (Izmit), Turkey, Earthquake,” Berkeley, 2000.

[10] M. Miyamjima *et al.*, “Site Investigation of the Sarpole-Zahab Earthquake, Mw 7.3 in SW Iran of November 12, 2017,” *JSCE Journal of Disaster FactSheets*, 2018.

[11] M. Khodaei, M. H. Saghafi, and A. Golafshar, “Seismic retrofit of exterior beam-column joints using steel angles connected by PT bars,” *Eng Struct*, vol. 236, no. October 2020, p. 112111, Jun. 2021, doi: 10.1016/j.engstruct.2021.112111.

[12] Wael Mohammed Hassan, “Analytical and Experimental Assessment of Seismic Vulnerability of Beam-Column Joints without Transverse Reinforcement in Concrete Buildings,” PhD Thesis, University of California, Berkeley, 2011. [Online]. Available: https://escholarship.org/uc/item/98384265

[13] M. S. Günay and K. M. Mosalam, “Structural Engineering Reconnaissance of the April 6, 2009, Abruzzo, Italy, Earthquake, and Lessons Learned,” *Pacific Earthquake Engineering*

Research Center, 2010, [Online]. Available: http://nisee.berkeley.edu/elibrary/Text/200607187

[14] National Information Service for Earthquake Engineering, "Pacific Earthquake Engineering Center," *University of California Berkeley*.

[15] G. Metelli, F. Messali, C. Beschi, and P. Riva, "A model for beam-column corner joints of existing RC frame subjected to cyclic loading," *Eng Struct*, vol. 89, pp. 79–92, 2015, doi: 10.1016/j.engstruct.2015.01.038.

[16] ACI-ASCE Committee 352, "Recommendations for Design of Beam-Column Connections in Monolithic Reinforced Concrete Structures," 2010.

[17] ACI committee 318, *Building Code Requirements for Reinforced Concrete and Commentary*. Farmington Hills: American Concrete Institute, 2019.

[18] M. Engindeniz, "Repair and strengthening of pre-1970 reinforced concrete corner beam -column joints using CFRP composites," *PhD Thesis*, no. August, p. 397, 2008.

[19] B. Novák, K. Ramanjaneyulu, C. Roehm, and S. Sasmal, "Comparison of Seismic Performance of D-region of Existing RC Structures Designed with Different Recommendations," *Journal of Structural Engineering*, pp. 46–51, 2008.

[20] M. Engindeniz, L. F. Kahn, and A.-H. Zureick, "Pre-1970 Rc Corner Beam-Column-Slab Joints: Seismic Adequacy and Upgradeability With Cfrp Composites," *14th World Conference on Earthquake Engineering (14WCEE)*, pp. 1–8, 2008.

[21] J. P. Moehle, "Existing Reinforced Concrete Building Construction: A Review of Practices and Vulnerabilities," 1998.

[22] ACI committee 318, *Building Code Requirements for Structural Concrete*. Farmington Hills, Mich.: American Concrete Institute, 1971.

[23] R. Park and T. Paulay, "Behavior of reinforced concrete external beam-column joints under cyclic loading," in *In Proceedings of the 5th World Conference on Earthquake Engineering*, Rome, 1973. [Online]. Available: http://www.iitk.ac.in/nicee/wcee/article/5_vol1_772.pdf

[24] ACI-ASCE Committee 352, "Recommendations for Design of Beam-Column Joints in Monolithic Reinforced Concrete Structures.," *American Concrete Institute*, vol. 73, no. 7, pp. 375–393, 1976, doi: 10.14359/11078.

[25] W. Nadir, A. Y. Ali, and M. M. A. Kadhim, "Structural behavior of hybrid reinforced concrete beam-column joints under cyclic load: State of the art review," *Case Studies in Construction Materials*, vol. 15, no. e00707, 2021, doi: 10.1016/j.cscm.2021.e00707.

[26] C. H. Henager, "Steel Fibrous, Ductile Concrete Joint for Seismic-Resistant Structures.," *American Concrete Institute*, vol. 53, pp. 371–386, 1977, doi: 10.14359/17703.

[27] T. Jiuru, H. Chaobin, Y. Kaijian, and Y. Yongcheng, "Seismic Behavior and Shear Strength of Framed Joint Using Steel-Fiber Reinforced Concrete," *Journal of Structural Engineering*, vol. 118, no. 2, pp. 341–358, 1992, doi: 10.1061/(asce)0733-9445(1992)118:2(341).

[28] S. J. Hwang, H. J. Lee, and K.-C. Wang, “SEISMIC DESIGN AND DETAILING OF EXTERIOR REINFORCED CONCRETE BEAM-COLUMN JOINTS,” in *13 th World Conference on Earthquake Engineering*, Vancouver, B.C., Canada, 2004, pp. 1–12.

[29] K. Shi, M. Zhang, T. Zhang, P. Li, J. Zhu, and L. Li, “Seismic performance of steel fiber reinforced high–strength concrete beam–column joints,” *Materials*, vol. 14, no. 12, 2021, doi: 10.3390/ma14123235.

[30] A. G. Tsonos, “Cyclic load behaviour of reinforced concrete beam-column subassemblages of modern structures,” *Earthquake Resistant Engineering Structures*, vol. 81, no. 1999, pp. 439–449, 2005, doi: 10.14359/18777.

[31] A. G. Tsonos, “Cyclic Load Behavior of Reinforced Concrete Beam-Column Subassemblages of Modern Structures,” *ACI Struct J*, vol. 104, no. 4, pp. 439–449, 2007, doi: 10.14359/18777.

[32] ACI 318, *Building Code Requirements for Structural Concrete*. Farmington Hills: American Concrete Institute, 2005. [Online]. Available: www.concrete.org

[33] ACI-ASCE Committee 352, “Recommendations for Design of Beam-Column Connections in Monolithic Reinforced Concrete Structures,” 2002.

[34] CEN Techn. Comm. 250/SC2, *Eurocode 2: Design of Concrete Structures-Part 1: General Rules and Rules for Buildings (ENV 1992-1-1) CEN*. Berlin, 1991.

[35] C. Techn. Comm. 250/SC8, *Eurocode 8: Earthquake Resistant Design of Structures-Part 1: General Rules and Rules for Buildings (ENV 1998-11/2/3) CEN*. Berlin.

[36] New Greek Earthquake Resistant Code, *(C.D.C.S.-1995)*. Athens, 1195.

[37] G. J. Parra-Montesinos, S. W. Peterfreund, and S. H. Chao, “Highly damage-tolerant beam-column joints through use of high-performance fiber-reinforced cement composites,” *American Concrete Institute*, vol. 102, no. 3, pp. 487–495, 2005, doi: 10.14359/14421.

[38] Ben Graybeal, “Bond Behavior of Reinforcing Steel in Ultra-High Performance Concrete,” *FHWA-HRT-14-089*, 2014.

[39] Ben Graybeal, “Design and Construction of Field-Cast UHPC Connections,” 2014. doi: 10.13140/2.1.2839.0087.

[40] Z. B. Haber, I. D. la Varga, B. A. Graybeal, B. Nakashoji, and R. El-Helou, “Properties and Behavior of UHPC-Class Materials,” *Fhwa-Hrt-18-036*, no. March, p. 153, 2018.

[41] Y. Huang, S. Grünewald, E. Schlangen, and M. Luković, “Strengthening of concrete structures with ultra high performance fiber reinforced concrete (UHPFRC): A critical review,” *Constr Build Mater*, vol. 336, no. March, p. 127398, 2022, doi: 10.1016/j.conbuildmat.2022.127398.

[42] A. Bentur and S. Mindess, *Fibre Reinforced Cementitious Composites:Modern Concrete Technology Series*, Second edi. NewYork, NY 10016,USA: Taylor & Francis, 2007. doi: 10.1201/9781482267747-8.

[43] A. E. Naaman and H. W. Reinhardt, “Proposed classification of HPFRC composites based on their tensile response,” *Materials and Structures/Materiaux et Constructions*, vol. 39, no. 5, pp. 547–555, 2006, doi: 10.1617/s11527-006-9103-2.

[44] A. E. Naaman, “Tensile strain-hardening FRC composites: Historical evolution since the 1960,” *Advances in Construction Materials 2007*, pp. 181–202, 2007, doi: 10.1007/978-3-540-72448-3_19.

[45] W. C. Liao, S. H. Chao, S.-Y. Park, and a. E. Naaman, “Self-Consolidating High Performance Fiber Reinforced Concrete: SCHPFRC,” Ann Arbor, USA, 2006.

[46] B. Graybeal, E. Brühwiler, B. Kim, F. Toutlemonde, Y. L. Voo, and A. Zaghi, “International Perspective on UHPC in Bridge Engineering,” *Journal of Bridge Engineering*, vol. 25, no. 11, p. 04020094, Nov. 2020, doi: 10.1061/(ASCE)BE.1943-5592.0001630.

[47] ASTM C1856, “Standard Practice for Fabricating and Testing Specimens of Ultra-High Performance Concrete,” *ASTM International*, vol. i, p. 4, 2017, doi: 10.1520/C1856.

[48] C.-C. Hung, S. El-Tawil, and S.-H. Chao, “A Review of Developments and Challenges for UHPC in Structural Engineering: Behavior, Analysis, and Design,” *Journal of Structural Engineering*, vol. 147, no. 9, p. 03121001, 2021, doi: 10.1061/(asce)st.1943-541x.0003073.

[49] S. Muzenski, Z. B. Haber, and B. Graybeal, “Interface Shear of Ultra-High-Performance Concrete,” *ACI Struct J*, vol. 119, no. 1, pp. 267–280, 2022, doi: 10.14359/51733008.

[50] ACI 239R, “Ultra-high-performance concrete: An emerging technology report,” *American Concrete Institute ACI 239*, 2018.

[51] B. Graybeal, “Ultra-High Performance Concrete UHPC,” 2011.

[52] E. Brühwiler, “‘Structural UHPFRC’: Welcome to the post-concrete era !,” in *First International Interactive Symposium on UHPC - 2016*, 2016. doi: 10.21838/uhpc.2016.key.

[53] K. Zmetra and B. A. Graybeal, “Design and Construction of UHPC-Based Bridge Preservation and Repair Solutions,” 2022, doi: 10.21949/1521867.

[54] A. M. Kodsy, “Repair and Strengthening of Concrete Bridges Using Ultra-High-Performence Concrete (UHPC),” University of Nebraska, Lincoln, Nebraska, 2022.

[55] V. Perry and G. Weiss, “Innovative Field Cast UHPC Joints for Precast Bridge Decks. Design, Prototype Testing and Projects,” *Designing and Building with UHPFRC*, pp. 421–436, 2013, doi: 10.1002/9781118557839.ch28.

[56] Y. L. Voo and S. J. Foster, “Malaysia , Taking Ultra High Performance Concrete Bridges To New Dimensions,” *AFGC-ACI-fib-RILEM Int. Symposium on Ultra-High Performance Fibre-Reinforced Concrete*, no. 1, pp. 1033–1042, 2017.

[57] Z. Hajar, J. Resplendino, D. Lecointre, J. Petitjean, and A. Simon, “Ultra-high-performance concretes: First recommendations and examples of application,” in *Proceedings of the fib Symposium 2004 - Concrete Structures: The Challenge of Creativity*, 2004, pp. 242–243.

[58] E. Denarié, “Structural rehabilitations with Ultra-High Performance Fibre Reinforced Concretes (UHPFRC),” *Concrete Repair, Rehabilitation and Retrofitting - Proceedings of the International Conference on Concrete Repair, Rehabilitation and Retrofitting, ICCRRR 2005*, vol. 12, no. 5, pp. 22–24, 2006.

[59] Z. B. Haber, K. Zmetra, and B. A. Graybeal, “Design and Construction of UHPC - Based Bridge Preservation and Repair Solutions,” 2022. doi: 10.21949/1521867.

[60] G. Doiron, “UHPC PIER REPAIR / RETROFIT EXAMPLES OF COMPLETED PROJECTS IN NORTH AMERICA,” *AFGC-ACI-fib-RILEM Int. Symposium on Ultra-High Performance Fibre-Reinforced Concrete*, no. 1, pp. 983–992, 2017.

[61] R. Park and T. Paulay, *Reinforced Concrete Structures*, First edit. Christchurch, New Zealand: John Wiley & Sons, 1975.

[62] T. Paulay, R. Park, and M. J. N. Priestley, “Reinforced Concrete Beam-Column Joints Under Seismic Actions.,” *American Concrete Institute*, vol. 75, no. 11, pp. 585–593, 1978, doi: 10.14359/10971.

[63] T. Paulay and A. Scarpas, “The Behaviour of Exterior Beam-Column Joint,” *Bulletin of the New Zealand Society for Earthquake Engineering*, vol. 14, no. 3, pp. 131–144, 1981, doi: 10.5459/bnzsee.14.3.131-144.

[64] T. Paulay and M. J. N. Priestley, *Seismic Design of Reinforced Concrete and Masonry Buildings*. Canada: John Wiley & Sons, Inc., 1992.

[65] G. Genesio, *Seismic Assessment of RC Exterior Beam- Column Joints and Retrofit with Haunches Using Post-Installed Anchors*. 2012.

[66] Y. Jemaa, “Seismic behaviour of deficient exterior RC beam-column joints,” *PhD Thesis*, p. 297, 2013.

[67] H. J. Lee and S. J. Hwang, “High-strength concrete and reinforcing steel in beam-column connections,” *Structures Congress 2013: Proceedings of the 2013 Structures Congress*, pp. 1606–1615, 2013, doi: 10.1061/9780784412848.140.

[68] M. R. Ehsani and J. K. Wight, “Exterior Reinforced Concrete Beam-To-Column Connections Subjected To Earthquake-Type Loading.,” *American Concrete Institute*, vol. 82, no. 4, pp. 492–499, 1985, doi: 10.14359/10361.

[69] T. KAKU, H. ASAKUSA, and M. AOKI, “Ductility Estimation of Exterior Beam-Column Subassemblages in Reinforced Concrete Frames,” *Journal of Structural and Construction Engineering (Transactions of AIJ)*, vol. 401, no. 0, pp. 87–96, 1989, doi: 10.3130/aijsx.401.0_87.

[70] S. Fuji and S. Morita, “Comparison between interior and exterior RC beam-column joint behaviour,” *ACI Symposium Publication*, vol. 123, pp. 145–166, 1991, doi: 10.14359/2836.

[71] M. R. Ehsani and F. Alameddine, “Design Recommendations for Type 2 High-Strength Reinforced Concrete Connections,” *ACI Struct J*, vol. 88, no. 3, 1991, doi: 10.14359/3108.

[72] R. H. Scott, “Intrinsic mechanisms in reinforced concrete beam-column connection behavior,” *ACI Struct J*, vol. 93, no. 3, pp. 336–346, 1996, doi: 10.14359/9693.

[73] C. C. Chen and G. K. Chen, “Cyclic behavior of reinforced concrete eccentric beam-column corner joints connecting spread-ended beams,” *ACI Struct J*, vol. 96, no. 3, pp. 443–449, 1999, doi: 10.14359/680.

[74] S. J. Hamil, “Reinforced Concrete Beam-Column Connection Behaviour,” *PhD Thesis*, p. School of Engineering, University of Durham, 2000.

[75] J. Hegger, A. Sherif, and W. Roeser, “Nonseismic Design of Beam-Column Joints,” *ACI Struct J*, vol. 100, no. 5, pp. 654–664, 2003, doi: 10.14359/12807.

[76] S. J. Hwang, H. J. Lee, and K. C. Wang, “Seismic design and detailing of exterior reinforced concrete beam-column joints, Proceedings of the 13th world conference on earthquake engineering, paper no. 0397, Vancouver,” *B.C., Canada*, no. 397, pp. 1–12, 2004.

[77] H. F. Wong, “Shear strength and seismic performance of non-seismically designed reinforced concrete beam-column joints,” Hong Kong University of Science and Technology, Hong Kong, 2005. [Online]. Available: http://lbezone.ust.hk/bib/b914043#

[78] S. J. Hwang, H. J. Lee, T. F. Liao, K. C. Wang, and H. H. Tsai, “Role of hoops on shear strength of reinforced concrete beam-column joints,” *ACI Struct J*, vol. 102, no. 3, pp. 445–453, 2005, doi: 10.14359/14416.

[79] H. J. Lee and J. W. Ko, “Eccentric reinforced concrete beam-column connections subjected to cyclic loading in principal directions,” *ACI Struct J*, vol. 105, no. 3, pp. 380–382, 2008.

[80] C. E. Chalioris, M. J. Favvata, and C. G. Karayannis, “Reinforced concrete beam–column joints with crossed inclined bars under cyclic deformations,” *Earthq Eng Struct Dyn*, vol. 37, no. 6, pp. 881–897, May 2008, doi: 10.1002/eqe.793.

[81] B. Li and S. A. Kulkarni, “Seismic Behavior of Reinforced Concrete Exterior Wide Beam-Column Joints,” *Journal of Structural Engineering*, vol. 136, no. 1, pp. 26–36, 2010, doi: 10.1061/(asce)0733-9445(2010)136:1(26).

[82] J. S. Kaung and H. F. Wong, “Effectiveness of horizontal stirrups in joint core for exterior beam-column joints with nonseismic design,” *Procedia Eng*, vol. 14, pp. 3301–3307, 2011, doi: 10.1016/j.proeng.2011.07.417.

[83] S. C. Chun and Y. S. Shin, “Cyclic testing of exterior beam-column joints with varying joint aspect ratio,” *ACI Struct J*, vol. 111, no. 3, pp. 693–704, 2014, doi: 10.14359/51686730.

[84] A. J. D. Durrani and J. K. Wight, “Behavior of Interior Beam-to-Column Connections Under Earthquake-Type Loading,” *ACI Journal Proceedings*, vol. 82, no. 3, pp. 343–349, 1985, doi: 10.14359/10341.

[85] Fuji and S. Morita, “Comparison Between Interior and Exterior R/C Beam-Column Joint Behavior,” *ACI Symposium Publication*, vol. 123, pp. 145–166, 1991, doi: 10.14359/2836.

[86] K. Kitayama, S. Otani, and H. Aoyama, “Development of Design Criteria for Rc Interior Beam-Column Joints,” *American Concrete Institute, Special Publication SP-123*, vol. 123, pp. 97–123, 1991.

[87] K. Oka and H. Shiohara, “Tests of high-strength concrete interior beam-column-joint subassemblages,” in *Earthquake Engineering. Tenth World Conference*, Balkema. Flotterdam, 1992, pp. 3211–3217.

[88] T. R. Gentry and J. K. Wight, “Wide Beam-Column Connections under Earthquake-Type Loading,” *Earthquake Spectra*, vol. 10, no. 4, pp. 675–703, Nov. 1994, doi: 10.1193/1.1585793.

[89] G. S. Raffaelle and J. K. Wight, “Reinforced concrete eccentric beam-column connections subjected to earthquake-type loading,” *ACI Struct J*, vol. 92, no. 1, pp. 45–55, 1995, doi: 10.14359/1474.

[90] J. M. LaFave and J. K. Wight, “Reinforced concrete exterior wide beam-column-slab connections subjected to lateral earthquake loading,” *ACI Struct J*, vol. 96, no. 4, pp. 577–585, 1999.

[91] K. Fumio, A. Keiko, S. Hitoshi, and O. Shunsuke, “Tests of Reinforced Concrete Interior Beam-Column Joint Subassemblage with Eccentric Beams,” *13th World Conference on Earthquake Engineering*, no. 185, 2004.

[92] G. Yasuaki and J. Osamu, “shear resistance of interior eccentric beam-column joints,” in *13th World Conference on Earthquake Engineering*, Vancouver, B.C., Canada, 2004, p. 649.

[93] M. Teraoka, K. Hayashi, S. Sasaki, and N. Takamori, “Estimation of Restoring Force Characteristics in the Interior Beam-and-Column Subassemblages of R / C Frames,” *Fujita Technical Research*, no. 41, pp. 1–12, 2005.

[94] S. Teng and H. Zhou, “Eccentric reinforced concrete beam-column joints subjected to cyclic loading,” *ACI Struct J*, vol. 100, no. 2, pp. 139–148, 2003, doi: 10.14359/12477.

[95] B. Li and C. L. Leong, “Experimental and Numerical Investigations of the Seismic Behavior of High-Strength Concrete Beam-Column Joints with Column Axial Load,” *Journal of Structural Engineering*, vol. 141, no. 9, p. 04014220, 2014, doi: 10.1061/(asce)st.1943-541x.0001191.

[96] H. Yang, W. Zhao, Z. Zhu, and J. Fu, “Seismic behavior comparison of reinforced concrete interior beam-column joints based on different loading methods,” *Eng Struct*, vol. 166, no. March, pp. 31–45, 2018, doi: 10.1016/j.engstruct.2018.03.022.

[97] H. Shiohara and F. Kusuhara, “COMPREHENSIVE SERIES OF TESTS ON SEISMIC PERFORMANCE OF REINFORCED CONCRETE BEAM-COLUMN JOINTS,” in *Proceedings of the 3rd international conference on advances in experi- mental structural engineering, SanFrancisco*, 2009, pp. 1–11.

[98] P. Alaee and B. Li, “High-Strength Concrete Interior Beam-Column Joints with High-Yield-Strength Steel Reinforcements,” *Journal of Structural Engineering*, vol. 143, no. 7, p. 04017038, 2017, doi: 10.1061/(asce)st.1943-541x.0001773.

[99] B. B. Canbolat and J. K. Wight, “Experimental investigation on seismic behavior of eccentric reinforced concrete beam-column-slab connections,” *ACI Struct J*, vol. 105, no. 2, pp. 154–162, 2008, doi: 10.14359/19730.

[100] G. N. Guimaraes, M. E. Kreger, and J. O. Jirsa, “Evaluation of joint-shear provisions for interior beam-column-slab connections using high-strength materials,” *ACI Struct J*, vol. 89, no. 1, pp. 89–98, 1992, doi: 10.14359/1299.

[101] C. G. Quintero-Febres and J. K. Wight, “Experimental study of reinforced concrete interior wide beam-column connections subjected to lateral loading,” *ACI Struct J*, vol. 98, no. 4, pp. 572–582, 2001, doi: 10.14359/10300.

[102] National Standard of Canada CSA A23.3:19, *Design of concrete structures*. Toronto, Ontario, M9W 1R3, 2019.

[103] N. Z. Standard, “Concrete Structures Standard Part 1: The Design of Concrete Structures,” Wellington, 1995.

[104] K. Sarsam and Z. M. K. Al-azzawi, “Shear Capacity of High-Strength Fiber Reinforced Concrete Beam-Column Joints,” vol. 28, no. 6, 2010.

[105] IS:13920-2016, “Ductile Design and Detailing of Reinforced Concrete Structures Subjected to Seismic Forces — Code of Practice,” *Bureau of Indian Standards, New Delhi*, no. July, pp. 1–121, 2016.

[106] P. G. Bakir and H. M. Boduroğlu, “A new design equation for predicting the joint shear strength of monotonically loaded exterior beam-column joints,” *Eng Struct*, vol. 24, no. 8, pp. 1105–1117, 2002, doi: 10.1016/S0141-0296(02)00038-X.

[107] Kazuo, Ohno, and T. Shibata, “On the Damage to the Hakodate College by the Tokachioki Earthquake, 1968,” *Proceedings of the U.S.-Japan Seminar on Earthquake Engineering with Emphasis on the Safety of School Buildings*, pp. 123–140, 1973, [Online]. Available: http://hdl.handle.net/2115/37920

[108] O. Joh, Y. Goto, and T. Shibata, “Behavior of Reinforced Concrete Beam-Column Joints With Eccentricity,” *Special Publication*, vol. 123, pp. 317–358, 1991, [Online]. Available: https://www.concrete.org/publications/internationalconcreteabstractsportal/m/details/id/2863

[109] ACI-ASCE Committee, “Recommendations for Design of Beam-Column Joints in Monolithic Reinforced Concrete Structures.,” *Journal of the American Concrete Institute*, vol. 82, no. 3, pp. 266–283, 1985, doi: 10.14359/11078.

[110] M. Shin and J. M. LaFave, “Seismic performance of reinforced concrete eccentric beam-column connections with floor slabs,” *ACI Struct J*, vol. 101, no. 3, pp. 403–412, 2004, doi: 10.14359/13100.

[111] B. B. Canbolat and J. K. Wight, “Experimental investigation on seismic behavior of eccentric reinforced concrete beam-column-slab connections,” *ACI Struct J*, vol. 105, no. 2, pp. 154–162, 2008, doi: 10.14359/19730.

[112] S. Pantazopoulou and J. Bonacci, “Consideration of Questions about Beam-Column Joints,” *ACI Struct J*, vol. 89, no. 1, pp. 27–36, 1993, doi: 10.14359/1281.

[113] R. L. Vollum, “Design and Analysis of Exterior Beam Column Connections,” University of London, London, 1998.

[114] B. E. ; M. C. M. E. Phu Trong Nguyen, “a Study of Shear Behavior of Reinforced Concrete Deep Beams,” *PMFSEL Report No. 82-1*, p. 250, 2013.

[115] C. P. Pantelides, C. Clyde, and L. D. Reaveley, “Performance-based evaluation of reinforced concrete building exterior joints for seismic excitation,” 2000. doi: 10.1193/1.1510447.

[116] S. H. Luk, “Seismic Performance and Post-Peak Behaviour of Reinforced Concrete Beam-Column Joints,” *PhD theisis*, no. August, 2013.

[117] P. R. Gefken and M. R. Ramey, “Increased joint hoop spacing in type 2 seismic joints using fiber reinforced concrete,” *ACI Journal*, vol. 86, no. 2, pp. 168–172, 1989, doi: 10.14359/2674.

[118] S. Hakuto, R. Park, and H. Tanaka, “Seismic load tests on interior and exterior beam-column joints with substandard reinforcing details,” *ACI Struct J*, vol. 97, no. 1, pp. 11–25, 2000, doi: 10.14359/829.

[119] G. Genesio, “Seismic Assessment of RC Exterior Beam- Column Joints and Retrofit with Haunches Using Post-Installed Anchors,” *PhD theisis*, 2012.

[120] C. Liu, “Seismic Behaviour of Beam-Column Joint Subassemblies Reinforced With Steel Fiber,” University of Canterbury, Christchurch, New Zealand, 2006.

[121] R. T. Leon, “Interior Joints with Variable Anchorage Lengths,” *Journal of Structural Engineering*, vol. 115, no. 9, pp. 2261–2275, 1989, doi: 10.1061/(asce)0733-9445(1989)115:9(2261).

[122] R. P. and H. T. Shigeru Hakuto, “Effect of Deterioration of Bond of Beam Bars Passing through Interior Beam-Column Joints on Flexural Strength and Ductility,” *ACI Struct J*, vol. 96, no. 5, 1999, doi: 10.14359/740.

[123] NZS 3101 PARTS 1 AND 2:1995, “Concrete structures standard - The design of concrete structures,” *New Zealand Standards* , 1995.

[124] Y. Mao *et al.*, “Bond and anchorage performance of beam flexural bars in beam-column joints using slag-based geopolymer concrete and their effect on seismic performance,” *Eng Struct*, vol. 273, Dec. 2022, doi: 10.1016/j.engstruct.2022.115062.

[125] L. M. Megget, R. C. Fenwick, and N. Amso, “Seismic performance of internal beam-column joints with 500 grade reinforcement,” in *2003 Pacific Conference on Earthquake Engineering* ,

[126] H. J. Lee, H. C. Chen, and T. C. Tsai, “Simplified Design Equation of Minimum Interior Joint Depth for Special Moment Frames with High-Strength Reinforcement,” *Int J Concr Struct Mater*, vol. 12, no. 1, Dec. 2018, doi: 10.1186/s40069-018-0303-2.

[127] H. J. Hwang, H. G. Park, W. S. Choi, L. Chung, and J. K. Kim, “Cyclic loading test for beam-column connections with 600 MPa (87 ksi) beam flexural reinforcing bars,” *ACI Struct J*, vol. 111, no. 4, pp. 913–924, 2014, doi: 10.14359/51686920.

[128] ACI committee 318, *Building Code Requirements for Structural Concrete*. Farmington Hills, Mich.: American Concrete Institute, 2011.

[129] N. Z. Standard, *The design of concrete structures, NZS 3101.1:2006*, no. 1. New Zealand, 2006.

[130] G. Kotsovou and H. Mouzakis, "Exterior RC beam-column joints: New design approach," *Eng Struct*, vol. 41, pp. 307–319, 2012, doi: 10.1016/j.engstruct.2012.03.049.

[131] N. Mitra and L. N. Lowes, "Evaluation, Calibration, and Verification of a Reinforced Concrete Beam–Column Joint Model," *Journal of Structural Engineering*, vol. 133, no. 1, pp. 105–120, 2007, doi: 10.1061/(asce)0733-9445(2007)133:1(105).

[132] ACI committee 318, *Building Code Requirements for Structural Concrete*. Farmington Hills, Mich.: American Concrete Institute, 2002.

[133] R. T. R. Institute, *Design standards for rail- way structures and commentary (concrete structures)*. Tokyo, Japan, 2004.

[134] S. Park, "Experimental and Analytical Studies on Old Reinforced Concrete Buildings with Seismically Vulnerable Beam-Column Joints," University of California, Berkeley, Berkeley, California, 2010.

[135] S. Park and K. M. Mosalam, "Parameters for shear strength prediction of exterior beam-column joints without transverse reinforcement," *Eng Struct*, vol. 36, pp. 198–209, 2012, doi: 10.1016/j.engstruct.2011.11.017.

[136] H. Dabiri, A. Kaviani, and A. Kheyroddin, "Influence of reinforcement on the performance of non-seismically detailed RC beam-column joints," *Journal of Building Engineering*, vol. 31, no. March, p. 101333, 2020, doi: 10.1016/j.jobe.2020.101333.

[137] S. H. Kang, T. H. Ahn, and D. J. Kim, "Effect of grain size on the mechanical properties and crack formation of HPFRCC containing deformed steel fibers," *Cem Concr Res*, vol. 42, no. 5, pp. 710–720, 2012, doi: 10.1016/j.cemconres.2012.02.011.

[138] H. Singh, *Steel Fiber Reinforced Concrete*, vol. 25, no. 277. in Springer Transactions in Civil and Environmental Engineering, vol. 25. Singapore: Springer Singapore, 2017. doi: 10.1007/978-981-10-2507-5.

[139] ACI Committee 544, "Report on Fiber Reinforced Concrete," *American Concrete Institute*, vol. 96, no. Reapproved, 2009.

[140] R. L. Jindal and K. A. Hassan, "Behavior of Steel Fiber Reinforced Concrete Beam-Column Connections.," *American Concrete Institute*, vol. 81, pp. 107–123, 1984, doi: 10.14359/6447.

[141] R. J. Craig, I. Kafrouni, J. Souaid, S. Mahadev, and H. W. Valentine, "Behavior of Joints Using Reinforced Fibrous Concrete," *American Concrete Institute*, vol. 81, pp. 125–168, 1984.

[142] A. Filiatrault, K. Ladicani, and B. Massicotte, "Seismic performance of code-designed fiber reinforced concrete joints," *American Concrete Institute*, vol. 91, no. 5, pp. 564–571, 1994, doi: 10.14359/4172.

[143] National Builiding Code of Canada, *Associates Committee on the National Building Code*. Ottawa, ON, Canada: National Research Council of Canada, 1990.

[144] A. Filiatrault, S. Pineau, and J. Houde, “Seismic behavior of steel-fiber reinforced concrete interior beam-column joints,” *American Concrete Institute*, vol. 92, no. 5, pp. 543–552, 1995, doi: 10.14359/905.

[145] M. GENCOGGLU and I. EREN, “An Experimental Study on the Effect of Steel Fiber Reinforced Concrete on the Behavior of the Exterior Beam-Column Joints Subjected to Reversal Cyclic Loading,” *Turkish J. Eng. Env. Sci.*, pp. 493–502, 2002, doi: 10.1016/j.compositesb.2009.12.003.

[146] K. Sarsam and Z. M. K. Al-azzawi, “Shear Capacity of High-Strength Fiber Reinforced Concrete Beam-Column Joints,” *Eng. & Tech. Journal*, vol. 28, no. 6, pp. 1253–1266, 2010.

[147] A. NISHIMURA, “Damage Analysis and Seismic Design of Railway Structures for Hyogoken-Nanbu (Kobe) Earthquake,” *Journal of JAEE*, vol. 4, no. 3, pp. 184–194, 2004, doi: 10.5610/jaee.4.3_184.

[148] K. Kojima, K. Watanabe, M. Shinoda, and M. Tateyama, “Outline of performance-based design for railway earth structures in Japan,” *Performance-Based Design in Earthquake Geotechnical Engineering*, 2009, doi: 10.1201/noe0415556149.ch8.

[149] H. Okamura, “Japanese seismic design codes prior to Hyogoken-Nanbu earthquake,” *Cem Concr Compos*, vol. 19, no. 3, pp. 185–192, 1997, doi: 10.1016/s0958-9465(97)00012-7.

[150] J. Niwa, K. Shakya, K. Matsumoto, and K. Watanabe, “Experimental Study on the Possibility of Using Steel Fiber–Reinforced Concrete to Reduce Conventional Rebars in Beam-Column Joints,” *Journal of Materials in Civil Engineering*, vol. 24, no. 12, pp. 1461–1473, 2012, doi: 10.1061/(asce)mt.1943-5533.0000536.

[151] R. Zhang, K. Matsumoto, T. Hirata, Y. Ishizeki, and J. Niwa, “Application of PP-ECC in beam-column joint connections of rigid-framed railway bridges to reduce transverse reinforcements,” *Eng Struct*, vol. 86, pp. 146–156, 2015, doi: 10.1016/j.engstruct.2015.01.005.

[152] J. Niwa, K. Shakya, K. Matsumoto, and K. Watanabe, “Experimental Study on the Possibility of Using Steel Fiber–Reinforced Concrete to Reduce Conventional Rebars in Beam-Column Joints,” *Journal of Materials in Civil Engineering*, vol. 24, no. 12, pp. 1461–1473, 2012, doi: 10.1061/(asce)mt.1943-5533.0000536.

[153] C. Röhm, B. Novák, S. Sasmal, R. Karusala, and V. Srinivas, “Behaviour of fibre reinforced beam-column sub-assemblages under reversed cyclic loading,” *Constr Build Mater*, vol. 36, pp. 319–329, 2012, doi: 10.1016/j.conbuildmat.2012.04.114.

[154] A. A. Abbas, S. M. Syed, and D. M. Cotsovos, “Seismic response of steel fibre reinforced concrete beam – column joints,” *Eng Struct*, vol. 59, pp. 261–283, 2014, doi: 10.1016/j.engstruct.2013.10.046.

[155] J. Shen and Y. Zhang, “Fiber-reinforced Mechanism and Mechanical Performance of Composite Fibers Reinforced Concrete,” *Journal Wuhan University of Technology, Materials Science Edition*, vol. 35, no. 1, pp. 121–130, 2020, doi: 10.1007/s11595-020-2235-3.

[156] H. R. Pakravan, M. Latifi, and M. Jamshidi, “Hybrid short fiber reinforcement system in concrete: A review,” *Constr Build Mater*, vol. 142, pp. 280–294, 2017, doi: 10.1016/j.conbuildmat.2017.03.059.

[157] W. Nguyen, M. J. Bandelt, W. Trono, S. L. Billington, and C. P. Ostertag, “Mechanics and failure characteristics of hybrid fiber-reinforced concrete (HyFRC) composites with longitudinal steel reinforcement,” *Eng Struct*, vol. 183, no. November 2018, pp. 243–254, 2019, doi: 10.1016/j.engstruct.2018.12.087.

[158] B. Hadassa Joice, A. A., and S. Brahmalla, “Review on Behavior of Hybrid Fiber-Reinforced Concrete,” in *Springer Proceedings in Materials*, Springer Proceedings in Materials, 2020, pp. 117–125.

[159] N. Banthia and S. M. Soleimani, “Flexural response of hybrid fiber-reinforced cementitious composites,” *American Concrete Institute*, vol. 102, no. 6, pp. 382–389, 2005, doi: 10.14359/14800.

[160] D. Kheni, R. H. Scott, S. K. Deb, and A. Dutta, “Ductility enhancement in beam-column connections using hybrid fiber-reinforced concrete,” *ACI Struct J*, vol. 112, no. 2, pp. 167–178, 2015, doi: 10.14359/51687405.

[161] IS 13920:1993, *Ductile Detailing of Reinforced Concrete Structures Subjected To Seismic Forces -Code of Practice*. New Delhi, India, 1993.

[162] A. E. Naaman and H. W. Reinhardt, *High Performance Fiber Reinforced Cement Composites 2 (HPFRCC2)*. London SE1 8HN, UK: E & FN Spon, 1996.

[163] M. J. Shannag, N. Abu-Dyya, and G. Abu-Farsakh, “Lateral load response of high performance fiber reinforced concrete beam-column joints,” *Constr Build Mater*, vol. 19, no. 7, pp. 500–508, 2005, doi: 10.1016/j.conbuildmat.2005.01.007.

[164] ACI Committee 318, *Building Code Requirements for Structural Concrete*. Detroit: American Concrete Institute, 1995.

[165] F. Yuan, J. Pan, Z. Xu, and C. K. Y. Leung, “A comparison of engineered cementitious composites versus normal concrete in beam-column joints under reversed cyclic loading,” *Mater Struct*, vol. 46, no. 1–2, pp. 145–159, 2013, doi: 10.1617/s11527-012-9890-6.

[166] N. Ganesan, P. V. Indira, and M. V. Sabeena, “Behaviour of hybrid fibre reinforced concrete beam-column joints under reverse cyclic loads,” *Mater Des*, vol. 54, pp. 686–693, 2014, doi: 10.1016/j.matdes.2013.08.076.

[167] ACI Committee 318, *Building code requirements for structural concrete*, vol. 2007. Farmington Hills: American Concrete Institute, 2008.

[168] S. Qudah and M. Maalej, “Application of Engineered Cementitious Composites (ECC) in interior beam-column connections for enhanced seismic resistance,” *Eng Struct*, vol. 69, pp. 235–245, 2014, doi: 10.1016/j.engstruct.2014.03.026.

[169] Institute Railway Technical Research, *Design standards for railway structures and commentary (concrete structures)*. 2007.

[170] R. Siva Chidambaram and P. Agarwal, “Seismic behavior of hybrid fiber reinforced cementitious composite beam-column joints,” *Mater Des*, vol. 86, pp. 771–781, 2015, doi: 10.1016/j.matdes.2015.07.164.

[171] S. H. Said and H. Abdul Razak, “Structural behavior of RC engineered cementitious composite (ECC) exterior beam-column joints under reversed cyclic loading,” *Constr Build Mater*, vol. 107, pp. 226–234, 2016, doi: 10.1016/j.conbuildmat.2016.01.001.

[172] M. hossein Saghafi and H. Shariatmadar, “Enhancement of seismic performance of beam-column joint connections using high performance fiber reinforced cementitious composites,” *Constr Build Mater*, vol. 180, pp. 665–680, 2018, doi: 10.1016/j.conbuildmat.2018.05.221.

[173] F. Hosseini, B. Gencturk, and S. L. Pour, “SEISMIC BEHAVIOR OF 3D ECC BEAM- COLUMN JOINTS IN SPECIAL MOMENT,” in *Eleventh U.S. National Conf erence on Earthquake Engineering*, Los Angeles, California Seismic: Integrating Science, Engineering & Policy, 2018.

[174] F. Hosseini, B. Gencturk, H. Aryan, and G. Cadaval, “Seismic behavior of 3-D ECC beam-column connections subjected to bidirectional bending and torsion,” *Eng Struct*, vol. 172, no. November 2017, pp. 751–763, 2018, doi: 10.1016/j.engstruct.2018.06.054.

[175] M. H. Saghafi, H. Shariatmadar, and A. Kheyroddin, “Seismic Behavior of High-Performance Fiber-Reinforced Cement Composites Beam-Column Connection with High Damage Tolerance,” *Int J Concr Struct Mater*, vol. 13, no. 1, 2019, doi: 10.1186/s40069-019-0334-3.

[176] A. Dehghani, A. R. Mozafari, and F. Aslani, “Evaluation of the efficacy of using engineered cementitious composites in RC beam-column joints,” *Structures*, vol. 27, no. May, pp. 151–162, 2020, doi: 10.1016/j.istruc.2020.05.045.

[177] M. H. Saghafi, A. Golafshar, M. S. Zareian, and A. H. Mehri, “Application of HPFRCC in beam–column joints to reduce transverse reinforcements,” *Structures*, vol. 31, no. October 2019, pp. 805–814, 2021, doi: 10.1016/j.istruc.2021.02.032.

[178] ACI Committee 318, *ACI 318-14*. Farmington Hills, Mich.: American Concrete Institute, 2014.

[179] D. Wang, J. Zhao, Y. Ju, H. Shen, and X. Li, “Behavior of beam-column joints with high performance fiber-reinforced concrete under cyclic loading,” *Structures*, vol. 44, pp. 171–185, Oct. 2022, doi: 10.1016/j.istruc.2022.07.090.

[180] Architectural Institute of Japan (AIJ), *AIJ standard for structural calculation of reinforced concrete structures*. Maruzen, Tokyo, 2010.

[181] G. Benjamin A., “Material Property Characterization of Ultra-High Performance Concrete,” *FHWA*, no. FHWA-HRT-06-103, p. 186, 2006.

[182] P. Qiao, Z. Zhou, and S. Allena, “Developing Connections for Longitudinal Joints between Deck Bulb Tees-Development of UHPC Mixes with Local Materials,” no. October, 2016.

[183] K. Wille, D. J. Kim, and A. E. Naaman, “Strain-hardening UHP-FRC with low fiber contents,” *Materials and Structures/Materiaux et Constructions*, vol. 44, no. 3, pp. 583–598, 2011, doi: 10.1617/s11527-010-9650-4.

[184] ASTM C230/C230M, “Standard Specification for Flow Table for Use in Tests of Hydraulic Cement 1,” *American Society for Testing and Materials*, 2014, doi: 10.1520/C0230_C0230M-14.

[185] “Standard Test Method for Flow of Hydraulic Cement Mortar 1,” *ASTM C1437*, 2015, doi: 10.1520/C1437.

[186] C. Shi, Z. Wu, J. Xiao, D. Wang, Z. Huang, and Z. Fang, “A review on ultra high performance concrete: Part I. Raw materials and mixture design,” *Constr Build Mater*, vol. 101, pp. 741–751, 2015, doi: 10.1016/j.conbuildmat.2015.10.088.

[187] MasterRoc MS 610, “https://www.master-builders-solutions.com/en-asiapacific/products/masterroc/masterroc-ms-610.”

[188] MasterGlenium 54, “https://www.master-builders-solutions.com/en-ae/products/masterglenium/masterglenium-54.”

[189] HEBEI YUSEN METAL WIRE MESH, “Copper-plated micro-filament steel fiber,” 2021. http://www.china-steelfiber.com.cn/caseshow.php?cid=28&id=68&lang=1

[190] ASTM A820, “Standard Specification forSteel Fibers for Fiber-Reinforced Concrete,” *ASTM*, pp. 1–4, 2016, doi: 10.1520/A0820_A0820M-16.

[191] DAVID J. ELWELL and GONGKANG FU, “Compression Testing of Concrete: Cylinders vs. Cubes,” New York, 12232-0869, 1995.

[192] M. Imam, L. Vandewalle, and F. Mortelmans, “Are current concerete strength tests suitable for high strength concrete?,” *Mater Struct*, vol. 28, no. 7, pp. 384–391, Aug. 1995, doi: 10.1007/BF02473073.

[193] B. Graybeal and M. Davis, “Cylinder or Cube: Strength Testing of 80 to 200 MPa (11.6 to 29 ksi) Ultra-High-Performance Fiber-Reinforced Concrete,” *ACI Mater J*, vol. 105, no. 6, pp. 105-M68, 2008.

[194] O. Q. Aziz and G. H. Ahmed, “Mechanical properties of Ultra High Performance Concrete (UHPC),” in *Twelfth International Conference on Recent Advances in Concrete Technology and Sustainability Issues Prague*, 2012. doi: 10.14359/51684273.

[195] Y. Kusumawardaningsih, E. Fehling, and M. Ismail, “UHPC compressive strength test specimens: Cylinder or cube?,” in *Procedia Engineering*, 2015, pp. 1076–1080. doi: 10.1016/j.proeng.2015.11.165.

[196] B. Graybeal, “Compression testing of ultra-high-performance concrete,” *Adv Civ Eng Mater*, vol. 4, no. 2, pp. 102–112, 2015, doi: 10.1520/ACEM20140027.

[197] ASTM C109/109M, “Standard test method for compressive strength of hydraulic cement mortars (Using 2-in. or cube specimens),” *ASTM*, vol. i, pp. 1–10, 2016, doi: 10.1520/C0109.

[198] ASTM C469, “Standard Test Method for Splitting Tensile Strength of Cylindrical Concrete Specimens,” *ASTM*, vol. i, pp. 1–5, 2011, doi: 10.1520/C0496.

[199] ASTM C78 / C78M, “Standard Test Method for Flexural Strength of Concrete (Using Simple Beam with Third-Point Loading),” *ASTM* , pp. 1–4, 2016, doi: 10.1520/C0078.

[200] ASTMC348, “Standard test method for flexural Strength of hydraulic-cement mortars,” *ASTM*, vol. i, pp. 1–6, 2014, doi: 10.1520/C0348-14.2.

[201] Z. Zhou and P. Qiao, “Direct tension test for characterization of tensile behavior of ultra-high performance concrete,” *J Test Eval*, vol. 48, no. 4, 2018, doi: 10.1520/JTE20170644.

[202] P. K. Mehta and P. J. M. Monteiro, *Concrete ,Microstructure, Properties and Materials*, Third Edition. McGraw-Hill, 2006. doi: doi=10.1036/0071462899.

[203] BS EN 12390-3, “Testing hardened concrete - Part 3: Compressive of test specimens,” pp. 1–16, 2019.

[204] ASTM A615/A615M, “Specification for Deformed and Plain Carbon-Steel Bars for Concrete Reinforcement,” *ASTM*, 2016, doi: 10.1520/A0615_A0615M-16.

[205] Quickmast 108, “https://www.dcp-int.com/qa/ar/products/kwyk-mast-108 .”

[206] Polypoxy NF, “https://www.henkelpolybit.com/en/products/waterproofing/waterproofing-others/epoxy-coatings/polybit-polypoxy-nf.html.”

[207] Sikadur®-330, “https://irq.sika.com/en/construction/refurbishment/structural-strengthening/sikadur-330.html.”

[208] N. W. Hanson and H. W. Connor, “Seismic Resistance of Reinforced Concrete Beam-Column Joints,” in *Proceedings ASCE*, 1967, pp. 533–560.

[209] H. , K. K. Takemura, “Effect of loading hysteresis on ductility capacity of reinforced concrete bridge piers,” *Journal of Structural Engineering*, vol. 43A, pp. 849–858, 1997.

[210] Federal Emergency Management Agency (FEMA), “Effects of Strength and Stiffness Degradation on Seismic Response,” Redwood City, California 94065, 2009. [Online]. Available: www.ATCouncil.org

[211] R. Leon and J. O. Jirsa, “Bidirectional Loading of R.C. Beam-Column Joints,” *Earthquake Spectra*, vol. 2, no. 3, pp. 537–564, May 1986, doi: 10.1193/1.1585397.

[212] O. Gunes, D. Lau, C. Tuakta, and O. Büyüköztürk, “Ductility of FRP-concrete systems: Investigations at different length scales,” *Constr Build Mater*, vol. 49, pp. 915–925, 2013, doi: 10.1016/j.conbuildmat.2012.10.017.

[213] Y. Park and A. H. -S. Ang, “Mechanistic Seismic Damage Model for Reinforced Concrete,” *Journal of Structural Engineering*, vol. 111, no. 4, pp. 722–739, 1985, doi: 10.1061/(asce)0733-9445(1985)111:4(722).

[214] S. Kar and K. C. Biswal, “External shear strengthening of RC beams with basalt fiber sheets: An experimental study,” *Structures*, vol. 31, no. January, pp. 305–315, 2021, doi: 10.1016/j.istruc.2021.01.094.

[215] B. Li, “Initial Stiffness of Reinforced Concrete Columns and Walls,” in *15th World Conference on Earthquake Engineering*, 2012, p. 10. [Online]. Available: https://www.iitk.ac.in/nicee/wcee/article/WCEE2012_0052.pdf

[216] T. El-Amoury and A. Ghobarah, “Seismic rehabilitation of beam-column joint using GFRP sheets,” 2002. [Online]. Available: www.elsevier.com/locate/engstruct

[217] J. Shafaei, A. Hosseini, and M. S. Marefat, “Seismic retrofit of external RC beam-column joints by joint enlargement using prestressed steel angles,” *Eng Struct*, vol. 81, pp. 265–288, Dec. 2014, doi: 10.1016/j.engstruct.2014.10.006.

[218] T. J. Sullivan, G. M. Calvi, and M. J. N. Priestley, “Initial stiffness versus secant stiffness in displacement based design,” in *13th World Conference of Earthquake Engineering (WCEE)*, Vancouver, B.C., Canada, 2004, pp. 581–626.

[219] R. C. Hibbeler, *Mechanics of Materials*, 10th ed. United Kingdom: Pearson Education, Inc., 2017. [Online]. Available: www.pearsonglobaleditions.com/hibbeler

[220] K. F. Sarsam, M. E. Phipps, K. F. Sarsam, and M. E. Phipps, “The shear design of in situ reinforced concrete beam-column joints subjected to monotonic loading,” *Magazine of Concrete Research*, vol. 37, no. 130, pp. 16–28, 1985, doi: 10.1680/macr.1985.37.130.16.

[221] L. Jin, L. Miao, J. Han, X. Du, N. Wei, and D. Li, “Size effect tests on shear failure of interior RC beam-to-column joints under monotonic and cyclic loadings,” *Eng Struct*, vol. 175, no. August, pp. 591–604, 2018, doi: 10.1016/j.engstruct.2018.08.092.

[222] IS 13920 : 2016, “Ductile Design and Detailing of Reinforced Concrete Structures Subjected to Seismic Forces,” 2019. [Online]. Available: https://www.nicee.org/IITK-

[223] H. Y. Choi and J. Y. Lee, “Strength Evaluation of Reinforced Concrete Beam-Column Joints,” in *15 WCEE*, 2012.

Appendix A

Table A-1 Experimental data for exterior RC beam-column joints

No.	Reference	Specimens name	Column details		Beam details				Joint details							Failure mode
			b_c (mm)	h_c (mm)	b_b (mm)	h_b (mm)	ρ_{top}	$\rho_{bott.}$	A_{sh} (mm^2)	S (mm)	fy (MPa)	$f_c^{`}$ (MPa)	N (kN)	$V_{exp.}$ (kN)	γ_j	
1	(Ehsani and Wight, 1985)	1B	299.7	299.7	259.1	480.1	1.93	1.93	508	112	437	33.6	178	570.36	1.10	J
2		2B	299.7	299.7	259.1	480.1	2.13	2.13	508	99	437	35	222	582.03	1.10	J
3		3B	299.7	299.7	259.1	439.4	1.93	1.93	508	84	437	40.9	222	572.15	1.00	BJ
4		4B	299.7	299.7	259.1	439.4	2.13	2.13	508	76	437	44.6	222	607.18	1.01	BJ
5		5B	340.3	340.3	299.7	480.1	1.91	1.91	508	109	437	24.33	356	672.82	1.18	J
6		6B	340.3	340.3	299.7	480.1	1.43	1.43	508	117	437	39.8	303	491.01	0.67	J
7	(KAKU, ASAKUSA and AOKI, 1989)	1	220	220	160	220	1.56	1.56	56	52	250	31.1	258	377.20	1.11	B
8		2	220	220	160	220	1.56	1.56	56	52	250	41.7	199	318.80	0.96	B
9		3	220	220	160	220	1.56	1.56	56	52	250	41.7	0	273.20	0.82	BJ
10		4	220	220	160	220	1.56	1.56	14	52	281	44.7	360	365.30	0.90	BJ
11		5	220	220	160	220	1.56	1.56	14	52	281	36.7	160	291.00	0.86	BJ
12		6	220	220	160	220	1.56	1.56	14	52	281	40.4	0	268.20	0.80	BJ
13		7	220	220	160	220	1.56	1.56	56	52	250	32.2	194	376.00	1.11	B
14		8	220	220	160	220	1.56	1.56	56	52	250	41.2	160	313.70	0.95	B
15		9	220	220	160	220	1.56	1.56	56	52	250	40.6	0	303.60	0.94	BJ
16		10	220	220	160	220	1.56	1.56	14	52	281	44.4	360	365.30	0.91	B
17		11	220	220	160	220	1.56	1.56	14	52	281	41.9	160	298.50	0.93	BJ
18		12	220	220	160	220	1.56	1.56	14	52	281	35.1	0	268.20	0.84	BJ
19		13	220	220	160	220	1.56	1.56	56	52	250	46.4	-100	314.80	0.78	BJ
20		14	220	220	160	220	1.56	1.56	14	52	281	41	160	298.50	0.92	BJ
21		15	220	220	160	220	1.56	1.56	14	52	281	39.7	160	298.50	0.95	BJ
22		16	220	220	160	220	1.56	1.56	56	52	251	37.4	0	362.30	1.00	B
23		17	220	220	160	220	1.56	1.56	56	52	251	39.7	0	227.70	0.70	CJ
24		18	220	220	160	220	1.56	1.56	56	52	251	40.7	0	154.30	0.47	CJ
25	(Fuji and Morita, 1991)	B1	220	220	160	250	1.67	1.67	56	50	297	30	98	246.20	1.08	J
26		B2	220	220	160	250	1.67	1.67	56	50	297	30	98	213.90	0.93	BJ
27		B3	220	220	160	250	1.67	1.67	56	50	297	30	343	272.70	1.19	J
28		B4	220	220	160	250	1.67	1.67	112	35	297	30	343	287.40	1.26	J

Table A-1 continued

No.	Reference	Specimens name	Column details		Beam details				Joint details							Failure mode
			b_c (mm)	h_c (mm)	b_b (mm)	h_b (mm)	ρ_{top}	$\rho_{bott.}$	A_{sh} (mm^2)	S (mm)	fy (MPa)	$f_c^{`}$ (MPa)	N (kN)	$V_{exp.}$ (kN)	γ_j	
29	(Ehsani and Alameddine, 1991)	LL8	356	356	311	508	1.52	1.52	381	102	446	55.1	294	860.30	0.98	BJ
30		LH8	356	356	311	508	1.52	1.52	381	61	446	55.1	294	838.00	0.94	BJ
31		HL8	356	356	311	508	1.92	1.92	381	102	446	55.1	507	986.60	1.11	J
32		HH8	356	356	311	508	1.92	1.92	381	61	446	55.1	507	985.70	1.12	BJ
33		LL11	356	356	311	508	1.52	1.52	381	102	446	75.8	285	769.10	0.74	J
34		LH11	356	356	311	508	1.52	1.52	381	61	446	75.8	276	934.10	0.90	BJ
35		HL11	356	356	311	508	1.92	1.92	381	102	446	75.8	587	967.50	0.93	J
36		HH11	356	356	311	508	1.92	1.92	381	61	446	75.8	605	1020.90	0.98	BJ
37		LL14	356	356	311	508	1.52	1.52	381	102	446	96.5	236	877.60	0.75	BJ
38		LH14	356	356	311	508	1.52	1.52	381	61	446	96.5	222	890.50	0.76	BJ
39		HH14	356	356	311	508	1.92	1.92	381	61	446	96.5	476	1032.40	0.88	BJ
40	(Scott, 1996)	C1	150	150	110	210	1.00	1.00	57	210	414	39.9	275	141.75	1.00	B
41		C1A	150	150	110	210	1.00	1.00	57	210	414	48	275	146.25	0.94	B
42		C1AL	150	150	110	210	1.00	1.00	57	210	414	33.36	50	119.25	0.92	J
43		C2	150	150	110	210	1.00	1.00	57	210	414	49.36	275	117.00	0.74	J
44		C3	150	150	110	210	1.00	1.00	57	210	414	36	275	139.50	1.03	B
45		C3L	150	150	110	210	1.00	1.00	57	210	414	35.5	50	117.00	0.87	J
46		C4	150	150	110	210	1.80	1.80	57	210	414	41.44	275	173.25	1.20	J
47		C4A	150	150	110	210	1.80	1.80	57	210	414	44.32	275	186.75	1.25	J
48		C4Al	150	150	110	210	1.80	1.80	57	210	414	35.8	50	166.50	1.24	J
49		C5	150	150	110	210	1.80	1.80	57	210	414	33	275	81.00	0.63	J
50		C6	150	150	110	210	1.80	1.80	57	210	414	39.8	275	128.25	0.90	J
51		C6L	150	150	110	210	1.80	1.80	57	210	414	45.8	50	153.00	1.00	J
52		C7	150	150	110	300	1.30	1.30	57	210	414	35.2	275	112.50	0.84	J
53		C8	150	150	110	300	1.30	1.30	57	300	414	44.5	275	96.75	0.64	J
54		C9	150	150	110	300	1.30	1.30	57	300	414	35.9	275	99.00	0.73	J
55	(Chen and Chen, 1999)	JC	500	500	300	500	1.56	1.56	579	75	399	20	0	771.73	0.86	BJ
56		JE	500	500	300	500	1.56	1.56	579	75	399	19.9	0	739.75	0.88	BJ
57		JS1	500	500	300	500	1.56	1.56	579	75	399	19.9	0	816.50	0.98	
58		JS2	500	500	300	500	1.56	1.56	579	75	399	21.2	0	825.00	0.96	
59		JS3	500	500	300	500	1.56	1.56	579	75	399	20.3	0	829.30	0.98	
60		JS4	500	500	300	500	1.56	1.56	579	75	399	20.1	0	835.70	0.99	

Table A-1 continued

No.	Reference	Specimens name	Column details		Beam details				Joint details							Failure mode
			b_c (mm)	h_c (mm)	b_b (mm)	h_b (mm)	ρ_{top}	$\rho_{bott.}$	A_{sh} (mm^2)	S (mm)	fy (MPa)	$f_c^{`}$ (MPa)	N (kN)	$V_{exp.}$ (kN)	γ_j	
61	(Hegger, Sherif and Roeser, 2003)	RK1	150	240	150	300	1.67	1.67	157	75	530	57.9	500	374.00	1.37	B
62		RK2	150	240	150	300	1.67	1.67	100	75	530	57.4	500	417.00	1.53	B
63		RK3	150	240	150	300	1.67	1.67	157	75	530	57.2	500	402.00	1.48	B
64		RK4	150	200	150	300	1.67	1.67	157	75	530	51.7	500	357.00	1.66	J
65		RK5	150	200	150	300	2.62	2.62	157	75	530	54.9	500	423.00	1.90	J
66		RK6	150	200	150	300	2.62	2.62	157	75	530	86.5	500	556.00	1.99	J
67		RK7	150	200	150	400	1.20	1.20	157	100	530	54.7	500	277.00	1.25	J
68		RK8	150	200	150	300	1.67	1.67	157	75	530	38.6	500	273.00	1.46	J
69	(Hwang, Lee and Wang, 2004)	70-3T44	420	420	320	450	1.65	1.65	508	97	436	76.8	196	1065.00	0.78	B
70		70-3T4	450	450	320	450	1.65	1.65	254	97	436	75.2	196	1110.00	0.74	B
71		70-2T5	450	450	320	450	1.65	1.65	402	146	469	76.6	196	1162.00	0.77	B
72		70-1T55	450	450	320	450	1.65	1.65	804	293	469	69.7	196	1126.00	0.78	B
73		28-3T4	550	550	380	500	1.23	1.23	254	122	436	35	196	1290.00	0.85	B
74		28-0T0	550	550	380	500	1.23	1.23	0	0	0	33	196	1138.00	0.77	BJ
75	Wong (Wong, 2005)	JA-NY03	300	300	260	400	0.69	0.69	141	200	500	34.9	471.15	302.60	0.57	BJ
76		JA-NY15	300	300	260	400	0.69	0.69	141	200	200	38.5	519.75	323.70	0.58	BJ
77		JB-NY03	300	300	260	300	0.96	0.97	141	150	200	34.2	461.7	327.60	0.62	BJ
78		BS-L-H1	300	300	260	450	0.91	0.91	142	150	500	33.3	449.55	389.30	0.75	J
79		BS-L-H2	300	300	260	450	0.91	0.91	142	90	500	42.1	568.35	479.30	0.82	J
80	Hwang et al.(Hwang *et al.*, 2005)	0T0	420	420	320	450	1.65	1.65	0	0	0	67.3	196	997.00	0.78	BJ
81		3T44	420	420	320	450	1.65	1.65	579	97	498	76.8	196	1065.00	0.78	B
82		1B8	420	420	320	450	1.65	1.65	0	0	0	61.8	196	1257.00	1.03	BJ
83		3T3	420	420	320	450	1.65	1.65	213	97	471	69	196	1132.00	0.88	BJ
84		2T4	420	420	320	450	1.65	1.65	325	146	498	71	196	1080.00	0.82	BJ
85		1T44	420	420	320	450	1.65	1.65	579	293	498	72.8	196	1039.00	0.78	BJ
86		3T4	450	450	320	450	1.65	1.65	325	97	498	75.2	196	1110.00	0.74	B
87		2T5	450	450	320	450	1.65	1.65	400	146	469	76.6	196	1162.00	0.77	B
88		1T55	450	450	320	450	1.65	1.65	800	293	469	69.7	196	1126.00	0.78	B
89	Lee & Ko (Lee and Ko, 2008)	S0	400	600	300	450	1.29	1.29	237	100	471	32.6	782.4	827.00	0.69	B
90		S50	400	600	300	450	1.29	1.29	237	100	471	34.2	820.8	814.00	0.64	B
91		W0	600	400	300	450	1.29	1.29	395	100	471	28.9	693.6	778.00	0.90	BJ
92		W75	600	400	300	450	1.29	1.29	395	100	471	30.4	729.6	781.00	0.89	BJ
93		W150	600	400	300	450	1.29	1.29	395	100	471	29.1	698.4	739.00	0.91	BJ

Table A-1 continued

No.	Reference	Specimens name	Column details		Beam details				Joint details							Failure mode
			b_c (mm)	h_c (mm)	b_b (mm)	h_b (mm)	ρ_{top}	$\rho_{bott.}$	A_{sh} (mm^2)	S (mm)	fy (MPa)	$f_c^{`}$ (MPa)	N (kN)	$V_{exp.}$ (kN)	γ_j	
94	(Li and Kulkarni, 2010)	EWB-1	300	900	800	300	1.41	1.41	402	100	460	64.1	0	1125.80	0.52	
95		EWB-2	900	300	800	300	1.41	1.41	402	100	460	65.9	0	1726.00	0.83	
96		EWB-3	300	900	800	300	1.41	1.41	402	100	460	47.8	0	1227.10	0.66	
97	(Li and Kulkarni, 2010)	BS-450	300	300	260	450	0.91	0.91	0	0	0	30.9	0	315.50		J
98		BS-450-H1T10	300	300	260	450	0.91	0.91	158	450	500	33.3	0	389.30	0.80	J
99		BS-450-H2T10	300	300	260	450	0.91	0.91	158	225	500	42.1	0	479.30	0.88	J
100		BS-600	300	300	260	600	0.66	0.66	0	0		36.4	0	283.90		J
101		BS-600-H2T8	300	300	260	600	0.66	0.66	100	300	500	41.8	0	360.10	0.66	J
102		BS-600-H4T8	300	300	260	600	0.66	0.66	100	150	500	29.7	0	342.40	0.75	J
103	(Chun and Shin, 2014)	H0.7S	300	300	250	200	2.84	2.13	332	75	430	34.8	0	646.00	1.33	B
104		H1.0S	300	300	250	300	1.82	1.36	332	75	430	34.8	0	563.00	1.16	B
105		H1.5S	300	300	250	450	1.14	0.85	332	75	430	34.8	0	498.00	1.02	BJ
106		H2.0S	300	300	250	600	0.83	0.62	332	75	430	48.2	0	526.00	0.92	BJ
107		H2.5S	300	300	250	750	0.65	0.49	332	75	430	48.2	0	454.00	0.79	BJ
108		H0.7U	300	300	250	200	2.84	2.13	234	75	430	34.8	0	611.00	1.26	B
109		H1.0U	300	300	250	300	1.82	1.36	234	75	430	34.8	0	529.00	1.09	B
110		M0.7S	300	300	250	200	2.84	2.13	332	75	430	34.8	0	596.00	1.22	B
111		M1.0S	300	300	250	300	1.82	1.36	332	75	430	34.8	0	557.00	1.14	B
112		M1.5S	300	300	250	450	1.14	0.85	332	75	430	34.8	0	530.00	1.09	BJ
113		M2.0S	300	300	250	600	0.83	0.62	332	75	430	48.2	0	493.00	0.86	BJ
114		M2.5S	300	300	250	750	0.65	0.49	332	75	430	48.2	0	455.00	0.79	N
115		M0.7U	300	300	250	200	2.84	2.13	234	75	430	34.8	0	683.00	1.40	B
116		M1.0U	300	300	250	300	1.82	1.36	234	75	430	34.8	0	592.00	1.22	B
117	(Chalioris, Favvata and Karayannis, 2008)	JCa-s1	100	200	100	200	1.57	1.57	101	100	470	20.6	41.2	69.37	0.76	BJ
118		JCa-s2	100	200	100	200	1.57	1.57	202	67	470	20.6	41.2	69.00	0.76	BJ
119		JCb-s1	100	200	100	200	1.57	1.57	101	100	470	23	46	104.90	1.09	J
120		JCb-s2	100	200	100	200	1.57	1.57	202	67	470	23	46	106.00	1.11	J

Table A-1 continued

No.	Reference	Specimens name	Column details		Beam details				Joint details							Failure mode
			b_c (mm)	h_c (mm)	b_b (mm)	h_b (mm)	ρ_{top}	$\rho_{bott.}$	A_{sh} (mm^2)	S (mm)	fy (MPa)	$f_c^{`}$ (MPa)	N (kN)	$V_{exp.}$ (kN)	γ_j	
121	(Hamil, 2000)	C4ALN1	150	150	110	210	2.05	1.16	57	200	500	47.3	50	182.58	1.36	J
122		C4ALN3	150	150	110	210	2.05	1.17	57	100	500	43.2	50	175.00	1.37	J
123		C4ALN5	150	150	110	210	2.05	1.17	57	50	500	52.3	50	199.50	1.41	B
124		C4ALH1	150	150	110	210	2.05	1.17	57	200	500	103	100	202.76	1.02	B
125		C4ALH3	150	150	110	210	2.05	1.17	57	100	500	114.3	100	217.78	1.04	B
126		C4ALH5	150	150	110	210	2.05	1.18	57	50	500	107.9	100	224.82	1.11	B
127		C6LN1	150	150	110	210	2.05	1.18	57	200	500	51.2	50	137.50	0.99	J
128		C6LN3	150	150	110	210	2.05	1.19	57	100	500	48.8	50	140.80	1.03	J
129		C6LN5	150	150	110	210	2.05	1.19	57	50	500	36.8	50	164.74	1.39	J
130		C6LH1	150	150	110	210	2.05	1.20	57	200	500	110	100	218.25	1.07	B
131		C6LH3	150	150	110	210	2.05	1.20	57	100	500	104.8	100	201.85	1.01	B
132		C6LH5	150	150	110	210	2.05	1.21	57	50	500	108	100	213.60	1.05	B

Table A-2 Experimental data for interior RC beam-column joints

No.	Reference	Specimens name	Column details		Beam details				Joint details							Failure mode
			b_c (mm)	h_c (mm)	b_b (mm)	h_b (mm)	ρ_{top}	$\rho_{bott.}$	A_{sh} (mm^2)	S (mm)	fy (MPa)	$f_c^{`}$ (MPa)	N (kN)	$V_{exp.}$ (kN)	γ_j	
1	(Durrani and Wight, 1985)	X1	362	362	279.4	419.1	1.50	1.10	508	152	352	34.3	222.4	840.00	1.05	BJ
2		X2	362	362	279.4	419.1	1.50	1.10	508	102	352	33.6	222.4	853.60	1.18	BJ
3		X3	362	362	279.4	419.1	1.12	0.82	508	152	352	31	222.4	628.70	1.09	BJ
4	(Fuji and Morita, 1991)	A1	220	220	160	250	1.69	1.87	56	50	297	40.2	147	412.00	1.56	J
5		A2	220	220	160	250	1.69	1.87	56	50	297	40.2	147	379.60	1.43	J
6		A3	220	220	160	250	1.69	1.87	56	50	297	40.2	441	412.00	1.56	J
7		A4	220	220	160	250	1.69	1.87	112	35	297	40.2	441	420.80	1.59	J
8	(Kitayama, Otani and Aoyama, 1991)	A1	300	300	200	300	2.05	2.05	84	45	326	30.6	177	826.20	1.66	J
9		A4	300	300	200	300	1.54	1.54	84	45	326	30.6	177	854.10	1.72	J
10	(Oka and Shiohara, 1992)	J-1	300	300	240	300	1.94	1.51	56	50	1374	81.2	834	1278.00	1.58	BJ
11		J-2	300	300	240	300	1.72	1.72	56	50	1374	81.2	834	1377.00	1.70	J
12		J-3	300	300	240	300	1.72	1.72	56	50	1374	81.2	834	1629.00	2.01	J
13		J-4	300	300	240	300	2.15	2.15	56	50	1374	72.8	834	1305.00	1.70	BJ
14		J-5	300	300	240	300	1.94	1.51	56	100	1374	72.8	834	1467.00	1.91	J
15		J-6	300	300	240	300	1.94	1.51	56	50	775	79.2	834	1359.00	1.70	BJ
16		J-7	300	300	240	300	1.51	1.08	56	50	775	79.2	834	1080.00	1.35	B
17		J-8	300	300	240	300	4.26	1.51	56	50	775	79.2	834	1539.00	1.92	J
18		J-10	300	300	240	300	1.94	1.51	56	50	598	39.2	417	972.00	1.72	J
19		J-11	300	300	240	300	4.26	1.51	56	50	401	39.2	417	1143.00	2.03	J
20	(Raffaelle and Wight, 1995)	1	355.6	355.6	254	381	1.02	0.72	284	89	441	28.6	89	604.95	1.04	BJ
21		2	355.6	355.6	177.8	381	0.97	0.68	284	89	441	26.8	89	420.80	0.99	BJ
22		3	355.6	355.6	190.5	381	0.95	0.64	284	89	441	37.7	89	471.50	0.89	BJ
23		4	355.6	355.6	190.5	558.8	0.63	0.42	284	89	441	19.3	89	412.40	1.08	BJ
24	(Hegger, Sherif and Roeser, 2003)	RA1	150	240	150	300	1.64	1.64	0	0	530	53.1	497	527.00		J
25		RA2	150	240	150	300	1.64	1.64	56	75	530	66.1	458	597.00	2.04	J
26		RA3	150	240	150	300	1.94	1.94	100	60	530	43.6	499	504.00	2.12	J
27		RA4	150	240	150	300	2.74	2.74	100	60	530	66.1	641	771.00	2.63	J
28		RA5	150	240	150	300	1.51	1.51	56	60	530	56.2	502	494.00	1.83	J
29		RA6	150	240	150	300	1.64	1.64	56	60	530	56.2	336	663.00	2.46	J
30		RA7	150	300	150	300	1.90	1.90	157	60	530	79.7	457	770.00	1.92	J
31	(Fumio *et al.*, 2004)	JE-0	320	280	180	300	1.58	1.58	64	100	364	27	0	609.30	1.68	J
32		JE-55	320	280	180	300	1.58	1.58	64	100	364	27	0	504.60	1.56	J
33		JE-55S	320	280	180	300	1.58	1.58	359	75	359	27	0	497.10	1.54	J

Table A-2 continued

No.	Reference	Specimens name	Column details		Beam details				Joint details							Failure mode
			b_c (mm)	h_c (mm)	b_b (mm)	h_b (mm)	ρ_{top}	$\rho_{bott.}$	A_{sh} (mm^2)	S (mm)	fy (MPa)	$f_c^{`}$ (MPa)	N (kN)	$V_{exp.}$ (kN)	γ_j	
34	(Joh, Goto and Shibata, 1991)	UM-0	450	300	200	350	1.66	1.66	56	50	355	24	540	810.00	2.00	J
35		UM-60	450	300	200	350	1.66	1.66	56	50	355	24.6	540	780.00	2.14	J
36		UM-125	450	300	200	350	1.66	1.66	56	50	355	25.2	540	670.00	1.82	J
37	(Teraoka *et al.*, 2005)	HJ-1	400	400	300	400	1.08	1.08	142	50	347	54.2	1734.4	1424.00	1.21	B
38		HJ-2	400	400	300	400	0.75	0.75	142	50	347	54.2	1734.4	1584.00	1.34	B
39		HJ-3	400	400	300	400	0.57	0.57	142	50	347	54.2	1734.4	1440.00	1.22	B
40		HJ-4	400	400	300	400	1.69	1.69	142	50	347	54.2	1734.4	2000.00	1.70	J
41		HJ-5	400	400	300	400	1.08	1.08	142	50	347	54.2	1734.4	2144.00	1.82	J
42		HJ-6	400	400	300	400	0.81	0.81	142	50	347	54.2	1734.4	2080.00	1.77	BJ
43		HJ-7	400	400	300	400	2.28	2.28	200	50	681	92.6	2963.2	2944.00	1.91	J
44		HJ-8	400	400	300	400	1.45	1.45	200	50	681	92.6	2963.2	2864.00	1.86	J
45		HJ-9	400	400	300	400	1.08	1.08	200	50	681	92.6	2963.2	2784.00	1.81	BJ
46		HJ-10	400	400	300	400	1.63	1.63	200	50	681	88.7	2838.4	3056.00	2.03	J
47		HJ-11	400	400	300	400	3.13	3.13	200	50	681	88.7	2838.4	4032.00	2.68	J
48		HJ-12	400	400	300	400	3.13	3.13	200	50	681	88.7	2838.4	4720.00	3.13	J
49		HJ-13	400	400	300	400	1.99	1.99	200	50	681	116.9	3740.8	3648.00	2.11	J
50		HJ-14	400	400	300	400	3.13	3.13	200	50	681	116.9	3740.8	4928.00	2.85	J
51		HJ-15	400	400	300	400	1.21	1.21	100	40	797	138.2	4422.4	3088.00	1.64	J
52		HJ-16	400	400	300	400	1.90	1.90	100	40	797	138.2	4422.4	4464.00	2.37	J
53	(Teng and Zhou, 2003)	S1	400	300	200	400	1.44	0.86	237	75	440	33	441	1032.00	1.50	BJ
54		S2	400	300	200	400	1.44	0.86	237	75	440	34	441	1032.00	1.47	BJ
55		S3	400	300	200	400	1.44	0.86	237	75	440	35	441	996.00	1.40	BJ
56		S5	400	200	200	400	0.92	0.55	237	50	440	39	343	600.00	1.20	BJ
57		S6	400	200	200	400	0.92	0.55	237	50	440	38	434	584.00	1.18	BJ
58	(Li and Leong, 2014)	NS1	300	450	250	500	0.73	0.73	314.16	65	357	61.65	0	608.85	0.57	B
59		AS1	300	450	250	500	0.73	0.73	314.16	65	357	61.65	2470	599.40	0.57	B
60		NS2	300	450	250	500	0.71	0.36	213.6	65	357	61.65	0	498.15	0.47	B
61		AS2	300	450	250	500	0.71	0.36	213.6	65	357	61.65	247	480.60	0.45	B
62		NS3	300	450	250	500	0.71	0.71	314.16	65	357	61.65	0	666.90	0.63	B
63		AS3	300	450	250	500	0.71	0.71	314.16	65	357	61.65	2470	661.50	0.62	B
64		NS4	300	450	250	500	0.56	0.36	314.16	85	357	61.65	0	421.20	0.40	B
65		AS4	300	450	250	500	0.56	0.36	314.16	85	357	61.65	2470	415.80	0.39	B

Table A-2 continued

No.	Reference	Specimens name	Column details		Beam details				Joint details							Failure mode
			b_c (mm)	h_c (mm)	b_b (mm)	h_b (mm)	ρ_{top}	$\rho_{bott.}$	A_{sh} (mm^2)	S (mm)	fy (MPa)	$f_c^{`}$ (MPa)	N (kN)	$V_{exp.}$ (kN)	γ_j	
66	(Yang *et al*., 2018)	CL-1	400	400	350	500	0.87	0.75	226.2	60	407	28.4	1136	1120.00	1.40	J
67		BL-1	400	400	350	500	0.87	0.75	226.2	60	407	23	920	1190.00	1.65	J
68		CL-2	400	400	300	500	1.43	0.95	226.2	50	368	30.56	1466.9	1162.00	1.50	J
69		BL-2	400	400	300	500	1.43	0.95	226.2	50	368	30	1440	1276.00	1.66	J
70		CL-3	350	450	250	400	1.88	0.94	226.2	60	464	27.44	1080.5	945.00	1.34	J
71		BL-3	350	450	250	400	1.88	0.94	226.2	60	464	23.84	938.7	1034.00	1.57	J
72		CL-4	400	400	300	500	1.21	0.76	226.2	50	362	24.16	966.4	947.00	1.38	J
73		BL-4	400	400	300	500	1.21	0.76	226.2	50	362	26.24	1049.6	1038.00	1.45	J
74	(Shiohara and Kusuhara, 2009)	B01	240	240	240	240	0.98	0.98	56	120	399	29	0	437.00	1.41	J
75		B02	240	240	240	240	1.22	1.22	56	120	399	29	0	551.00	1.78	J
76		B03	240	240	240	240	1.92	1.92	56	120	399	29	0	472.00	1.52	J
77		B04	240	240	240	240	0.98	0.98	56	120	399	29	0	434.00	1.40	J
78		B05	240	240	240	240	1.22	1.22	56	120	399	29	0	545.00	1.76	J
79		B06	240	240	240	240	1.22	1.22	56	120	399	29	0	548.00	1.77	J
80		B07	240	240	240	240	1.07	1.07	56	120	399	29	0	437.00	1.41	J
81		B08	240	240	240	240	1.18	1.18	56	120	399	29	0	434.00	1.40	J
82		B09	240	240	240	240	2.09	2.09	56	120	399	29	0	690.00	2.22	J
83		B10	240	240	240	240	2.30	2.30	56	120	399	29	0	719.00	2.32	J
84		D01	240	340	240	170	1.81	1.81	56	85	399	32.4	0	309.00	0.67	J
85		D02	240	340	240	170	1.81	1.81	56	85	399	32.4	0	376.00	0.81	J
86		D03	240	340	240	170	1.81	1.81	56	85	399	32.4	0	425.00	0.92	J
87		D04	240	340	240	170	2.54	2.54	56	85	399	32.4	0	317.00	0.68	J
88		D05	240	340	240	170	2.54	2.54	56	85	399	32.4	0	289.00	0.62	J
89		D06	240	340	240	170	2.54	2.54	56	85	399	32.4	0	318.00	0.68	J
90		D07	240	340	240	170	2.54	2.54	56	85	399	32.4	0	356.00	0.77	J
91		D08	240	340	240	170	3.98	3.98	56	85	399	32.4	0	583.00	1.26	J
92	(Alaee and Li, 2017)	IN80	300	450	250	500	0.71	0.36	157	65	500	80	0	810.00	0.67	BJ
93		IH80	300	450	250	500	0.71	0.36	157	85	700	80	0	729.00	0.60	BJ
94		IH80A	300	450	250	500	0.71	0.36	157	85	700	80	3240	1026.00	0.85	BJ
95		IN100	300	450	250	500	0.71	0.36	157	65	700	100	0	553.50	0.41	BJ
96		IH100	300	450	250	500	0.71	0.36	157	65	700	100	0	742.50	0.55	BJ
97		IH60	300	450	250	500	0.50	0.50	157	85	700	60	0	837.00	0.80	BJ
98		IH60A	300	450	250	500	0.50	0.50	157	85	700	60	2430	850.50	0.81	BJ

Table A-2 continued

No.	Reference	Specimens name	Column details		Beam details				Joint details							Failure mode
			b_c (mm)	h_c (mm)	b_b (mm)	h_b (mm)	ρ_{top}	$\rho_{bott.}$	A_{sh} (mm^2)	S (mm)	fy (MPa)	$f_c^{`}$ (MPa)	N (kN)	$V_{exp.}$ (kN)	γ_j	
99	(Gentry and Wight, 1994)	WB1	356	356	864	305	0.78	0.61	284	102	441	27.6	89	616.10	0.83	J
100		WB2	356	356	762	305	0.79	0.59	284	102	441	27.6	89	643.10	0.85	B
101		WB3	356	356	864	305	0.76	0.60	284	102	441	27.6	89	725.60	0.94	BJ
102		WB4	356	356	864	305	0.98	0.81	284	102	441	27.6	89	813.70	1.07	B
103	(LaFave and Wight, 1999)	EWB-1	356	356	864	305	1.02	0.64	284	89	482	29	0	752.70	0.99	B
104		EWB-2	356	356	864	305	0.81	0.64	284	89	482	30.3	0	820.00	0.90	B
105		EWB-3	305	508	940	305	1.04	0.85	213	76	482	34.5	0	1094.70	0.81	B
106	(Shin and LaFave, 2004)	SL1	457	330	279	406	0.46	0.32	213	83	468	29.9	0	645.00	1.09	BJ
107		SL2	457	330	178	406	0.46	0.32	213	83	468	36.1	0	649.40	1.44	BJ
108		SL3	457	330	279	406	0.46	0.32	213	83	551	47.4	0	645.00	0.81	B
109		SL4	279	368	279	406	0.54	0.38	213	83	579	31.1	0	791.80	1.36	BJ
110	(Canbolat and Wight, 2008)	1-S	356	356	203	381	1.17	0.76	508	95	437	29	196	778.40	1.58	BJ
111		2-S	534	356	254	457	1.06	0.57	508	95	437	39	289	863.00	1.26	BJ
112		3-S	534	356	254	457	1.06	0.57	508	95	437	29	234	827.40	1.40	BJ
113		1-N	356	356	203	381	1.08	0.76	508	95	437	29	184	569.40	1.06	BJ
114		2-N	356	534	254	457	1.33	0.97	508	95	437	39	231	809.60	0.80	BJ
115		3-N	356	534	254	457	1.57	1.09	508	95	437	29	169	1156.50	1.32	BJ

Hand calculation of the control specimen designed based on ACI 318-19 and ACI-ASCE 352.

No.	Calculation and discussion	Code reference
1.	**Specimen Dimension** a) Column dimension The column dimension was selected based on the development length of longitudinal reinforcement of beam framed into the column. The top longitudinal steel reinforcement must be provided with hooks to develop its yield strength at the face of the column. The development length of the standard hook can be calculated as follow: $l_{dh} = greater\ of \begin{cases} \left(\frac{0.24 f_y d_b}{\lambda\sqrt{f_c`}}\right) = 235mm \\ 8d_b = 80mm \\ 150\ mm \end{cases}$ When longitudinal beam reinforcement passes through a beam-column joint, the joint depth h must be at least the greatest of (a) through (c): a) 20 d_b of the largest Grade 420 longitudinal bar =200 mm b) 26 d_b of the largest Grade 550 longitudinal bar=260 mm Use column dimension of $(250\ mm \times 250\ mm)$, which provides a development length equal to 244 mm	ACI 318 18.8.5.1 ACI 318 18.8.2.3
	b) Beam dimension Use 180mm in width and 250 mm in total depth	
2.	**Design of beam**	
	a) Flexural strength $b = 180\ mm, h = 250\ mm,\ \ f_y = 596Mpa\ and\ f_c` = 37\ Mpa$ $A_s = 6\emptyset 10mm\ and\ A_s` = 3\emptyset 10mm$ $d = 250 - 20 - 6 - 10 - 12.5 = 201.5mm$ $\rho = \frac{A_s}{bd} = 0.013, \quad \rightarrow \quad \rho_{min.} < \rho < \rho_{max.}$ $a = \frac{A_s f_y}{0.85 f_c` b} = \frac{6 \times 78.5 \times 596}{0.85 \times 37 \times 180} = 49.58\ mm$ $M_n = A_s f_y (d - a/2)$ $= 6 \times 78.5 \times 596(201.5 - 50.13/2) \times 10^{-6} = 49.53 kN.m$ $M_n = P \times l\ , \quad \rightarrow$ P = 90.23 kN *for one beam* (control)	
	b) Shear strength	
	Hoops shall be provided in the following regions of a beam: (a) Over a length equal to twice the beam depth measured from the face of the supporting column toward midspan, at both ends of the beam	ACI 318 18.6.4.1

No.	Calculation and discussion	Code reference
	(b) Over lengths equal to twice the beam depth on both sides of a section where flexural yielding is likely to occur as a result of lateral displacements beyond the elastic range of behavior.	
	The first hoop shall be located not more than 50 mm from the face of a supporting column. Spacing of the hoops shall not exceed the least of (a) through (d): (a) d/4 =50 mm (b) 150 mm (c) For Grade 420, 6db of the smallest primary flexural reinforcing bar =60mm (d) For Grade 550, 5db of the smallest primary flexural reinforcing bar =50 mm	ACI 318 18.6.4.4
	$A_{v,min}/s = greater \begin{cases} 0.062\sqrt{f_c`}\,\frac{b_w}{f_{yt}} \\ 0.035\,\frac{b_w}{f_{yt}} \end{cases}$ $A_{v,min}/s = greater \begin{cases} 0.062 \times \sqrt{37} \times \frac{180}{617} = 0.11 control \\ 0.035 \times \frac{180}{617} = 0.01 \end{cases}$ The beams are reinforced by$\emptyset 6mm$ @$50mm\ c/c$ $A_v/s = \frac{2 \times (\pi/4) \times 6^2}{50} = 1.13 > A_{v,min}/s$	ACI 318 9.6.3.4
	$V_c = 0.17\sqrt{f_c`}\ b_w\ d$ $V_c = 0.17 \times \sqrt{37} \times 180 \times 201.5 \times 10^{-3} = 27.5kN$ $V_s = \frac{A_v \times f_{yt} \times d}{s}$ $V_s = \frac{2 \times (\pi/4) \times 6^2 \times 617 \times 201.5}{50 \times 1000} = 140.6\text{kN}$ $V_n = (V_c + V_s)$ $\rightarrow\ P = (27.5 + 140.6) \quad \rightarrow \text{P} = 168.1\ \text{kN}$ for one beam Check the cross-section diamension $V_u \leq \left(V_c + 0.66\sqrt{f_c`}\ b_w\ d\right)$ $V_u = 75\ kN < 168.1\ kN$	ACI 318 22.5.5.1 ACI 318 22.5.8.5.3 ACI 318 22.5.1.2
3.	**Column design**	
	a) Flexural strength	
	$A_g = 250 \times 250\ mm, A_s = 8\emptyset 12\ mm\ ,\ \ \rho = \frac{A_s}{A_g} = 0.0144$	
	$0.01 < \rho < 0.06$	ACI 318 18.7.4.1

No.	Calculation and discussion	Code reference
	A constant axial load equivalent to $0.15\ A_g f_c^{`}$ will be applied to the column to represent service load $P_{axial} = 0.07\ A_g f_c^{`} = 150\ kN$ The nominal moment capacity of the upper column can be calculated as follow: $\frac{P_n}{A_g f_c^{`}} = \frac{280\times1000}{250\times250\times37} = 0.064, \quad \gamma = \frac{250-2\times32}{250} = 0.744, say\ 0.7$ $From\ the\ interaction\ curve\ diagram$ $\rightarrow R_n = 0.1 = \frac{M_n}{A_g f_c^{`} h} \qquad \rightarrow M_n = 57.8\ kN.m$ The applied load on the lower column is: $P_{axial} = 150 + 180 = 330\ kN$ $k_n = 0.23, \gamma = 0.7 \ \rightarrow\ R_n = 0.145, \rightarrow M_n = 67.96\ kN.m$	
	$\sum M_c > \frac{6}{5} \sum M_b$ (strong column-weak beam)	ACI 318 18.7.3.2
	$\sum M_{nc} = 57.8 + 67.96 = 125.76\ kN.m$ $\sum Mn_b = 49.53 + 49.53 = 99\ kN.m$ $\sum M_c > \frac{6}{5} \sum M_b$ ok	
	b) Transverse reinforcement	ACI 318 18.7.5.1
	Transverse reinforcement shall be provided over a length ℓ_o from each joint face.	
	Length ℓ_o shall be at least the greatest of (a) through (c): (a) The depth of the column at the joint face or at the section where flexural yielding is likely to occur=250mm (b) One-sixth of the clear span of the column=125mm (c) 450 mm	
	Spacing of transverse reinforcement shall not exceed the least of (a) through (d): (a) One-fourth of the minimum column dimension=62.5mm control (b) For Grade 420, 6db of the smallest longitudinal bar=72 (c) For Grade 550, 5db of the smallest longitudinal bar (d) so, $100\ mm \le s_o \le 150\ mm$	ACI 318 18.7.5.3
	The amount of transverse reinforcement	ACI 318 18.7.5.4
	For $P_u \le 0.3 A_g f_c^{`}\ and\ \ f_c^{`} \le 70MPa$ $A_{sh}/s\ b_c = greater\ of \begin{cases} 0.3\left(\frac{A_g}{A_{ch}} - 1\right)\frac{f_c^{`}}{f_{yt}} = 0.01 \\ 0.09\frac{f_c^{`}}{f_{yt}} = 0.0054 \end{cases}$ $A_{sh}/50 \times 200 = 0.01 \ \rightarrow A_{sh} = 100mm^2$ $A_{sh,provide} = 4 \times 28.27(4Ø6mm) = 113.1mm^2\ \ ok$ *Use* *Ø6 mm @50 mm*	

No.	Calculation and discussion	Code reference
4.	**Joint shear strength** In accordance to ACI-318, the shear strength of the corner joint can be calculated as follows:	
	a) Shear strength	
	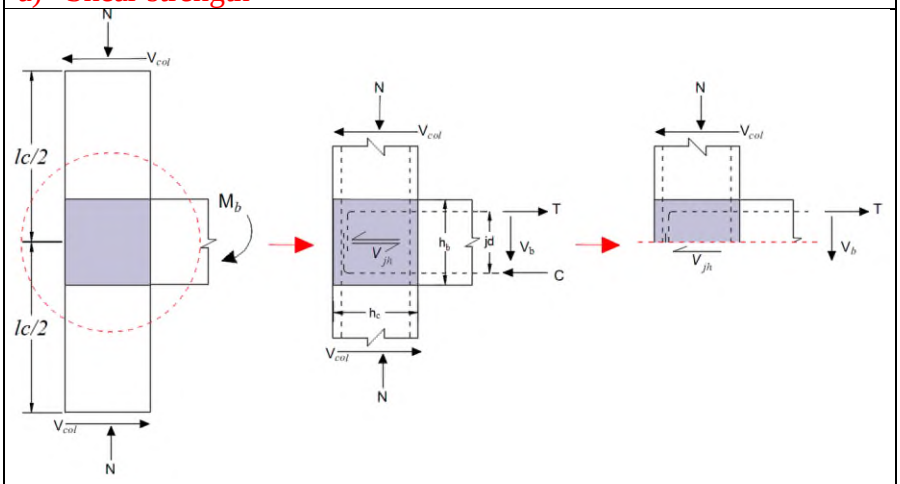	
	$M_n\ of\ beam = M_u subjected\ on\ joint = 41.14\ kN.m$ $V_{col.} = \frac{M_n}{l} = \frac{49.53}{1.0} = 49.53\ kN.m$ $V_{uj} = A_s f_y - V_{col.} = 6 \times 78.5 \times 1.25 \times 596 - 49.53$ $= 280.7\ kN$	
	$V_{cj} = \gamma \sqrt{f_c'} b_j h_c$	ACI 318 15.4.2
	$\gamma = 1\ for\ corner\ joint\ (Type\ 2\ connection)$ $h_c = the\ depth\ of\ column\ in\ the\ direction\ of$ $joint\ shear\ being\ considered = 250\ mm$ $b_c > b_b \rightarrow b_j = min.\begin{cases} b_b + 2x = 180 + 70 = 250\ mm \\ b_b + b_c = 180 + 250 = 430\ mm \end{cases}$ $b_c < b_b \rightarrow b_j = b_c$ $V_{cj} = 1 \times \sqrt{37} \times 250 \times 250 \times 10^{-3}$ $= 380.17\ kN$ $V_{cj} > V_{uj}\ \ ok$ 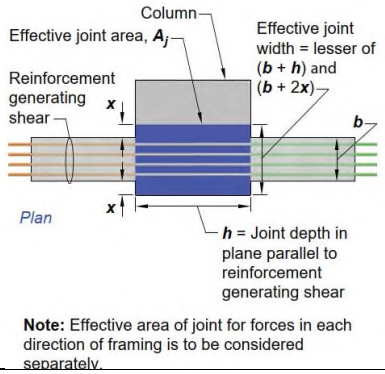 **Note:** Effective area of joint for forces in each direction of framing is to be considered separately.	
	b) Joint transverse reinforcement	ACI 318 18.8.3
	Because the joint is not confined on all four sides, the transverse reinforcement in the column must be continued, unchanged, through the joint. *Use* *Ø6 mm @50 mm*	

Table C-1: Mechanical properties of cement.

Mechanical Properties	Test results	IQ.S No. 5/2019
Initial setting time (min)	70	≥ 45 min
Final setting time (min)	255	≤ 600 min
Fineness (m^2/kg)	303	≥ 250 m^2/kg
Compressive strength, MPa		
3 days	17.39	≥ 15 MPa
7 days	27.06	≥ 23 MPa

Table C-2: Chemical analysis of cement.

Chemical composition	% by weight.	Limits of IQ.S No.5/2019
Lime	61.25	------
Silica	19.78	------
Alumina	3.41	------
Iron oxide	4.8	------
Sulfate	2.29	≤ 2.5 % If C3A< 5% ≤ 2.8 % If C3A > 5%
Magnesia	1.72	≤ 5%
Ratio	0.914	≤ 3.5%
Loss on ignition	2.42	≤ 4%
Insoluble residue	0.85	≤ 1.5 %
Lime saturation Factor	0.953	(0.66–1.02)%

Table C-3: Chemical properties of coarse aggregate used in NSC.

Properties	Test results	IQ.S No. 45/2016
Specific gravity	2.66	------
Sulfate content SO3	0.03%	≤ 0.1 %
Absorption	0.6%	------
Clay content	0.2%	≤ 3%

Table C-4: Grading of coarse aggregate used in NSC.

Sieve Size (mm)	Passing %	
	Coarse aggregate	IQ.S No. 45/2016
37.5	100	100
20.0	100	100 - 95
9.5	43	60 - 30
5.0	3	10 - 0

Table C-5: The chemical and mechanical properties of fine aggregate used in UHPC and NSC.

Properties	Test results	IQ.S No. 45/2016 zone (2)
Specific gravity	2.6	------
Fineness modulus	3.8	≤ 5 %
Sulfate content SO_3	0.22%	≤ 0.5 %
Absorption	2%	------

Table C-6: Grading of fine aggregate used in UHPC and NSC.

Sieve size (mm)	Passing %	
	Fine aggregate	IQ.S No. 45 Zone (2)
9.5	100	100
4.75	91	90 - 100
2.36	83	75 - 100
1.18	74.8	55 - 90
0.60	57.2	35 - 59
0.30	24.2	8 - 30
0.15	7.2	0 - 10

جمهورية العراق
وزارة التعليم العالي و البحث العلمي
جامعة بابل
كلية الهندسة
قسم الهندسة المدنية

السلوك الإنشائي لمفاصل العتب-العمود الركنية المنفذة من الخرسانة المسلحة الهجينة تحت تأثير الأحمال الاحادية و الدورية

اطروحة
مقدمة إلى قسم الهندسة المدنية في كلية الهندسة-جامعة بابل و هي جزء من متطلبات نيل درجة دكتوراه فلسفة في الهندسة المدنية-إنشاءات

من قبل

وســـــــام نـــــادر نجم عبد الله

إشراف

الأستاذ الدكتور عمـــــار ياســـــر علي

2023 م

1444 هـ

الخلاصة

تلعب مفاصل العتب-العمود دورًا مهمًا في الحفاظ على سلامة الهياكل الخرسانية المسلحة أثناء الزلزال. من المعروف أن هذه المفاصل تسبب أضرارًا كبيرة وقد تؤدي إلى انهيار المبنى إذا لم يتم تصميمها بشكل مناسب. في السنوات الأخيرة ، تم إجراء العديد من التطوير لتحسين الأداء الزلزالي لمكونات المبنى ، بما في ذلك مفصل العتب-العمود. ومع ذلك ، على الرغم من هذه التحسينات ، لا تزال مفاصل العتب-العمود الخارجية ، وخاصة المفاصل الركنية ، عرضة للتلف الشديد أثناء الزلازل.

لمعالجة هذه المشكلة ، تم إجراء دراسة تجريبية لتحسين أداء مفاصل العتب-العمود الركنية باستخدام الخرسانة فائقة الأداء (UHPC) بدلاً من الخرسانة ذات المقاومة العادية (NSC) في منطقة المفصل. تم انشاء اثنين وعشرين مفصل ركني خرساني مسلح مصغر و تم اختباره تحت الحمل الدوري والرتيب. كانت المتغيرات الرئيسية هي وجود حديد التسليح العرضي في قلب المفصل أم لا ، مادة المفصل ، وتشكيل UHPC في منطقة المفصل ، وتباعد حديد التسليح العرضي للاعضاء الانشائية المجاورة للمفصل ، وطول التثبيت المطمورالذي يمر عبر المفصل وكذلك اسلوب التحميل .

أظهرت نتائج الدراسة أن استخدام UHPC في منطقة المفصل يمكن أن يؤدي إلى تحول في آلية الفشل من فشل قص المفصل الهش إلى فشل الانحناء ، والذي ينتج عن إنشاء مفصل بلاستيكي في واجهة المفصل-العتب. بالإضافة إلى ذلك ، يعمل UHPC على تحسين مقاومة القص ، وقدرة تحمل الأحمال بمقدار يتراوح من 27% الى 54%، وامتصاص الطاقة يصل الى 163% ، وتحمل الضرر ، على الرغم من عدم استخدام حديد التسليح العرضي في قلب المفصل. علاوة على ذلك ، فإن استخدام UHPC في منطقة المفصل يسمح بتقليل حديد التسليح العرضي في الاعتاب والأعمدة ، مما يقلل من تزاحم حديد التسليح في منطقة المفصل. علاوة على ذلك ، فإن استبدال NSC في منطقة المفصل بـ UHPC يقلل من طول التثبيت لقضبان حديد التسليح الطولية للاعتاب الواجب توفيرها في قلب المفصل من 25 مرة بقدر قطر قضبان حديد التسليح الطولي للاعتاب و الموصى به من قبل معظم المدونات العالمية الى 15 مرة بقدر قطر قضبان حديد التسليح الطولي للاعتاب و ذلك لما تمتلكه UHPC من قوة ربط عالية .

من ناحية أخرى ، فإن استخدام قضبان GFRP كتقوية مثبتة بالقرب من السطح (NSM) يظهر أداءً فائقًا مقارنة باستخدام قضبان GFRP المستخدمة داخليًا.

من الناحية النظرية ، تميل معظم المدونات العالمية إلى المبالغة في تقدير قوة القص لمفاصل العتب-العمود وقد لا تكون مناسبة للاستخدام في التصميم. هذا يمكن أن يؤدي إلى وصلات غير كفوئة ويضر بالسلامة الهيكلية الشاملة للمباني الخرسانية المسلحة أثناء الزلازل أو غيرها من الأحداث. بناءً على الدراسة التحليلية ، تم اقتراح تعديل لاحد المدونات يوفر حسابًا أكثر دقة لمقاومة القص لمفاصل العتب-العمود الخارجية.